Selective Laser Sintering of Polycaprolactone/Bioceramic Composite Bone Scaffolds

By

Szilvia Eosoly, MSc, MIEI

This thesis is submitted for the award of degree of

Doctor of Philosophy

Materials Processing Research Centre

School of Mechanical and Manufacturing Engineering

DUBLIN CITY UNIVERSITY

Supervisor: Dr. Lisa Looney

August 2009

Declaration

I hereby certify that this material, which I now submit for assessment on the programme of study leading to the award of Doctor of Philosophy is entirely my own work, that I have exercised reasonable care to ensure that the work is original, and does not to the best of my knowledge breach any law of copyright, and has not been taken from the work of others save and to the extent that such work has been cited and acknowledged within the text of my work.

Signed:

(Candidate)

ID No.: 57100250

Date: 7 August, 2009

Acknowledgments

There are many people that I would like to thank for helping me to carry out this work. Thanks to my supervisor Dr. Lisa Looney, and for Dr. Dermot Brabazon for his help and support.

Sincere thanks to Dr. Stefan Lohfeld at the National University of Ireland, Galway for granting access to selective laser sintering facilities, for his suggestions and advice and for his invaluable help in the experiments throughout this work.

Thank you to my fellow PhD students Diana Garcia-Alonso, Irina Pascu, Nihail Engin Vrana, Yurong Liu and Marcin Lipowieczki for their continuous support encouragement and friendship. A big thank you to Nihal Engin Vrana for carrying out all degradation and cell culturing work and for his useful advice and discussions.

The assistance of the following people is also acknowledged:

- Dr. Bela Pukanszky at the Budapest University of Technology and Economics for granting access to DSC and DMA equipments, and for all staff of the faculty for their support in carrying out the thermal analysis experiments,
- Dr. Gerard Ryder and Anthony Tansey at the Institute of Technology, Tallaght for granting access to SLS facilities to carry out preliminary experiments detailed in Appendix I,
- Dr. John O'Dwyer and Dr. Craig Sturrock at Waterford Institute of Technology.

Thanks to Tamas Szucs for his invaluable help and support throughout this work.

This research has been supported by a Marie Curie Early Stage Research Training Fellowship of the European Community's Sixth Framework Programme under contract number MEST-CT-2005-020621.

Publications arising from this work

Journal Papers

S. Eosoly, D. Brabazon, S. Lohfeld, L. Looney, Selective laser sintering of hydroxyapatite/poly-ε-caprolactone scaffolds, ***Acta Biomaterialia***, accepted for publication 2009 July (DOI:10.1016/j.actbio.2009.07.018)

S. Eosoly, S. Lohfeld, D. Brabazon, Effect of hydroxyapatite on biodegradable scaffolds fabricated by SLS, ***Key Engineering Materials***, Vols. 396-398 (2009) pp 659-662

Conference Papers

Eosoly, S., Ryder, G., Tansey, T. and Looney, L., Accuracy and mechanical properties of open-cell microstructures fabricated by selective laser sintering, ***Eighteenth annual Solid Freeform Fabrication Symposium***, University of Texas at Austin, August 2007

Szucs, T.D., Eosoly, S., Liu, Y., and Brabazon, D., 3D Printing of Calcium Phosphate Based Bone Scaffolds, ***9th National Conference on Rapid Design, Prototyping, and Manufacturing***, eds Jacobson D, Bocking CE, Rennie AEW, 2008, CRDM/Lancaster University, 13th June 2008, pp. 49-57, ISBN 978-0-948314-55-1

Szucs, T.D., Eosoly, S., Brabazon, D., and Olah, L., FEA and experimental mechanical property comparison of 3DP bone scaffold geometries, ***8th National Conference on Rapid Design, Prototyping & Manufacture,*** eds Jacobson D, Bocking CE, Rennie AEW, 2007, CRDM/Lancaster University, 15th June 2007, pp. 23-30, ISBN 9-780948314-537.

Abstracts in Conference Proceedings

S. Eosoly, G. Ryder, S. Lohfeld, A. Menyhard, B. Pukanszky, D. Brabazon, L. Looney, Effect of Material Composition in Selective laser sintering of biodegradable scaffolds, ***Bioengineering in Ireland 15 Conference***, Limerick, January 2009 (oral presentation)

S. Eosoly, D. Brabazon, S. Lohfeld, L. Looney, Selective laser sintering of hydroxyapatite/poly-ε-caprolactone scaffolds, ***European Materials Research Society Fall Meeting***, Warsaw, September 2008 (oral presentation)

S. Eosoly, G. Ryder, T. Tansey, L. Looney, Selective laser sintering of bioresorbable microstructures, ***8th World Biomaterials Congress***, Amsterdam, 2008 May (poster presentation)

Table of Contents

TABLE OF FIGURES

LIST OF ABBREVIATIONS

ANOVA	analysis of variance
CCD	central composite design
CSA	cross sectional area
CT	computer tomography
DFM	design for manufacturing
DMA	dynamic mechanical analysis
DOE	design of experiments
DSC	differential scanning Calorimetry
DTA	differential Thermal Analaysis
ECM	extracellular matrix
ED	energy density
FDA	Food and Drug administration
FDM	fused deposition medeling
FP	laser fill power
FTIR	Fourier transform infrared spectroscopy
GA	Gibson-Ashby
HA	hydroxyapatite
HCA	hydroxycarbonate-apatite
HDPE	high density polyethylene
MRI	magnetic resonance imageing
OP	outline laser power
P	laser power

PA	polyamide
PCL	poly caprolactone
PEEK	poyetheretherketon
PLG	poly-l-lactide-co-glycolide
PLLA	poly-l-lactic-acid
PVA	poly vinyl alcohol
RM	rapid manufacturing
RP	rapid prototyping
RSM	response surface methodology
SEM	scanning electron microscopy
SLS	selective laser sintering
SS	scan spacing
SSF	solid freeform fabrication
TCP	tricalcium phosphate
TGA	thermograviometric analysis
v_{beam}	laser speed

NOMENCLATURE

˚C	degrees Celsius
Da	Dalton
E	modulus of the lattice structure
E_s	modulus of the solid material the lattice is made of
n	scan count
p	probability
R^2	regression coefficient
R_a	surface roughness
T_c	crystallization temperature
T_m	melting temperature
T_{pb}	part bed temperature
v_{beam}	laser speed
W	watts
wt%	weight percent
Z	connectivity
z_{layer}	layer thickness
ΔH_c	crystallization enthalpy
ΔH_f	melting enthalpy, heat of fusion
ε	strain
λ	wavelength
ρ	density

σ	stress
σ_y	yield strength of the lattice structure
σ_{ys}	yield strength of the solid material the lattice is made of

ABSTRACT

Selective Laser Sintering of Polycaprolactone/Bioceramic Composite Bone Scaffolds

S Eosoly

Selective Laser Sintering (SLS), a powder based rapid prototyping technology has the potential to fabricate the complex geometries with intricate and controllable internal architecture required for tissue engineering applications. Challenges relate to scale of features, mechanical properties and getting the right porosities and surface characteristics.

In this work polycaprolactone, a bioresorbable elastomer, and its composites with hydroxyapatite were studied and fabricated as three-dimensional lattice structures. Thermal and morphological characterisation of the candidate powders was carried out to select suitable compositions for fabrication. Capabilities of the technology are explored with special emphasis on anisotropy of fabricated 3D micro-lattices, which has not been investigated previously. The effect of material composition, including different weight percentages of hydroxyapatite are investigated in terms of thermal and mechanical behaviour, surface characteristics and biocompatibility.

The influence of SLS processing parameters on mechanical properties, accuracy and porosity of the scaffolds are extensively examined using response surface methodology (RSM). Scan spacing and outline laser power were found to be the most significant parameters in determining part properties. The most commonly used SLS process parameters were mathematically related to the examined response functions, and models that can predict mechanical and dimensional properties of fabricated scaffolds were developed. The developed models are better predictors of these properties than delivered energy density that is traditionally used to give some guidance on resulting part characteristics. Furthermore, less explored SLS parameters such as scan count and part position were also examined and part properties were found to be very sensitive to these parameters even at constant delivered energy density levels.

Overall, this work demonstrates that by exploiting insights gained into orientation effects and parameter influences on mechanical properties, micro and macrostructure and therefore on scaffold performance SLS is a viable manufacturing technology for fabricating biodegradable microstructures for application in bone tissue engineering.

1 INTRODUCTION

Treatments for damaged or lost bone tissue include transplantation, surgical reconstruction, drug therapy and synthetic prostheses. Current treatments have many drawbacks and limitations. Bone substitutes either have limited availability or there is a high risk of infection. These limitations and associated problems have urged the development of synthetic, trustable implants that mimic human tissue. The focus of this thesis is bone tissue engineering that intends to produce patient-specific biological substitutes using biodegradable scaffolds to overcome the limitations of existing clinical treatments.

1.1 Aim of this study

The question that motivated this research work was whether SLS (Selective Laser Sintering) is a viable manufacturing technology for fabricating bone tissue scaffolds. To give an explicit answer, the following need to be considered:

- What are the capabilities and limitations of current SLS technology when shifting its function from rapid prototyping to direct manufacturing of 3D biodegradable scaffolds with micron-scale features?
- Although the SLS system used can only sinter polymers, is it possible to improve characteristics of the scaffold in terms of surface characteristics and mechanical properties by introducing a ceramic phase similar to the inorganic component of natural bone?
- How do SLS process parameters influence mechanical properties and dimensions of biodegradable 3D structures having micron-scale features?

With these in mind the research question was addressed by three studies designed to:

1.) Clarify anisotropy and microporosity issues associated with the manufacturing technology in the context of lattice structures, and
2.) Reveal the influence of ceramic addition (ie. changing polymer/ceramic ratio) on mechanical properties, surface characteristics and biocompatibility of fabricated scaffolds.
3.) Develop mathematical models that directly relate process parameters of the manufacturing technology to mechanical properties, accuracy and porosity of the scaffolds.

1.2 Outline of the experimental work

A flowchart of the experimental work is shown in Figure 1.1. Preliminary experiments were initially carried out to manufacture micron-scale lattice structures using polyamide powder brand named Duraform® (the default material for the SLS system used). The aim was to explore the capabilities of the system in terms of fabricable feature size, and to identify important process parameters using Taguchi's screening experiments. Details and results of these experiments can be found in the Appendix I.

Another set of preliminary experiments was carried out using polycaprolactone powder in order to identify parameter ranges that can be used for part fabrication. These experiments served as a base for establishing the research goals of this work.

Powder preparation, and its thermal and morphological characterisation was also part of the preliminary work, and results are presented in Section 4.1.

The three piers of this thesis (mechanical anisotropy, influence of material composition and influence of process parameters) are introduced in detail.

The first the mechanical behaviour of fabricated structures and their anisotropy is examined. It was observed during the preliminary experiments, and is also supported in published literature that anisotropy of parts fabricated via SLS is inherent to the manufacturing process. SLS has been adopted by many research groups (see Section 2.3) as a possible manufacturing technology for tissue scaffolds, however orientation dependence of fabricated scaffolds (or lattice structures in general) has not been examined to date. Therefore, the aim of this work is to describe the strong orientation dependence of the fabricated lattice structures. Orientation dependence was examined in three different lattices: simple cubic, Gibson-Ashby, and reinforced cubic. Tests for the simple cubic geometry have been carried out using three different particle sizes.

Alongside geometry, material composition is also of significant importance in creating a suitable scaffold. Polycaprolactone is an FDA-approved polymeric material with successful clinical history, however it has limitations. Biodegradable polyesters are known to release acidic degradation products, and polycaprolactone is a strongly hydrophobic material that is not favourable for cell attachment.

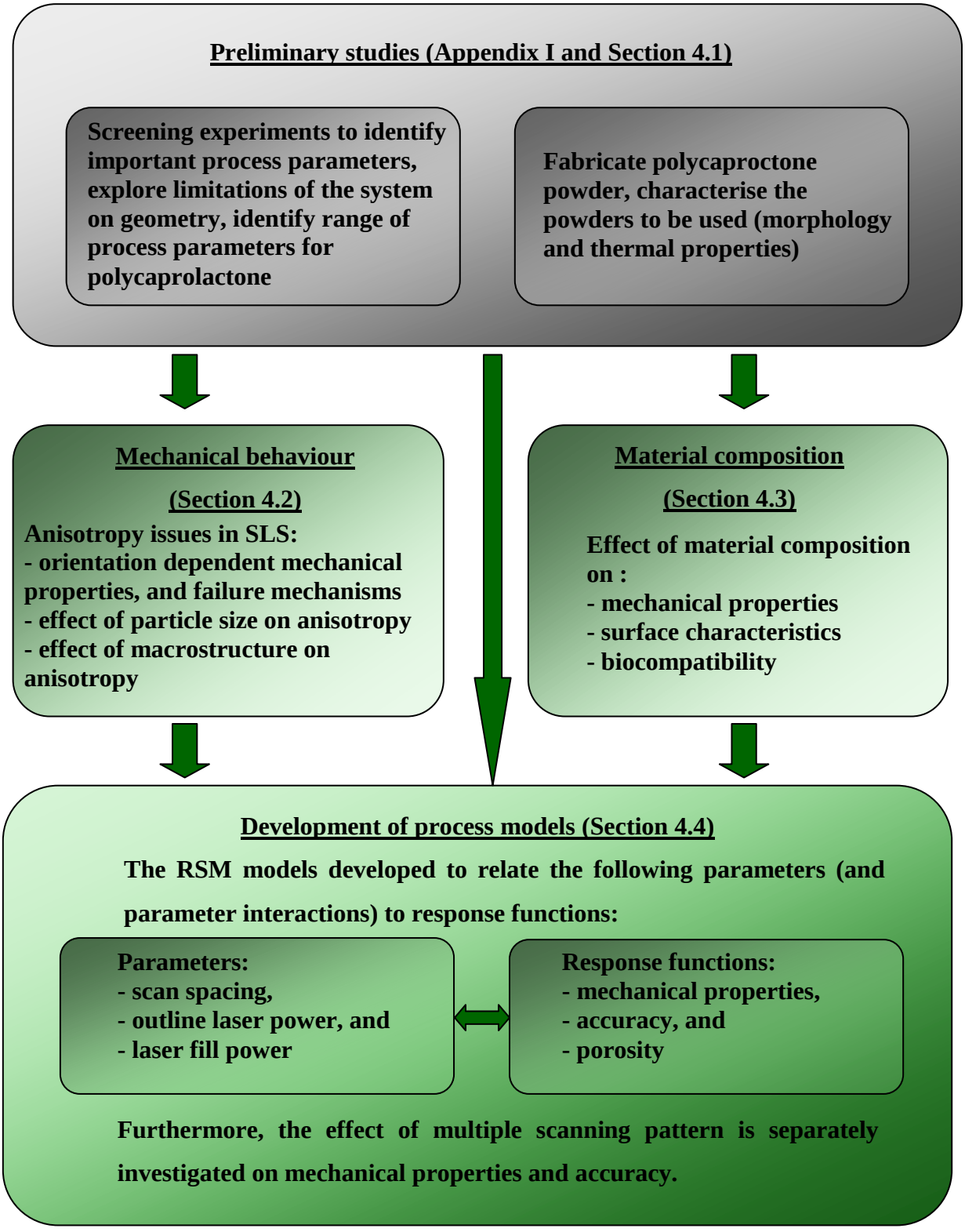

Figure 1.1 Framework of studies undertaken in this research

Therefore the incorporation of a calcium phosphate ceramic material that resembles the constituents of natural bone could be advantageous for many reasons. It is hypothesised that addition of hydroxyapatite will improve:

- surface characteristics (hydrophilicity, surface roughness),
- mechanical properties (when added in small quantities), and
- biocompatibility of fabricated scaffolds.

It has been seen during the preliminary experiments – and is also known from literature that mechanical properties, part dimensions and porosity can be altered by changing SLS process parameters. An extensive statistical analysis was carried out using RSM (Response Surface Methodology) to formulate mathematical models that describe the relationships between scan spacing, outline laser power, laser fill power and the above listed response functions.

1.3 Thesis outline

This thesis is divided into a number of sections.

Chapter 2 introduces the field of tissue engineering, basic requirements for bone tissue scaffolds and the SLS manufacturing process. A comprehensive literature review is also presented, highlighting state of the art research in the following areas:

- influence of SLS process parameters on part properties,
- SLS fabrication of scaffolds,
- characterisation of cellular solids, and
- properties of polycaprolactone scaffolds.

Chapter 3 details the materials, equipment and experimental methods used in this work. 3D models of the fabricated geometries are also introduced. The various mechanical testing, surface characterisation, biocompatibility and cell culturing procedures are outlined. The RSM and the statistical DOE (Design of Experiments) used for investigation of process parameter effects are discussed.

The results from this work are presented and discussed in Chapter 4. Relevant basic characterisation of the powders used (polycaprolactone, hydroxyapatite and tricalciumphosphate) is detailed in Section 4.1. Data on the orientation dependence of mechanical characteristics of scaffolds are given (Section 4.2), followed by a thorough

analysis and discussion of these results. Section 4.3 presents the findings from investigations on the dependence of various properties of scaffolds on material composition. The statistical experimental work to develop mathematical models that describe the relationships between the response functions (mechanical properties, dimensional measures) and process parameters are presented in Section 4.4.

The conclusions drawn from this research are outlined in Chapter 5.

2 LITERATURE REVIEW

2.1 Introduction

Before elaborating on the state-of-the art knowledge in SLS processing of bone scaffolds, it is necessary to first introduce bone and the concepts of bone tissue engineering and also to give a basic introduction to selective laser sintering.

2.1.1 Introduction to bone tissue engineering

Bone is a relatively hard and lightweight natural composite mainly made up of collagen fibril, and hydroxyapatite. The extraordinary mechanical behaviour of bone arises from its nanocomposite nature and the various levels of hierarchical structure. Detailed reviews on bone structure and properties can be found elsewhere [1-4]. Bone contains about 60 wt% of mineral, 30 wt% of organic matrix and 10 % of water. The matrix of bone primarily consists of Type I collagen fibrils that are arranged into layers, and in between these layers mineral crystals are deposited [1]. The organic content of bone is highly aligned, resulting in a very anisotropic structure. Collagen is predominantly responsible for its viscoelastic and good energy absorbtion properties, while the inorganic component present in the form of hydroxyapatite (with ionic substitution) is mainly responsible for compressive strength and stiffness. At the same time bone is a living tissue, its matrix contains about 15 wt% of cells including osteocytes (bone cells), osteoclasts (bone resorbing cells), and osteoblasts (bone building cells). Bone tissue engineering intends to produce patient-specific biological substitutes when this tissue is damaged or lost. Bone tissue engineering involves growing the relevant cells (osteoblasts) in-vitro into the required 3D form. However, cells lack the ability to independently grow in favoured 3D orientations, instead they randomly migrate in 2D [5]. In addition most primary organ cells, including bone cells, are anchorage-dependent and require a specific environment for growth [6]. Therefore, 3D porous matrices (scaffolds) to which the cells can attach and colonize, are required in tissue engineering.

These scaffolds aim to mimic the function of the extra cellular matrix (ECM) of the tissue by providing a temporary template for tissue growth. Cells adhere to the scaffold, proliferate, migrate and differentiate while secreting their own ECM. The three primary roles of the scaffold are [7]:

- to serve as an adhesion substrate for cells, promoting the adhesion and differentiation,
- to provide temporary mechanical support to the newly grown tissue by defining and maintaining a 3D structure,
- to define the space that will shape the regenerating new tissue with the appropriate function.

The design and fabrication of a porous 3D scaffold – the subject of this research – is the first stage in tissue engineering bone. There are strict requirements for the material used, as the implanted scaffold has to be biocompatible and should not produce any imunogenic response [8]. It has to be ensured during design and fabrication that scaffolds are osteoconductive. It means that they possess an interconnected, open pore structure to allow cell attachment, proliferation and migration, and also to enable new vessel penetration, diffusion of physiological nutrients and the removal of metabolic waste from the adhered cells [8].

Attachment and differentiation of osteoblasts in the surface of the biomaterials is a key factor to tissue formation and regeneration [8]. Cell attachment requires the absorption of proteins onto the surface of the material that can be guided by chemical functionality and material surface texture [9]. An extensive review on the role of material surfaces including porosity was published by Boyan et al. [10].

Pore size is of critical importance as too small pores can limit vascularisation and may prevent cells from entering the scaffold, while too large pore sizes can result in poorly connected tissue growth and excessively week scaffolds. It was found that osteoblasts have a preference for pore size of 200 - 400 μm. The indicated pore size range not only facilitates cell attachment and proliferation but also allows for vascularisation. Furthermore, in terms of surface properties a high surface to volume ratio is essential in order to increase the number of cell attachments. The scaffold surface must also be able to absorb the necessary proteins and growth factors that induce osteoblast lineage (osteoinductivity).

Moreover, mechanical properties of the scaffold have to be similar to those of the neighbouring tissue to prevent stress shielding and bone resorption [8]. As summarised in a review by Reilly and Burstein [11], the compressive elastic modulus of cortical bone is 3-30 GPa, while its strength is in the range of 9-300 MPa depending on anatomical location and testing direction. Trabecular bone exhibits significantly lower

values, and there are even greater variations with anatomic location. Among reported data for compressive elastic constants (E) in the distal radius values are as low as 1 MPa, while in the distal femur, values are as high as 3 GPa. In terms of compressive strength, reported values range between 0.03 and 30 MPa, depending on the anatomical site and porosity [12]. Besides the match in mechanical properties the newly formed bone should also be able to form a strong bond with the scaffold (osteointegrity).

The objective of this study is the fabrication of cancellous bone scaffolds for non-load bearing applications aiming to fulfil the above listed requirements. In the past many manufacturing technologies have been adapted for the fabrication of scaffolds. There are problems associated with conventional scaffold fabrication technologies, like compression moulding / particulate leaching, fibre bonding, gas foaming, phase separation, solvent casting and freeze drying. Some of these technologies involve the use of porogens and organic solvents, and most can only produce scaffolds with limited thickness and of random internal architecture including pore size, pore shape and special distribution [13, 14]. Produced scaffolds lack consistency and reproducibility both in mechanical properties and in their structure. Techniques that involve the use of organic solvents are not desirable as residual traces can result in toxic effects and inflammatory responses in-vitro.

The current project examines selective laser sintering as potential technology in the field of tissue engineering.

2.1.2 Introduction to Selective Laser Sintering (SLS)

Selective Laser Sintering (SLS), a Solid Freeform Fabrication (SFF) or Rapid Manufacturing (RM) technology enables the design and fabrication of scaffolds with predefined internal and external architectures, therefore overcoming the limitations of conventionally used scaffold fabrication technologies [14-16]. Furthermore, patient specific data can be obtained from Computer Tomography (CT) or Magnetic Resonance Imaging (MRI) scans to create customized CAD models and RM technologies can fabricate a scaffold with the exact external shape required to fit the damaged tissue site. In general, RM technologies enable the fabrication of geometrically complex parts that can potentially have graded compositions. Typically, designers have tailored their designs to facilitate manufacturing, as reflected by the Design for Manufacturing (DFM) approach, while RM technologies provide new opportunities to include complexities in shape, material and hierarchical structure into the fabricated parts [17, 18]. SLS is an

additive, powder based manufacturing process that was developed at the University of Texas at Austin and in 1986. It was commercialized by DTM Corporation that was later acquired by 3D systems (Valencia, CA). In this process powder particles are selectively fused layer-by-layer as opposed to traditional manufacturing that uses material removal to define the final object geometry. The object is built layer-by-layer from an STL file generated from CAD data. The STL file consists of an unordered list of triangular slice facets representing the outside surface of the object. The triangular facets are described by 3 vertices (a set of X, Y and Z coordinates) and a normal unit vector which indicates the outside surface of the object. The geometry is sliced according to the set layer thickness, and this slice data is used for manufacturing the individual layers.

The working principle of SLS is illustrated in Figure 2.1. The system consists of a powder bed in the middle, two powder supply beds on the sides and a laser source above the part beds. The laser beam is positioned by the movement of two mirrors. The laser beam selectively scans the surface of the powder bed according to the slice data of the STL file.

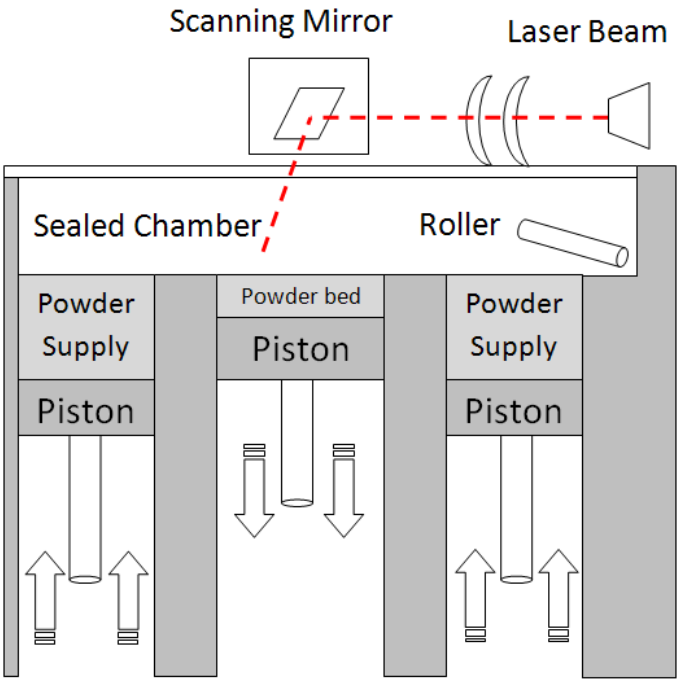

Figure 2.1 Working principle of SLS

The interaction of the laser beam with the powder rises the temperature of the powder particles to their melting point that results in sintering or fusion of the neighbouring particles. When one layer is sintered, the powder supply bed is raised, the powder bed is

lowered and a new layer of powder is deposited on the top of the powder bed by a roller. The sintering process is repeated until the 3D part is ready.

The most important process parameters that are adjustable by the user include laser fill power (P_{fill}), outline laser power ($P_{outline}$), scan speed (v_{beam}), scan spacing (SS), layer thickness (z_{layer}), scan count (n) and part bed temperature (T_b). The scanning pattern in one sintering layer consists of an outline and a fill pattern as illustrated in Figure 2.2. The latter is a raster scan filling in the outline scan. It is possible to disable either the outline or the fill scan completely. Scan spacing is the distance between two neighbouring scan lines in the fill scan pattern. Scan count indicates how many times the scan patterns are repeated within one layer. Layer thickness is the depth the part piston lowers for each layer.

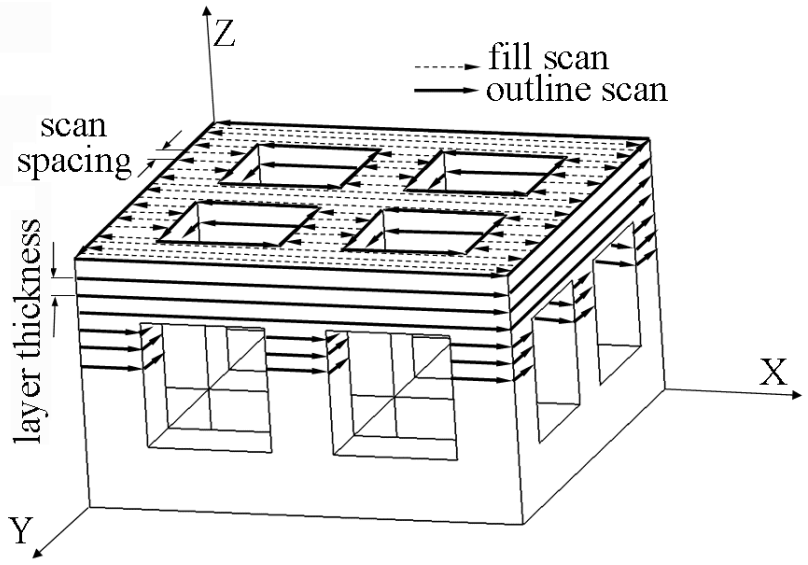

Figure 2.2 SLS process parameters and scan patterns in different directions

Scan speed is the speed at which the laser beams moves across the powder surface. In newer SLS machines (Sinterstation 2500^{plus} and newer) fabricated by 3D Systems this parameter is not adjustable, but set to 1778 mm/s for the outline scan and 5080 mm/s for the fill scan. Part bed temperature is important for reducing the necessary laser power and distortion in the sintering process. If the powder bed temperature is kept close to the T_m this reduces thermal gradients in the solidifying molten polymer, and also reduces the polymer viscosity allowing it to flow and spread properly, and gives sufficient time to relax.

Energy density (ED [J/mm^2]) is a measure of the amount of energy per unit area supplied to the powder bed surface. It is a function of laser fill power (P [W]), scan spacing (SS [mm]) and laser beam speed (v_{beam} [mm/s]). Nelson defined ED as [19]:

$$ED = \frac{P}{SS \times v_{beam}} \quad \text{Eq. 2.1}$$

Energy density is used to guide parameter variations while maintaining the same basic properties of fabricated parts. The equation does not take into account small changes in transient conduction, radiation and sintering potential and therefore, in practice, parts fabricated at a constant energy density (but using different parameter settings) can exhibit variations in part strength, feature detail, curl and surface finish [20].

SLS technology has the advantage that it can produce parts from a wide range of raw materials including polymers, ceramics, metals, and glass [21]. Commercially available materials traditionally used in SLS are not biodegradable, although some are biocompatible. However, theoretically, all powdered materials that can be melted but are not degraded by the laser beam during sintering can be processed via SLS [22]. However, it has to be pointed out that typical SLS systems on the market can only sinter polymers or metals with low melting temperature as they are installed with low power lasers.

Material selection is of particular importance since material properties (along with fabrication parameters) primarily determine the mechanical properties and the surface qualities of the fabricated part. Therefore, understanding the relationship between material properties and processing parameters is critical.

The SLS system used in this research is a DTM Sinterstation 2500^{plus} installed with a 25 W CO_2 laser that can only process polymers. When processing polymer – ceramic composites in this system, the polymer serves as a binder material while the ceramic serves as a structural or functional material and fabrication parameters are therefore mainly dependent on the polymer. For these reasons, this review focuses mainly on polymers.

Since SLS is a heat transfer process thermal properties of the polymer are of critical importance [21]. The most important characteristics of polymers are the glass transition temperature (T_g) or the melting temperature (T_m), depending on whether an amorphous, semi-crystalline or crystalline polymer is used. Below T_g the polymer is in glass state

and the molecular motion along the chains is frozen. If the molecular motion increases the elastic modulus rapidly drops. T_m is the temperature above which the polymer becomes a highly viscous liquid. During the transition from glass state to rubber like state there are also changes in the specific volume and the heat capacity. Close to the T_m specific volume of crystalline polymers changes significantly. Therefore crystalline materials shrink when they cool down from T_m. If the cooling is uneven it can result in distortion. Other physical and thermal properties of the material that influence the fabrication process include: specific heat, thermal conductivity, particle size, and density.

2.2 Influence of SLS process parameters on part properties

This review mainly focuses on four part properties (namely, mechanical properties, density, accuracy and surface roughness) that are considered important for a functional scaffold intended for use in tissue engineering. These properties are dependent on three things:

- morphology of the powder used,
- material properties of the powders used, and
- SLS parameters.

Of these, SLS parameters are the main subject of this review. Most of the studies introduced in this section were carried out using Duraform (polyamide), polycarbonate or metals with low melting temperature, as these are the materials traditionally used in SLS. The materials used in the studies reviewed are summarised in Table 2.1.

Mechanical properties and density

During the SLS process, powders are subjected to low compaction forces, and thus fabricated objects exhibit a porous structure when low energy densities are delivered to the layers. This porosity is a key requirement for successful TE scaffolds, however on the other hand low density negatively effects other properties of the sintered parts including strength and stiffness [23].

Ref	Author	Materials	Ref	Author	Materials
19	Nelson et al.	polycarbonate/ polyamide	**39**	Chatterjee et al.	low carbon steel
20	Evans	carbide composites	**40**	Kruth, Kumar	metal powder mixture
21	Gibson, Shi	various polymers	**41**	Simichi et al.	iron
22	Wiria et al.	PCL/HA	**43**	Low at al.	polyamide
26	Song et al.	CuSn 89/11	**44**	Cheah et al.	polyamide
28	Ho et al.	polycarbonate	**45**	Leong et al.	PCL, PLLA
29	Caulfield et al.	polyamide	**47**	Ning et al.	Cu-based alloy
30	Dewidar et al.	steel	**48**	Williams et al.	PCL
32	Savalani et al.	polyamide /HA	**51**	Wang et al.	RapidSteel®
33	Subramanian et. al.	alumina/polymer	**53**	Raghunath et al.	polyamide
34	Chua et al.	PVA/HA	**55**	Becchewar et al	polyamide
35	Hao et al.	PE/HA	**56**	Ning et al.	copper based metal
37	Hardro	polymer	**57**	Partee et al.	PCL
38	Simchi et al.	iron			

Table 2.1 Materials used to study the effect of SLS process parameters on various part properties

Density (and therefore mechanical properties) of the SLS fabricated parts is primarily influenced by particle size. The relationship between the particle size and the density is inversely proportional, that is, small particle size can increase density. Fine powders show very good inter-particle connectivity due to the large surface area and the greater number of contact points. Also, the binding mechanism in liquid state sintering is based on a capillary force that is proportional to the reciprocal of the particle size [24]. Numerical simulations showed that molecular weight of the polymer also affects the quality of the fabricated part through melting viscosity, as higher density can be achieved if melting viscosity is lower [25]. To date no studies has addressed the relative importance of material properties versus powder morphology or process parameters.

It is generally accepted in literature that density and mechanical properties are otherwise primarily determined by delivered energy density [19, 20, 22, 24, 26-35]. Increase in

delivered energy density improved mechanical properties in all reported cases up to a limited value. This effect is due to the fact that increased energy density results in better sintering and therefore increased part density and improved mechanical properties. When maximum density is achieved further increase in delivered energy density does not affect mechanical properties, furthermore excessive energy levels can result in degradation of the polymer that will affect it negatively.

Energy density is directly proportional to laser power and inversely proportional to scan speed and scan spacing (Eq. 2.1). These parameters have been investigated individually, or as part of a design of experiments approach. Increase in laser power improved mechanical properties in all reported cases [36-38], however it was suggested that an optimal laser power value should be found to achieve proper mechanical strength and porosity, and at the same time, avoid curling and distortion that can be the result of too high laser power (or energy density)[21]. The effect of scan spacing was also investigated by several research groups [36, 38-41]and its inverse relation to density and mechanical properties was confirmed. Laser speed is also inversely related to mechanical properties such as strength, stiffness, and hardness [26, 40, 41].

Song et al. [26] examined sintered density and sintering depth (both directly related to mechanical properties) as a function of delivered energy density and compared the effect of laser powers, scan spacing and laser speed. It was found that changes in scan spacing and laser speed had significantly greater influence than laser power.

The effect of part bed temperature on sintering density was investigated by Tontowi and Childs [31], and found that part bed temperature (while other parameters are kept constant) results in increased part density. The authors have also developed a model based on experimental results for the prediction of part density. The results of this study suggested that part bed temperature should be as high as possible. Although high sintering temperatures result in lower polymer viscosity that increases density and therefore mechanical properties, this flow can also cause shear stresses between layers that can result in curling or distortion [21]. Increase in part strength with increased part bed temperature was also confirmed by Jain et al. [42]. Low et al. [43] also found that average porosity had an inverse linear relationship with part bed temperature.

Layer thickness is another significant parameter in determining density and therefore mechanical strength of fabricated parts. Chatterjee et al. [39] and Jain et al. [42] investigated its effect using a design of experiments approach (surface response and

Taguchi's orthogonal arrays, respectively) and found that increase in layer thickness results in lower part density and weaker parts. Chatterjee et al. examined layer thickness and scan spacing simultaneously, and found that both are important in determining porosity and density, however dependence is more on layer thickness than on scan spacing. Furthermore, authors found that of the two parameters, hardness is only sensitive to changes in layer thickness.

The effect of scan line length (length of the scan vector in the fill scan pattern between changing directions) was also investigated. Gibson and Shi [21] observed that shorter scan vectors result in more uniform temperature distributions and have better mechanical properties. It was also suggested that if the positioning allows a shorter scan vector, strength and density improves since temperature is uniform during sintering while larger cross sectional areas result in more curling and distortion. Cheath et al. [44] demonstrated that when a single line is sintered the start and end portion of the line will have a denser structure that is caused by the extra deposited surface energy due to the acceleration and deceleration of the laser beam (dwell time). This phenomenon arises from the inertia of the scanning mirrors. The findings of this study and the fact that SLS induces porosity in the inner structure of the fabricated parts proved successful in other applications too, such as fabrication of drug delivery devices [43-45]. The study by Low et al. also demonstrated the ability of this manufacturing process to create a dense outer wall and a porous interior due to the dwell time at the start and end of each scan line [43].

Part strength is also dependent on orientation of the part within the powder bed [33, 46, 47]. Mechanical properties along the x- and y- directions are determined by the various scanning patterns, whether scan lines of the fill scan pattern are parallel or perpendicular to the loading direction. While, in the z-direction the most important parameter is layer thickness. Jain et al. [42] found significantly higher tensile strength and modulus when testing samples in the x-direction parallel to the scan lines of the fill scan. Caulfield et al. [29] found Young's modulus and the yield strength of parts parallel to layer direction were significantly higher than perpendicular to layer direction. The poor mechanical properties in the second case are the result of layer delamination, if the delivered energy density is low, the layers are not able to attach on top of each other properly. The authors also found that parts became more isotropic that is - less orientation dependent - with increased delivered energy density. Ning et al. [47] suggested scan line length not only effect part strength but also its anisotropy.

Mechanical properties have also been found to vary within one part: in the middle layers the mechanical properties are better than in the other regions, since they are far from the boundaries and cooling is slower [21].

Accuracy

For fabricating successful tissue engineering scaffolds, besides mechanical properties accuracy is also important. However, it is not possible to maximize both. Maximum density and therefore mechanical properties can only be achieved with settings that result in excess powder fused to the surface, thus limiting accuracy [21]. For example, increase in delivered energy density improves mechanical properties but also increases heat conduction, therefore excess powder is melted and fused to the boundaries of the scaffold that increases dimensions and corrupts accuracy.

The smallest attainable feature in SLS is predominantly defined by the powder particle size [25], the focused laser beam diameter and the heat transfer in the powder bed [25, 48]. Small particles size can increase precision, but on the other hand, an over-small particle size of the polymer powder will make it difficult to spread the powder, because it causes the powder to self unite. Furthermore, smaller particles sinter much faster when trapped inside scaffold pores or at scaffold boundaries that may result in dimensional inaccuracy, and makes excess powder removal difficult [48]. Crystallinity is also thought to largely affect precision of sintered parts, as shrinkage is more dominant with increasing crystallinity. If the melting and crystallization temperature of the polymer differ greatly, dimensional accuracy is better. After sintering these material's liquid state should be preserved for a while during the cooling process to ensure that the SLS part is not easily warped [25]. In simulations and experimental work carried out by Child et al., it was found that accuracy (similarly to densification) is most sensitive to material properties such as changes in activation energy and heat capacity of the polymer, and factors like powder bed density and layer thickness only have secondary effects.

Accuracy of fabricated parts varies significantly within the powder bed from its centre to the borders of the platform [49]. To achieve better accuracy in various applications, parts should be placed as close to the centre as possible. The reasons for this are that:

- the distance from the mirror to the powder surface varies from the centre to the border, that can affect laser focus, and

- the laser enters the powder surface at an angle – is only vertical in the centre point - , this can change the sintered part shape related to the laser beam.

Currently 3D Systems' slicing algorithms assumes that the laser beam has a uniform bullet shape along the surface of the whole platform, and these errors are not compensated.

Caufield et al. [29] reported that accuracy, like mechanical properties is orientation dependent. The differences in accuracy in the different building directions are the result of different scanning patterns.

In terms of dimensional accuracy part bed temperature has the opposite influence to that seen for density and mechanical properties. Lower sintering temperatures are more favourable, where neighbouring particles stick together without becoming liquid [50].

Shrinkage is a very important phenomenon in terms of accuracy, and therefore it has been widely investigated [51-53]. Different shrinkage rates occur throughout the part because the temperature of the most recently sintered layer is higher. The higher temperature of the new layer causes the previous layer to shrink. The newly sintered layer transfers heat to the previously sintered layer so its temperature becomes higher than the layer underneath and it causes shrinkage during cooling. This phenomenon is repeated for each layer, hence the bottom part of the specimen experiences repeated cycles of shrinkage, consequently greater shrinkage than the top. There are two methods to minimize shrinkage: adjust build conditions or make some allowances to compensate for the distortion. Generally increased energy density results in increased shrinkage. If high energy density is used it is possible that the energy is transferred from the scanned powders to the neighbouring powder and this results in inaccurate specimens. If energy density is constant, shrinkage can be reduced by increasing interaction time by reducing scan speed. This means reduced heat induction rate, therefore temperature differences between layers can equalize [24]. Yang et al. measured shrinkage rates experimentally and developed a model that proposed direction dependent (x, y, and z) compensations for the shape distortions caused by phase changes during the SLS process. This work only investigated shrinkage dependence on position within the part bed and did not include the influence of process parameters on shrinkage rate in the developed model. Raughunath et al. [53] developed an orientation dependent shrinkage model using the Taguchi method. It was found that of the examined parameters, laser power and scan line length are the most significant process variables influencing shrinkage in the x-

direction, while along the y-direction laser power and laser speed and along the z-direction laser speed, scan spacing and part bed temperature are more important.

Surface roughness

Surface characteristics of fabricated parts are also important when fabricating scaffolds for tissue engineering applications. The acceptable surface roughness range is between 5-50 μm. Importantly, this applications aims for the opposite effect to traditional rapid prototyping or rapid manufacturing applications where the aim is to minimise surface roughness. This parameter is considered as a good indicator of sintering efficiency, however very few surface roughness models have been published to date. Song et al. showed that delivered energy density and all its determining parameters (laser power, scan spacing, laser speed) has a considerable influence on surface roughness. Tumer et al. [54] showed that layer thickness and part orientation have a strong effect on surface quality when conducting a factorial design of experiments, the only investigated parameter that was not found significant in the examined range was laser power. More recently, Bacchewar et al. [55] developed a statistical model for determining surface roughness using the following input variables: laser power, laser speed, build orientation, scan spacing and layer thickness. It was found that surface roughness of the top surface of fabricated parts is determined by build orientation and layer thickness, while that of the bottom surface is determined by build orientation, layer thickness and laser power.

Ning et al. [56] developed an intelligent parameter selection system based on the feed-forward neural network with back propagation learning algorithm to achieve better mapping between process parameters (scan speed, laser power, scan spacing and layer thickness) and mechanical properties, geometric accuracy and surface roughness. However, the system was developed for direct laser sintering of metals.

To date only one model has been proposed (by Partee et al. [57]) for relating process parameters to part properties of selective laser sintered polycaprolactone micro-lattices. However, this work only examined process parameters at two levels, and did not include orientation or outline laser power that is thought to be important during the sintering of microstructures. Furthermore, the developed model is not able to predict strength and stiffness of the samples, nor dimensions of the fabricated features.

2.3 SLS fabrication of scaffolds

This section details all work that has been published on directly selective laser sintering polymer and polymer ceramic/composite scaffolds as this is the subject of the current study. This literature served as a starting point and guideline throughout this work.

Two main approaches are used to manufacture porous matrices for tissue engineering applications via SLS. The first uses the fact that porosity is inherent to the powder based technology. Laser sintered parts have unintentional, manufacturing induced porosity that to some extent can be guided by process parameters, and powder characteristics such as particle shape, size or size distribution. The second approach, on the other hand, aims to fabricate scaffolds with pre-designed internal architecture.

2.3.1 Intrinsic porosity

Groups at the Nanyang Technological University, Singapore published numerous research papers on the manufacturing of bone scaffolds using various materials via the first approach. These groups argue that SLS provides good user control over the microstructure of created scaffolds by adjusting process parameters. In all these studies thin solid disks or single layers were fabricated to test suitability of the material for SLS and to assess the microstructure of the fabricated scaffold. The SLS system used was a DTM Sinterstation 2500 in all these experiments. In general, these papers are very good on parameter dependence, but low on quantitative morphological characterisation, such as porosity, interconnectivity or pore size of fabricated structures.

In 2002 Tan et al. [58] produced polyetheretherketon-hydroxyapatite (PEEK-HA) scaffolds and optimized processing parameters on pure PEEK by varying one parameter at a time. PEEK is a bioinert, semi-crystalline polymer with melting temperature of 343 ˚C and glass transition temperature of 143 ˚C.

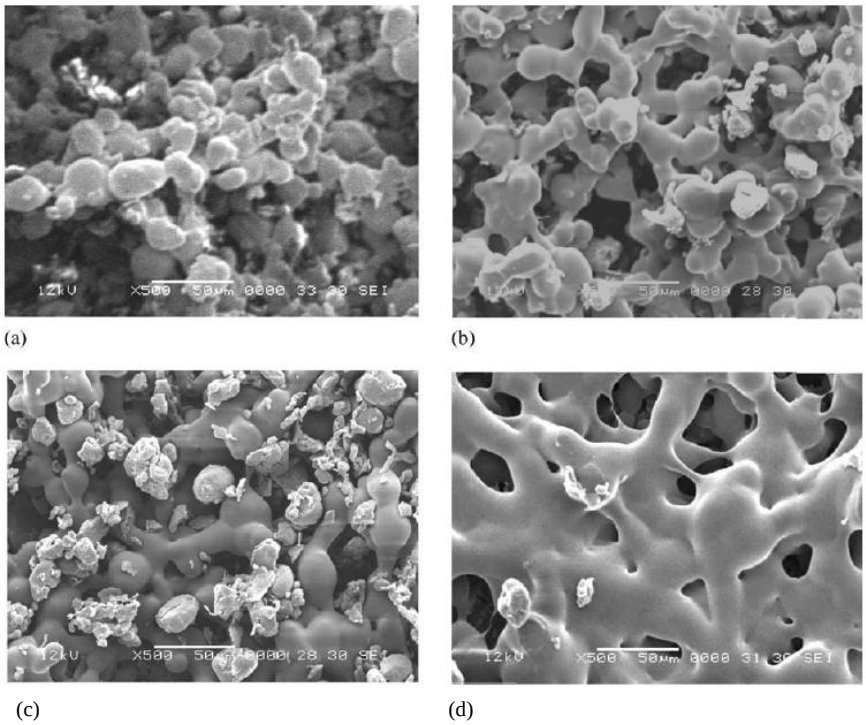

Figure 2.3 Micrographs of PEEK microporous structures fabricated at part bed temperature of 140 ˚C and laser power of (a) 9 W, (b) 12 W, (c) 16 W, and (d) 20 W [58]

Average particle size of PEEK was 25 µm and 90% of the HA particles were below 60 µm. The laser power was varied between 9-28 W and the part bed temperature between 110-140 ˚C, all other parameters were kept constant including the laser speed of 5080 mm/s. Figure 2.3 shows micrographs of the morphology of the scaffolds fabricated at various laser powers. The use of part bed temperature of 140 ˚C combined with laser power between 16-21 W was found to be the most favourable for creating microporous structures. A highly dense morphology that would not facilitate tissue ingrowth was formed at higher laser powers and at 28 W specimens were charred. Below this laser power range, although neck formation between particles was observed, obtained specimens were too fragile, and delamination occurred near the edges indicating that adjacent layers were not properly bonded. These optimal parameters were used to manufacture PEEK/HA composite scaffolds with varying HA content up to 40 wt%. This paper demonstrated the ability of fabricating PEEK scaffolds via SLS, however it only showed qualitative analysis of the surface morphology using microscopic examination. Furthermore PEEK is not a bioresorbable polymer and therefore is not favourable for tissue engineering applications.

In 2005, Chua et al. [34] sintered polyvinyl alcohol (PVA) / hydroxyapatite (HA) scaffolds. PVA is a biodegradable, semi-crystalline hydrogel with T_m=220-240 ˚C and

T_g=58-85 ˚C. PVA powder was used to find suitable working parameters. The part bed temperature was kept constant at 65˚C, and scan speed and laser beam power were varied between 3-20 W and 1270-5080 mm/s, respectively. Well defined interconnectivity and structural integrity was achieved when 10-15 W of laser beam power was used at 1270-1777 mm/s scan speed. At lower energy densities, there was insufficient necking, and at higher energy densities flaming or charring was observable. The group tested composites that were prepared using two different technologies: physical blending and by dissolving PVA in distilled water and mixing it with spray-dried HA suspension. Composites prepared by physical blending contained 10, 20 and 30 wt% of HA while the suspension contained 70% of HA. Sintering of physically blended PVA/HA at 15 W using 1270 mm/s scan speed resulted in good structural integrity and interconnectivity of the microstructures. Due to the low PVA content of the spray dried composites no fusing and limited necking was experienced. Fabrication of specimens with such high HA content was not successful, and increasing the energy density induced flaming of the PVA. As the wt% of HA increased the sintering effect became weaker, since the amount of binder was reduced. In this set of experiments, additionally to the morphological assessment, bioactivity analysis of specimens containing 10 wt% of HA was also carried out in SBF (simulated body fluid). HCA (hydroxy-carbonate-apatite) formation on the surface of the scaffold was observed. However, HA particles were found in the SBF after 9 days indicating the loosened bound between PVA and HA during the bioactivity test possibly as a result of swelling of the water soluble hydrogel.

In a later study, Wiria et al. [59] (from the same research group) attempted to improve the sintering of PVA composites containing 21.5 wt% HA. The particle size of the as-received powder was between 42-372 µm. It was further ground, and sieved to achieve batches of 10-75 µm and 50-100 µm. The authors have tested methods for blending the polymer and ceramic powders: using a ball mill mixer and tumbler mixer. It was found that the ball mixer was more efficient to homogenously mix the blend. The tested parameter range for the 10-75 µm batch was:

- Laser power: 10-20 W
- Part bed temperature: 65-75 ˚C
- Scan speed: 1270-2540 mm/s

Figure 2.4 shows the morphology of the fabricated microstructures.

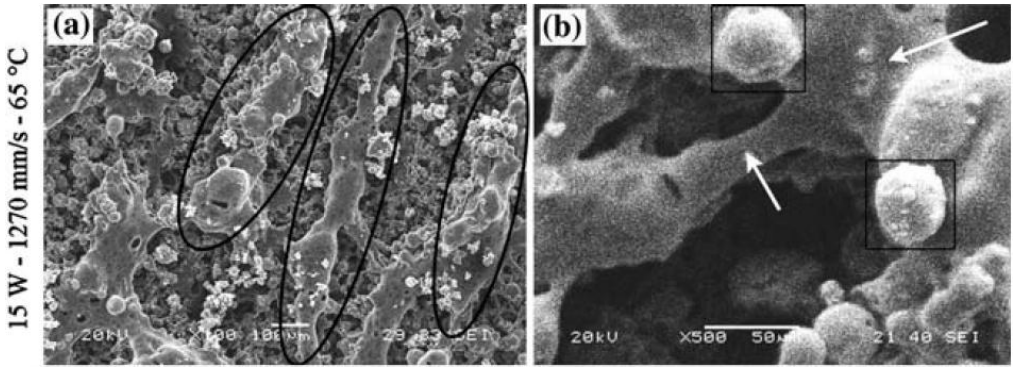

Figure 2.4 Sintered PVA composites containing 21.1 wt% HA using powder batch 10-75 µm at (a) low magnification, and at (b) high magnification [59]

They found that, when the scan speed was too slow, shifting of the already sintered parts was seen each time the roller deposited a new layer of powder. The roller shifted the previous layers when it was slightly curled due to the high thermal gradients that lead to residual stresses that are relieved by the shape change (curl). Optimal parameter settings were found to be 80 ˚C part bed temperature, 13 W laser power and 2032 mm/s laser speed resulting in well bonded and structurally rigid specimens. Of the two batches of powders tested the 50-100 µm batch worked better as problems of uneven powder layering were observed with the 10-75 µm batch. (The problem is associated with powder sticking to the roller during the layering process.) The degradation of PVA starts slightly above its melting temperature, however the authors confirmed via FTIR that chemical composition of PVA was not altered when sintering at the optimal parameter settings.

Tan et al. [60] demonstrated the ability of SLS to process various biodegradable polymers including PVA, PCL (poly-caprolactone), and PLLA (poly-l-lactic-acid). Furthermore, they confirmed the processability of PEEK and its composites with HA. PCL is a semi-crystalline polyester, with a melting temperature of 60 ˚C, and with glass transition temperature of (-60 ˚C). PLLA is polyester with high mechanical properties (significantly higher than PCL or PVA), a melting temperature between 172.2-186.8 ˚C and glass transition temperature of 60.5 ˚C. Table 2.2 summarizes the process parameter ranges tested for each material. The authors assessed fabricated scaffolds via microscopic examination of the surface morphology. Parameter ranges that were found to be suitable for scaffold production are indicated in red, in parenthesis. The particle sizes used are also listed in the table.

Material	Particle size (µm)	$T_{partbed}$ (˚C)	Laser power (W)	Scan speed (mm/s)
PCL	60	30-55 (40)	1-7 (2-3)	3810-5080 (3810)
PLLA	90	60 (60)	10-15 (12-15)	1270 (1270)
PVA	100	60-65 (65)	10-15 (13-15)	1270-5080 (1270-1778)
PEEK	25	110-140 (140)	9-28 (16-21)	5080 (5080)
PEEK/HA	25/60	140 (140)	16 (16)	5080 (5080)

Table 2.2 Examined parameter settings (black) and suitable parameters for scaffold fabrication [60]

When delivered energy density was low (lower part bed temperature, lower laser power or higher laser speed) limited necking between particles and delamination between layers was observed. On the other hand excess energy density resulted in dense parts, charring or curling and wrapping of individual layers. In the PEEK/HA composites HA content was increased from 10 to 40 wt%, and it was concluded that HA content should be kept below 40 wt% to preserve structural integrity when using the above indicated parameter settings.

From the same group Wiria et al. [22] manufactured disk shaped PCL/HA scaffold specimens with different HA content. SLS of PCL with 100 µm average particle size was examined at part bed temperature of 40 ˚C using laser power range of 2-4 W, and scan speed range between 1016-5080 mm/s. Sintering was assessed via microscopic examination. Optimal scaffolds were obtained using 3W laser power at 5080 mm/s scan speed. For the fabrication of composite scaffolds the authors used two morphologically different HA, type 'R' with high surface area (15-20m^2/g), and type 'S' with 10% higher crystallinity, significantly lower surface area (1-2 m^2/g) and greater particle size. To successfully fabricate composite scaffold containing 'S' type HA, the delivered energy density had to be doubled, and for scaffolds containing 'R' type HA had to be tripled. For all compositions, 'R' type samples needed to be scanned at a lower scan speed to achieve the same sintering result. 'R' type HA had a smaller particle size and therefore covered and insulated PCL particles better. Figure 2.5 shows microstructure of the fabricated scaffolds.

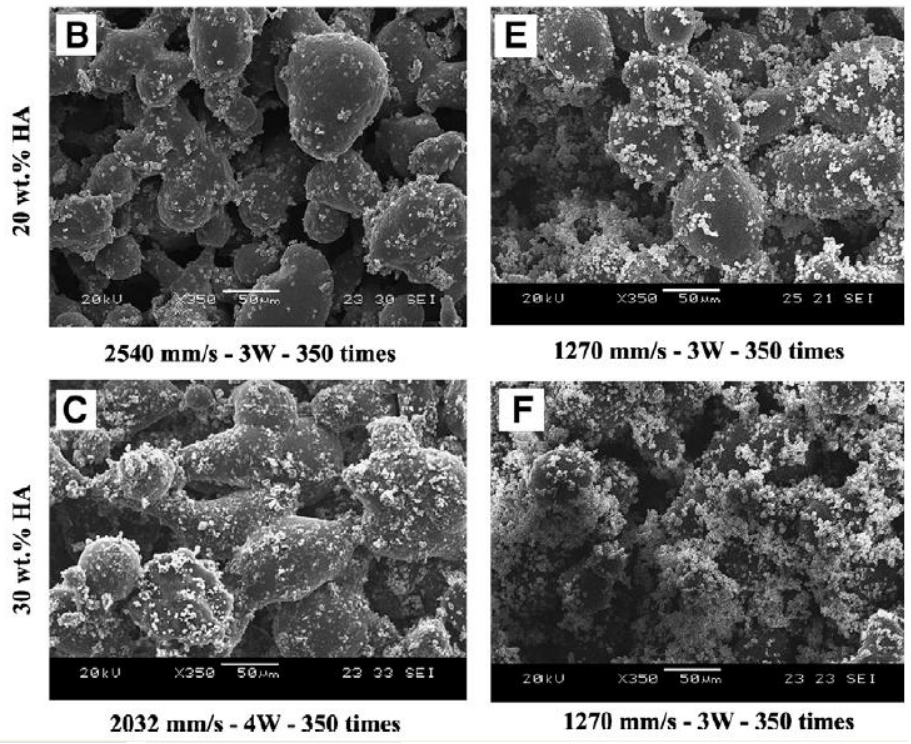

Figure 2.5 Micrographs of sintered specimen (B, C – using 'S' type HA, E, F – using 'R' – type HA) [22]

Increasing the laser power by 1 W did not increase necking intensity between the particles, necking width stayed 25 µm. However, 33% reduction in scan speed lead to 24% increase in necking intensity. Besides morphological characteristics, the authors also reported results of compressive mechanical testing for all samples, and bioactivity and cell culturing experiments for composites containing 10 wt% 'S' type HA. Mechanical properties of solid disk samples are summarized in Table 2.3.

HA type and wt% content in PCL	Young's Modulus [MPa]	Yield stress at 2% strain offset [MPa]
S 10	33.91±2.45	3.96±0.45
S 20	23.69±1.97	2.53±0.21
S 30	56.62±4.61	5.79±0.82
R 10	102.06±11.26	11.54±0.8
R 20	71.49±9.44	7.06±1.21
R 30	34.73±6.36	3.22±0.66

Table 2.3 Mechanical properties of PCL/HA composites [22]

It has to be noted that process parameters for the different HA types and contents were different. Bioactivity and cell culture studies showed that there was HCA formation on the surface of the scaffolds and cells were able to attach to the surface and grow and proliferate after 12 days of cell culturing.

The most recent study from the research group in Singapore in conjunction with Imperial College London was published by Simpson et al. [61] on the fabrication of PLG (poly-l-lactide-co-glycolide) and its composites with HA ('S'type) and HA/β-TCP (tricalcium-phosphate) blend. Single layers were sintered using two PLG powder batches: 50-125 μm and 125-250 μm testing various part bed temperatures (65-100 ˚C), scan speeds (1016-1905 mm/s) and laser powers (5-30 W). The most favourable parameters were found to be 100 ˚C, 1270 mm/s and 25 W, respectively. These parameters were used for both batches; however the 125-250 μm batch exhibited a lesser degree of sintering. When sintering HA composites it was seen that the small HA particles (90 % below 14 μm) formed a shell around the PLG particles that insulated the polymer and the particles could not dissipate their heat by contacting other particles. The authors argued that the use of HA with larger particle size might help to prevent shell formation around the PLG particles. HA/β-TCP composites (12 wt%) with bigger particle size sintered reasonably well. In terms of mechanical strength optimal parameters were found to be at T_{pb}=180 ˚C, 1651 mm/s laser speed, and 10 W laser power. This composition was also used to fabricate multilayer samples (4 layers). Horizontal shifting of the layers (shown in Figure 2.6) was seen when the roller deposited a new layer.

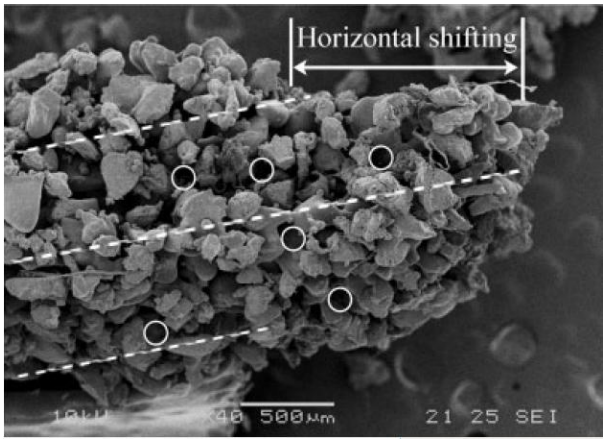

Figure 2.6 Shifting of horizontal layers in 125-250 μm PLG samples with 40 wt% HA/β-TCP. White circles indicate pores of approximately 125 μm diameter

Reduction in roller speed did not help to prevent shifting of layers. The reason for shifting can be slight wrapping of specimen edges, or the fact that some particles are larger in certain orientations than the set layer thickness (0.279 mm), and these particles can catch on the roller. Increasing layer thickness slightly reduced the shifting and it was argued that the use of spherical shaped particles could possibly solve the problem. SEM images showed that pore size of the samples was approximately 125 µm.

Samples (40 wt% HA/β-TCP) were fabricated for testing accuracy, porosity, mechanical properties and molecular weight. Dimensions in the x-direction (parallel to the roller) were reproduced well with ±0.6 mm, while in the y-direction parts were constantly 0.5 mm bigger than the nominal dimension. Average porosity was 46.5 % . Compressive modulus was 130 MPa and strength 8.6 MPa that is within range of the mechanical properties of natural trabecular bone. After sintering a slight reduction in molecular weight was seen, however it was still above 100 000 Da.

It was attempted to fabricate samples with designed porosity (dimensions of the designed structure are not reported), but the powder was trapped within the designed pores and therefore porosity could not be controlled properly.

Another research group at Loughborough University, UK is also promoting the fabrication of tissue scaffolds using the first method. In all cases, of their research an experimental SLS system was used for sintering. The system is installed with a CO_2 laser with output power between 0.2 and 10 W that can be driven at scan speeds of 0.2-10 000mm/s. The laser beam is focused to a spot size of 193 µm. In 2006, Hao et al. published two papers on the fabrication HDPE (high density polyethylene)/HA composite scaffolds [35, 62]. HDPE is bioinert polymer widely used in medical applications however it is not bioresorbable. To increase its bioactivity HA (30 and 40 vol%) was added to the polymer. Instead of pure physical blending, the mixture was compounded in an extruder and the resulting composite was ground and sieved below 250 µm. Using this method segregation of different elements can be avoided. Scan speed and laser power was varied to fabricate single layers. Height of the layers and their morphology was examined. By decreasing scan speed from 4800 to 300 mm/s the fabricated layer thickness increased from 0.45 to 1.6 mm (at P= 7.2 W and T_{pb}=110 ˚C). When increasing laser power from 2 to 10 W, the height of sintered samples increased from 0.6 to 1.2 mm (at v_{beam}= 1200 mm/s and T_{pb}=110 ˚C). Fusion of particle also increased with increasing power. At power of 2.4 W observed pores were between 200-

400 µm, increasing laser power resulted in denser layers and smaller pores. The morphology of HA particles was also evaluated as it is essential to expose HA particles on the surface to ensure bioactivity of the scaffolds. As laser power was increased, more and more HA was exposed to the surface, due to complete melting of the composite particle, however too high laser power resulted in degradation of the polymer. When comparing different HA compositions it was seen that higher HA content resulted in lesser sintering, that was in agreement with previous findings [58].

In a second set of experiments similar conclusions were made about the influence of scan speed and laser power [35]. Additionally the effect of energy density was also examined and it was confirmed that higher energy density creates higher sintered density and greater part dimensions. However it was also pointed out that the same energy density with different laser power and scan speed can result in differences. Porosity of fabricated structures was over 70 % in all cases and owing to this, strength of most specimens was insufficient for conventional mechanical testing. The authors also examined the effect of different particle sizes and particle size distributions (0-50, 50-75, 75-106 and 0-106 µm). Larger particles resulted in increased part height while smaller particles resulted in greater densification and relatively higher shrinkage due to more intensive sintering activity. The binding mechanism in liquid phase sintering is based on the capillary force that is inversely proportional to particle size [63] and smaller particles have greater surface area, also resulting in more intensive sintering.

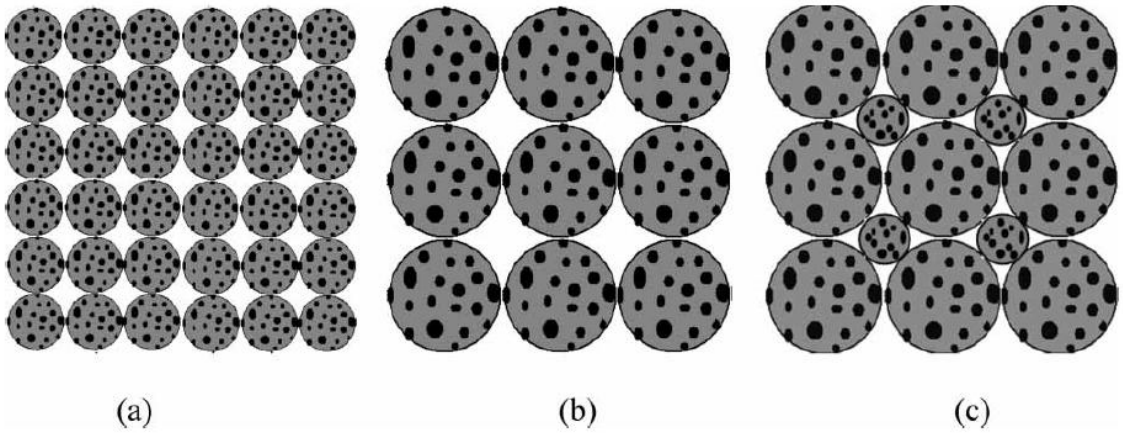

Figure 2.7 Scheme of interparticle connectivity in powders for (a) small particles, (b) large particles, and (c) the mixture of small and large particles [35]

Particle size distribution was also found to play a major role in the formation of interparticle connectivity [35]. As shown in the schemes of interparticle connectivity in

Figure 2.7 mixture powders of small and large particles have higher area of surface contact resulting in better interconnectivity.

In a more recent study, Zhang et al. [64] investigated the dynamic mechanical properties of these porous microstructures. Additionally to the HDPE/HA composites, PA and PA/HA composites were also examined. DMA (dynamic mechanical analysis) in 3-point-bending mode was performed to determine storage and loss modulus and damping properties. It was seen that storage modulus increased with increasing laser power and with decreasing particle size. The effect of part density was also examined and compared to the theoretical model proposed by Gibson and Ashby (Section 2.4) that suggests that stiffness of a cellular solid is quadratically proportional to modulus. The experimental data followed the trend, however the range of data was too small to define a mathematical equation with confidence. Damping factor (tan δ – energy dissipated during deformation) showed no difference for the various particle sizes or laser powers below 60 ˚C. However, the addition of HA reduced tan δ as HA limited motion of the polymer chains.

Savalani et al. [32] aimed to identify the maximum amount of HA that can be incorporated into PA microstructures. The authors also did extensive morphological characterisation. Most of their work to date has been based on qualitative morphological assessment, with little work done on quantitative assessment. The composites used were sieved below 75 μm. The effect of HA content was examined at four levels: 58, 63, 71 and 78 wt%. Only materials with 58 wt% HA produced successful results, the laser power and scan speed processing window for this composition ranged between 4-10 W and 4500-8000 mm/s, respectively. The amount of HA had a great influence on sintering as a result of significant reduction in specific heat capacity of the composite powder. Depending on the laser power used (3.4-10 W), the cross sections of the scaffolds revealed average pore sizes between 61 and 67 μm showing that a 9% variation can be achieved by changing laser power in the examined range. In the examined laser speed range (3400-8350 mm/s) open porosity changed between 34 and 46 %, while average pore between 60 and 68 μm. A possible explanation for the mild effect on pore size is that pore formation is more dependent on particle size, shape and morphology than on process parameters.

2.3.2 Designed porosity

Fabricating scaffolds via SLS using the second approach – when the pore structure of the scaffold is predesigned – is less explored in literature.

Tan et al. [65] at Nanyang Technological University fabricated designed 3D PEEK (25μm) / HA (60μm) scaffolds with varying HA content (10-40 wt%). Fabricated scaffold are shown in Figure 2.8 designed strut length was 1.5 mm and designed pore size was 600μm.

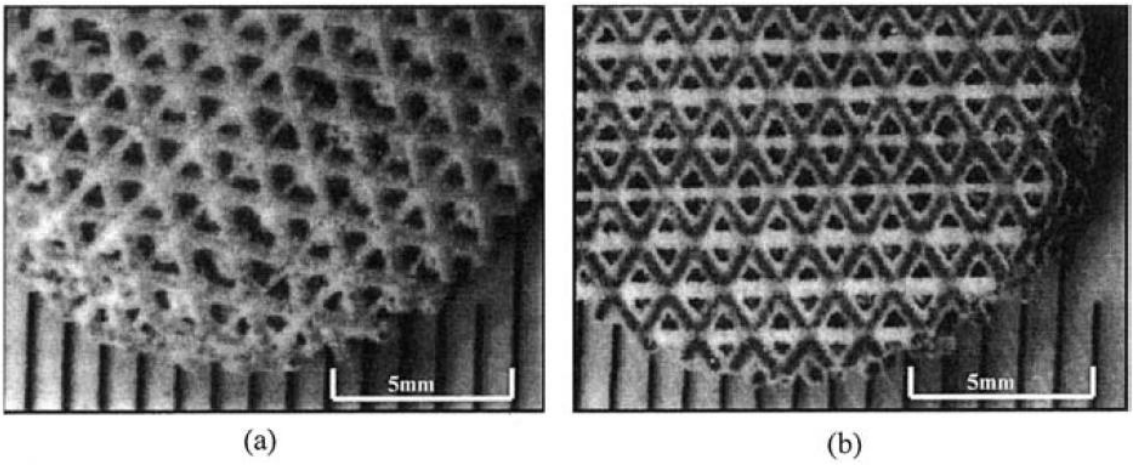

Figure 2.8 Microscopic views of (a) the top and (b) the bottom of a PEEK-HA composite scaffold [65]

Microporosity parameters within the struts controlled via process was still present. It was found that porosity of scaffolds decreased with increasing HA content. Macroporosity was defined by the CAD model, however structural accuracy of the fabricated part was not verified by the authors. The fabrication of the same geometry have also been documented elsewhere [66].

Chua et al. [67, 68] carried out significant work on cell-based geometry optimization for tissue engineering applications and some of the designed structures have been fabricated via SLS. However, no assessment or characterisation of fabricated parts was carried out.

Most work in the field of selective laser sintering designed 3D matrices was carried out at the University of Michigan [48, 57, 69]. The SLS system used in their studies was a commercially available DTM Sinterstation 2000. In 2003, Das et al. [69] sintered scaffolds with different architectures using PA at default parameter settings. Periodic cell based microstructures with 800 μm orthogonal channels and 1200 μm pillars, having a relative density of 53.7 % were successfully fabricated. Bioactivity test showed

that scaffolds support cell viability. Histology after implantation showed the presence of regenerated and mineralized bone tissue.

Furthermore, the capability of SLS to fabricate biomimetic architectures derived from µ-CT or µ-MRI of human proximal femur was also demonstrated in this study. The geometries of bone structures obtained from the µ-CT data were scaled up (4×) as features in range of 10-100 µm cannot be fabricated with the used SLS system.

In a later study Williams et al. [48] manufactured PCL scaffolds with 3D orthogonal periodic architecture by preheating the powder bed to 49.5 ˚C and using 4.5 W power and 1257 m/s scan speed. Struts of the scaffolds had an average porosity of approximately 20%. The designed orthogonal pores ranged from 1.75 – 2.5 mm producing scaffolds with volumetric porosity of 63-79%. Designed and fabricated geometries are shown in Figure 2.9.

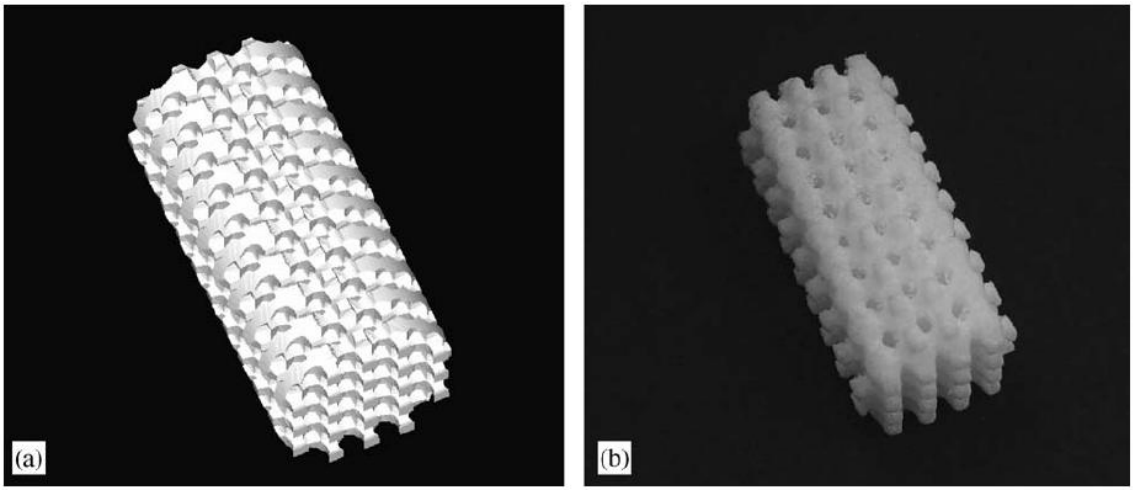

Figure 2.9 (a) STL design file for the periodic cell based porous scaffold with 1.75 mm channels, (b) fabricated PCL scaffold [48]

The designed geometry was not accurately reproduced, since excess powder was sintered and bonded to the surface of the pore architecture, as a result the actual macroporosity of the scaffold was less than the designed porosity. The manufactured scaffolds were incompletely dense in the design solid regions which increased overall porosity. Compressive modulus of the manufactured scaffolds was 52-67 MPa, and compressive yield strength was 2-3 MPa, which is in the range of human trabecular bone. In vivo cell culturing was carried out and results showed that SLS processed PCL scaffolds enhanced tissue in-growth.

Partee et al. [57] optimized the parameter setting for the above experiment by applying a 2 level factorial design of experiments, using five different parameters: laser power: 4.1 - 5.4 W, scan speed 1079.5 - 1231.9 mm/s, scan spacing 76.2 - 152.4 μm, part bed temperature 46 – 48 ˚C, powder layer delay 0 - 8 s. The authors defined the ideal SLS processed part as fully dense, where material is present in the design, dimensionally accurate, easy to remove from the support bed, including excess powder removal. The optimal parameter combination found was: P=4.1 W, v=1279.5 mm/s, scan spacing of 152.4 μm, T_{pb}=46˚C powder layer delay 0s. Scaffolds fabricated at optimal parameter settings are shown in Figure 2.10.

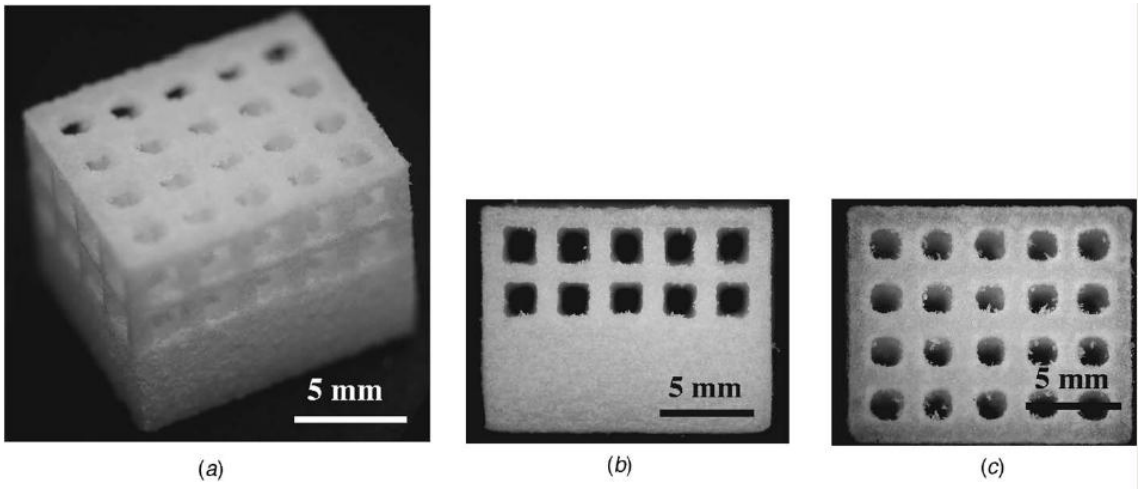

Figure 2.10 SLS processed PCL parts fabricated at optimally determined parameters (a) isometric view, (b) side view, and (c) top view [57]

With these settings the authors could achieve 94% density for the designed solid regions and dimensional accuracy for the outer dimensions within 3%-8% of design specifications.

The most recent study was published last year by Zhou et al. [70] from the University of Hong Kong on SLS fabrication of scaffolds using PLLA/carbonated HA microspheres. PLLA and PLLA/HA composite (with particle size of 5-30 μm) microspheres were fabricated via oil-in-water emulsion/solvent evaporation technique and processed on a Sinterstation 2000. Parts were built in 45˚ orientation to reduce anisotropy. Sintering conditions that were found to be suitable processing PLLA and PLLA/HA composite microspheres are listed in Table 2.4.

Sintering parameter	PLLA	PLLA/HA
Scan spacing [mm]	0.15-0.21	0.15-0.21
Part bed temperature [˚C]	30-40	30-60
Layer thickness [mm]	0.1	0.1
Scan speed [mm/s]	1257	1257
Laser fill power [W]	11-15	11-19

Table 2.4 Sintering parameters suitable for processing PLLA and PLLA/HA microspheres [70]

It was noticed that deposition of composite microspheres was easier as they flowed more easily than PLLA microspheres. Sintered areas were not fully dense, (see Figure 2.11) micropores were present.

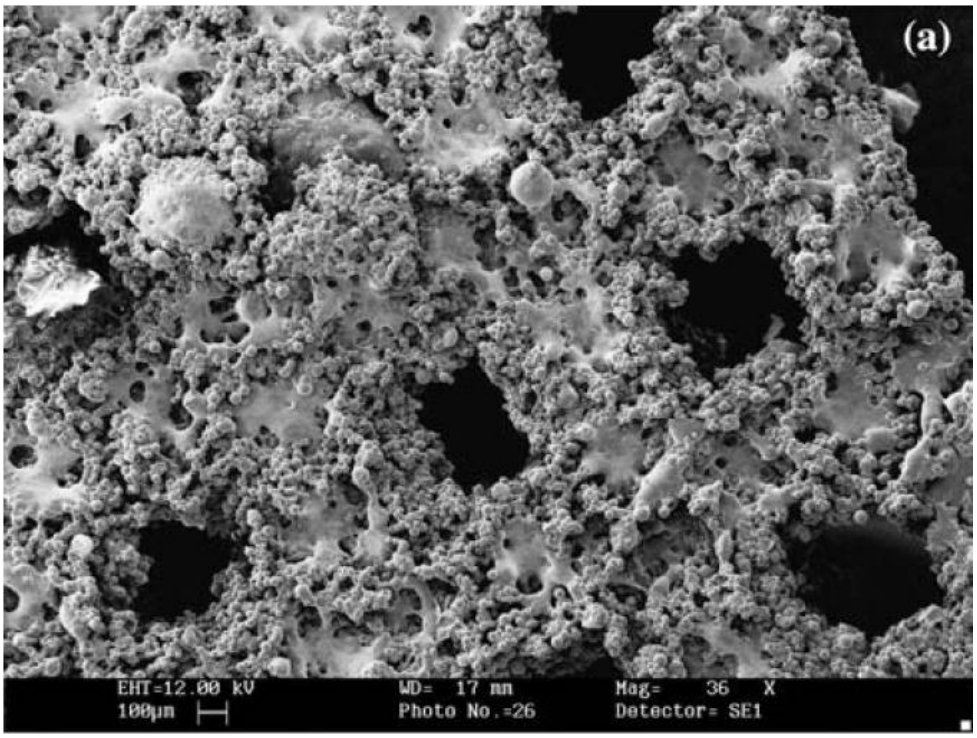

Figure 2.11 SEM image showing the structure of sintered PLLA scaffolds [70]

In agreement with previously introduced studies, the degree of sintering for the composite powder was lower when using the same process parameters.

The above review shows that to date no studies have addressed the anisotropy issues associated with sintered scaffolds. The present work will examine this question in detail with respect to mechanical properties.

Although the effect of the addition of a ceramic component has been examined on mechanical properties, its influence on surface characteristics and biocompatibility

remains less explored. The current study aims to describe the influence of material composition on these properties. Furthermore, the influence of powder particle size is also integrated into the examination of the effect of material composition on mechanical properties.

From the above overview of the published work on fabricating porous scaffold using selective laser sintering, it can be seen that most groups used a trial and error method to find usable processing parameters. In most cases only general trends were identified on the effect of parameters based on qualitative morphological observations. Only one study was published that used statistical analysis and optimization techniques to find an ideal solution for the process parameter combinations [57]. Furthermore, only a limited number of studies carried out detailed characterisation of fabricated scaffolds and reported mechanical properties or accuracy.

The current project aims to overcome these limitations and use a more systematic approach to find optimal parameter settings for different material compositions of PCL/HA blends by using design of experiments approach employing multiple parameter levels. Materials selection was based on successful clinical history of the materials. The objective is to develop mathematical models to describe the relationships between process parameters and part properties that will help to select parameter prior manufacturing to achieve certain properties. Furthermore, this study also aims to carry out a comprehensive characterisation of the fabricated scaffolds, in terms of composition, mechanical properties, anisotropy and microstructure.

2.4 Characterisation of cellular solids

Cellular solids can be thought of as composites made up of solid and air, where the solid parts consists of an interconnected network of struts, membranes, plates or shells which form their edges and faces. When cellular solids have an open-cell structure and are made up of struts they are often called lattices. The scale of lattice materials is in the order of millimetres or micrometers and therefore they can be viewed both as materials and as structures. At one level, they are a mechanical structure of connected struts, however in another level they can be thought of as a material. Cellular materials are abundant in nature: wood, cork, cancellous bone, sponge, coral are all cellular solids.

Cellular solids, also called foams are key to tissue engineering. They represent the first step in tissue regeneration by providing a porous matrix on which cells can be seeded to initiate bone formation. Besides, cancellous bone itself is a cellular solid, and therefore in an approach to mimic its extracellular matrix, cellular solids are an obvious choice. The structures fabricated in the current study to be used as bone scaffolds also belong to this category of materials. In fact, 3D scaffolds fabricated via SLS exhibit a double cellular structure. The designed macrostructure is a periodic lattice structure while the struts within the lattice are cellular solids with a stochastic microstructure.

The book by Gibson and Ashby [71] gives an excellent review on basic mechanical behaviour of cellular solids. A schematic compressive stress-strain curve for an elastic-plastic foam (also a solid/air composite) is shown in Figure 2.12. Initially the response is stiff and linear, then the response becomes progressively softer until a local load maximum develops, marking the yield strength of the cellular solid and indicating the beginning of plastic deformation. Beyond this point is a long collapse-plateau with approximately constant stress. The response finishes with the regime of densification in which the stress rises steeply again.

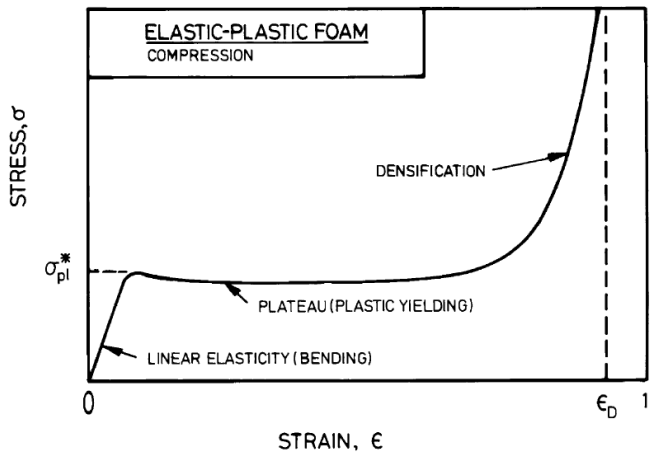

Figure 2.12 Schematic uniaxial stress–strain curves for elastic–plastic polymeric foam in compression [41]

The linear elasticity is controlled by cell wall bending. The plateau is associated with the collapse of cells – by elastic buckling in elastomeric foams and by formation of plastic hinges in foam which yields. Further strain, after cell walls are completely collapsed and opposing cell walls touch, compresses the solid itself giving a final region of steeply increasing stress [71]. This response is shared by many polymeric cellular solids, especially those that can be treated as a continuum. In order to treat a lattice structure as a continuum, it had to be ensured that the ratio of specimen dimension to

unit cell size was more than 20 [72]. However in many cases, when lattices are being designed and fabricated there is a lower number of unit cells within the structure. Examination of these structures elucidates what is behind the collapse plateau regime of the material response. Work by Papka and Kyriakides [73, 74] on 2D polycarbonate honeycombs gives some guidance on the underlying mechanism. Figure 2.13 shows the compressive stress-strain curve of the structure and the corresponding deformations. The initial linear elastic response and the densification regime is the same as shown for typical foams.

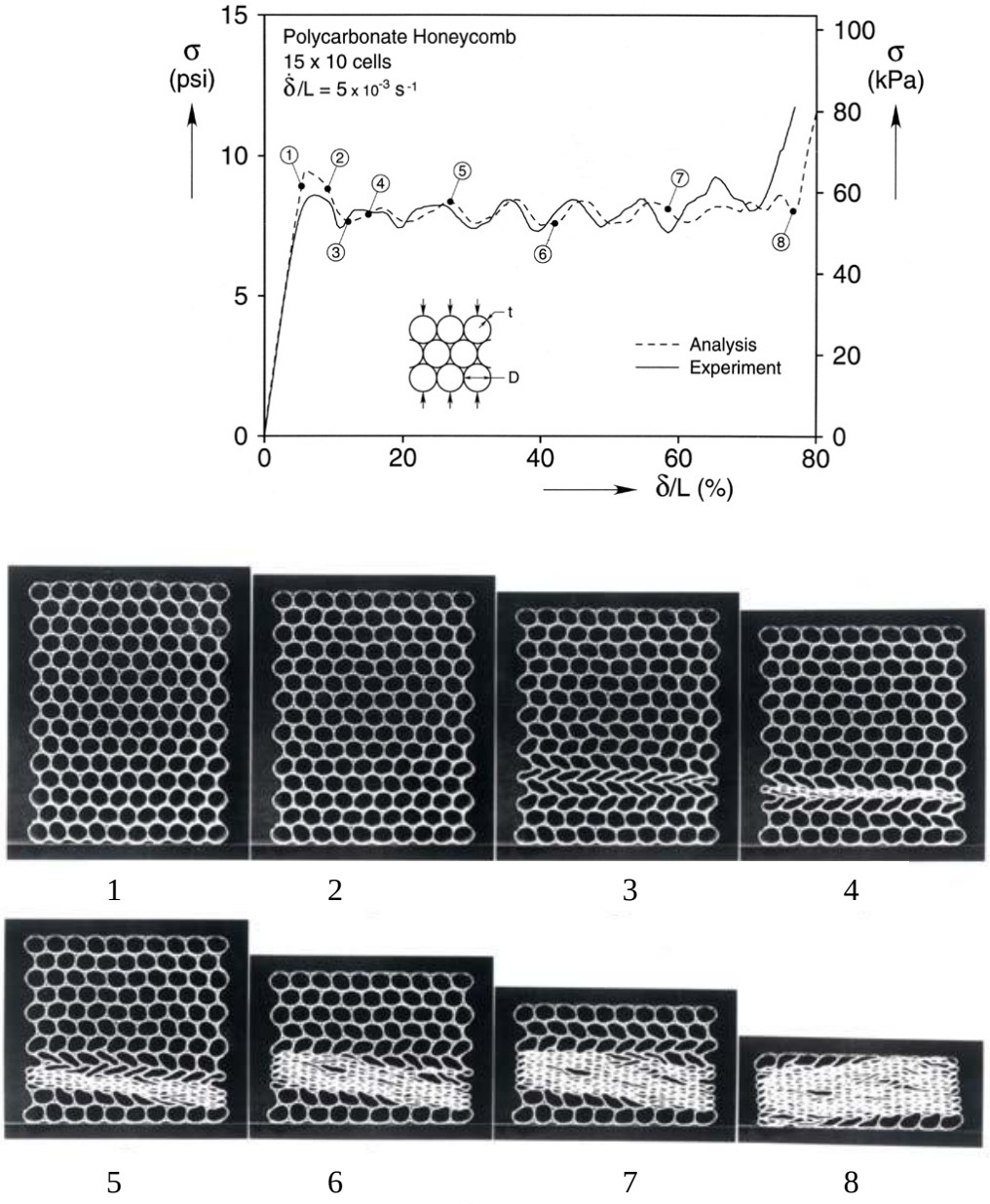

Figure 2.13 Force-displacement crushing response of polycarbonate honeycomb and corresponding sequence of deformed configurations [73]

However, after the yield point the deformation starts to localize in a narrow zone (1-2 layers). The deformation of these layers weakens the subsequent layers, which collapse next. This process is repeated until the crushing propagates through the specimen. This propagation is responsible for the spiky features of the collapse plateau in the compressive response.

When using lattices, understanding the relationships that relate the microstructure and the base material to the mechanical properties of the foam is very important. The factors that dominate mechanical behaviour of these structures are:

- properties of the bulk material,
- relative density of the structure,
- size and shape cell edges and faces,
- topology (connectivity).

In the past the main focus of interest was on relative density and to develop models that relate it to mechanical parameters [71].

Young's modulus of lattice materials as a function of relative density can be determined using simple beam theory. The relationship can be adequately represented by the power-law expression:

$$\frac{E}{E_S} = A\rho^a \qquad \text{Eq. 2.2}$$

where E is modulus of the lattice, E_S is modulus of the solid material the lattice is made of. For stretching dominated structure a=1, in contrast a=2 for bending dominated structures. The pre-exponent constant A is dependent upon geometry, and is typically in the order of 0.3-0.5. According to beam theory, macroscopic yield strength of the perfect lattice can also be calculated as follows:

$$\frac{\sigma_y}{\sigma_{yS}} = B\rho^b \qquad \text{Eq. 2.3}$$

where σ_y is yield strength of the lattice, σ_{yS} is yield strength of the solid material the lattice is made of. For stretching dominated structures b=1 and for a bending dominated structure b=3/2. The pre-exponent constant B is dependent upon geometry but typically is in the order of 0.3-0.5.

Nowadays, the main focus of research in mechanical behaviour of cellular materials concentrates on topology. The failure mode of a structure can be shifted from bending to stretch dominated by changing its topology. Stretching dominated structures have far greater strength and stiffness than those where bending is the dominant-mode of failure (soft-mode). As an example, a low-connectivity lattice (ie. foam) with a relative density of 0.1 is less stiff by a factor of 10 than a fully stretch dominated lattice (triangulated lattice) of the same relative density [75].

Many research groups concentrated on connectivity (Z) that describes the number of struts meeting in each node. It was found that a sufficient condition for a lattice to be stretch-dominated is that the unit cell of the structure satisfies Maxwell's criterion for static determinacy [76]. The criterion for 3D is as follows:

$$b - 3j + 6 \geq 0 \qquad \text{Eq. 2.4}$$

where b is the number of struts and j is the number of nodes in the unit cell. Structural analysis of pin jointed structures showed that high nodal connectivity (Z), Z≥5 is needed for structural rigidity [76].

If connectivity is lower, a pin jointed structure behaves as a mechanism while a structure with rigid joints behaves as a compliant bending dominated structures. Foams and most cellular solids with stochastic internal geometry are of this type, compliant bending dominated structures. Deshpande et al. [77] further examined the criteria for designing stretch dominated lattices for a special type of lattices called lattices with similarly situated nodes (nodes are similarly situated if the remainder of the structure appears the same and in the same orientation when viewed from any of the nodes). They showed that the necessary and sufficient condition for the structures to be stretch dominated is that connectivity at each node is Z≥12.

However, for the full gain to be realized the structure must be predominantly stretch-dominated, weak stretch domination offers only a marginal solution. A relevant and interesting 2D structure examined by Deshpande et al. [77] is shown in Figure 2.14. On the large scale the structure is homogeneous and deformation of struts (formed by the shaded areas) is not possible without stretch-dominated failure. However this case does not realize full gain of a stretch-dominated structure because the interior of each macro-square (pores circumscribed by the shaded macro-struts) still deforms by bending of cell edges.

This example well illustrates an issue that is anticipated with lattice structures fabricated via SLS, as similar hierarchy will be present. On the macro-scale, the geometry could be designed to be stretch dominated, however fabricated struts of this structure will be porous, that is, the material of the struts is stochastic foam and deformation within the strut is expected to be bending dominated.

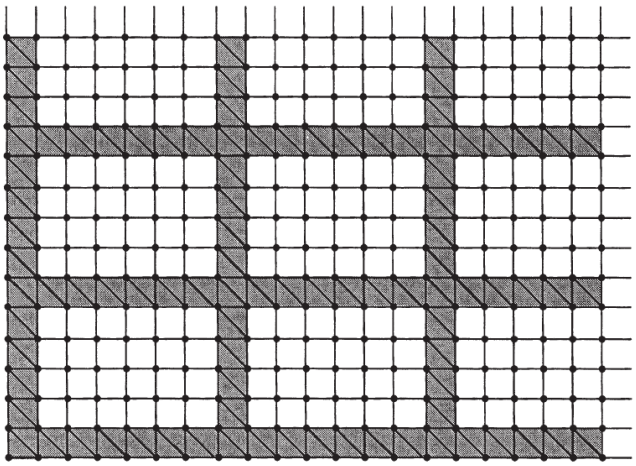

Figure 2.14 Statically indeterminate structure that is minimally stretch dominated [77]

The literature detailed so far used a more traditional approach and based their models on an idealized unit cell or repeating unit, as it was shown that a unit cell can capture essential microstructural features of the material. The most widespread model is a cubic cell based model developed by Gibson and Ashby [71], while more recently, tetrakadecehedral cells have been used by Zhu et al. [78] and by Li et al. [79] to develop structure property relations for open foams.

These models are very appropriate for periodic lattice structures, and although they also prove useful in estimating mechanical properties of foams, they are very limited for pertinent modelling of stochastic foams. Changes in size and shape of cell edges can be accounted for, however perturbations and microstructural imperfections are completely excluded from these models, that is a problem when the microstructure of many cellular solids is random and disordered. In recent years, large efforts have been made to explore these perturbations in order to better understand the mechanical behaviour of these structures. Introduction of these effects is not the subject of this review, and the influence of different irregularities of features can be found in the following references:

- irregular cell shapes and sizes [80-84],

- variation in cell wall thickness [85],
- inhomogeneous cell wall distribution [86],

The weakness of most of these models is that they examine only one type of imperfection at a time. Although, a large amount of work has been done in this area, prediction of overall mechanical response based on cell geometry, base material and more recently topology and perturbations is still very limited, and understanding of mechanical behaviour remains restricted. From small to intermediate deformations mechanical properties can be predicted well by using FEA or beam theory. However, for larger deformations, where non-linearities are dominant, it becomes a demanding task.

Additive manufacturing technologies like SLS opens new possibilities for the fabrication of predesigned cellular solids, and therefore for experimental investigation and understanding of the mechanical behaviour of these structures. Additive technologies enable fabrication of functional cellular structures with desired microstructure tailored for specific needs. Before the introduction of these technologies it was hard to precisely control shape, size and geometry of foams or lattice structures on the millimetre or micron scale, therefore it was hard to experimentally investigate the relationship between mechanical properties and topology of the microstructure. To date only a few research papers have been published on the mechanical characterisation of designed 3D lattices fabricated using an additive manufacturing technology. In 2004, Woß et. al [87] produced periodic lattices via SLS that had the same designed relative density using various unit cells (simple-cubic, translated-cubic, body-centered-cubic, reinforced-cubic, and Gibson-Ashby geometry). The authors have experimentally shown that strength, stiffness and energy absorbtion efficiency of structures of a given relative density can be varied independently by varying the designed structure. In 2008, Singamaneni et al. [88] demonstrated that organised porous microstructures with continuous open pores can be fabricated via interference lithography with intriguing mechanical properties such as lattice controlled crack propagation, high toughness and high energy dissipation.

The potential in microarchitectural design and its fabrication via additive manufacturing is huge, however manufacturing induced changes to the designed structure has to be accounted for. When using SLS for the manufacturing of lattices two main issues have to be considered:

- microporosity within the struts is inherent to the manufacturing technology (as SLS is a powder based technology), and
- fabricated parts are orientation dependent in terms of mechanical properties (to some extent because designed dimensions are reproduced differently in the various building direction, but also due to the different scanning patterns in the different directions).

The proposed experiments will be carried out to examine the following hypotheses:

- Part orientation does not only slightly alter mechanical properties (like strength and modulus) but also changes the failure mechanism within the lattice structure.
- Particle size of the powder used affects mechanical properties not only by altering the relative density of the solid parts but also changing its topology (connectivity) and sintering behaviour
- SLS is able to reproduce the stretch and bending dominated lattices

2.5 Properties of PCL and PCL composite scaffolds

Bone scaffolds are fabricated from a biocompatible material that does not elicit immunological or clinically detectable foreign body reaction. Currently the fabrication of bone scaffolds is driven by FDA approved bioresorbable polymers [89, 90] such as collagen [91-95], polylactides [96, 97], polyglycolides [98], their copolymers [99, 100] and polycaprolactone (PCL) [101-110] combined with osteoconductive ceramics such as hydroxyapatite (HA) or tricalcium phosphate (TCP). As polycaprolactone is used throughout this work, this review will focus on its biocompatibility and other relevant properties

Polycaprolactone is a bioresorbable semi-crystalline (up to 69%) linear aliphatic polyester with glass transition temperature of -60˚C and melting temperature of 59-64˚C, depending on its crystallinity [111]. The molecular weight of PCL samples varies from 10 000 to 200 000 Da. PCL is subjected to hydrolytic degradation due to the subsceptibility of its aliphatic ester linkage to hydrolysis [107].

Degradation of PCL in comparison to polyglycolic (PGA) and polylactic acid (PLA) is slow. Its degradation and resorption kinetics are considerably slower, due to its hydrophobic character and high crystallinity. It degrades in a period of over two years making it suitable for long term applications. Its high molecular weight coupled with

hydrophobicity and slow degradation rate allows matching the rate of bone tissue ingrowth. The degradation of PCL can be divided into two phases. No (or very moderate) weight loss is observed during the initial phase of the biodegradation process if molecular weight is in range of 50 000 -200 000 Da. This phase is characterised by chain scission. The second phase of biodegradation is characterized by the decrease in the rate of chain scission and the onset of weight loss. The decreased rate of chain scission is associated with an increase in crystallinity, since cleavage takes place in the amorphous region of the polymer [107, 112-114].

The in vivo degradation process was studied by Chen et al [115] by implanting low molecular weight PCL copolymer microspheres in rats. Hydroxycaproic acid, derived from complete hydrolysis of the polymer, and tritiated water were the only metabolites detected. The mechanism of bioabsorption was also examined at the implant site. This revealed the presence of intracellular polymer particles and demonstrated the role of phagocytosis during the final stage of polymer degradation.

In vivo bone ingrowth into PCL scaffold has been investigated by several research groups. Rohner et al. [116] reconstructed orbital defects (2 × 2 cm) in pig using PCL scaffolds fabricated via fused deposition modeling (FDM). The study concluded that after 3 month of implantation the scaffold is able induce bone ingrowth required for reconstructing craniofacial and orbital defects. Williams et al. [48] also demonstrated the capability of SLS fabricated PCL scaffolds to induce bone ingrowth into its micropores using μ-CT scans. The measured bone mineral density of regenerated bone was 510 mg/cm^3, that is within the range of normal human trabecular and cortical bone (120 and 1100 mg/cm^3, respectively). Histological staining also confirmed the presence normal bone morphology including osteocytes, trabeculated structures and marrow space.

Despite the positive results on bone ingrowth and degradation, concern is given to possible acidic degradation products that can change pH levels at the implantation site. This phenomenon has been reported for other biodegradable polyesters, and incorporation of calcium phosphate ceramics helped to buffer their detected acidic by-products [117-119]. Furthermore, it is generally accepted that incorporation of HA or TCP also improves osteoconductivity and osteointegration of the scaffold, due to its similarity to the mineral content of natural bone and by providing physiological minerals which could be incorporated in bone regeneration [120]. Osteoconductive

ceramics like HA or TCP form a bioactive bond (bio-chemical) to bone and a layer of hydroxycarbonate-apatite (HCA) crystals is built up, which binds the collagen fibrils of the newly formed bone. The presence of HCA also enhances the cellular response and increases collagen production [34]. The crystal size of the inorganic content of natural bone that is, carbonated HA is at the nanometer scale and it is considered to be important for the mechanical properties of bone. Webster and colleagues [6, 121] have shown significant increase in protein absorption and osteoblast adhesion on nano-sized ceramic surfaces compared to the traditional micron scale surface. This is possibly due to increased surface area and hydrophilicity. With decreasing particle size the observed osteoblast adhesion increased.

In the present work incorporation of HA and TCP into the polymer matrix is examined, as these materials have a long and successful clinical history. Calcium phosphates are not the subject of this section. Comprehensive reviews on calcium phosphates and their application in medicine were published by Dorozhkin [122], Bohner [123], Livingstone [124], and most recently by Dorozhkin [125]. A review on in vitro biocompatibility characterization of PCL, PCL/HA and PCL/TCP composites is given below.

The biocompatibility of biomaterials is related to cell behaviour on contact with these substrates and particularly to cell adhesion to their surface. Surface characteristics of materials, including their topography, chemistry or surface energy, play an essential part in osteoblast adhesion on biomaterials [126]. Adhesion to the surface of the biomaterial involves physico-chemical linkages between cells and materials involving ionic forces, van der Walls forces, etc. in the short term and various biological molecules: extracellular matrix proteins, cell membrane proteins, and cytoskeleton proteins which interact together to induce signal transduction, promoting the action of transcription factors and consequently regulating gene expression in the long term [126]. The extracellular matrix of bone is composed of 90% collagenic proteins and of 10% non-collagenic proteins. All these proteins are synthesized by osteoblasts and most are involved in adhesion [126]. Therefore, interaction of osteoblasts with the scaffold interface is a crucial aspect of studying the biocompatibility of 3D templates for tissue-engineering applications.

Hutmacher et al. [102] evaluated proliferation and differentiation response of human fibroblast cells on rapid prototyped (FDM-fused deposition modelling) 3D PCL scaffolds. According to this study human fibroblasts colonize on the struts and bars of

an FDM-fabricated PCL scaffold and form a cell-to-cell and cell-to-extracellular-matrix interconnective network throughout the entire 3D honeycomb-like architecture. Marra et al. [105] investigated PCL composites seeded with fresh bone marrow. The study demonstrated that after 8 weeks of incubation there was collagen production and cell proliferation throughout the scaffold. Corden et al. [127] also showed adhesion and spread of cells on PCL material of different molecular weights. The authors also noticed that adhesion and proliferation is also dependent on surface topography.

Shor et al. demonstrated that scaffolds with 25 wt% HA exhibit improved cell activity compared to pure PCL scaffolds fabricated via precision extrusion deposition. Although, Alamar Blue (proliferation assay) showed no statistical difference between PCL and PCL/HA, PCL-HA scaffolds had significantly higher ALP activity (ALP: an enzyme produced by differentiating osteoblasts and is responsible for construction of bone matrix). The SEM images also confirmed that PCL-HA scaffolds produced more mineralized matrix, compared to PCL [108].

It was seen by several groups that the presence of HA in the PCL scaffolds only slightly affects biological response. Comparing FDM fabricated PCL and PCL/HA scaffolds seeded with human marrow mesenchymal stem cells, Enders et al. [128] found that initially cells in the PCL-HA scaffolds showed less metabolic activity, but reached the same level as PCL by day 28. Chim et al. [101] also reported no significant difference between PCL and PCL/HA scaffolds fabricated by FDM when using human calvarial osteoblasts.

Ciapetti et al. [129] tested PCL and PCL/HA (40 wt%) scaffolds prepared by phase inversion and casting technique, and it was found that when examining metabolic activity of Saos-2 cells, the HA reinforced samples scored higher values compared to pure PCL. The same was observed for the release of ALP (early marker of mineralization), which reached a detectable amount in cultures at 7 days from seeding. In the 30 day experiment, once again the metabolic activity of the cells on the HA added polymers was more intense and formation of mineralized nodules was also found to increase. SEM micrographs revealed that after 4 weeks the surfaces were fully covered by osteoblast like cells in both cases. Polygonal cells were covering the surface of the micro/macroporous PCL and PCL/HA composite.

Causa et al. [104] examined the Saos-2 cell response of different compositions of PCL/HA composites (13 and 32 vol % HA) fabricated via phase inversion and casting

technique. The release of ALP was higher for cells grown in PCL/13 vol% HA. This trend was confirmed with human osteoblasts (hOB) (tested on compositions 13,20,32 vol% HA). Osteoblasts on PCL/32 vol% HA never reached the ALP levels measured for the other scaffolds. After 4 weeks hOB showed high level of confluence on each scaffolds on the SEM images. Cells were multilayered with evident cytoplasmic filopodia providing intercellular communication, and a consistent extracellular network underneath. Cells on PCL/32 vol% HA grew slowly and showed a less differentiated phenotype during growth of scaffold.

Besides material composition osteoblast/material interaction also depends on the surface aspects of materials such as topography, chemistry or surface energy. These surface characteristics determine how biological molecules adsorb to the surface and also the orientation of adsorbed molecules [10]. The first phase of cell adhesion depends on adhesion proteins and then the quality of this adhesion influences morphology of the cells, and their capacity for proliferation and differentiation. Surface characteristics of an implant, particularly roughness, may control tissue healing and therefore subsequent implant success. The hydrophilic and hydrophobic characteristics of a material are also of great importance for cell adhesion. Cell adhesion is generally better on hydrophilic surfaces [126].

One of the main concerns with PCL is its low mechanical properties compared to other biodegradable polyesters. Therefore PCL scaffolds are not intended for use in load bearing applications. Enhancement of mechanical properties can possibly be achieved by reinforcing PCL with HA or TCP particles, which – as discussed above – also improves osteoconductivity of the polymer.

Causa et al. [104] tested the tensile properties of different compositions of PCL/HA composites (0, 13, 20, 32 vol% HA). Unreinforced PCL showed the lowest mechanical properties. Elastic modulus increased up to 20 wt% HA addition; however a decrease was seen for the composition containing 32 wt% HA. The tensile yield strength slightly decreased with 20 and 32 wt% of HA addition. However, higher amount of HA lead to a lower value of strain at rupture at any rate, as the materials became more brittle. The strengthening mechanism of HA within PCL samples is to be ascribed to the stiffer mechanical properties of HA. The reinforcing effect is evident when the amount of HA does not exceed the values of 20 vol%, as above this value a drop in mechanical

properties is observed. Similar reinforcing effects have been observed by Azevedo et al. [130], Guarino et al. [109] and Chen at al. [131].

The above review demonstrates that PCL and its composites are viable materials for the fabrication of bone scaffolds. These materials are used throughout so that this work can focus on the manufacturing related research questions introduced in Section 1.1.

1.) As shown in the review, many research groups have already adapted SLS as a manufacturing technology for scaffold productions, however capabilities and limitations of the current technology have not been exploited in this field.
2.) The effect of ceramic phase addition has been investigated on mechanical properties of scaffold produced via SLS, however anisotropy of the parts was not taken into account when examining these effects. Moreover, surface characteristics have not been examined.
3.) To date no models have been developed that can predict the mechanical and dimensional properties of microstructures based on SLS process parameters.

3 MATERIALS AND METHODS

This chapter outlines the materials, equipment, experimental and design procedures that were used throughout this research.

3.1 Materials

All the materials selected (polycaprolactone, hydroxyapatite, and tricalciumphosphate) for this research have a long and successful clinical history. Furthermore, these materials are widely investigated in the field of bone tissue engineering as has been shown in section 2.5. This allowed sharpening the focus of this research to the manufacturing technology.

Polycaprolactone (PCL) pellets were purchased from Sigma Aldrich Chemical Co. (catalog no. 440744). Properties of the material provided by the supplier are listed in Table 3.1.

Average nominal molecular weight:	**~80 000 (determined by GPC)**
Melt index:	**1.0g/10 min (125 ˚C /0.3 MPa)**
Impact strength:	**350 J/m (Izod, ASTM D 256-73A, notched)**
Hardness:	**55 (Shore D, ASTM D 2240-75)**
Melting temperature:	**60 ˚C**
Density:	**1145 kg/m^3 at 25 ˚C**
Elongation:	**800-1000% (ultimate at 0.85mm/s)**

Table 3.1 Thermal and mechanical properties of PCL as provided by the supplier

For SLS processing, polymers in powder form are needed. PCL is not commercially available as powder, but is sold in the form of ~3 mm pellets. Two methods were adopted to produce PCL powder: microsphere preparation and cryogenic grinding. PCL microspheres were prepared using an oil-in-water emulsion/solvent evaporation technique. 10 g of PCL was dissolved in 100 ml dichloromethane. The resulting w/o emulsion was poured into 1 l of de-ionized water containing 1% PVA (emulsifier) where it was again emulsified under continuous stirring. Stirring was continued for 3 h at 500 rpm, to evaporate the organic phase. The microparticles formed were filtered and dried.

Mechanical grinding of the PCL pellets was first attempted in-house using A11 IKA analytical mill in the presence of dry ice. The fabricated powder was sieved through a

sieve with 150 μm aperture size, and approximately 1 kg of powder was produced this way. PCL150 is used to identify this powder batch.

Due to the time and labour intensive nature of in-house grinding, 20 kg of PCL was sent to be cryogenically ground by Solid Composites, Germany. The fraction of resulting powder below 100 μm was used for SLS, and amounted to about 5 kg. PCL100 and PCL75 are used to identify the powder batches according to the aperture size of the sieve used.

The hydroxyapatite (HA) powder used in the experiments was sold under the brand name Captal 60-1 (Plasma Biotal Ltd.). According to the supplier it had an average particle size of 45±5 μm and bulk density of 1.3 g/ml^3. PCL/HA powder blends containing 10, 20, 30 and 40 wt% of HA for thermal analysis and 15 and 30 wt% of HA for SLS processing were produced by physical blending. (Accordingly, the labels PCL/15HA and PCL/30HA are used.)

β-tricalciumphosphate (TCP) powder brandnamed Whitlockite was purchased from Plasma Biotal Ltd. On average, 83 % of the powder is β-TCP and the remaining 17 % is α-TCP as indicated by the supplier.

3.2 Powder characterisation

Before SLS processing morphology and thermal properties of the powders used in this study were characterized.

Scanning Electron Microscopy (SEM)

Morphology of the powder particles were examined using a Zeiss EVO LS15 SEM. The samples were gold coated and were examined under high vacuum.

Particle size analysis

A Malvern Mastersizer Type S Laser Diffractometer (Malvern Instruments Ltd., UK) was used to carry out particle size analysis of the PCL powders. It is a single lens laser diffraction system that uses a small helium-neon laser (~2 mW) to measure the size of the particles and produces a profile of the particle size distribution within the powder. Water was used to fill the sample preparation unit and about 2 g of powder was added, then it was stirred for several minutes, and then the suspension was passed through the beam of laser light.

Thermal Analysis

Thermogravimetric Analysis (TGA) and Differential Thermal Analysis (DTA) was carried out on the PCL powder to examine its thermal behaviour and expected degradation temperature. This was done using a Stanton Redcroft Differential Thermal Analyser / Thermogravimetric Analyser. A 10 mg sample of PCL powder was heated up from room temperature to 550 ˚C in an aluminium pan at heating rate of 2 ˚C/min.

A Perkin Elmer Diamond Differential Scanning Calorimetry (DSC) was used to study and compare the thermal behaviour of PCL and its composites with HA and TCP. Samples of about 6 mg were used for each run. Separate calibrations for the baselines were made for the selected heating and cooling rates each day. Calibration for the temperature and energy scale was carried out using a pure indium standard. The DSC analysis was performed under nitrogen gas atmosphere. Samples were held at 0 ˚C for 1 min, and then were heated from 0 ˚C to 130 ˚C at 5 ˚C/min and held for 5 min. Then samples were cooled down to 0 ˚C, held for 1 min and heated to 130 ˚C again at 5 ˚C/min. The heat flow was recorded and analyzed during cooling and during the second heating. The melting temperatures and enthalpies of fusion (ΔH_f) were determined from the endothermic peaks of the DSC. From the exotherms of the cooling curves it was also possible to derive the non-isothermal crystallization temperatures (Tc) and enthalpies.

PCL150 powder was used to carry out all thermal characterisation.

3.3 Fabrication of scaffolds

All specimens for SLS fabrication were designed using Pro/ENGINEER® and were exported into STL file format.

All samples were manufactured on a DTM Sinterstation 2500^{plus} (3D Systems, Valencia, CA) installed with a low power (25 W), λ=10.6 μm continuous wave, CO_2 laser focused to a 400 μm spot. The SLS system was located at the National University of Ireland, Galway, and therefore access to the equipment was limited. For processing PCL and its composites the size of the powder bed and the feed bed were reduced, so that the machine could operate using smaller amounts of powder.

Process parameters are set via DTM's Build Setup interface that is a user friendly software application. In the software, DuraForm (polyamide) powder was selected as the material used, its recommended parameter settings were loaded into the software and individual process parameters were changed to enable processing of PCL powder.

When not indicated otherwise the following parameters were used to fabricate the PCL and PCL composite lattices:

- laser fill power: 10 W,
- outline laser power: 5 W,
- scan spacing: 0.15 mm,
- layer thickness: 0.15 mm,
- part bed temperature: 38 ˚C.

The system used does not allow the manipulation of laser speeds, the default values for outline and fill scan speed are 1778 mm/s and 5080 mm/s respectively.

These parameters have been selected based on literature and the preliminary screening work on the current SLS system. As introduced in Section 2.2, there is a considerable amount of work published on SLS processing of PCL. All these studies' scaffolds were fabricated on an older version of DTM Sinterstation than that used in the current work. In the new version of the machine some parameters (for instance, laser speed) that could be altered in older versions are fixed, furthermore settable parameter ranges are also narrower in order to make the system more user-friendly. Preliminary studies were carried out to find suitable working parameters.

Part bed temperature is a critical parameter and has great influence on the fabrication process itself and on the resulting part properties. Williams et al. [48] used 49.5 ˚C, and Partee et al. [57] found that the optimal part bed temperature is 46 ˚C. These temperatures were tried, however resulted in hardening of the powder bed and therefore induced problems during layer deposition. The temperature was therefore lowered. The system worked properly when nominally set to 38 ˚C, however it stabilized at 40 ˚C after the warm-up stage. The same temperatures were found to work for PCL by the research group at Nanyang Technological University [22, 60]. As for the applied laser fill power, in general significantly lower values were used (2-4.5 W), the used systems enabled reducing the laser speed that results in higher delivered energy densities. The used laser power by Wiria et al. [22] for processing PCL at scan-spacing of 5080mm/s –

that is the fixed value in the current system- and part bed temperature of 40 ˚C was still significantly lower, between 2-4 W.

Layer thickness was selected based on the particle size of the powders used. If particles are bigger than the set layer thickness it could result in uneven powder deposition. In-house ground PCL sieved below 150 µm, and had the biggest particle size, therefore selected layer thickness was 150 µm.

None of the previous studies have reported the use of outline scan that is also included in this work, as it is expected to have significant effects due to the small feature size of the designed geometries.

Once parts were manufactured, an extra 2 mm of powder was deposited to allow for part cooling without significant thermal gradients within the powder bed. When the powder bed cooled down to room temperature, parts were removed and excess powder was brushed off from the exterior and the internal architecture was cleaned using compressed air.

3.3.1 Studies on anisotropy and microporosity

The main objective of this study was to explore anisotropy issues associated with SLS. While it is known from literature that mechanical anisotropy is inherent to fabricated parts, it has not been qualitatively assessed on lattice structures to date. The current study examines anisotropy of fabricated samples at various microporosity levels. The microstructure of the struts was changed by varying particle size (PCL150, PCL100, and PCL75).

The geometry was built from simple cubic elements and is shown in Figure 3.1 with all associated dimensions. Designed strut thickness is 0.6 mm and designed pore size is 1.2 mm. The aim of the experiment is to reveal issues of anisotropy, therefore fabricated samples were compressed in the main building directions (x,y and z). Since the designed geometry is not identical in the main building directions, it had to be rotated to ensure that geometrical differences were not affecting mechanical behavior. Figure 3.1 illustrates the positioning of the sample when it was intended to be compressed parallel to the z-axis.

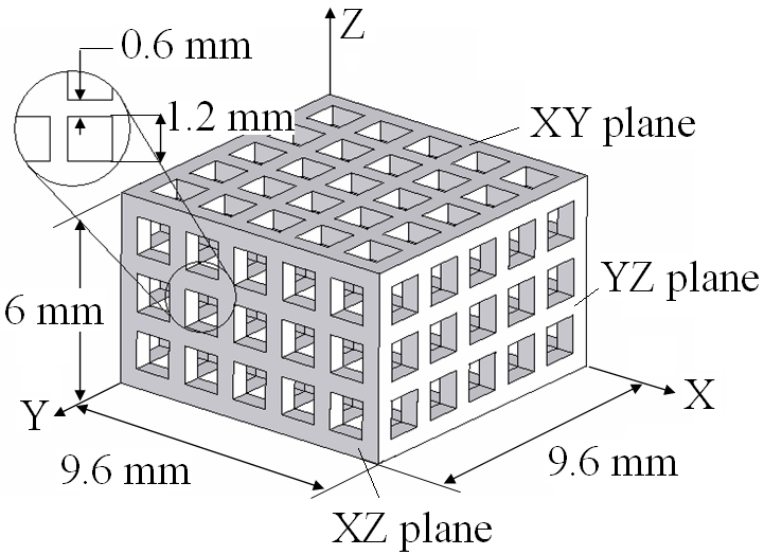

Figure 3.1 Geometry of designed lattice structures and its positioning when intended for mechanical testing along the z-direction. (z-direction is parallel to the movement of the pistons and x-direction is parallel with the scan lines of the fill scan)

To test the samples in the x-direction, parts during fabrication were positioned by rotating 90˚ around the y-axis, and to do the testing in the y-direction parts were rotated 90˚ around the x-axis. Seven replicates were manufactured in each direction for each powder batch (PCL150, PCL100, and PCL75), and samples were subjected to uniaxial compression testing.

Anisotropy of lattice structures with different designed geometries were also studied. Details of the geometries and results can be found in Appendix III.

3.3.2 Studies on material compositions

The aim of these studies was to see the effect of material composition on mechanical properties, surface characteristics and biocompatibility of fabricated scaffolds.

Different geometries were required for the various characterisations. Figure 3.2 illustrates the designed geometries (solid disk, 3D cubic lattice, 2D cubic lattice and solid bars) and lists the type of characterisation tests they were subjected to. Directional dependence of the samples was not examined except for compression testing of the 3D lattices. Parts were fabricated in two sets, one using PCL150, the other PCL100. When not indicated otherwise, the following material compositions were used: PCL, PCL containing 15 wt% HA (PCL/15HA), and PCL containing 30 wt% HA (PCL/30HA).

Set 1 using PCL150 and its blends

At an earlier stage of the project when only the in-house ground PCL powder was available solid disks and 3D lattices were fabricated.

Solid test bars were also produced, however these geometries were only fabricated from the PCL and PCL/15HA.

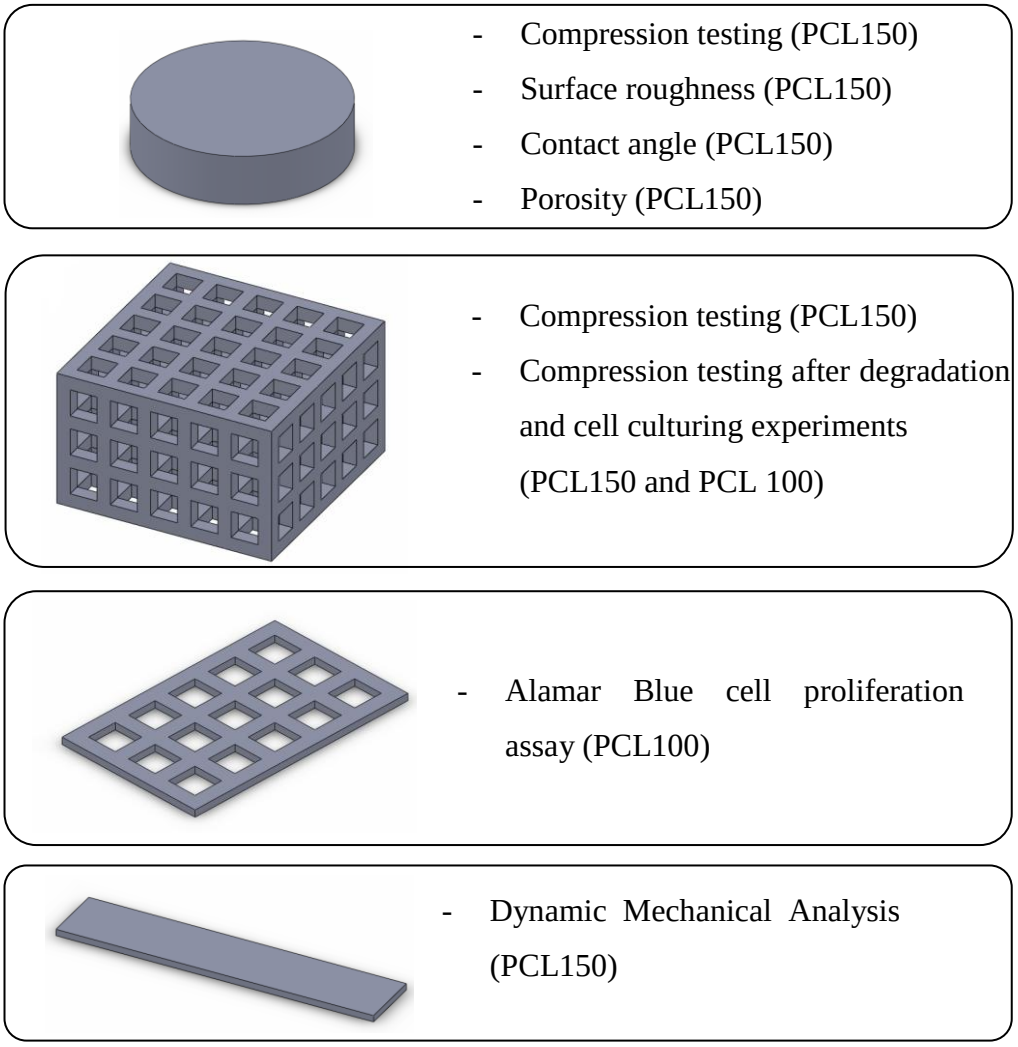

Figure 3.2 Designed geometries and characterisation methods used (from top to bottom: disk, 3D lattice, 2D lattice and bars)

Simple disks with diameter of 12 mm and height of 3 mm were subjected to compression testing, surface roughness, contact angle and porosity measurements. Seven replicates were fabricated for each material composition.

3D lattices (dimensions are shown in Figure 3.1) were fabricated for accuracy analysis and compression testing. Seven replicates were produced for each material composition.

Test bars with dimensions of $6.3\times20\times2.8\ mm^3$ were fabricated for DMA. Four replicates were fabricated for each material composition. The delivered energy density for fabricating these samples was increased in order to ensure great incorporation of HA particles into the polymer matrix. The scan spacing used was reduced to 0.12 mm, and laser fill power was increased to 13 and outline laser power to 8 W.

Set 2 using PCL100 and its blends

At a later stage of the project when PCL powder with smaller particle size became available 2D and 3D cubic lattices were fabricated.

Biocompatibility of the 2D lattices (outer dimensions of 6×9.6×2 mm, strut size of 0.6mm and pore size of 1.2 mm) was tested using Alamar blue cell proliferation assay. Five replicates were fabricated for each material composition.

3D lattices were fabricated for directional dependent compressive testing using the same material compositions. Seven replicates were fabricated for each material composition.

3D lattices were also fabricated for compression testing after degradation tests and cell culturing experiments to see the effect of cell culturing on mechanical behaviour. In this case directional dependence was not examined, all samples were built along z-axis of the SLS system. Three treatments were examined: degradation, and 1 and 2 weeks of cell culturing. Three replicates were fabricated for each material composition in each treatment.

3.4 Characterisation of scaffolds

All characterisation procedures related to mechanical testing, microstructure and biocompatibility analysis are detailed here.

3.4.1 Mechanical testing

Fabricated structures were subjected to compression and tensile testing, and dynamic mechanical analysis in tensile mode to assess their mechanical properties.

Compression testing

Compressive mechanical properties of the fabricated lattice structures were tested according to ISO 604 standards using a 5 kN load cell at crosshead speed of 1 mm/min and with a 1 N preload. The same procedure was used for the designed solid disks,

except the preload was increased to 10 N. A flat plate was used to apply uniformly distributed load on a Zwick/Roell universal testing machine. Compressive modulus, and compressive yield strength (referred to as compressive strength throughout this work) values were obtained using Zwick/Roell Text Expert II software. All testing was carried out at room temperature.

Tensile testing

Tensile mechanical properties of the fabricated specimens were tested according to ISO 527 standards using a 500 N load cell at crosshead speed of 1 mm/min and with a 1 N preload on a Zwick/Roell universal testing machine. Tensile modulus, yield strength and yield strain values were obtained using Zwick/Roell Text Expert II software. All testing was carried out at room temperature.

Dynamic mechanical analysis

Dynamic mechanical analysis (DMA) was carried out using Perkin Elmer DMA 7. The testing configuration was tension. A constant dynamic force of 10 N, and a constant static force of 10 N were applied at loading frequency of 1 Hz. The characterisation was carried out by tests performed in the temperature range of -90 to 50 ˚C at a heating rate of 2˚C/min. The constant dynamic force was used instead of the more commonly used constant stress, as an implant is subjected to constant forces in-vivo, while constant strain would be deformation dependent.

3.4.2 Microstructure

Contact angle

The contact angle of water on the sintered surface of the solid disk samples was measured using ArtCAM 130 MI BW monochrome camera, and FTA200 contact angle analyzer software. Static approach was used to analyze initial contact angle, and contact angle evolution after 1, 2 and 3 s.

Scanning Electron Microscopy

Surface morphology of the sintered parts were examined using a Zeiss EVO LS15 SEM. Samples were gold coated when examined under high vacuum. No coating was used when the SEM was operated in variable pressure mode.

Surface roughness

Surface topology and accuracy of the fabricated specimens were examined using scanning electron microscopy (SEM). Surface profile was obtained using optoNCDT laser profiler. Obtained data was analyzed in Matlab 7.5.1 and surface roughness (Ra) was calculated.

µ-Computer Tomography (µ-CT)

Samples were sent to Waterford Institute of Technology, and scanned using µ-Computer Tomography (µCT) (v|tome|x L 300, Phoenix x-ray). The limiting resolution is between 1-5 µm and depends on the operating voltage (30-300 kV). Tomographic imaging is achieved by acquiring a series of radiographs at different angles around 360˚. The series was reconstructed using VolumeGraphics® and image-stacks were generated that were analyzed in Matlab® as described in the following section.

3.4.3 Image analysis of µ-CT data

One of the main goals of this work is to develop a mathematical model that directly relates feature dimensions to SLS process. Data from the µ-CT was analysed to obtain the required data for developing the models.

Matlab7.5.0 (R2007b) was used to analyze the image stacks obtained from the µ-CT. Separate routines were written to analyze outer dimensional accuracy of the features and effective cross sectional area of struts in the lattices. The routines were integrated into a 'for' cycle, so that the process was automated and the routine was performed in all images associated with a strut (100 images for each strut covering a 450 µm length). Struts built in the three main directions were examined separately. The routines worked with pixels, and therefore they had to be converted to µm. (1 pixel=4.5 µm). Two routines were created for measuring apparent (outer) and effective cross sectional area (CSA) of the struts. Examples of the output images of the routines are shown in Figure 3.3.

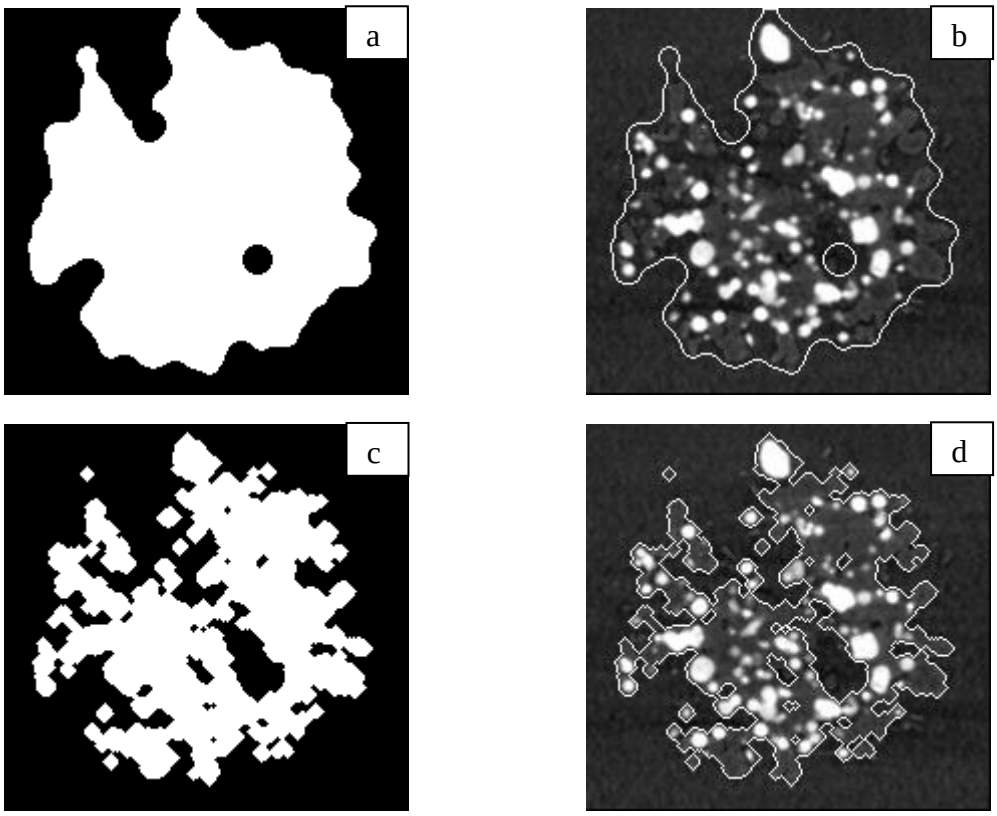

Figure 3.3 Output images of the first routine: (a) resulting binary image after morphologically closing the strut cross section (b) perimeter of the closed binary image superimposed on the original image. Output images of the second routine: (c) resulting binary image after morphological opening strut cross section, (d) perimeter of the opened binary image superimposed on the original image

Routine for measuring apparent CSA

Images were read into Matlab workspace from the image stacks and were cropped so that cross section of only one strut was analyzed at a time, but with the cropped area circumscribing the strut area. The cropped images were converted to greyscale intensity images.

Noise reduction was performed via median filtering of the images. It is a non-linear digital filtering technique that is often used to remove 'salt and pepper' type of noise. Contrast of the images was increased by mapping the intensity values of the original greyscale image and changing to the new values such that 1% of data is saturated at low and high intensities of the original image.

Images were then converted into a binary image based on a manually selected threshold. Manual selection of the threshold was necessary as the different scans (total 15) had different intensity values. Example output images of the routine are shown in Figure 3.4. It can be seen on the converted binary image that selection of the correct threshold

can be problematic (indicated with arrows). The problem is that there are beam hardening artifacts in the data set that appear to be light bands. Trying to select the best greyscale value for the surface of the sample is therefore made difficult as these bright bands are being calibrated as solid rather than air.

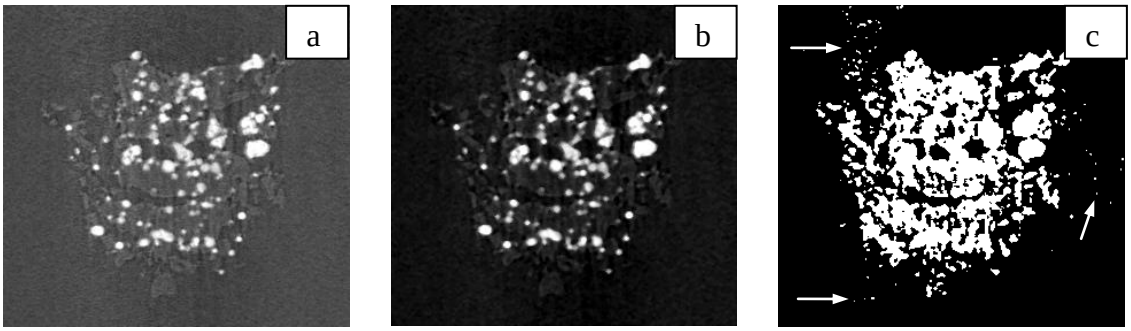

Figure 3.4 Image processing of the cropped image: (a) original image, (b) image after noise filtering and contrast adjustments, and (c) image converted to a binary image after thresholding

It can be possible to use certain filters to further reduce the beam hardening artefact. However, due to the low density and therefore low intensity of the polymer within the composite it was not an option for these scans. Therefore, it was chosen to perform a morphological closing operation in the background. To do that the binary image was inverted, the closing operation was performed and the image was inverted back.

Then the morphology of the resulting binary image (cross section of the strut) was closed using a disk shaped structuring element with a radius of 15 pixels. Then, the cross section of the strut was identified as an object. Perimeter of the object was defined and superimposed on the original image to enable verification that the correct areas have been identified as solid.

Once an object is labelled in the binary image, Matlab can calculate its area and store it in a structure array with other properties of the object such as its perimeter, orientation, major axis length or solidity. Measured areas were pulled from the structure array and exported to a text file.

Routine for effective CSA

Porosity of a strut can be determined by subtracting its actual area (effective cross sectional area) from the area defined by its outer perimeter. The area defined by its outer perimeter was obtained from the previous routine.

To determine the effective cross sectional area (CSA) of a strut some modifications were made to the 'routine for accuracy analyses'. After thresholding and converting the greyscale image to binary image and morphologically closing its background, instead of morphologically closing the cross section of the strut it was subjected to morphological opening.

Morphological opening can be used to remove small objects – that could possibly appear during thresholding due to remaining noise in the image – while preserving the shape and size of larger objects in the image. Morphological opening is erosion followed by dilation of the objects of the binary image using the same structuring element (disk of 1 pixel in diameter) for both operations. Identified objects were labelled and sum of the area of all objects was exported to a text file.

3.4.4 Biocompatibility tests

Biocompatibility (osteoblast adhesion and proliferation) of fabricated scaffolds was assessed. Furthermore, the effect of cell culturing on mechanical properties was also investigated in order to compare the tested material compositions in terms of biocompatibility.

Biocompatibility tests were not carried out by author. Nihal Engin Vrana, a colleague in DCU carried out the following degradation and cell culturing experiments according to the procedures detailed in Appendix II:

- Degradation (mechanical testing)
- Cell attachment (fluorescent microscopy, SEM, mechanical testing)
- Cell proliferation (Alamar blue assay)

Morphological analysis via SEM, and mechanical testing of cell cultured samples, and related data analysis was carried out by the author.

3.5 Design of experiments and statistical analysis

In the following, the first section introduces the design of experiments approach used to test the significance of process parameters and develop models that relate part properties to process parameters. The second section presents the statistical analysis used to compare treatment groups. The last section introduces how the models that describe the effect of process parameters on mechanical properties and dimensional accuracy were developed.

3.5.1 Central composite design

Approaches that examine one parameter at a time assume that process parameters do not interact and that the response variable is only a function of the single varied parameter. In fact, mechanical properties, accuracy and porosity of specimens obtained via SLS processing, are a result of the interactive influences of the different process parameters. When a combination of several independent variables and their interactions affect the measured responses, response surface methodology (RSM) is an effective tool for investigating the manufacturing process [132]. Response surface plots can be employed to study the system relationships and locate the optimum within the range of investigated variables. The effect of each factor is evaluated by contrasting the average response when the factor was not changed with the average result when it was changed. In this technique, a least squares model is fitted to the experimental data which relates the output variables to the input parameters. Responses can then be represented as a polynomial regression equation of the following form:

$$R = b_0 + b_1x_1 + b_2x_2 + b_3x_3 + b_4x_1x_2 + b_5x_2x_3 + b_6x_1x_3 + b_7x_1^2 + b_8x_2^2 + b_9x_3^2 \qquad \text{Eq. 3.1}$$

where R is the response; x_1, x_2 and x_3 are the factors or variables; and b_1-b_8 are coefficients of regression representing the effect of the variables or the effect of the interactions of the variables.

The central composite experimental design (CCD) technique is often used to implement the RSM [133]. CCDs are more robust than other designs as they are rather insensitive to missing data and provide high quality predictions over the entire design space. In the present work, a five level CCD is used to estimate the coefficients of a quadratic model that describes the dependence of accuracy, porosity and mechanical properties on selected process parameters (laser fill power, outline laser power, scan spacing).

In design of experiments the levels of the investigated factors are coded, usually (-1) represents the lowest level (0) the midpoint and (1) the highest level of the investigated factor. The coding in CCD is slightly different. As shown in Figure 3.5 the CCD used has three groups of design points:

- two level factorial design points

In the current work three factors were investigated, therefore there are eight factorial design points: [(coded value for factor_1, coded value for factor_2, coded value for factor_3)]

(-1,-1,-1) (-1,-1,1) (-1,1,-1) (-1,1,1) (1,1,-1) (1,-1,1) (1,1,-1) (1,1,1)

- axial points (also called star points)

  The star points have all of the factors set to 0 (that is the midpoint), except for one factor that is set to (+α) or (– α). The value of α in the current design was calculated for rotatability (α=1.68179). There are six axial points in the current CCD setup:

  (+ α,0,0) (– α,0,0) (0, + α,0) (0, – α,0) (0,0, + α) (0,0, – α)

- centre points

  Centre points are design points that have all factor levels set to 0, that is the midpoint of each factor range (0,0,0). Centre points are normally repeated 4-6 times to get a good estimate of pure error for the lack of fit test, and ensure that the design is statistically sound.

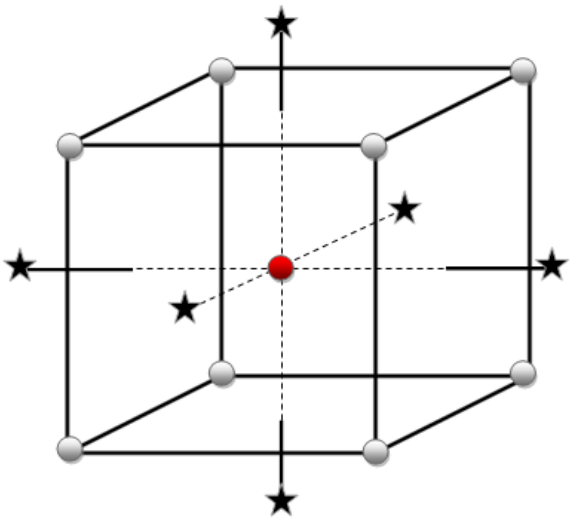

Figure 3.5 Central composite design on three factors

In the current CCD, centre points were repeated five times. Instead of running only one experiment for factorial and axial points, they were also repeated four times when mechanical behaviour was examined.

Adequacy of a proposed model from this analysis was checked using analysis of variance (ANOVA). Statistical significance of the model, the parameters and their interactions were examined using sequential F-test (p-value), lack-of-fit test, signal to

noise ratio and other adequacy measures (R^2, adjusted R^2 and predicted R^2). The computations were performed with the aid of the Design-Expert® software.

A *p*-value less than 0.05 (i. e. 95 % confidence interval) indicates that the examined parameter is statistically significant. Insignificant parameters and parameter interactions were determined as those having *p*-values higher than 0.05 and were excluded from the model via backward elimination. Constructed models were only considered significant at $p < 0.0001$ with higher confidence interval (99.99%). Furthermore, the proposed model was only accepted if signal to noise ratio was higher than 4, R^2 was over 0.7 and adjusted R^2 and predicted R^2 were in reasonable agreement (difference is less than 0.2).

3.5.2 Statistical analysis

When the effect of a single parameter was examined, ANOVA was used to compare means of several treatment groups as ANOVA generalizes Student's two-sample t-test for more than two groups. This statistical analysis was applied when examining the effect of material composition on mechanical properties.

3.5.3 Developing process models

Part-dependent process parameters (can be set separately for each part in the build) were examined to directly relate their effect on mechanical properties and accuracy measurements. Laser fill power, outline laser power, scan count, scan spacing and orientation were investigated.

The effect of build-dependent SLS parameters that are known to have significant influence on part properties were not investigated here. Although it is well established in literature that part bed temperature has a significant effect on part properties (also confirmed during the preliminary studies), most SLS systems – including the one used throughout this study – are first generation machines and lack precise feedback control. Part bed temperature is measured by infrared sensors with ±7-8 ˚C error according to thermocouple measurements carried out prior to using the current the system. The SLS system records the infrared sensor measurements throughout the fabrication period. Actual temperature is greatly influenced by factors such as temperature of the room where the machine is located. For these reasons, the effect of this parameter was not investigated. The suitable temperature window is within the range of the measured error. Furthermore, part bed temperature is a build dependent parameter, that is, once its value is changed it is applied to all parts in the build. Examination of this parameter effect would require several builds, which is very time consuming as the chamber has to

be inerted with N_2 prior each build. That limits the number of builds to one (or in ideal case maximum of two) per day. Due to limited access to the SLS system these experiments were not included. Layer thickness was kept constant at 150 µm for the same reason.

Preliminary studies showed that the effect of using multiple scans within a single layer is very strong. Therefore to be able to examine all parameters in a wider range, multiple scanning was examined individually, while the other four parameters were analyzed in a central composite design.

Central Composite Designs

This work developed mathematical models to describe the relationships between process parameters (laser fill power, outline laser power and scan spacing) and response functions (mechanical properties, feature dimensions and porosity). 3D lattice structures (Figure 3.1) were fabricated at various parameter settings in the three main manufacturing directions. Parameters were varied according to the CCD described in Chapter 3.5.1. Coded and natural values of design factors are summarized in Table 3.2.

Design factors/Coded values	**−1.68**	**−1**	**0**	**+1**	**+1.68**
X_1**: laser fill power (W)**	7	8	9.5	11	12
X_2**: outline laser power (W)**	2	3	4.5	6	7
X_3**: scan spacing (mm)**	0.1	0.12	0.15	0.17	0.19

Table 3.2 Coded and natural values of design factors (coded values are dimensionless and are shown in bold)

The upper and lower ranges of process parameters in Table 3.2 were selected according to the following criteria. When the highest energy density was delivered to the powder bed that is the highest laser fill power of 12 W and the smallest scan spacing of 0.1 mm were applied, the powder was visibly strongly melted by the laser beam. In contrast, applying the lowest laser fill power (7 W) and the largest scan spacing (0.2 mm) resulted in weakly sintered, fragile structures. As the speed of the outline scan is significantly lower than that of the fill scan, the outline power in the centre point of the design space was set to be half of the corresponding laser fill power. Three replicates were fabricated at each design point except the centre point that was replicated four times.

Table 3.3 outlines the CCD matrix that was followed when conducting this work. The whole CCD was repeated for the three main manufacturing directions using the PCL100/30HA powder blend. Fabricated samples were subjected to compressive testing and μ-CT scanning.

Run	Laser fill power [W]	Outline laser power [W]	Scan spacing [mm]
1	8	3	0.12
2	11	3	0.12
3	8	6	0.12
4	11	6	0.12
5	8	3	0.17
6	11	3	0.17
7	8	6	0.17
8	11	6	0.17
9	7	4.5	0.15
10	12	4.5	0.15
11	9.5	2	0.15
12	9.5	7	0.15
13	9.5	4.5	0.1
14	9.5	4.5	0.19
15	9.5	4.5	0.15

Table 3.3 Design matrix used to conduct the Central Composite Design

Multiple scanning

Scan count (the number of fill scans on a single layer) was examined at five levels. While varying its value it was ensured that the total amount of energy density delivered to the part stays constant. To achieve this, parallel with increasing scan count, laser fill power was reduced. The following treatments were applied to the parts:

- 1 × 6 W
- 2 × 3 W
- 3 × 2 W
- 4 × 1.5 W
- 5 × 1.2 W

All other parameters were kept at their default values indicated in the beginning of Chapter 3.3. The standard 3D cubic lattice geometry that was used throughout this work was subjected to compression testing along the z-direction (n=5). Tensile properties were also examined using a 2D lattice geometry shown in Figure 3.6. Outer dimensions were 9.6×49.2×2 mm, strut size was 0.6 mm and pore size 1.2 mm.

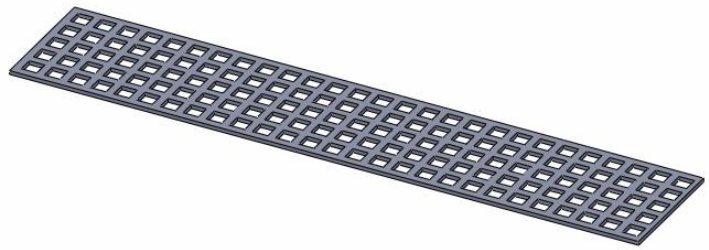

-

Figure 3.6 CAD model of 2D lattice structures for tensile testing

Directional dependence was examined in the x and y direction (long axis of the sample was positioned parallel to the x- and y- axis of the machine) as the powder bed reduction that enables using smaller amounts of powder did not allow for the fabrication of 50 mm long part in the z direction. Indirectly, changes in part bed temperature were also examined. It was noticed that during sintering, heat builds up in the powder bed, and sintering of each subsequently deposited layer is improved. The 2D lattices were positioned on top of each other leaving 0.45 mm (3 layers) and 0.15 mm (1 layer) between the samples. In each direction five replicates were produced.

4 RESULTS AND DISCUSSIONS

This chapter has four sections. The first section introduces the thermal and morphological characterisation of powders used. The last three sections correspond to the studies designed to address the posed research questions:

- mechanical anisotropy (Section 4.2),
- effect of ceramic phase addition (Section 4.3),
- effect of process parameters and developed mathematical models (Section 4.4).

4.1 Powder manufacturing and characterisation

Characterisation was carried out on powders proposed to be used in this research as it is important to know the morphological and thermal properties to help interpret the results of the experiments.

4.1.1 Thermal analysis of PCL

Besides its proven biocompatibility and its bioresorbable nature, PCL was selected as it has great thermal stability above its melting point over a large temperature range. The DTA/TGA curve of PCL in Figure 4.1 confirms the melting peak of the polymer at 60 ˚C, and it also shows that no weight or decomposition takes place below 300 ˚C. That provides a wider temperature range for thermal processing than most other bioresorbable polymers.

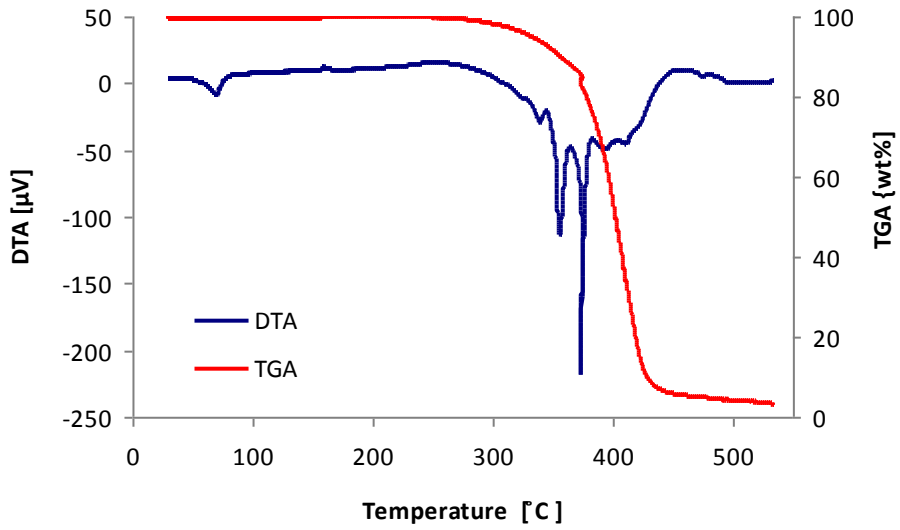

Figure 4.1 DTA and TGA of pure poly-ε-caprolactone showing the melting peak and decomposition of the material

This makes PCL a favourable material for SLS fabrication. Energy density delivered to the powder bed needs to be high to achieve sound mechanical properties. This will

cause highly elevated temperatures, however the TGA curve proves that PCL will not undergo thermal degradation below 300 ˚C.

4.1.2 PCL powder fabrication and morphological characterisation

There were two methods used to fabricate powder from the as-received 3 mm PCL pellets:

- microsphere preparation via w/o/w (water-in-oil-in-water) double emulsion technique,
- mechanical grinding in the presence of dry ice/liquid nitrogen

Microspheres were successfully fabricated using the double emulsion technique; the morphology of the fabricated particles is shown in Figure 4.2 (b). Average diameter of the microspheres was 300 µm, and about 40 wt% was under 150 µm. Particle size of the microspheres could be easily altered during the fabrication process. It can be reduced by increasing the stirring speed or elevating the temperature during stirring. However, it was decided not to proceed as during fabrication an organic solvent is used to dissolve PCL and although the solvent is evaporated at a later stage, traces can remain in the microspheres that can induce toxic effects in vivo. Furthermore the process is very time consuming and inefficient, and therefore only suitable for fabrication of small quantities. The powder beds of the SLS machine were reduced, so that smaller quantities of PCL powder can be used, however a single build still requires a minimum of 1 kg powder (depending on particle size).

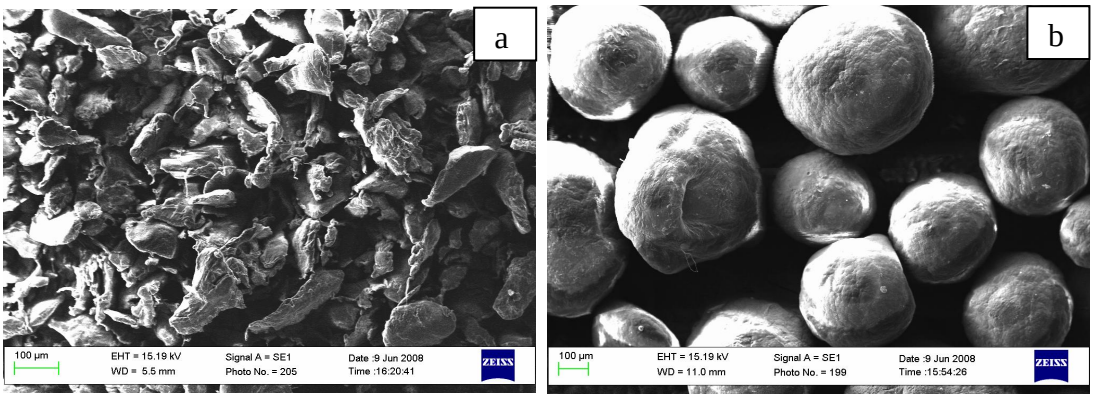

Figure 4.2 SEM images of (a) cryogenically grinded PCL and (b) PCL microspheres

The other method used for fabricating scaffolds was cryogenic mechanical grinding using an analytical mill. The fabricated powder was sieved through a sieve with 150 µm aperture size. Approximately 30 wt% of the fabricated powder went through the sieve, overall 1.5 kg of powder was fabricated in-house using this method. The morphology

and particle size distribution of the powder is shown in Figure 4.2 (a) and Figure 4.3, respectively. An advantage compared to the microspheres is that the mechanically ground powder had a significantly higher surface to volume ratio as it can be seen in the above micrographs.

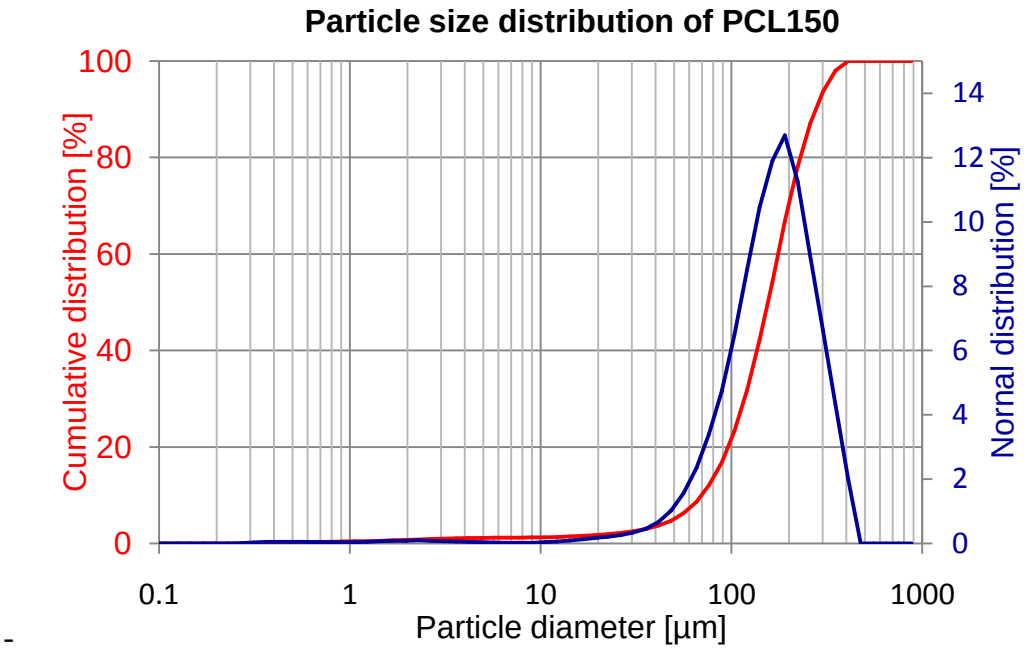

Figure 4.3 Normal (black) and cumulative (red) particle size distribution in house ground PCL150

The powder was sieved through a sieve with 150 µm aperture size, and is referred to as PCL150. Average particle size of this powder was 135 µm, and 90 % of the particles were between 65 and 290 µm as measured by laser diffractometry. The micrographs revealed that fabricated PCL particles are non-spherical, and have an elongated shape, explaining the presence of the large amount of particles above the aperture size of the sieve.

This batch was used at the earlier stages of the project to fabricate PCL and PCL composites scaffolds. However, due to the small capacity of the analytical mill (20 g) this process also proved relatively inefficient, and an alternative solution had to be found.

PCL pellets were sent to Solid Composites Ltd. and were cryogenically ground by the company, 60 wt% of the milled powder was below 100 µm. This powder is referred to as PCL100 and was used as-received. Its morphology and particle size distribution are presented in Figure 4.4 and Figure 4.5, respectively.

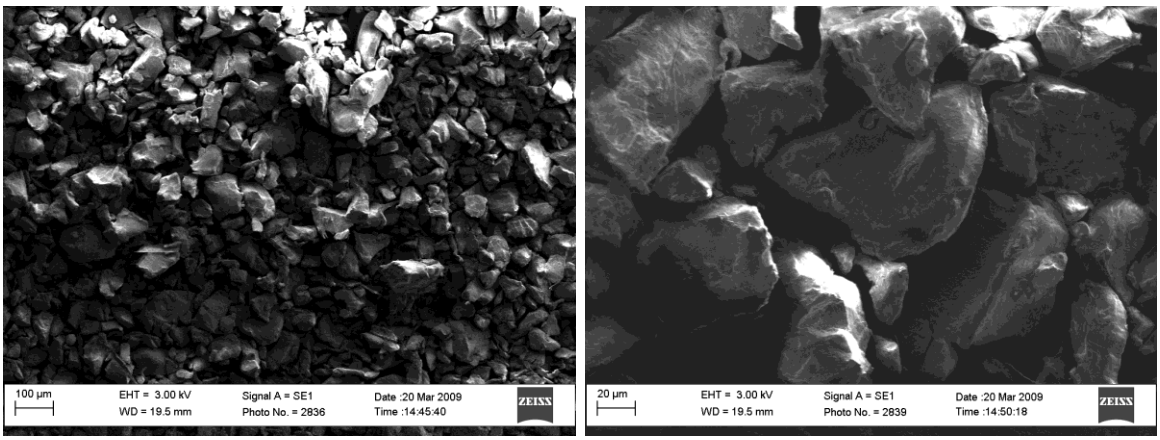

Figure 4.4 Morphology of the as-received powder ground by Solid Composites Ltd.

Average particle size of this batch was 56 µm, and 90 % of the particles were between 22 and 130 µm. Compared to the in-house prepared batch there was significant reduction both in particle size and in particle size distribution.

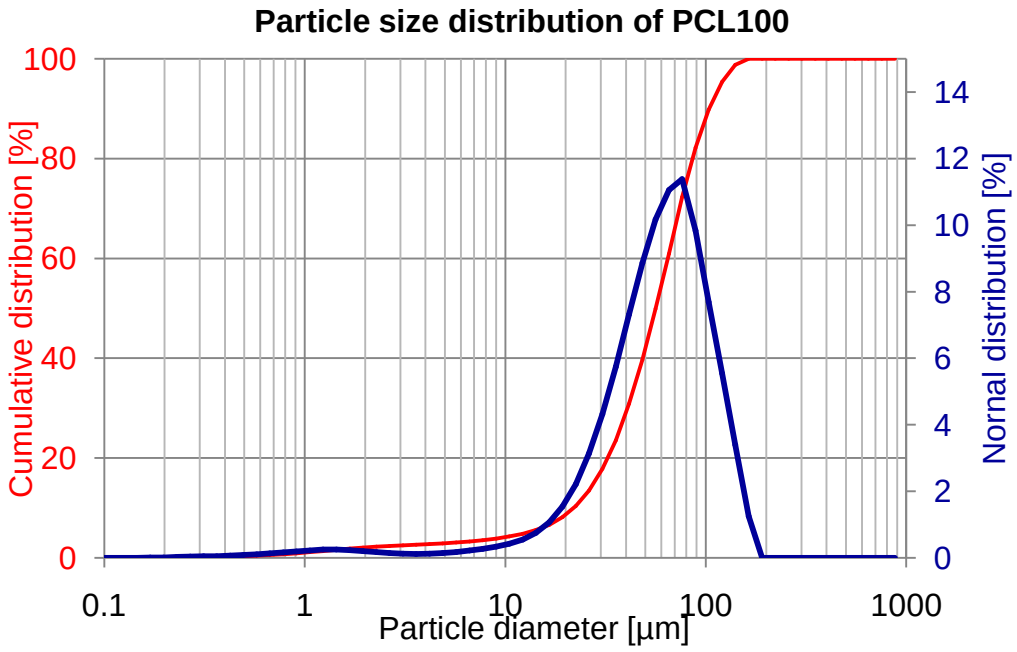

Figure 4.5 Particle size distribution PCL100 powder ground by Solid Composites Ltd.

As reduction in particle size is associated with increased mechanical properties due to increased packing density, further reduction of the particle size was attempted by sieving the as-received powder through a sieve with 75 µm aperture size. The particle size distribution of the sieved powder is shown in Figure 4.6.

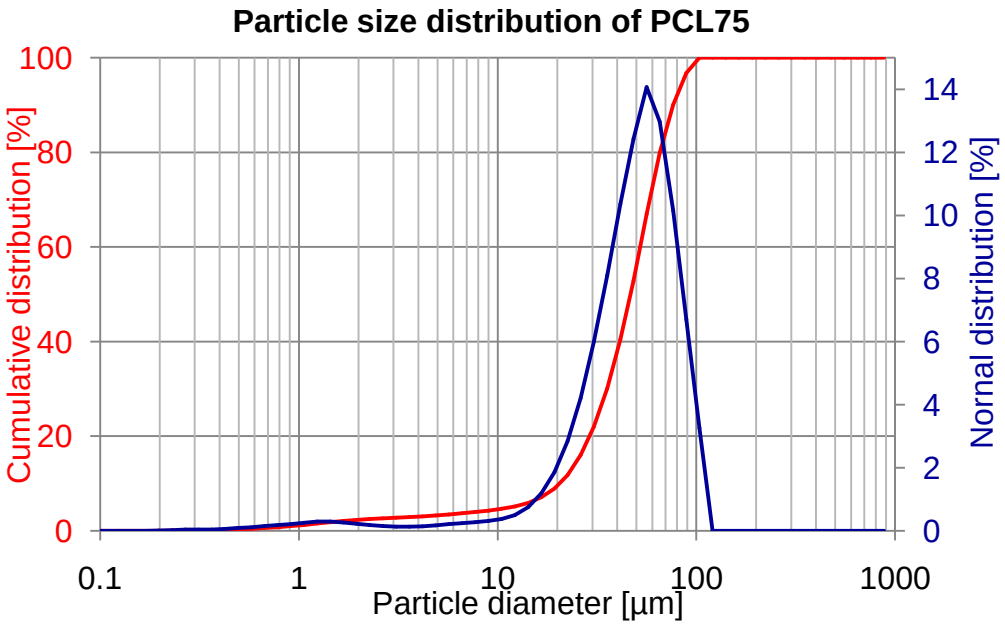

Figure 4.6 Particle size distribution PCL powder ground by Solid Composites Ltd. and sieved below 75 µm

Sieving slightly reduced the average particle size of the powder from 56 to 47 µm along with the particle size distribution since 90% of the particles were between 21 and 77 µm as opposed to 22 and 133 µm in the previous case.

The use of reduced particle sized powder is expected to result in improved mechanical response and better accuracy of fabricated parts.

4.1.3 Morphological characterisation of ceramic powders

Particle size distribution of the ceramics used (HA and TCP) was also measured and normal and cumulative distributions are presented on the graphs of Figure 4.7 and Figure 4.8.

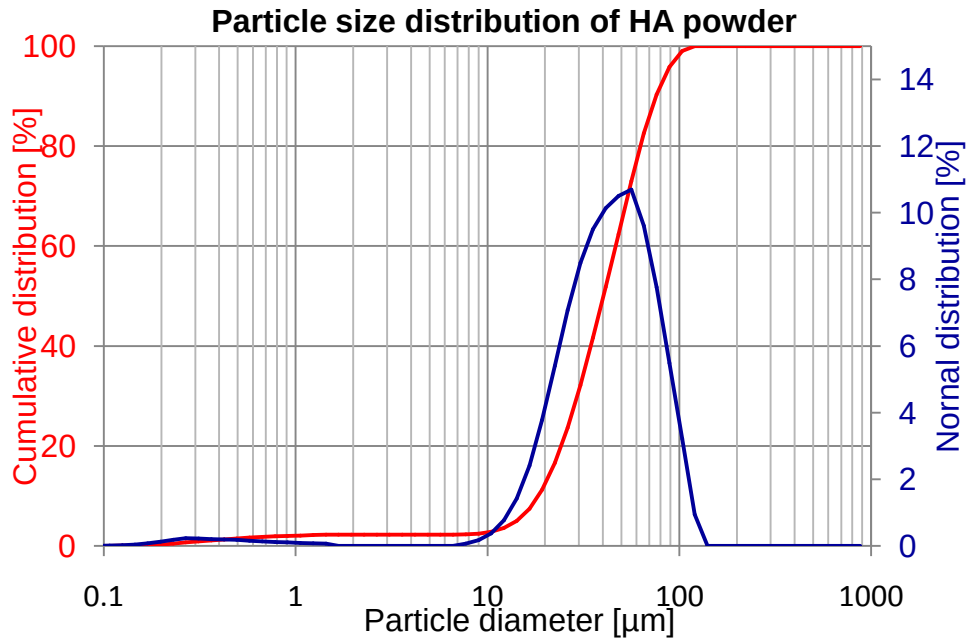

Figure 4.7 Particle size distribution of used HA powder (Captal 60-1, Plasma Biotal Ltd.)

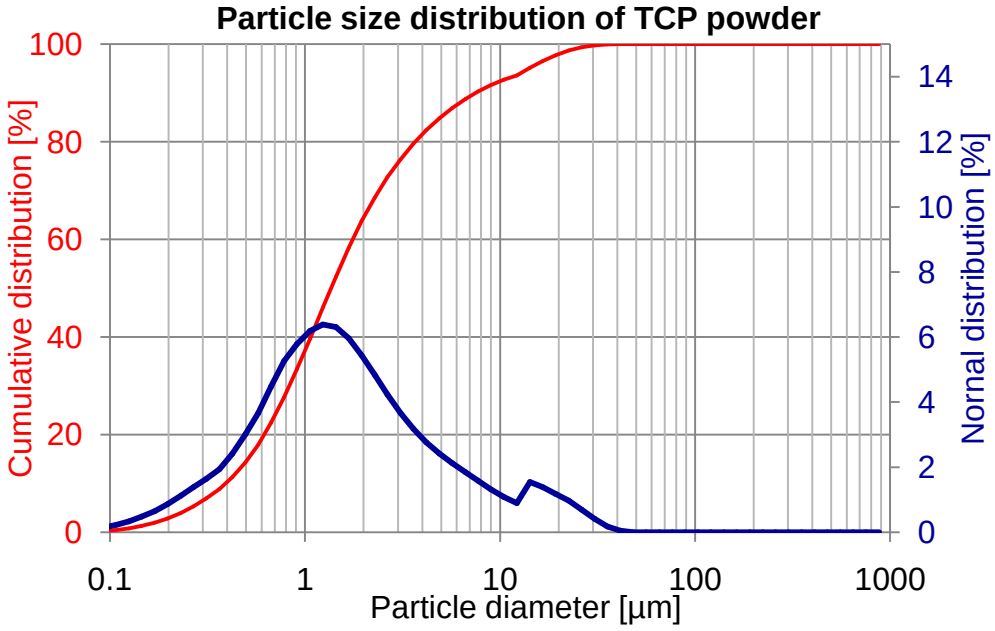

Figure 4.8 Particle size distribution of used TCP powder (Whitlockite, Plasma Biotal Ltd.)

Great differences were found between the particle sizes of the two powders. HA had an average particle size of 43 µm with 90 % of the particles being between 14 and 88 µm, while TCP had an average particle size of 3 µm with 90 % of the particles being between 0.3 and 14 µm. The smaller particle sized ceramic was expected to better integrate into the polymer during sintering.

4.1.4 Thermal analysis of PCL blends

Scaffolds were fabricated via SLS processing of the PCL powder and its blends with HA and TCP. Since SLS is a thermal process, it is important to know whether the addition of these ceramic particles has any effect on the melting or crystallization peak, or on the melting or crystallization enthalpy. For example, if the addition of the ceramic phase significantly reduces or increases melting temperature, it is important to know prior processing the powder, so that processing parameters can be adapted accordingly. Thermal properties of powder blends are also important in interpreting accuracy or mechanical testing results. For instance, if the introduction of HA into the polymer increases crystallinity (that can be seen from the change in heat of fusion) that could induce an increase in mechanical properties. Therefore, when comparing compressive behaviour of scaffolds with different compositions fabricated at various parameter settings it is important to know if any increase can be contributed to increase in crystallinity. Also, being aware of a significant change in melting temperature can be important in interpreting accuracy or porosity results. If the addition of ceramic particles significantly increases melting temperature of the polymer, that can reduce sintering or fusing between particles (at a given delivered energy density level) resulting in less intensive heat conduction during sintering. That will produce increased porosity in the microstructure and better accuracy in the outer dimensions of the struts as less powder will stick to its outer surface.

Thermal properties of the powder blends were derived from the exotherms and endotherms of the DSC curves. In general, it is not necessary to repeat the DSC measurements of a given material multiple times. However in the current case blends were tested and, although care was given to homogenously mix the powders, there can be slight variation between the tested compositions. For this reason all measurements were repeated three times.

Figure 4.9 shows the DSC curve of pure PCL powder. PCL has a melting peak (T_m) at 59.76 ˚C with a melting enthalpy (ΔH_f) of 55.08 J/g, and it has crystallization peak (T_c) at 37.06 ˚C with crystallization enthalpy (ΔH_c) of -48.77 J/g.

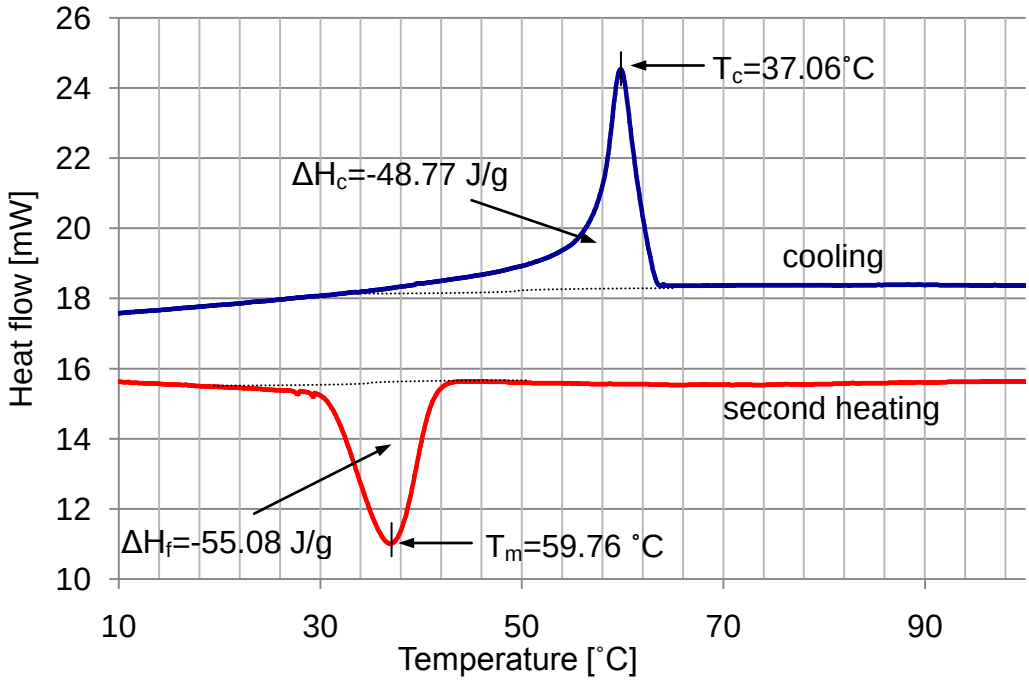

Figure 4.9 DSC curve of PCL powder

DSC curves of the HA and TCP blend exhibited the same characteristics with only slight variations in peaks and enthalpies.

Measured changes in crystallization enthalpy are shown in Figure 4.10. It was seen that the addition of either HA or TCP considerably reduces crystallization enthalpy of the polymer.

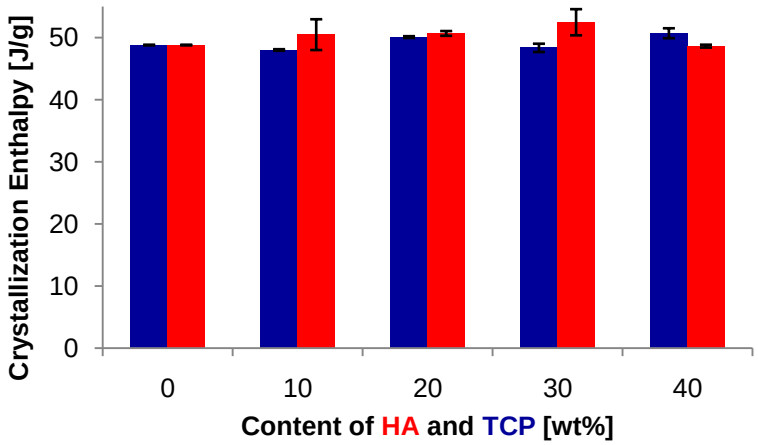

Figure 4.10 Change in crystallization enthalpy as a function of added ceramic content

There were great variations between the values obtained for the same material compositions that are likely to be the result of inhomogeneous mixing that induce

differences in the actual polymer content of the powder. In general differences between the different compositions were not significant.

Other additives to PCL have been shown to decrease crystallization enthalpy. For example, PCL/chitin composites have been examined to be used in tissue engineering applications and Yang et al. [134] reported reduction in crystallization enthalpy when testing chitin/PCL blends.

Changes in heat of fusion (ΔH_f, or melting enthalpy) induced by the addition of the ceramic particles was derived from the endotherm of the second heating curve. The crystallinity (X_c) of PCL in the composite can be calculated from the measured heat of fusion according to the following equation:

$$X_c = \Delta H_f / (\omega \times \Delta H_{f,100\%}) \qquad \text{Eq. 4.1}$$

Where ω is the polymer content, and $\Delta H_{f,100\%}$ and ΔH_f indicate the heat of fusion for 100% crystalline PCL and for the measured composite, respectively. The value of $\Delta H_{f,100\%}$ was taken as 142 J/g for calculation [135]. The induced changes in heat of fusion and crystallinity by addition of different wt % of HA and TCP are summarized in Table 4.1.

HA content [wt%]	**ΔH_f (measured) [J/g]**	**Crystallinity [%]**	**TCP content [wt%]**	**ΔH_f (measured) [J/g]**	**Crystallinity [%]**
0	-55.1±0.0	39±0.0	0	-55.10±0.0	39±0.0
10	-48.0±1.8	38±1.3	10	-49.97±0.6	39±0.4
30	-41.5±3.8	37±2.7	20	-43.25±1.4	38±1.0
30	-36.1±1.6	36±0.4	30	-36.20±0.5	36±0.4
40	-32.3±1.1	38±0.8	40	-32.75±1.6	38±0.1

Table 4.1 Changes in heat of fusion (ΔH_f) and crystallinity induced by introduction of different percentages of ceramic phase into the polymer powder

Results show that the addition of a ceramic component does not significantly change the melting enthalpy, and therefore it does not have a statistically significant effect on crystallinity of the PCL powder. The observed variations (slight decrease in crystallinity with the addition either HA or TCP) can be attributed to the variation of material composition within the blends. The change was not statistically significant, even when comparing PCL to the blends with the highest ceramic content using one-way ANOVA.

It can be concluded that interaction between the ceramic component and the polymer during crystallization and melting is not sufficient to induce changes in crystallinity of the polymer.

Current findings on crystallinity of the PCL/HA blends are consistent with the results of a study carried out by Hao et al. [136], when examining the thermal behaviour of PCL/HA composites. Their study also concluded that difference in crystallization kinetics resulting from different HA content is insufficient to induce a change in crystallinity of the PCL component, contrary to what is seen for other biodegradable additives such as starch. Wang et al. [137] found that the addition of 27% of starch and 10 wt % of plasticizer can indeed increase crystallinity of PCL.

Melting and crystallization peaks were also measured and compared for each composition. The melting temperature of PCL blends is determined by both the thermal history of the sample and its ceramic content. As the tested samples were cryogenically milled, variations that could be associated with thermal history of the samples have been eliminated. Figure 4.11 shows the change in melting temperature as a function of ceramic content.

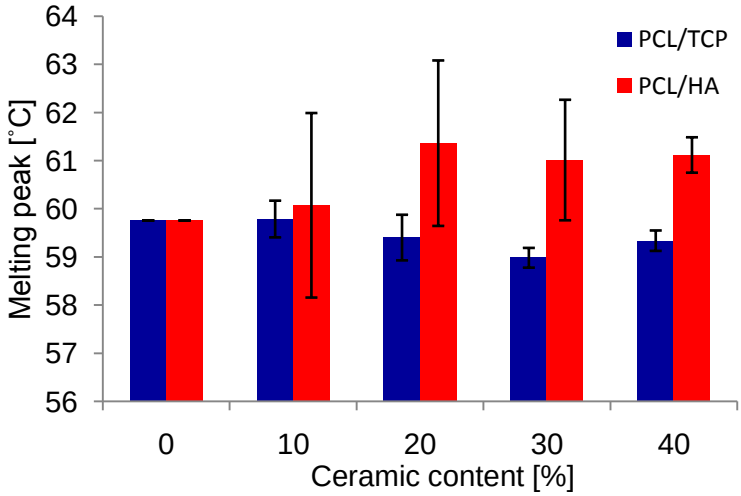

Figure 4.11 Melting peak of PCL/HA and PCL/TCP composites as a function of ceramic content

The addition of HA has slightly increased the melting peak of PCL (1-1.5 ˚C), however the increase was only significant over 20 wt% of HA content. TCP had the converse effect, it slightly decreased the melting peak. The decrease was only present and statistically significant over 30 wt% of TCP content. In general, changes in melting temperature indicate that the crystal structure of the polymer changed to some extent, for instance increase in melting peak usually is the result of higher degree of order in the crystal structure, the crystals are more perfect or much thicker. Current results indicate that the introduction of ceramic into the polymer induces slight changes in the crystal structure. Current results confirm the findings of Chen et al. [138]. When testing

different PCL/HA compositions the authors found that the addition of HA slightly increased the melting peak of PCL. Hao et al. [136] while finding that the addition of HA changes the melting peak of PCL, notes the opposite effect, a decrease with increasing HA content. However, it has to be pointed out that samples tested in this study were solvent-cast or melt quenched and these processing technologies introduce thermal history and can also change the crystal structure of PCL.

The findings of the current study (that HA increases melting temperature and TCP decreases it) are surprising as upon removing the samples from the DSC after the measurements were completed, visual observation of the samples would suggest a reverse tendency. After subjecting the two PCL blends to the same thermal treatment, particles of the PCL/HA powder mixture fused completely together forming a unique integrate melt, while no fusing or necking was observed between the particles of the PCL/TCP powder. Therefore, the observed decrease in melting peak of PCL/TCP blends was likely to be due to the fact, that during the second heating the particles were still small (below 150 μm) and melted more easily.

A similar observation was reported during sintering PCL/HA composites by Wiria et al. [22] and during the sintering of PLG/HA composites by Simpson et al [61]. In the latter study, the particle size distribution of the HA powder used (with 10, 50 and 90 % of particles below 1, 4 and 15 μm) was similar to the particle size distribution of the TCP powder (with 10, 50 and 90 % of the particles below 0.42, 1.4 and 9 μm) used in the current experiment. In the present study particles were even smaller and the batch contained a considerable amount of nano-particles too.

In Simpson's study HA particles formed a shell around the PLG particles that insulated the polymer and could not dissipate its heat by contacting other polymer particles. The authors argued that the use of HA with larger particle size might help to prevent shell formation around the PLG particles. In the current study the HA had significantly bigger particles (with 10, 50 and 90 % of the particles below 19, 41 and 76 μm), and the blend completely melted together suggesting that shell formation did not occur, agreeing with their hypothesis.

Shell formation occurred in the current study around the PCL particles when using the small particle size TCP. The above results suggest that necking formation between particles is only slightly affected by the composition of the added ceramic and strongly dependent on its particle size. Many previous studies showed that using other

fabrication methods, the incorporation of small-microparticles or nanoparticles into a polymer matrix can significantly increase its mechanical properties [104, 130, 138]. However, when physically blended polymer/ceramic powder is used for sintering, small particle form a shell around the polymer that can reduce or completely inhibit sintering and neck formation between the particles resulting in low connectivity, high porosity and inferior mechanical properties.

Instead of pure physical blending of the powders, Hao et al. [35, 62] used a different method for preparing PE/HA composite powders for fabricating scaffolds. The powder blend was extruded and the extruded composite was milled. When the particle size of the ceramic phase is very small, this method of powder preparation can be considerably more advantageous during SLS processing.

These results also suggest that using the currently investigated materials, significantly higher temperatures and delivered energy density will be required during the sintering of PCL/TCP blends than for the PCL/HA blends in order to achieve the same microstructure.

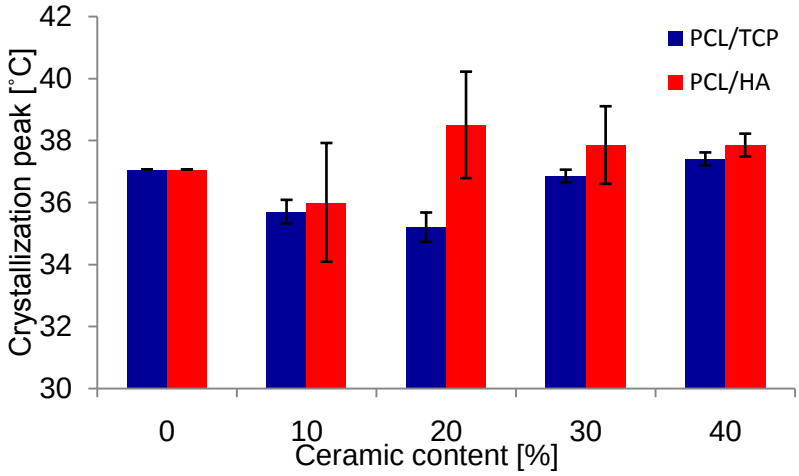

Figure 4.12 Crystallization peak of PCL/HA and PCL/TCP composites as a function of ceramic content

The non-isothermal crystallization of the composites was studied by cooling the melt samples. The change in average non-isothermal crystallization temperature is illustrated in Figure 4.12. There was no statistically significant difference between peaks of the HA blends except blend containing 40 wt% HA. TCP in small quantities (up to 20 wt%) reduced crystallisation peak while in larger quantities slightly increased it. In general, the addition of the same amount of TCP resulted in lower peaks than the addition of

HA, suggesting that crystallization of the polymer during cooling is more facilitated by the TCP particles than by HA particles. Again significant variations are likely to be due to inhomogeneous powder mixtures, therefore incremental increase of ceramic content are not discussed here. However, the difference between pure PCL powder and the blends containing 40 wt% of ceramic particles was significant. Changes in the melting peak reflect that addition of 40 wt% HA or TCP affects the crystallization kinetics of PCL. The increase in crystallization temperature suggests that HA and TCP facilitate the crystallization of PCL under cooling, possibly by acting as a nucleating agent.

4.1.5 Summary and conclusions

Of the two powders fabricating processes cryogenic milling was chosen over microsphere preparation, as it was more efficient, does not require the use of organic solvents and resulting particles have a higher surface to volume ratio.

Particle size analysis showed that the average particle sizes of the fabricated PCL batches are 135, 56 and 47 µm for PCL150, PCL100, and PCL75. Average particle size of the HA powder was 43 µm and that of TCP was 3 µm.

Possible changes in thermal properties induced by the anticipated heat treatment during SLS processing were analyzed using DSC. Addition of ceramic content reduced crystallization and melting enthalpy as the actual polymer content decreased, however the change was not sufficient to induce any changes in the crystallinity of the polymer that could alter its mechanical properties. The addition of HA increased melting temperature while TCP slightly reduced it. Analysis of crystallization peaks suggested that crystallization of the polymer is better facilitated by TCP than HA particles. Upon removing the samples from the DSC, it was noticed that subjecting the powder blends to heat treatment at 130˚C (twice) twice is not sufficient to induce neck formation between PCL particles in the PCL/TCP blend.

Based on the above characterisations PCL and its blends with HA were selected for SLS processing. The main issue with PCL/TCP blends was the ceramic shield formation around the PCL particles. This insulates the polymer and prevents neck formation between particles even at temperatures as high as 130 ˚C, which is significantly over the melting temperature of the polymer. The shield formation is contributed to the small particle size of the TCP powder.

4.2 Mechanical anisotropy of fabricated structures

The objective of this study was to examine orientation dependence of fabricated samples as anisotropy is inherent to the manufacturing technology and although its presence is established in literature it has not been explored qualitatively in detail and it has not been examined in the context of lattice structures. Studies that aimed to fabricate scaffolds for tissue engineering applications did not examine orientation dependence of the samples. Samples were tested in one direction only (z) – that was parallel to the building direction. In-vivo, a scaffold can be subjected to multidirectional loading, and will fail in the weakest direction first. Depending on parameter settings structures can be weakest along the x-direction (parallel to the fill scan lines), and therefore reporting mechanical properties of the scaffolds only in the z-direction (parallel to building) can be misleading.

Fabricated structures exhibit a double cellular structure by having a designed macrostructure and a somewhat random microstructure. Macroporosity of the scaffolds is defined and can be tailored by the designed CAD models while microporosity within the struts of the designed structures can be guided by SLS process parameters or by the morphology of the powder.

Orientation dependence of scaffolds having different topologies was examined using various macro and microstructures. The macrostructure was varied by changing the basic element of the designed periodic structure from simple cubic, to Gibson-Ashby and reinforced cubic. As the effect of process parameters is examined in detail later on, the microstructure of the struts (within the designed simple cubic microstructure) was manipulated only by using powders with different particle sizes. The micro and macrostructure of the scaffolds were altered separately.

4.2.1 Anisotropy of lattices with different microstructures

Lattice structures were successfully fabricated using all three PCL powder batches (Figure 4.13). However, when using the 75 μm powder it was noticed that during powder deposition large amounts of powder stuck to the roller resulting in uneven layer deposition. During the sintering of PVA powder of similar particle size (10-75 μm) the same problem was noticed by Wiria et al. [59]. The reduction of particle size was attempted as smaller particles are associated with better densification and therefore

improved mechanical properties and Hao et al. [35] reported no problems during deposition of a similar particle size range.

Figure 4.13 Photograph of fabricated 3D lattices (9.6×9.6×6 mm^3)

Testing and analysis of these samples was still carried out, since upon removal of the parts from the powder bed and after depowdering visual observation suggested that the parts were successfully built. The lattices were reasonably accurate, easy to handle and no sign of layer shifting or delamination was observable. The clumping problem was not noticed for the other two powder batches that had slightly bigger particle size.

Compressive behaviour of fabricated PCL scaffolds was in agreement with the mechanical behaviour reported in literature for cellular solids / lattice structures fabricated by other means. However, there were significant variations observed between the mechanical behaviour in the three testing directions and between the parts fabricated with different particle sizes. In general, compressive stress-strain curve of a polymeric (elastic-plastic) lattice structure or foam consists of three distinct regions. The initial linear elastic region is followed by a plateau, and finally the response ends in a steeply rising stress. Two variations of this behaviour were observed. Most samples exhibited strain – softening characteristics. Although, this type of stress-strain response could be schematized as shown in Figure 4.14, there were great variations in the yielding behaviour and in the shape of the plateau.

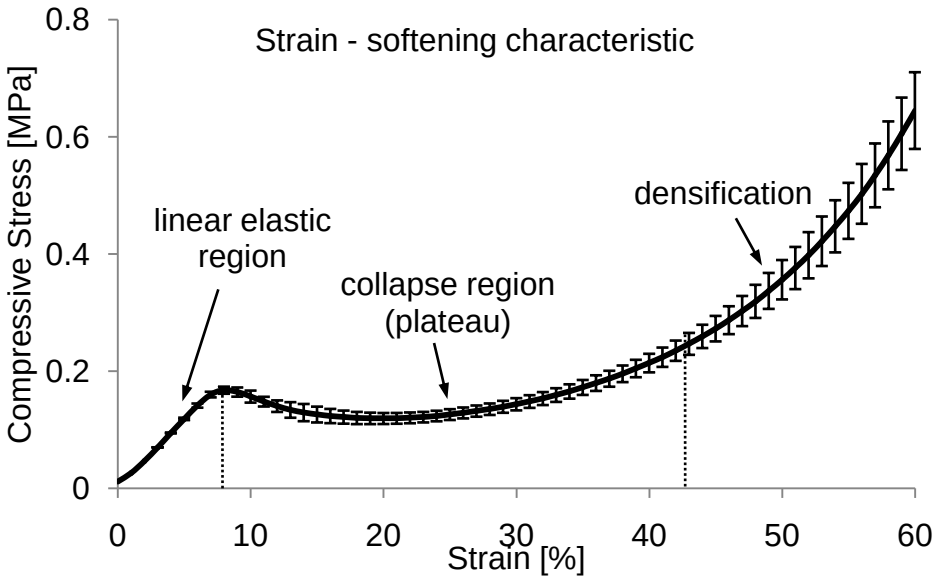

Figure 4.14 Strain softening behaviour of lattices subjected to uniaxial compression (data is for lattices fabricated from 150 µm PCL and tested along the y-axis, n=7).

In some cases the strain softening was more intensive (indicated by a significant drop of compressive stress beyond the yield point) while in other cases the decrease was barely noticeable. This is associated with the great variations in cross sectional area, porosity and therefore second moment of area of the struts resulting in different failure mechanisms.

The shape of the plateau also varied, in some cases the stress stayed constant beyond the yield point representing a more compliant structure, in other cases the stress-strain response showed a concave curvature in this region. At high strain values densification was observed that is indicated by the intensive increase in slope in the stress-strain curve.

Strain-hardening behaviour was observed in one case (x-direction, 125 µm PCL powder) and is presented in Figure 4.15. The three distinct regions can clearly be differentiated in this case too. Although these samples did not exhibit a clear yield point, slight reduction in the amount of stress increase can be observed after the linear elastic region indicating the start of a non-linear elastic region. At slightly higher strains another reduction is observed marking the initiation of plastic collapse, but the curve maintained a monotonically increasing trajectory. This response represented the most compliant, bending dominated structure possibly due to its highest porosity and weak connections between particles in the load bearing struts. Again, the curve ends with steeply rising stress implying densification of the sample.

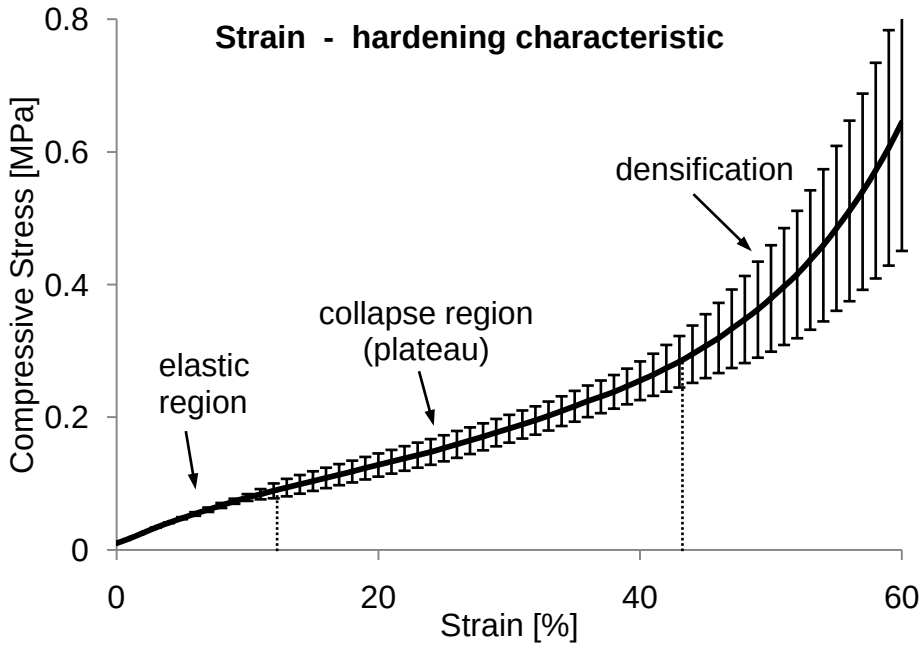

Figure 4.15 Strain - hardening behaviour of lattices subjected to uniaxial compression (data is for lattices fabricated from 150 µm PCL and tested along the x-axis, n=7).

As plastic collapse and densification of the scaffold is not allowable in in-vivo use, samples were only examined up to their yield point and results in this chapter are only presented below 15% of strain (unless yield point was above this strain value).

A quick reminder on the meaning of different testing directions is given below:

- x – direction: testing was performed parallel to the scan lines of the laser fill pattern (that is also parallel to the movement of the roller),
- y – direction: testing was performed perpendicular to the scan lines of the laser fill pattern,
- z – direction: testing was performed parallel to the movement of the powder bed (perpendicular to the surface of the powder bed).

Mechanical behaviour of scaffolds fabricated using different particle sizes will be outlined and reviewed separately, and will be related and compared to each other at the end.

Directional dependence of scaffolds fabricated from PCL150

The mean (n=7) of compressive modulus for scaffolds that were fabricated using PCL150 changed between 0.76 and 1.31 MPa depending on the testing direction. It was

the lowest in the x-direction (0.76±0.11 MPa), slightly increased to 1.02±0.1 MPa when tested in the z-direction, and was the highest, 1.3 MPa when tested in the y direction.

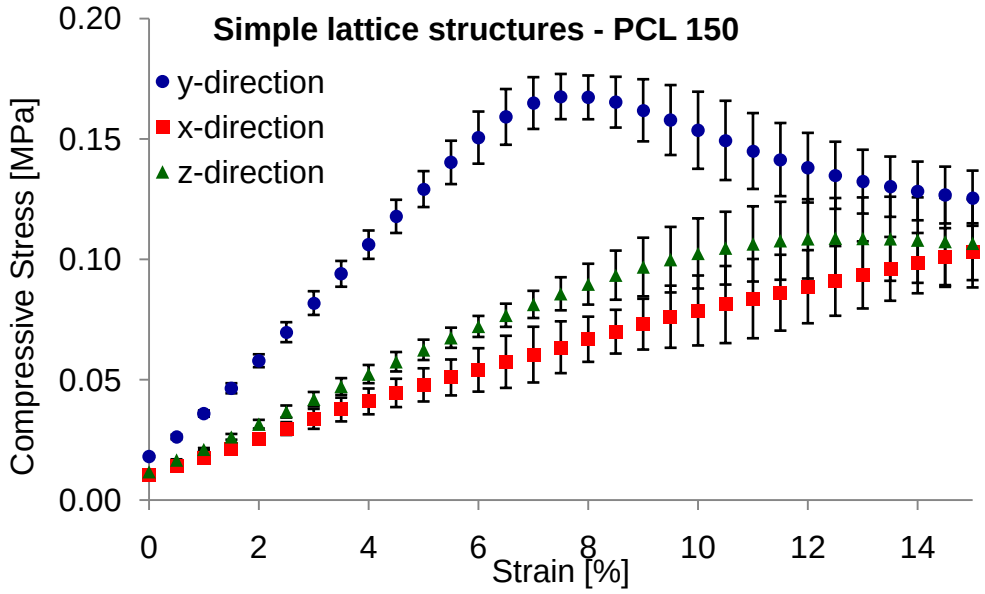

Figure 4.16 Stress-strain response of scaffolds fabricated using the PCL150 powder along the principal manufacturing directions

The same trend was observed for the compressive strength. It was the lowest in the x-direction (0.066±0.006 MPa), significantly increased when tested in the z-direction (0.11±0.014 MPa) and was the highest when tested in the y-direction.

As showed in Figure 4.16, stress-strain responses along the testing directions demonstrated very different characteristics. Samples tested along the x-direction were the weakest, did not have a yield point and they exhibited strain-hardening behaviour. Samples tested along the y-axis were the strongest and showed a very clear yield point followed by intensive strain – softening.

Scaffolds tested along the z-direction although exhibited a yield point it was less distinctive, also instead of an intensive strain hardening, a plateau with almost constant stress was observed.

These differences can be partly explained the different geometry of the struts in the different building directions. The images presented in Figure 4.17 show that as a result of different scanning patterns in the various building direction, the cross-section of the struts is distinct in each direction.

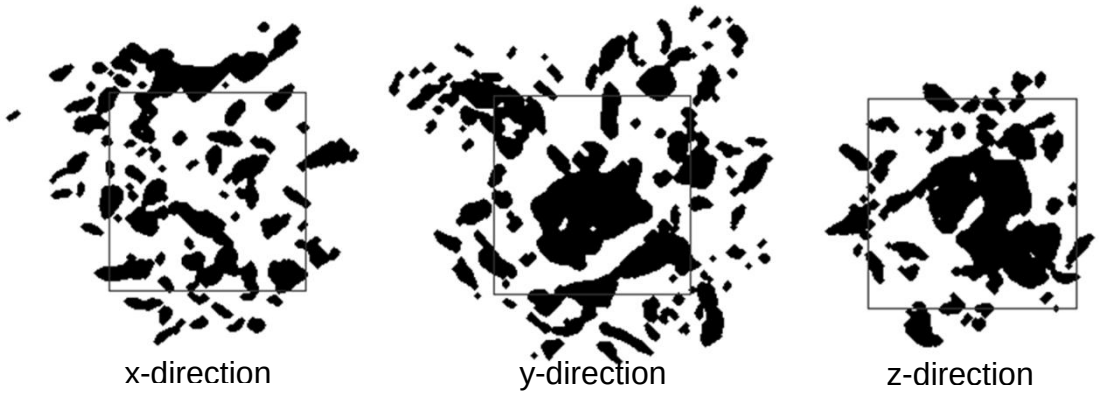

Figure 4.17 Example cross-sections of the load bearing struts (built from PCL150) in the three main building directions derived from µ-CT data. The designed cross sectional area is superimposed on the images, black areas represent the polymer

Struts were designed to have a square-shaped cross-section of 0.6 mm × 0.6 mm (0.36 mm^2). The above µ-CT images show that the shape of the cross section is not preserved, the outer dimensions are not well reproduced, and that struts although designed to be solid have high porosity. Average apparent and effective cross sectional areas (CSA) and calculated porosity is presented in Table 4.2.

direction	Apparent CSA [mm^2]	Effective CSA [mm^2]	Porosity [%]
x	0.45±0.11	0.28±0.08	38
y	0.53±0.16	0.44±0.11	17
z	0.36±0.13	0.29±0.09	19

Table 4.2 Apparent and effective cross sectional area and calculated porosity of struts fabricated in the different directions

The bigger effective cross sectional area and lowest porosity in the y-direction explains the considerably better mechanical properties in this direction. However, effective CSA of the struts is not likely to be a determining factor by itself, topology of the microstructure is also a consideration as it determines whether the structure is bending or stretch dominated. The most compact struts were y-struts with the best connectivity between sintered particles exhibiting stretch dominated behaviour resulting in the best mechanical properties but followed with strain softening beyond its yield point. On the other hand, structures in the x-direction had low mechanical properties, they exhibited no yield point and showed strain hardening throughout as structures in this direction were bending dominated and more compliant.

Directional dependence of scaffolds fabricated from 100 µm PCL powder

Modulus of scaffolds fabricated from this batch was the highest in the y-direction. (2.84±0.05 MPa), values very slightly lower in the x-direction (2.4±0.30 MPa) and were

the lowest in the z-direction (1.66±0.22 MPa). Compressive strength was again highest in the y-direction (0.94±0.12 MPa), it was significantly lower in the z-direction (0.39±0.04 MPa) and was the lowest in the x-direction (0.25±0.03 MPa). In terms of stress-strain response, scaffolds tested along the x-direction showed a different type of behaviour (Figure 4.18).

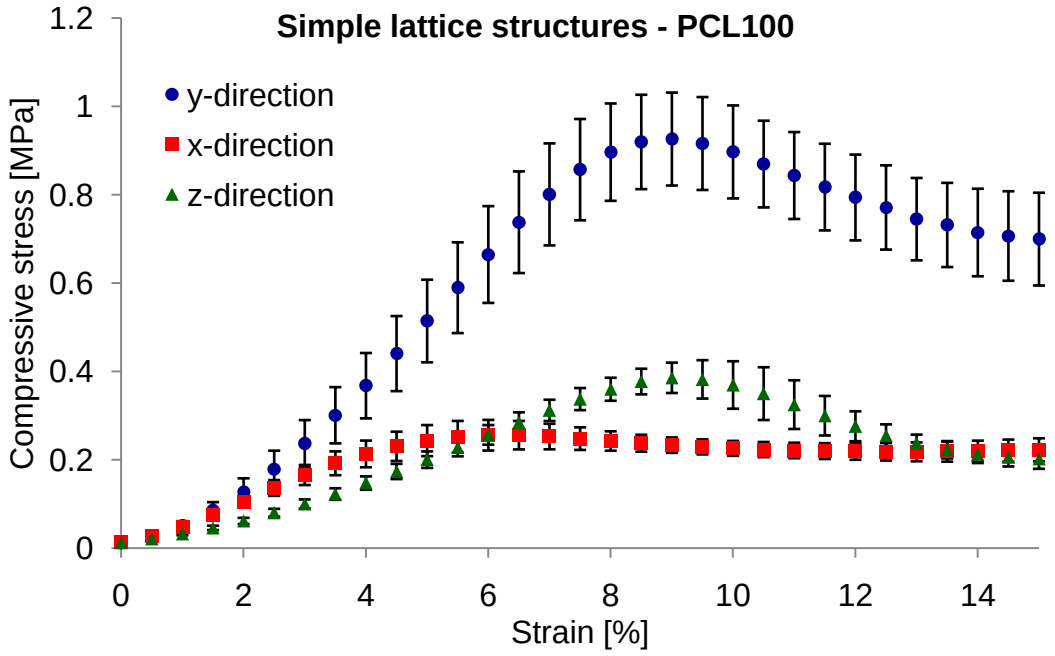

Figure 4.18 Stress-strain response of scaffolds fabricated using the PCL100 powder along the principal manufacturing directions

A yield point could be identified on the response but the strong post-yield softening that was present in the y- and z-directions, was not observed. Although stress values – and compressive properties (both strength and modulus) – were significantly higher in the y-direction, the character of the two curves (y, z) was similar as illustrated in Figure 4.18.

Cross section of the struts was examined via µ-CT, and typical shapes are shown in Figure 4.19. Average cross sectional areas of the struts were very similar to the values obtained for the previous data set (parts fabricated from 150 µm PCL powder), however there were meaningful distinctions between the shapes of the two datasets. Outer dimensions were significantly over the designed value, and microstructure of the struts had substantial porosity when using 150 µm powder for production of the scaffolds. When using smaller powder particles for SLS, the outer dimensions of the struts were significantly reduced, however were still slightly over the designed value. Porosity was also considerably reduced in all directions. Average effective cross sectional area (and corresponding porosity) of the struts was obtained from the µ-CT data and was

0.29±0.03 mm^2 (27%), 0.47±0.03 mm^2 (11%), and 0.31±0.02 mm^2 (25%) for the struts built in the x-, y-, and z-direction, respectively.

x-direction y-direction z-direction

Figure 4.19 Example cross-sections of the load bearing struts (built from PCL100) in the three main building directions derived from µ-CT data, the designed cross sectional area is superimposed on the images

As seen with the PCL150 powder, the average cross sectional area of struts fabricated in the y-direction was significantly higher, these struts also had the lowest porosity explaining best mechanical properties in this direction.

The importance of topology of the strut microstructure is well illustrated by the fact that struts that have similar effective cross sectional area (formed from PCL150 and PCL100), and therefore the similar relative density produce a two-fold increase (for instance, from 1.31 to 2.84 MPa in the y-direction) in compressive modulus by using a smaller particle size. There was also a four-fold increase in compressive strength (for instance, from 0.17 to 0.94 MPa in the y-direction) of the struts in all direction.

The compressed scaffolds were examined under SEM to study the failure mechanisms of the structures. Figure 4.20 presents micrographs of compressed struts in each direction after applying strains below 25 % and over 50 %.

When struts were tested along the x-direction load bearing struts first buckled, at 25 % strain delamination within some of the load bearing struts was already clearly visible. With more severe buckling of the x-struts, tension was generated in the z-struts, and drastic stretch-dominated failure of the z-struts occurred through delamination. The mechanism in the y-direction was slightly different. It was seen during compression testing that y-struts did buckle, however upon removing the applied 20 % strain (although measured yield point was at 9 %) struts recovered their original shape, suggesting that deformation of the y-struts was elastic. However, severe buckling of the

y-struts generated tension in the connecting z-struts, especially, when neighbouring y-struts buckled in different directions. Therefore the yield point observed at 9 % strain marks yielding of the z-struts through stretching.

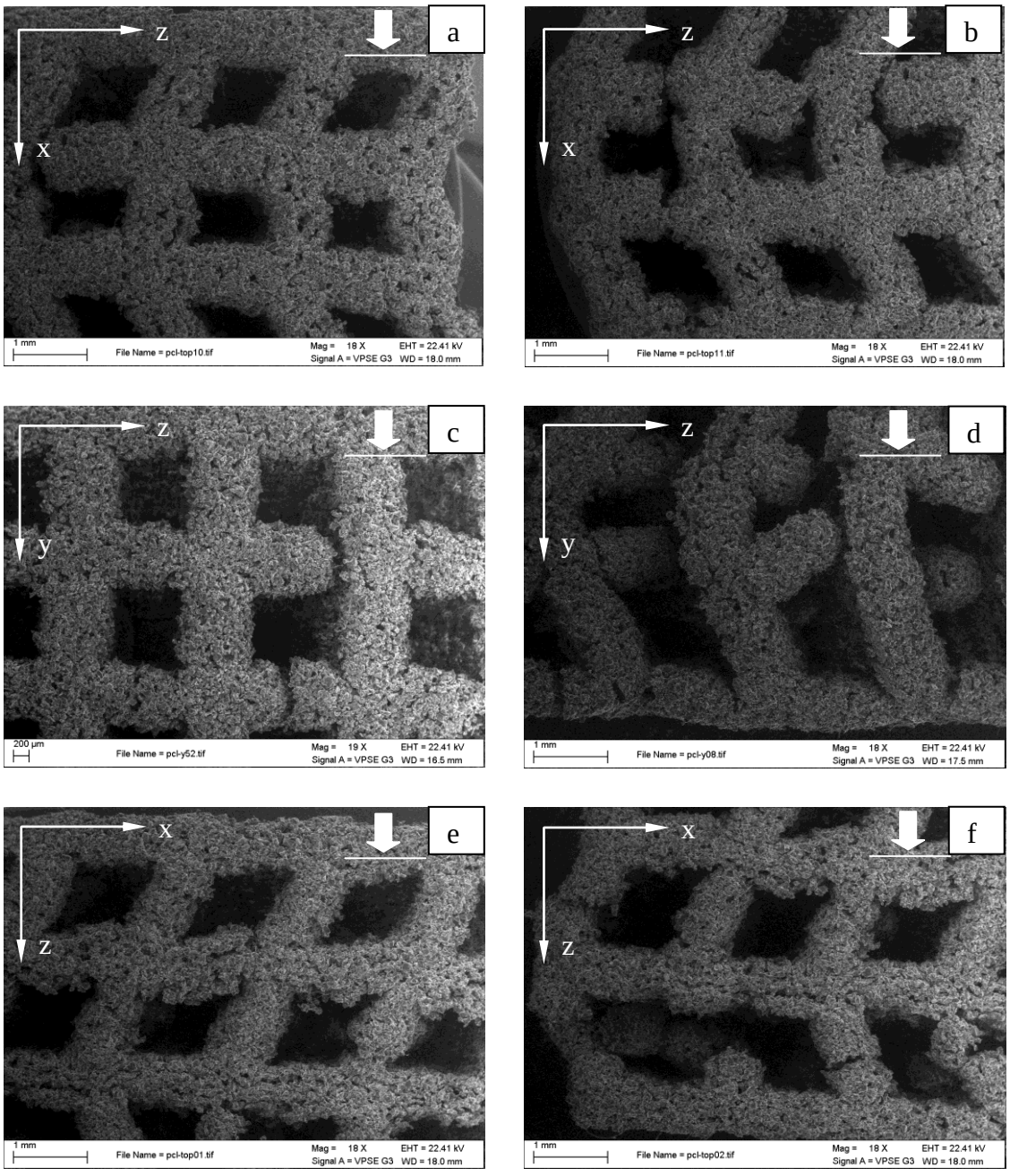

Figure 4.20 SEM images of compressed scaffolds fabricated PCL100 : (a) scaffold compressed along x-axis to strain below 25 %, (b) scaffold compressed along x-axis to 50 % of strain, (c) scaffold compressed along y-axis to strain below 25 %, (d) scaffold compressed along y-axis to 50 % of strain, (e) scaffold compressed along z-axis to strain below 25 %, (f) scaffold compressed along z-axis to 50 % of strain

Micrographs shown in Figure 4.21 confirm that yielding occurs through stretching and that the fabricated structures are stretch dominated when struts are compressed along the y-direction.

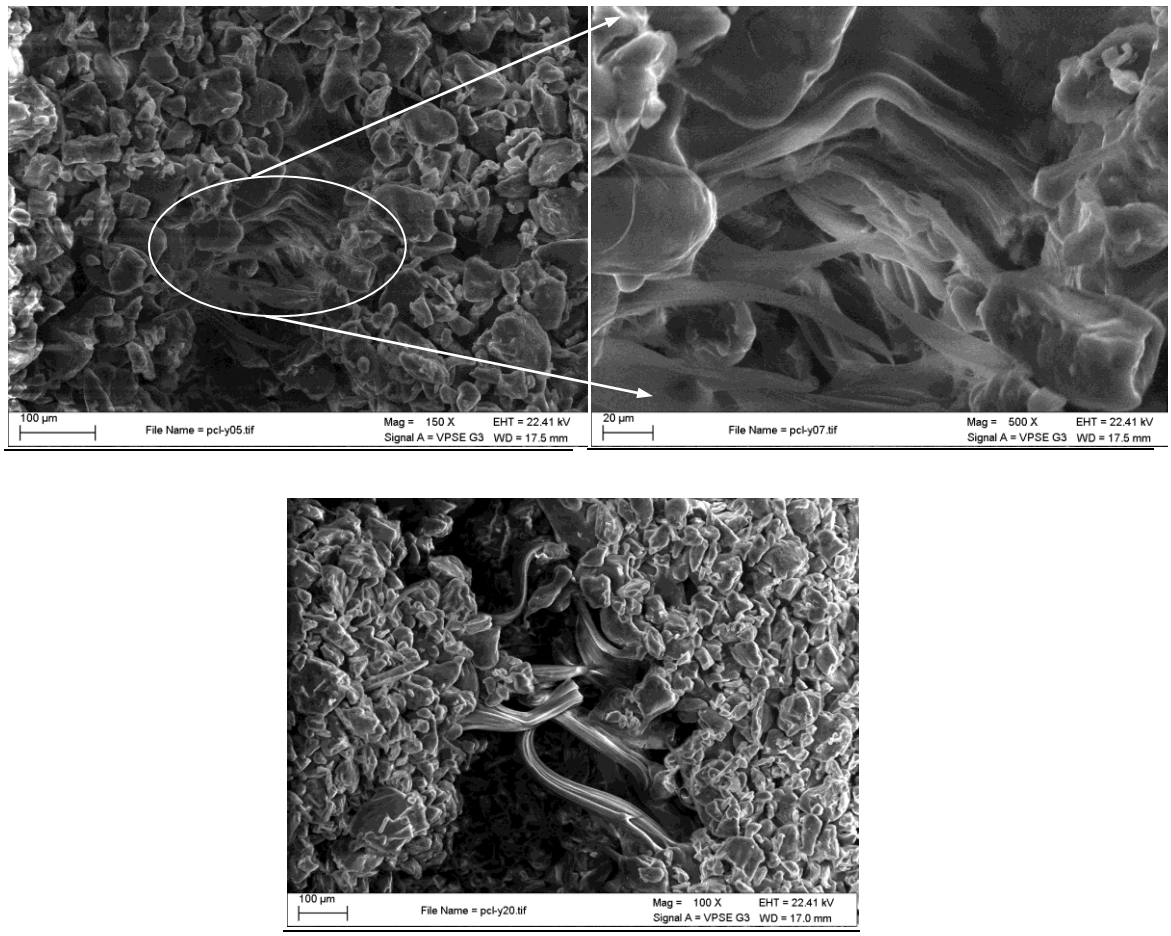

Figure 4.21 SEM images showing stretch-dominated failure of z-struts when tested along the y-direction

When tested along the z-direction failure mechanism of scaffolds was very different from the ones previously observed in the x- and y-directions. The load bearing z-struts undergo plastic bucking and plastic hinges were formed at the junctions of x and y struts. Hinge formation is facilitated by delamination or shifting of formed layers normal to loading.

Overall the compressive properties obtained were significantly lower than those reported by Williams et al. [48] for PCL with similar particle size. The differences are partly due to the different geometries, but the main issue was probably the part bed temperature that was 10 °C higher in Williams' study. Increased part bed temperature is known to improve mechanical properties; the SLS system used could not operate with PCL powder at part bed temperature set higher than 38°C.

Directional dependence of scaffolds fabricated from 75 µm PCL powder

Compressive modulus of scaffolds was highest in the y-, and z- directions, 2.78±0.23 MPa and 2.90±0.18 MPa, respectively. There was no statistically significant

difference between the two groups. Compressive modulus of samples tested along the x-axis (0.86±0.14 MPa) was three-fold below the values obtained for the other two directions. Strength was also highest in the y-direction (0.46±0.03 MPa), followed by the x-direction (0.22±0.02 MPa), and was the weakest in the z-direction (0.14±0.015 MPa).

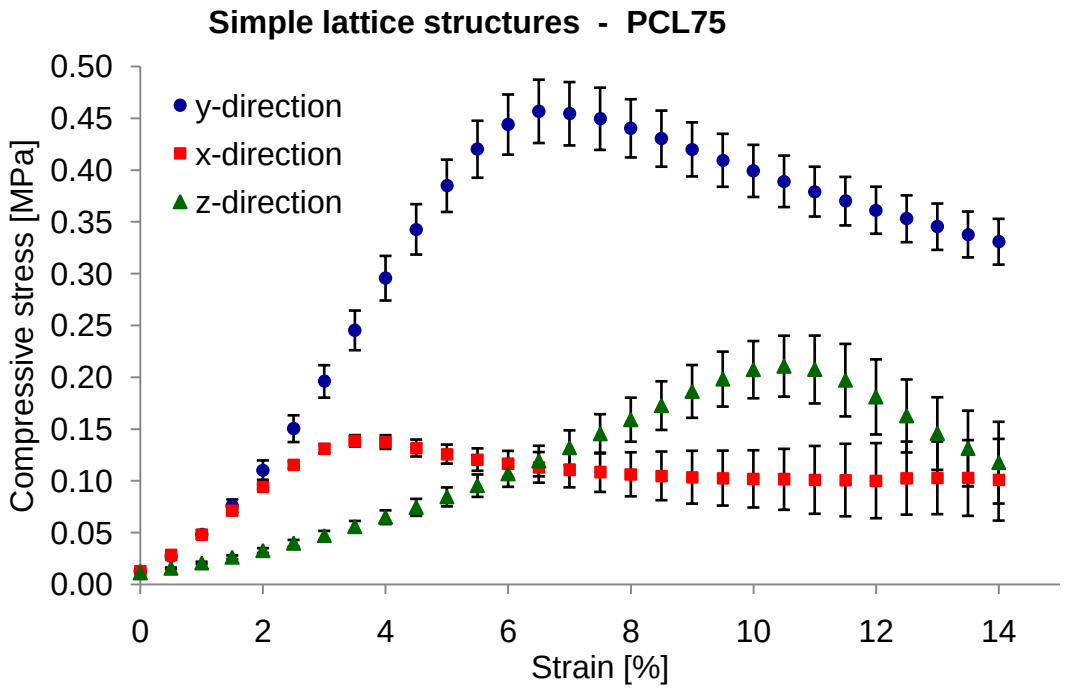

Figure 4.22 Stress-strain response of scaffolds fabricated using the PCL75 powder along the principal manufacturing directions

As shown in Figure 4.22, stress-strain response varied significantly among the testing directions, but all curves exhibited a distinct yield point followed by strain softening. As in the previous cases, scaffolds yielded first when tested along the x-direction, followed by the y-, and z-direction. Overall, compressive modulus of the scaffolds in the z-direction significantly improved by further decreasing particle size of the raw powder, it did not induce any change in the y-direction, while a three-fold decrease was seen in the x-direction. Furthermore, the use of this powder batch had a strong deteriorating effect on compressive strength, especially in the z- and y-directions. Also, in the x-direction (that is the weakest and plastic collapse occurs first) scaffolds yielded at significantly lower strain values, slightly over 3 %, instead of the previously observed 5 % in the preceding two datasets. Deterioration of mechanical properties was not expected with the use of smaller particle size powder, and therefore compressed parts were examined under SEM.

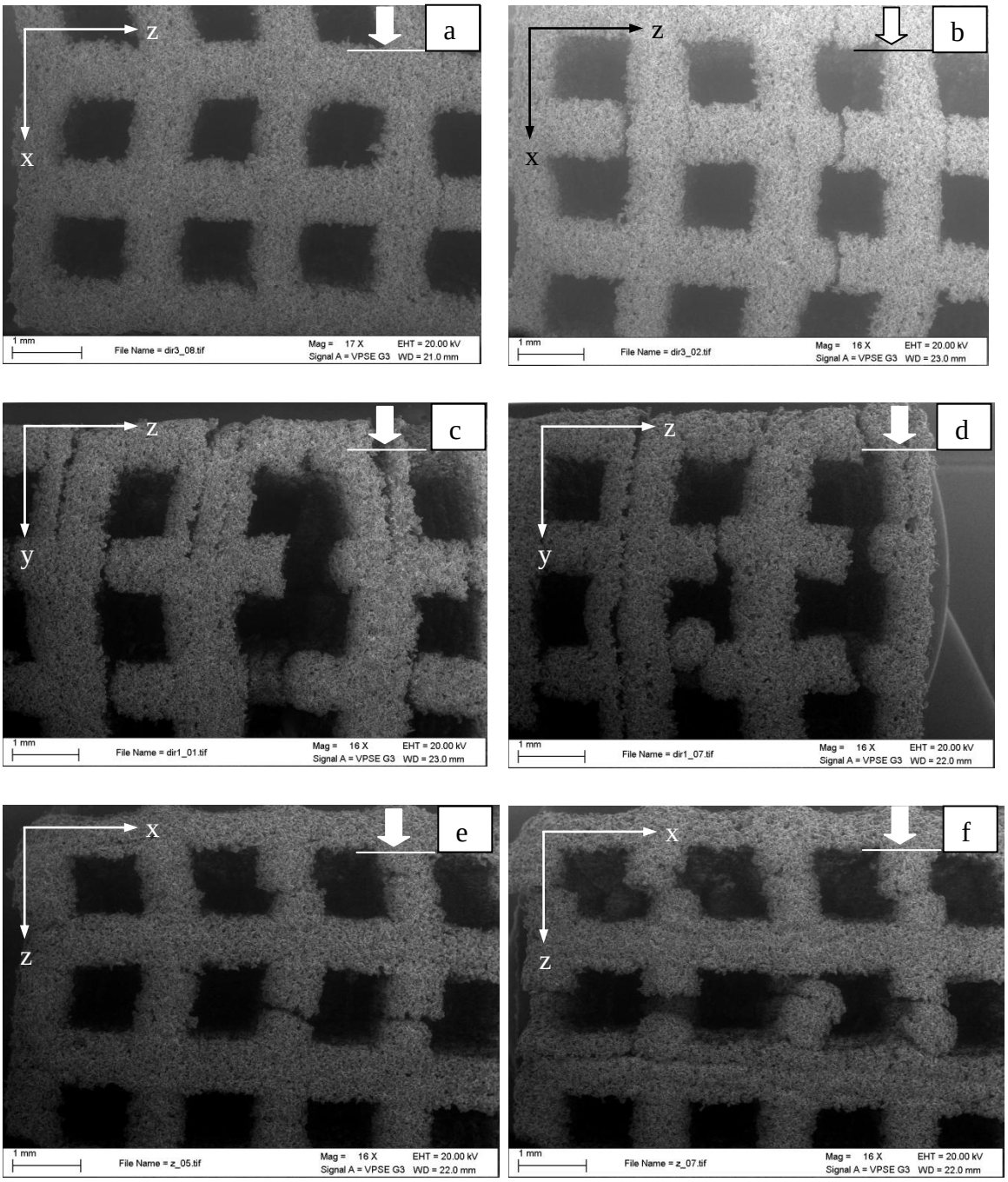

Figure 4.23 SEM images of compressed scaffolds fabricated from PCL75: (a-b) scaffold compressed along x-axis to strain below 15 %, (c-d) scaffold compressed along x-axis to strain below 15 %, (e-f) scaffold compressed along x-axis to strain below 15 %.

Figure 4.23 presents the micrographs of scaffolds compressed in the three main building directions. As shown in the above micrographs, failure mechanism in the x-direction is similar to the mechanism found in the previous case. Yielding of the structure occurs through delamination between layers parallel to the direction of loading. There was a significant drop in modulus; and also there was a slight decrease in yield strength and considerable reduction in yield strain. Substantial deterioration of mechanical properties

in this direction at low strain values is likely to be due to the previously described problem of uneven layer deposition during manufacturing of the samples, rather than the decrease in particle size. Comparisons between the micrographs of the previous data set and the current samples indicate that while in the previous case delamination occurred throughout the structure somewhat homogeneously, in the current case delamination was concentrated to certain layers and was more severe. These findings confirm that certain subsequent layers were not bound properly to each other due to uneven layer deposition.

In the y-direction, modulus did not decrease however there was a substantial drop in yield strength and a considerable amount of reduction in yield strain with the use of the PCL75 powder batch. SEM images revealed the same failure mechanism as in the x-direction: severe delamination concentrated to certain layers. While with the use of the previous powder batch (PCL100) y-struts only experienced elastic deformations even at strains as high as 20 %, in the current case plastic deformation occurred within these struts at strains as low as 6-7 % due to uneven layer deposition and therefore poor bonding between these layers.

Again, mechanical behaviour in the z-direction was inherently different from the other two directions as deposited layers in this case are perpendicular to the loading direction. When tested in this direction, a firm and sound increase was observed in modulus, which can be associated with the use of the smaller particle size. Failure of the scaffold in this direction occurred the same way as when using the previous powder batch. Load bearing z-struts buckled, plastic hinges were formed either around the conjunction of the z-x-struts, or along the unevenly deposited layers and finally at high strains layers shifted on each other when the hinges failed. The profound amount of decrease in yield strength can also be associated with the uneven layer deposition.

A summary of the results for the different testing directions and for the different particle sizes are presented on the charts of Figure 4.24 and Figure 4.25. The graphs show clear and meaningful differences both when comparing testing directions and particle sizes. The graphs show that scaffold fabricated from PCL100 powder had the best mechanical performance, and PCL150 was the weakest in all directions. Particle size was found to be an influential parameter in determining mechanical performance, not only in terms of compressive strength and stiffness but also in determining the mode of deformation and failure within the structure.

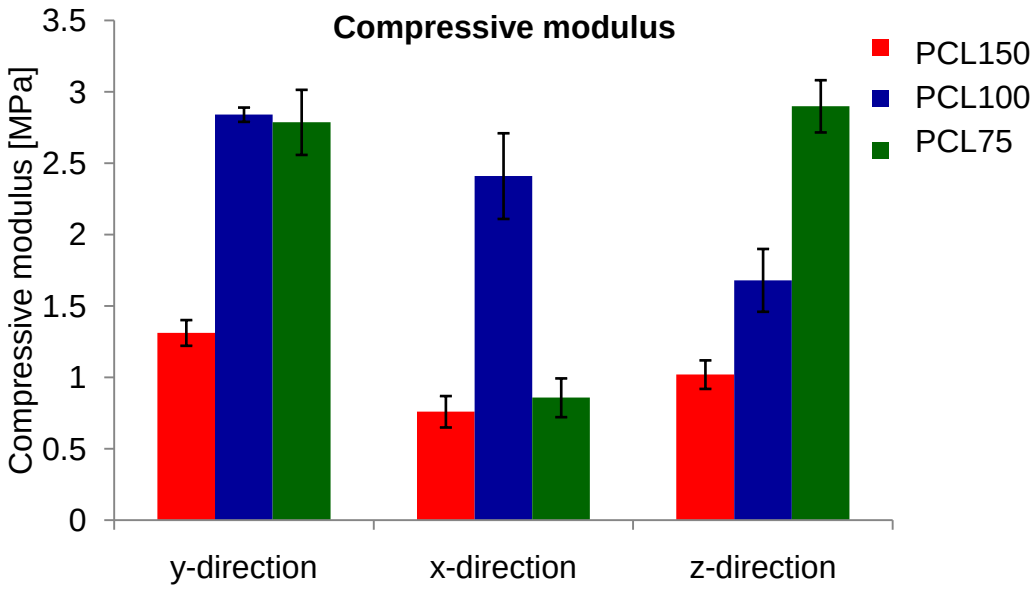

Figure 4.24 Compressive modulus of samples in the three main manufacturing directions using various particle sizes of PCL powder for fabrication

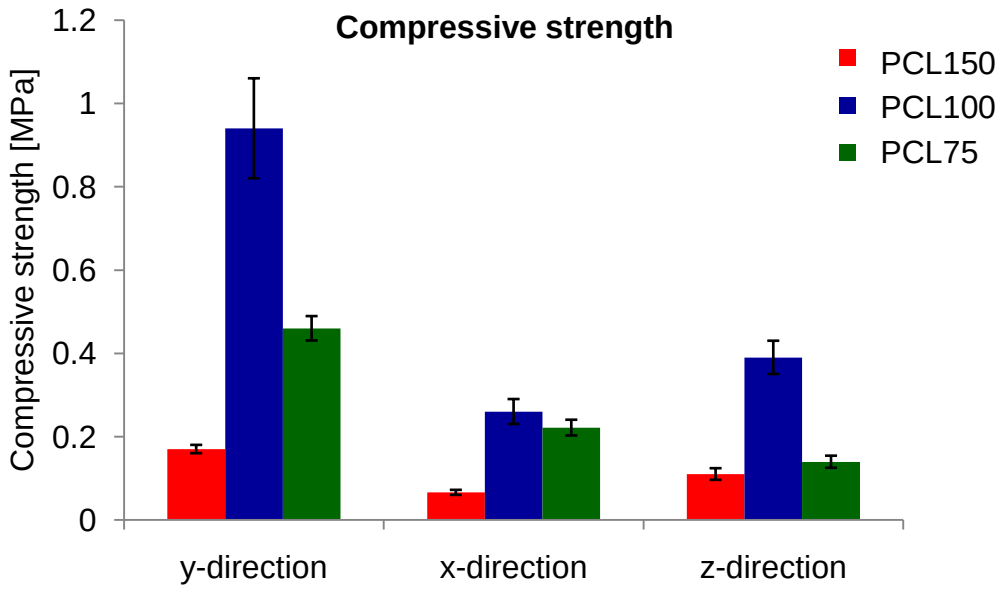

Figure 4.25 Compressive strength of samples in the three main manufacturing directions using various particle sizes of PCL powder for fabrication

The study demonstrated the strong orientation dependence of fabricated micro-lattices that are partly due to the differences in reproduced geometry, porosity and topology of the struts. Scaffolds showed the best performance in the y-direction. Differences resulting from geometrical deviations can potentially be compensated by scaling the

CAD file, while deviations in porosity and topology are more dependent on process parameters and particle size.

4.2.2 Summary and conclusions

One of the objectives of this research is to assess SLS as a potential manufacturing technology for fabricating tissue scaffolds and show its limitations that have not been pointed out before, as the technology was not designed for fabricating micro-lattices. It is argued by many research papers and reviews [14, 15, 139] that SLS, among other RP technologies, is capable of fabricating intricate geometries with complex internal architecture, and its application for scaffold fabrication is promoted. Its limitations have not been explored completely to date, especially not on micro lattices, where due to the small, micron-scale feature sizes these effects are more pronounced. One of these issues is mechanical anisotropy that was the subject of this section. This study was concerned with understanding the response of SLS fabricated lattice structures to uniaxial compression along the three main manufacturing directions. The following conclusions have been derived:

- Fabricated parts are strongly orientation dependent. Up to three-fold variations were observed between the different directions. In general, y-direction is the strongest and x or z is the weakest. To make the structures isotropic, direction dependent scaling of the CAD file is suggested as these variations are partly due to the differences in fabricated feature size in the different directions.
- The micro-features are not accurately reproduced with current SLS technology, not only are there dimensional inaccuracies but the shape of the struts is not reproduced properly. This issue is discussed in more detail in Section 4.4.4.
- In literature most studies only report mechanical testing of samples along the z-direction that can be misleading as this is not necessarily the weakest direction. In addition, the character of the stress-strain response in this direction is not representative for all directions.

The orientation dependence of lattices with different micro- and macro-topology has been tested and the following conclusions can be made:

- By changing the microstructure of the struts (porosity and connectivity of sintered particles) by varying particle sizes, increases of the order five-fold can be achieved in mechanical properties

- By changing the designed microstructure (at nearly constant relative density level) variation in the order of ten-fold can be induced in mechanical properties, the compressive response can be shifted between bending and stretching dominated, furthermore the mode of failure can be altered.

Uneven powder deposition results in deterioration of mechanical properties. The bonding between certain layers is limited and it results in severe and concentrated deformations along these layers. Except for the compressive modulus in the z-direction, strength and stiffness of the lattices were below the anticipated values, as the use of reduced particle size (average 47 μm) was expected to improve mechanical properties.

4.3 Influence of material composition

PCL is a bioresorbable polymer widely used in TE applications as it undergoes hydrolytic degradation to natural metabolites over a predictable time scale matching new bone formation, and is often combined with calcium phosphate based ceramics when intended for bone regeneration. The addition of HA to PCL can be advantageous for many reasons. It is known that during degradation PCL can release acidic degradation products. The inclusion of HA in the polymer matrix has been shown to reduce it [117-119]. Many researchers - examining the PCL/calcium phosphate composites - reported that addition of a ceramic component increased mechanical properties, improved surface properties and cell attachment (see Section 2.5). Calcium phosphate is a natural constituent of bone and therefore it is thought to facilitate osteoblast cell attachment and osteointegration due to the structural similarity to the mineral phase of bone. Besides osteoconductive enhancement, the introduction of HA (rigid bone like particles) to the polymer matrix may improve surface morphology. The aim of this set of study was to examine and evaluate these influences on selective laser sintered scaffolds. Various amounts of HA have been added to the PCL powder to fabricate scaffolds. Surface characteristics including surface roughness and hydrophobicity, biocompatibility and compressive mechanical properties of the scaffolds are examined in order to find a favourable composition.

4.3.1 Surface properties

It has been shown that rough surfaces and high surface to volume ratio is favourable for cell attachment [10]. From a tissue engineering point of view a great advantage of powder based manufacturing technologies including SLS, is that fabricated feature surfaces are rough and therefore have large surface to volume ratios that result in larger cell contact area. Surface roughness is greatly dependent on the particle size of the processed powder and can also be influenced by process parameters. A typical surface profile of PCL disks fabricated for this study is shown in Figure 4.26. The measured surface roughness (R_a) of PCL disks was 33.24±12.74 μm and, as it is shown in Table 4.3, this value was not significantly altered by changing the material composition.

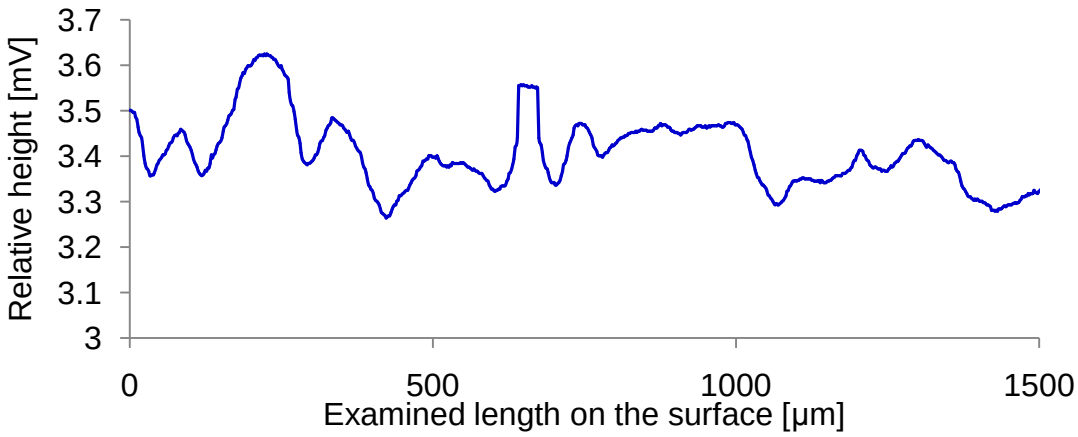

Figure 4.26 Typical surface profile of the top surface of PCL150 disks

In recent years, 2D micropatterning of biomaterial surfaces has been investigated and was found to promote the adhesion of different cell types [140, 141]. Matsuzaka et al. evaluated the behaviour of osteoblast like cells on micro-grooved surfaces that had feature sizes in range of 2-50 µm, and found that these surfaces enhance the production of mineralized ECM. Furthermore, these surfaces can be used to control orientation of cells and mineralized ECM. When comparing cell attachment to micro-grooves with feature sizes between 2-10 µm it was found that cells, and their extensions, closely followed the surface on smooth and wider grooved (>5 µm) substrates while narrow grooves (<2 µm) were bridged. It was also shown that on wider grooved substrates, focal adhesions were spread throughout the surface and on narrow grooves focal adhesions were limited to the edges of surface ridges [142]. The measured surface roughness of the fabricated samples is within the range of 2-50 µm therefore the scaffold surface produced is expected to promote cell adhesion and production of mineralized ECM.

Material	Surface roughness-R_a [µm]
PCL	33.24±12.74
PCL/15HA	38.84±12.83
PCL/30HA	32.47±4.74

Table 4.3 Measured surface roughness values of solid disks with different material compositions

When examining surface morphology of fabricated 3D lattices, SEM images (Figure 4.27) show neck formation between PCL particles indicating that the final densification stage of sintering where pores are eliminated from the designed solid regions was not reached. Therefore accuracy and roughness of the scaffolds were primarily determined

by the particle size (mean 135 μm) of the PCL that was greater than that of HA (43 μm).

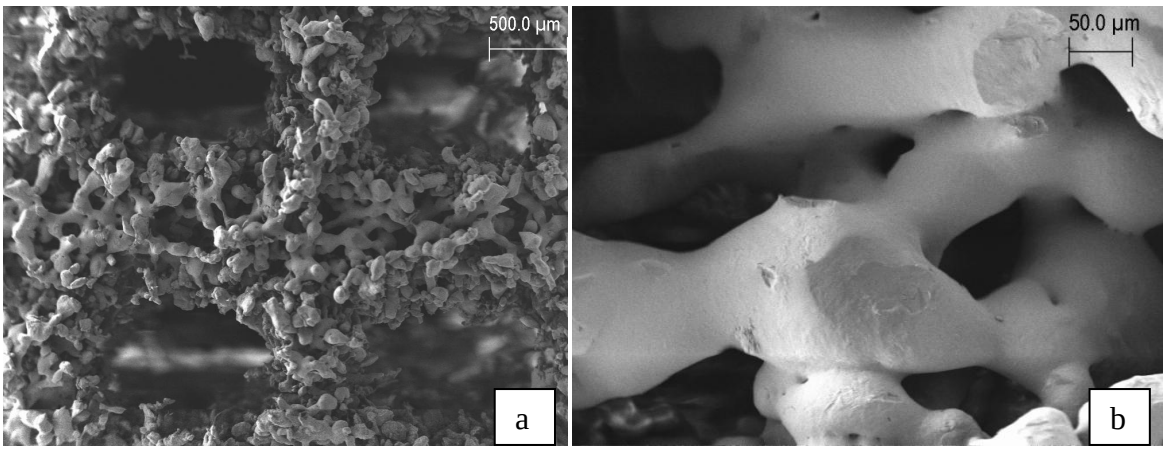

Figure 4.27 (a) SEM image of designed macropores of the fabricated PCL scaffolds (b) SEM image of microporosity in the designed solid regions of the fabricated PCL scaffolds

Surface roughness is identified in literature as a good indicator for sintering of the polymer. However as it can be seen in the μCT (Figure 4.28 (a)) and SEM images of compressed samples (Figure 4.28 (b)), in many cases it is only the inner part of the strut that is properly sintered.

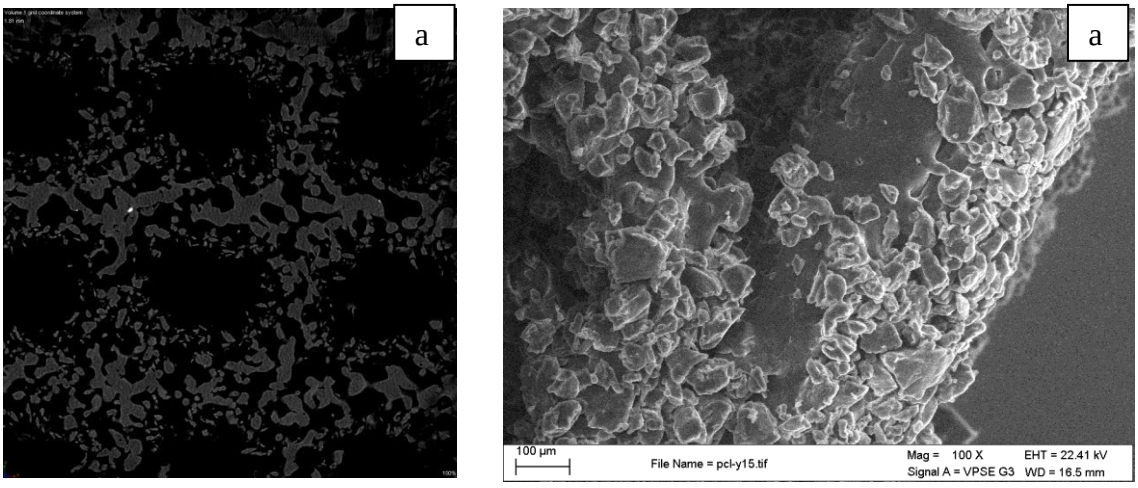

Figure 4.28 (a) Significant difference between the inner and outer structure of the struts, (b) Delamination of during compression revealing the sintered and more solid inner structure of the struts

The outer surface that can be seen SEM images or be measured when measuring surface roughness, is the powder stuck to the sintered areas covering the outer surface everywhere. In the μ-CT images it is clearly visible that within the struts the PCL particles are fused together, while on the outer surface small particles (that preserve the original mean particle size of 135 μm) area stuck to the structure.

Besides surface roughness, hydrophilicity of the scaffold surface is also a necessary consideration for cell attachment and proliferation. Initial contact angle of pure PCL scaffolds was 104±5.5º indicating a hydrophobic surface, and was constantly decreased by the addition of HA. The initial contact angle for composites with 15 wt% of HA decreased to 98±13.6º and with 30 wt% HA to 83±16.9º. Results demonstrated the ability of added HA powder to reduce hydrophobicity of the PCL scaffolds. Large variations measured for the same compositions are due to inhomogeneous distribution of HA particles on the micron scale (Figure 4.29). The diameter of the water drop was approximately 2-3 mm and the obtained contact angle was greatly influenced by the number of HA particles covered by its perimeter.

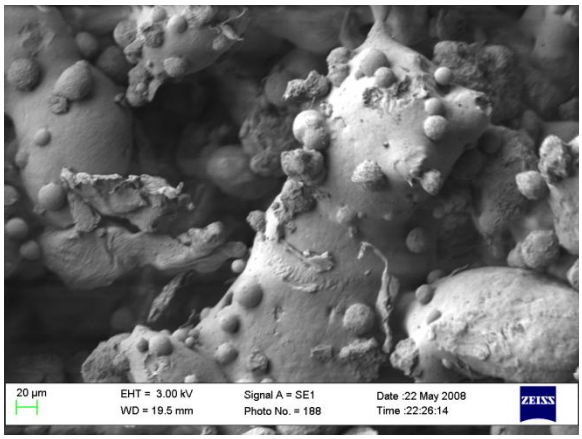

Figure 4.29 SEM image of designed solid regions of selective laser sintered PCL scaffolds containing 30 wt% of HA

Contact angle of water on the surface of parts with 0 and 15 wt% HA did not change significantly in the examined 3 s interval; however specimens with 30 wt% of HA were completely wettable as the water drop was soaked in within 3 s. The hydrophobicity of the scaffolds was decreased and wettability was increased by the addition of HA, making them more attractive for cell attachment [143].

In relation to the contact angle measurements it has to be pointed out that since the samples were porous, and had considerable surface roughness, values obtained were also affected by these features. Therefore, although the observed tendencies are likely to be valid for the examined composition, actual values can be significantly different for smooth biomaterial surfaces, or for surfaces fabricated using a different manufacturing technology.

4.3.2 Mechanical properties

4.3.2.1 Specimens fabricated from PCL150

Compression of solid disks

First of all, it has to be noted that microporosity was present both in the designed solid disks and in the designed solid regions of the sintered scaffolds as shown in Figure 4.29. Average measured relative density of the disks was 0.47. All solid disks were fabricated and tested along the z-direction to reveal tendencies initiated by the addition of HA. Results are summarized in Table 4.4.

Material	Compressive modulus [MPa]
PCL	3.75±0.38
PCL/ 15wt% HA	4.58±0.34
PCL/ 30wt% HA	5.58±0.62

Table 4.4 Stiffness of solid disks fabricated using different material compositions

For the designed solid disks increase in HA content resulted in a linear increase in compressive modulus from 3.75±0.38 MPa for pure PCL scaffolds to 5.58±0.62 MPa for scaffolds with 30 wt% of HA content. Although, in particle reinforced composites the matrix mainly bears the loading, HA particles can inhibit the movement of molecular chains in the matrix, explaining the observed improvement in mechanical properties. However, HA particles would agglomerate at higher concentrations, resulting in deterioration of compressive properties [13].

Compression of Lattices

As it has been shown in the previous chapter fabricated scaffolds are not isotropic, their mechanical behaviour fundamentally depends on the manufacturing direction, and therefore dependence of mechanical properties on the composition was examined in all three manufacturing directions. Measured compressive modulus and strength values are summarized in Figure 4.30 and Figure 4.31.

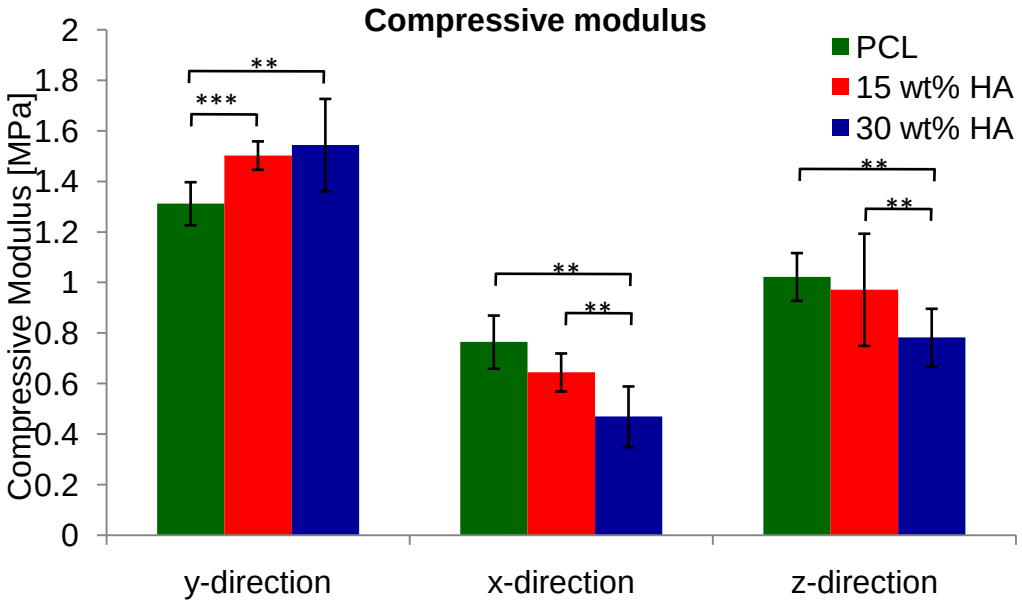

Figure 4.30 Dependence of compressive modulus of scaffolds fabricated from PCL150 powder in the different building directions (*, ** and * indicate significance at p<0.1, p<0.05 and p<0.01, respectively)**

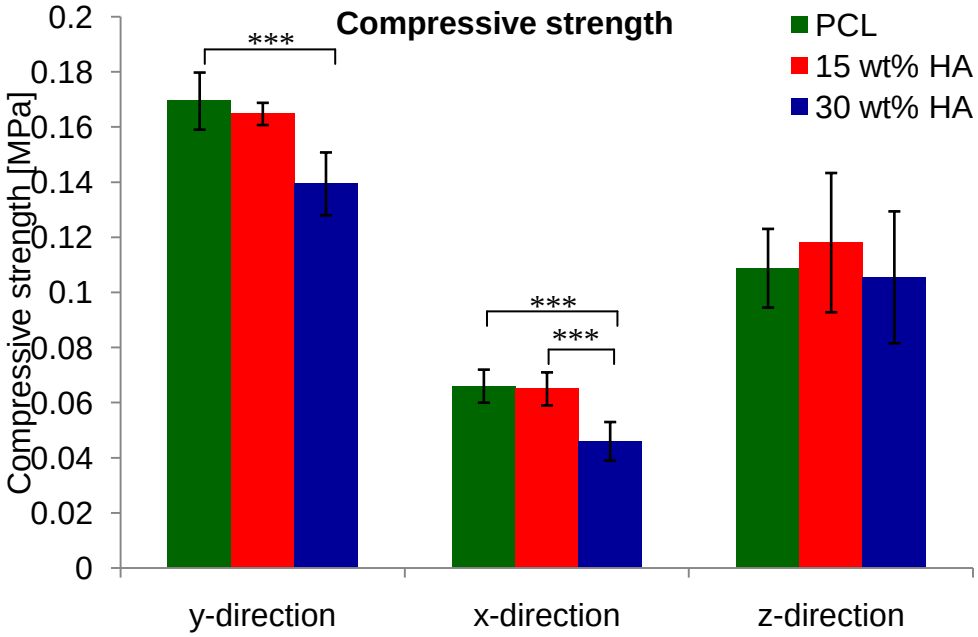

Figure 4.31 Dependence of compressive strength of scaffolds fabricated from PCL150 powder in the different building directions (*, ** and * indicate significance at p<0.1, p<0.05 and p<0.01, respectively)**

The figures show that in the various manufacturing directions the addition of HA had different effect on compressive properties; therefore results are discussed separately in the three manufacturing directions and are compared at the end.

Results for X direction

Although a slight deterioration of mechanical properties was seen in the x-direction with the inclusion of 15 wt% HA, decrease in compressive modulus (from 0.76±0.11 MPa for PCL to 0.64±0.08 MPa for the composite) or compressive strength (from 0.066±0.006 MPa for PCL to 0.065±0.006) was not statistically significant. However, the introduction of 30 wt% HA into the PCL matrix resulted in significant drop in both properties. Compressive modulus was decreased to 0.47±0.12 MPa, and compressive strength to 0.046±0.007 MPa.

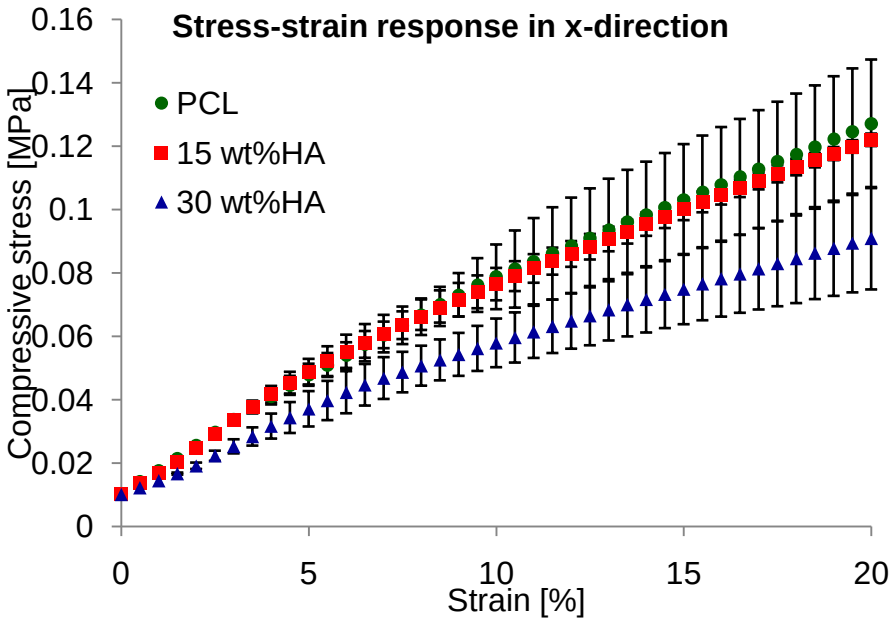

Figure 4.32 Stress strain response in the x-direction for the three deferent compositions

As it is shown in Figure 4.32 the character of the stress strain curve was not altered by the change in material composition.

Results for Y direction

In the y-direction, the addition of 15 wt% HA had considerably increased compressive modulus from 1.32±0.09 MPa to 1.5±0.06 MPa, compressive strength of the samples was not altered (0.17±0.01 MPa and 0.164±0.04 MPa for PCL and PCL/15wt% HA, respectively). Further increase of HA content did not have statistically significant effect on compressive modulus, as it stayed at 1.54±0.18 MPa, but it induced a meaningful drop in compressive strength to 0.14±0.01 MPa. Again, change in material composition did not initiated significant changes in the shape of the stress-strain response or the failure mechanism of the scaffolds, however post-yield strain softening became more intensive as it is illustrated in Figure 4.33.

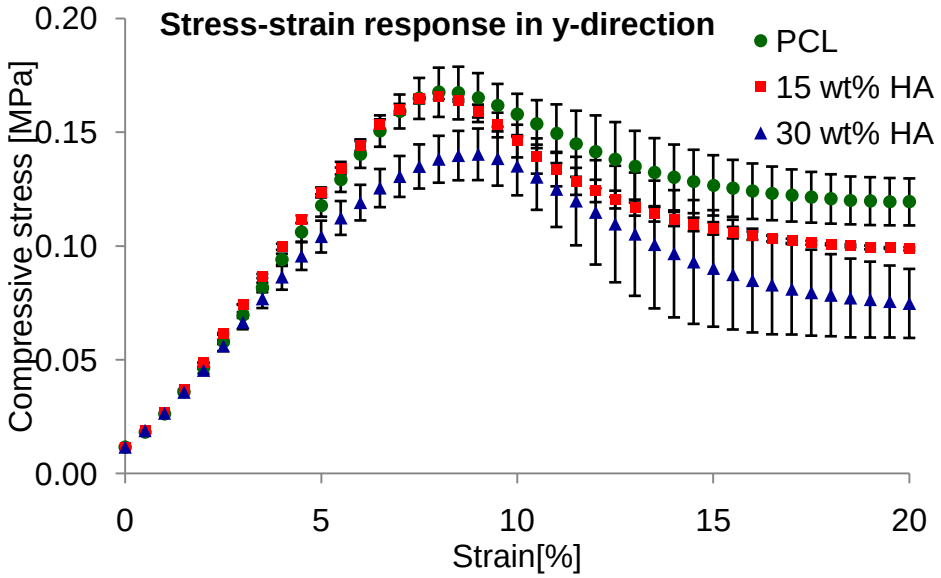

Figure 4.33 Stress strain response in the y-direction for the three different compositions

Results for Z direction

In the z-direction, compressive modulus of the lattices was not affected by the addition of 15 wt% HA (1.02±0.09 MPa and 0.97±0.22 MPa, respectively for PCL and the composite), however further increase of HA content resulted in a significant drop (0.78±0.11 MPa). No meaningful change was observed in compressive strength by changing the material composition (0.11±0.01, 0.12±0.03 and 0.11±0.02 MPa for the PCL, 15 and 30 wt% HA, respectively).

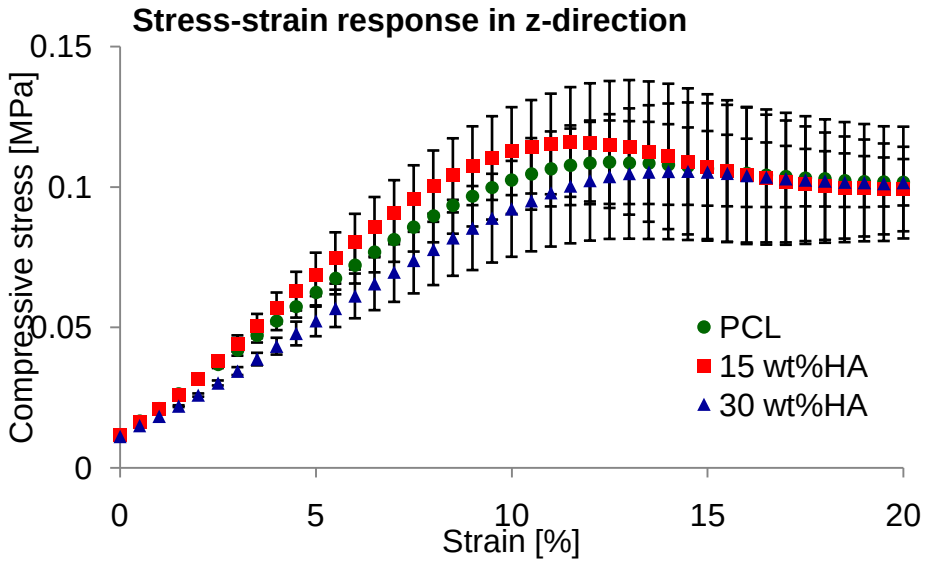

Figure 4.34 Stress strain response in the z-direction for the three different compositions

No significant change in the character of the stress-strain response or in the dominating failure mechanism was induced by varying the material composition, as shown in Figure 4.34.

From the above results it can be concluded that in the x- and z-directions, in general the addition of 15 wt% HA did not change mechanical properties, while further increase of HA resulted in significant reduction of compressive modulus and slight drop in compressive strength. Changes were most significant in the y-direction: addition of HA increased stiffness but decreased strength. Porosity of the struts was the lowest and therefore incorporation of HA particles into the polymer matrix was most efficient in this direction. Good incorporation of HA particle could inhibit the movement of molecular chains in the matrix, explaining the observed improvement of stiffness in this direction. In the other two directions, the struts were too porous and incorporation of HA particles was less adequate. In these directions, as there was only moderate neck formation and fusion between the PCL particles, the HA particles only consolidated partially into the surface of the PCL particles (Figure 4.29). The high amount of exposed HA particles is likely to be advantageous for cell attachment and osteointegration, but it has a negative effect on mechanical properties.

Due to significant reduction of mechanical properties in the x- and z-direction, the use of PCL/15 wt% HA is more favourable, at the current parameter settings with the powder particle size used.

A decrease in powder particle size is expected to improve integration of HA particles into the polymer matrix. Since, PCL particles that have higher connectivity and packed density results in better thermal conductivity and therefore better sintering and fusion between particles. Incorporation of HA could also be improved by changing process parameters and delivering higher energy density to the powder bed, that is the subject of the following section (Section 4.4).

DMA of solid bars

Test bars used for DMA were designed to be solid. Fabricated samples were tested along the x-direction, therefore values obtained represent the lowest among the three manufacturing directions. Delivered energy density was increased (compared to the fabrication of lattices and solid disks) so that good incorporation of HA particles is

ensured. Measured relative density of fabricated samples was 0.68 for the PCL and 0.65 for the composite bars.

The storage modulus (E'), loss modulus (E'') and loss factor (tan δ) versus temperature curves of pure PCL and PCL/HA composite samples measured at loading frequency of 1 Hz are shown in Figure 4.35 and Figure 4.36.

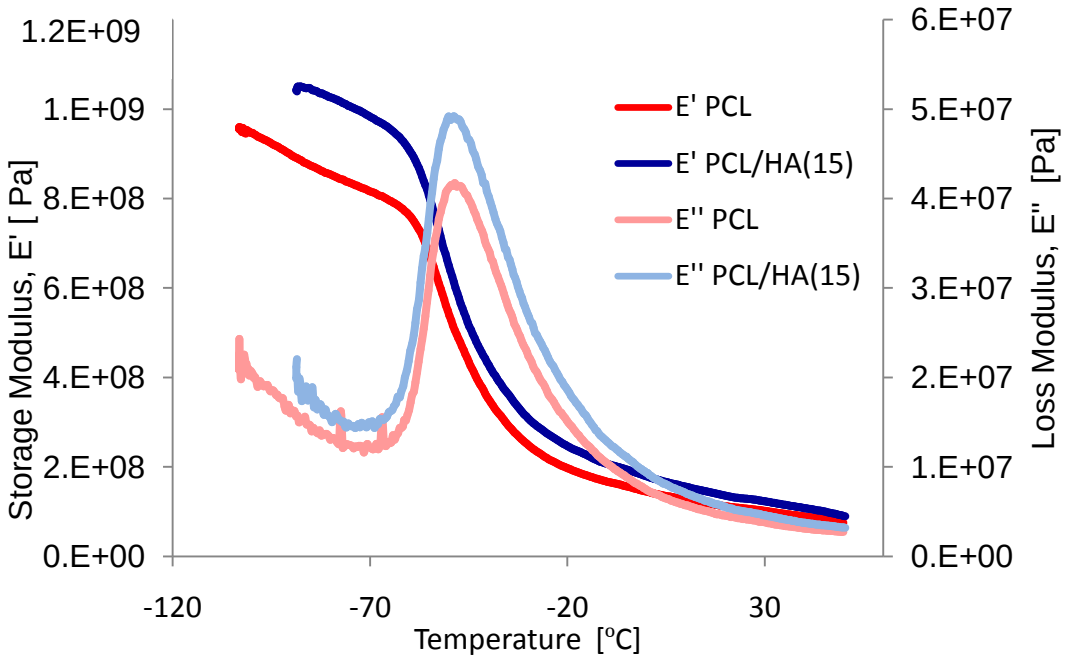

Figure 4.35 Effect of 15 wt% HA addition on the storage and loss modulus

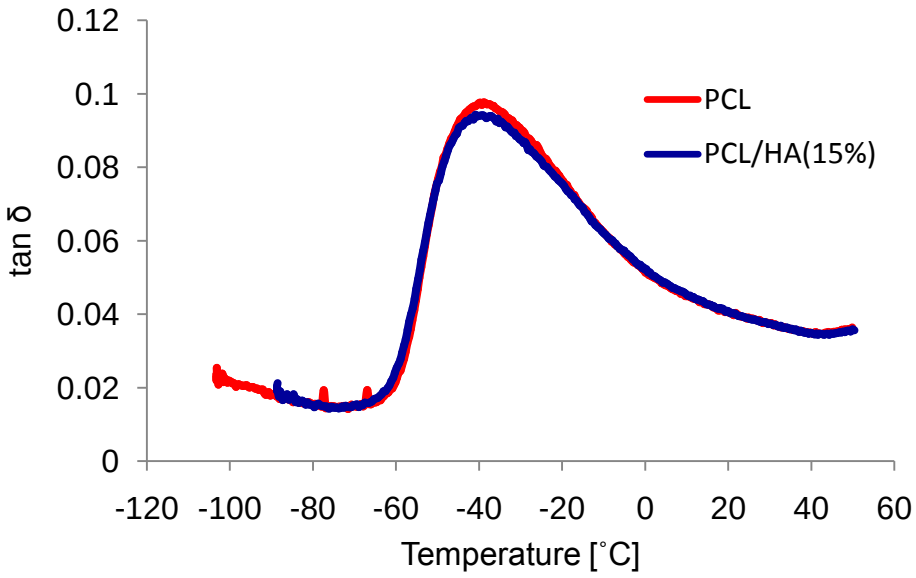

Figure 4.36 Effect of 15 wt% HA addition on damping properties of the samples

The loss peak was located around -50 ˚C. Both the loss and storage modulus increased with the addition of HA, however the loss factor was not significantly altered, nor was

T_g (that is the peak transition temperature of the tan δ). The width of the loss peak also changed indicating that the relaxation process of PCL was affected by the addition of HA.

Tensile storage modulus of PCL samples at room temperature was 106 MPa and increased to 129 MPa with the addition of 15 wt% HA. These values are in the range reported for cancellous bone [12, 144]. The measured damping, tan δ was higher both at room and body temperatures (0.038 at 25˚C and 0.035 at 37˚C) than the values reported by Guedes et al. [145] (0.02 and 0.025, respectively).

The significant increase compared to the compressive modulus of solid disk is partly due to the increased delivered energy density used for fabricating these samples resulting in increased fusion between the PCL particles and more exhaustive integration of HA particles than in the previous cases. When integration of HA particles is good, they can act as a reinforcing agent by limiting the movement of molecular chains in the polymer matrix. PCL is more compliant and has significantly lower mechanical properties than other biodegradable polyesters (such as PCL or PGA), because its T_g is below room temperature, and therefore the movement of molecular chains is not frozen. This motion can be limited to some extent by the addition of HA particles that results in increase of mechanical properties.

Increase in mechanical properties was also expected in tension as fabricated specimens are cellular solids, and therefore, in compression the deformation is bending dominated, that is a soft-mode of deformation, while tension is a hard-mode and results in higher stiffness values.

HA addition had a reverse effect on tensile mechanical properties of solid test bars than seen than for the compressive properties of lattices in the x-direction. It was argued that decrease of stiffness in compression is due to the fact that HA particles are not properly integrated into the polymer matrix due to limited fusion between the particles. Coalescence of PCL particles was more intense due to increased delivered energy density during the fabrication of test bars for DMA. Therefore the same effect was seen as for the y-direction in compression (Figure 4.30), where the addition of 15 wt% HA significantly increased stiffness.

To further test the hypothesis that HA particles increase stiffness of the samples when properly integrated into the polymer matrix, compression testing of lattices with

different compositions was repeated using a smaller particle size (PCL100). The use of smaller particle size is expected to increase the stiffness of lattices for two reasons:

- better fusion due to increased initial connectivity of the PCL particles and better thermal conductivity of the powder bed, and
- better incorporation of HA particles resulting in limitation of molecular chain movement in the polymer matrix.

4.3.2.2 Specimens fabricated from PCL100

During fabrication of the specimens using the PCL/15HA powder blend, in certain layers uneven layer deposition was observed, that can affect the mechanical behaviour.

Compressive properties measured are summarized in the graphs of Figure 4.37 and Figure 4.38. It is apparent from the graphs that mechanical properties (especially strength) of the parts containing 15 wt% HA significantly deteriorated. It was not expected that the addition of 15 wt% HA decreases strength while a further increase to 30 wt% increases it, and it is very likely that deterioration of mechanical properties occurred due to the observed uneven layer deposition. Therefore this material composition was excluded from the analysis.

Stress-strain responses for the two material compositions in the three main testing directions are not presented here, as the shape and character of the PCL curves were not affected, similar to what was seen with the bigger particle size. Stress-strain curves of PCL lattices for this particle size are shown in Figure 4.18.

When comparing compressive properties of this data set to the previous one (PCL150 powder) an enormous improvement can be seen. Stiffness was increased by a factor of two in y- and z-direction, and by a factor of three in the x-direction, and improvement of strength was even more conspicuous. Up to five-fold increase was seen in the y- and z-directions and a ten-fold increase in the x-direction.

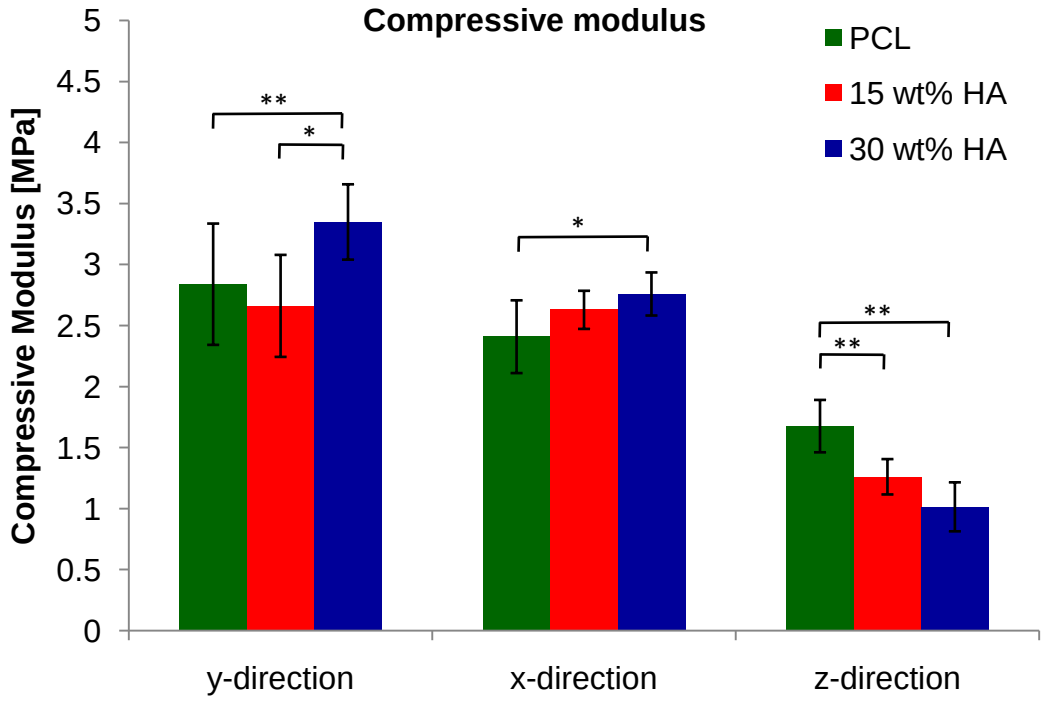

Figure 4.37 Dependence of compressive modulus of scaffolds fabricated from PCL100 powder in the different building directions (*, ** and * indicate significance at p<0.1, p<0.05 and p<0.01, respectively)**

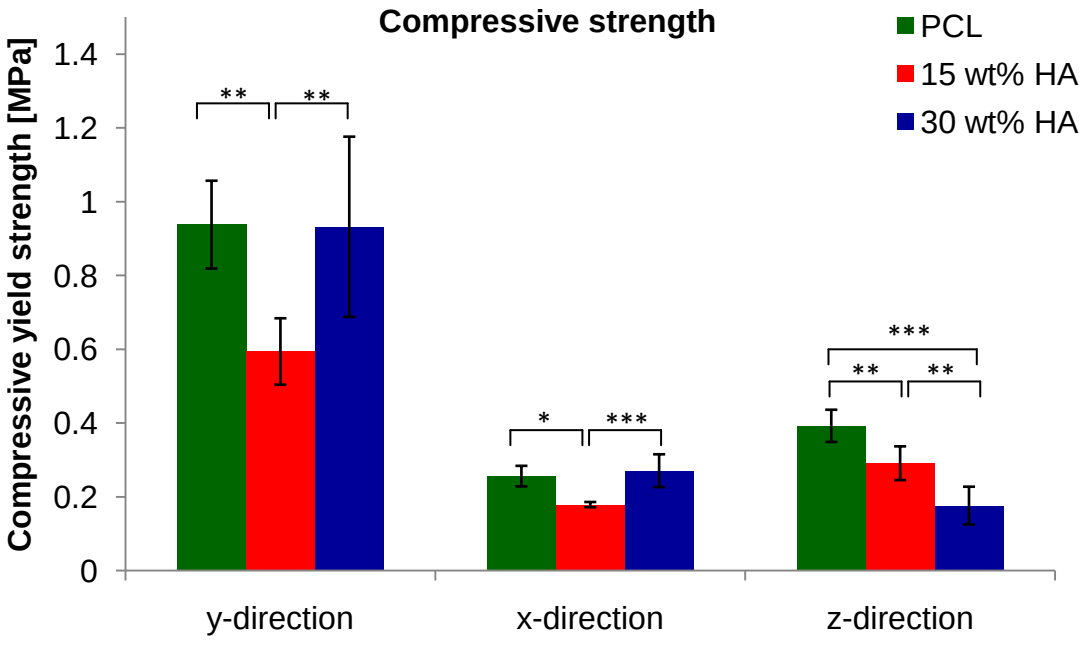

Figure 4.38 Dependence of compressive strength of scaffolds fabricated PCL100 powder in the different building directions (*, ** and * indicate significance at p<0.1, p<0.05 and p<0.01, respectively)**

Overall - in the current dataset -, stiffness was increased by addition of 30 wt, HA in the x- and y-directions, while no significant change in strength was seen. In the z-direction, however both strength and stiffness were still significantly decreased.

In the x-direction, compressive modulus increased from 2.41±0.30 MPa to 2.76±0.18 MPa with the addition of 30 wt% HA, while strength remained constant (0.26±0.03 MPa and 0.27±0.04 MPa for PCL and the composite, respectively).

In the y-direction, compressive modulus increased from 2.84±0.50 MPa to 3.35±0.31 MPa with the addition of 30 wt% HA, and again, strength remained constant (0.94±0.12 MPa and 0.93±0.12 MPa for PCL and the composite, respectively).

In the z-direction, compressive modulus decreased from 1.68±0.21 MPa to 1.02±0.2 MPa with the addition of 30 wt% HA, and again, strength remained constant (0.39±0.04 MPa and 0.18±0.05 MPa for PCL and the composite, respectively).

As expected, the addition of HA increased stiffness in the x- and y-direction when using smaller particle size and improved packing density. However stiffness was reduced in the z-direction. Data from µ-CT indicated that the layer thickness used for this particle size resulted in poor sintering at the bottom of each layer. Therefore porosity of z-struts in certain areas was higher than anticipated. At these regions incorporation of HA particles was poor, which explains the observed reduction in stiffness with the addition of HA. Results of the µ-CT analysis are discussed in detail in Chapter 4.4.2.

Greater amounts of HA could possibly be incorporated into the structures up to 50 wt%, if SLS processing parameters would be optimized. However, above this level even if sintering of the layer is better, HA particles are likely to agglomerate that would result in inferior mechanical properties.

4.3.3 Degradation and cell culturing studies

Cell cultured samples fabricate from PCL100 for microscopic observations and mechanical testing, and results of the Alamar blue assay (Table 4.5) were supplied by Engin Vrana, a colleague at DCU.

Adhesion and proliferation of osteoblasts on the lattices fabricated via SLS was evidenced through SEM, and µCT. Quantification of cell attachment and proliferation was through Alamar blue assay and mechanical testing of samples at certain time points of cell culturing.

SEM images show the spreading and growth of cells onto the material. Cells covered the surface of the macroporous PCL as well as its composites with HA. Three days after cell seeding cells, were spread and intercellular connections were maintained through cytoplasmatic elongations as shown in Figure 4.39. Cells were also visible within the micropores.

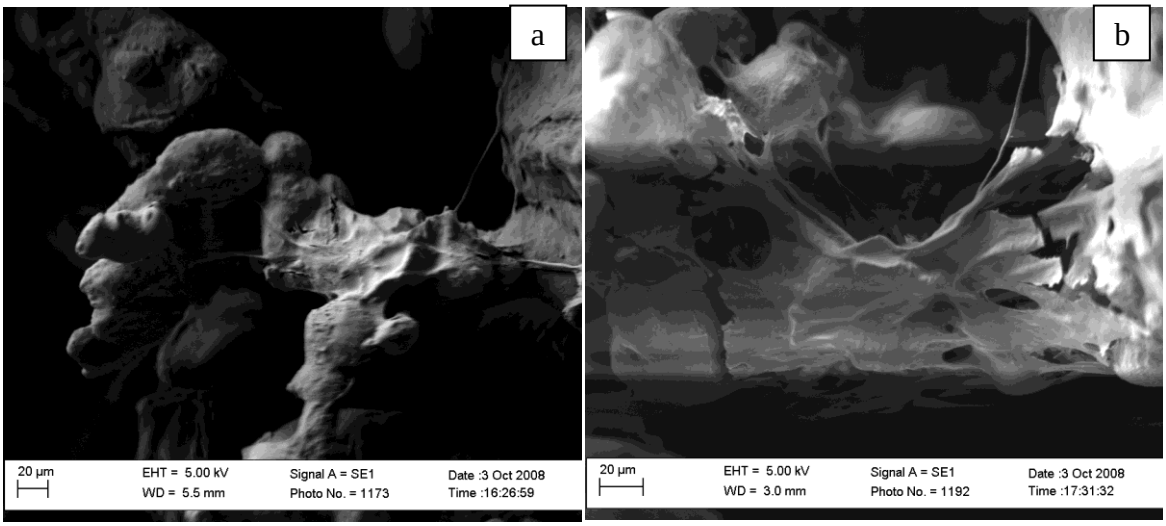

Figure 4.39 (a) Presence and (b) cytoplasmatic elongation of cells on PCL/15wt%HA scaffolds after 2 days of cell culturing (SEM)

After 3 days, cells were seen to spread on the surfaces, with areas of cell confluence as well as areas with few cells (Figure 4.40).

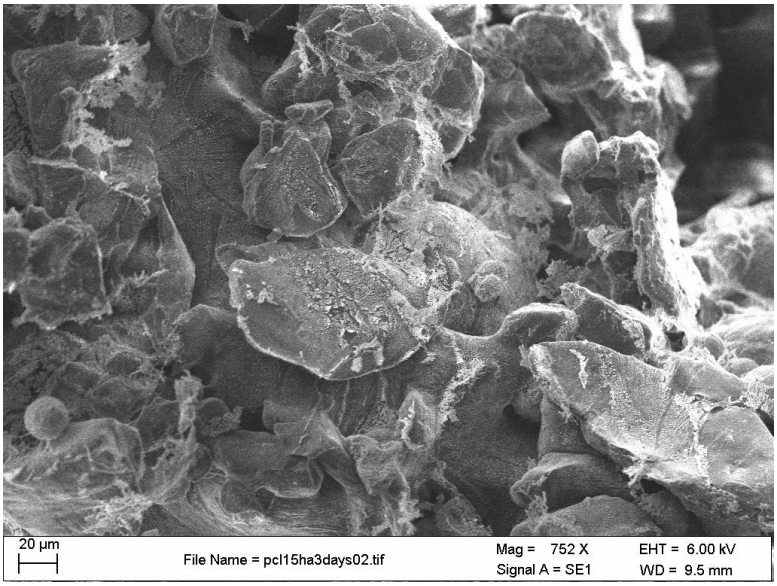

Figure 4.40 Cells partially covering the surface of PCL/15wt%HA scaffolds after 2 days of cell culturing (SEM)

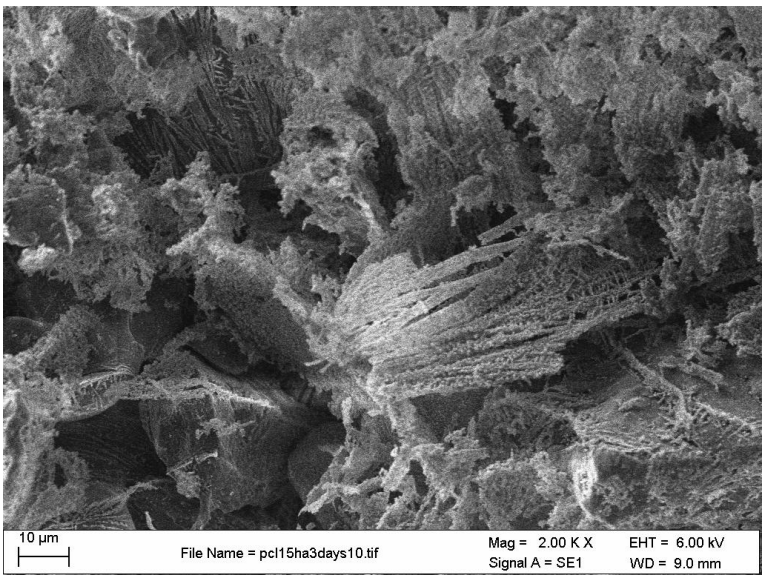

Figure 4.41 Areas of cell confluence on PCL/15wt%HA scaffolds after 2 days of cell culturing (SEM)

In some areas as shown in the SEM image of Figure 4.41 the surface of the scaffolds were fully covered by osteoblast like cells. Adhesion of cells to the biomaterial surface and cell-cell connection can be observed. Cells appear flattened on the surface and cytoplasmic extentions going deeper into the micropores of the polymeric matrix that suggest cell migration into the scaffold. The formation of cell layer on the selective laser sintered composites supports significant proliferation of adhered cells.

The images introduced so far only showed evidence of adhesion, growth and bone forming activity of osteoblasts on the outer surfaces of the 3D scaffold. The main concern however with 3D matrices is whether cells are able to migrate into the full depth of the scaffold. To reveal the spatial distribution of cells within the microspores of the struts of the scaffolds µCT was used.

Figure 4.42 shows reconstructed scaffolds in 3D, indicating the changes in internal architecture of the struts. After 1 week of incubation in PBS (phosphate buffered saline) the loosely connected particles were washed off from the struts and the surface of the scaffolds became slightly smoother.

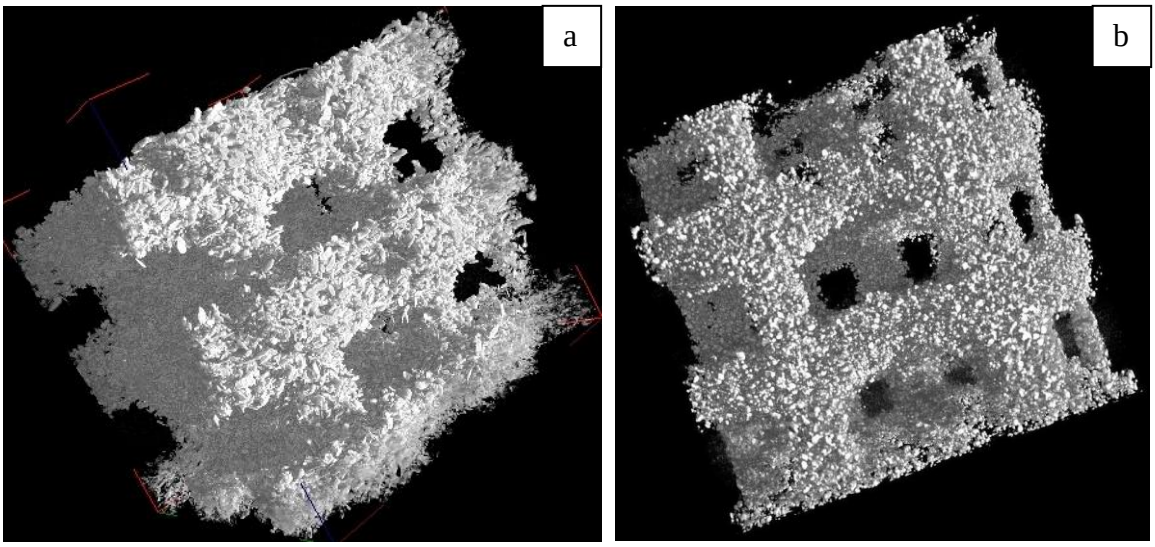

Figure 4.42 3D representation of (a) PCL scaffolds and (b) cell seeded PCL scaffolds - reconstructed µCT data

Osteoblasts are clearly visible on the seeded scaffolds marked by the higher intensity parts, however the changes on the surface of the scaffold is better emphasized on the close-ups of Figure 4.43 and Figure 4.44.

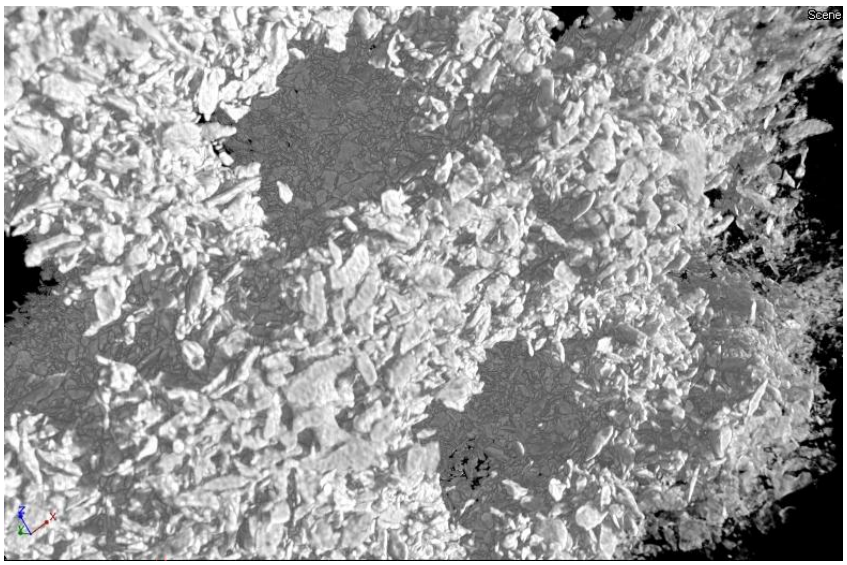

Figure 4.43 Struts of PCL scaffold reconstructed from µCT data

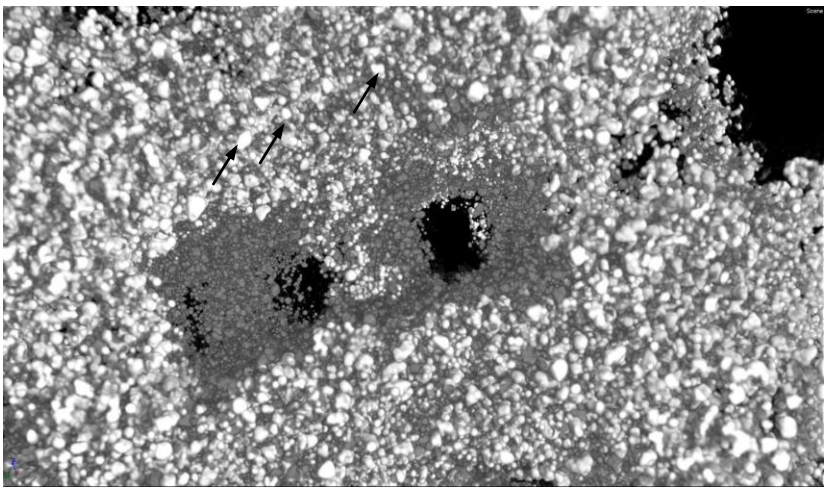

Figure 4.44 Struts of PCL scaffolds reconstructed from µCT data

The cross sections of scaffolds were also examined to confirm the presence of cells within the microstructure of the struts. A set of representative slices are shown in Figure 4.45. In case of unseeded samples two phases were present in the images: polymer (bright), air (dark),while in case of cell seeded structures three phases were evident: fixed cells (bright), polymer (medium), air (dark).

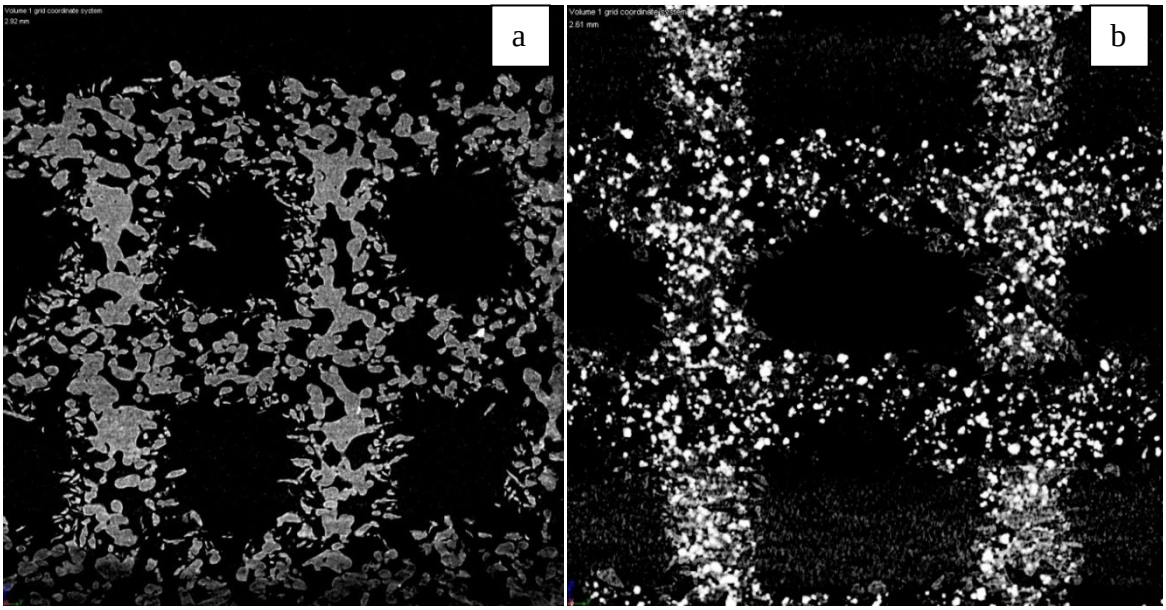

Figure 4.45 Internal cross-section of (a) PCL scaffolds and (b)cell seeded PCL scaffolds from µCT data

It is visible that in the cell seeded scaffolds osteoblasts, are encapsulated within the micropores of the struts. The average width of the struts was around 800 µm, therefore these cross sectional images confirm that cells penetrated ~400 µm deep into the microstructure of the struts.

Quantitative analysis - Alamar blue and mechanical testing

HA undergoes some level of degradation in in-vivo conditions. This gradual dissolution releases calcium and phosphate ions that can potentially influence nearby cell populations, and may enhance bone cell mineralization and bonding to the surrounding tissue. Furthermore, during degradation bioresorbable polyesters can release acidic degradation products and the addition of HA is known to compensate this acidic release through the alkaline calcium phosphate [146]. However, there are conflicting short-term results reported in literature about the effect of HA addition to PCL composites in terms of cell attachment, proliferation and differentiation. Some authors claim that the presence of HA in PCL scaffolds has little or no effect on biological response [29, 101, 109, 128]. Others show that scaffolds with 25 wt% of HA demonstrate improved cell differentiation compared to PCL scaffolds [108]. In the current experiment two compositions (15 wt% and 30 wt%) are compared.

Alamar blue assay was used to determine cell viability and proliferation at different time points (7 and 14 days). It is a non-destructive assay where a dye detects the metabolic activity of the cells (by change in colour due to reduction in the dye according to metabolic activity of the cell). Alamar blue staining is an indirect indication of cell viability and metabolism as the dye, a fluorescent end product of mitochondrial activity is released outside the cells where it can be quantified. The results of the assay are presented in Table 4.5.

Cell no.	15% HA	30% HA
Day 7	~2 000 000	~250 000
Day 14	~3 000 000	~1 000 000

Table 4.5 Results from Alamar blue assay for different composition after 7 and 14 days of culturing (data provided by Nihal Engin Vrana)

Data in Table 4.5 is presented as an average of six samples. A statistically significant difference ($p<0.05$) was seen in the cell numbers over the cultured time and also between the different compositions. An active proliferation period was seen on the samples, cell numbers increased over time until day 14 for both material compositions.

In general, composites with lower HA content (15 wt%) showed better metabolic activity compared to the higher HA content. In the first 7-day period, PCL/15 wt% HA samples performed significantly better, as there was a ten-fold increase in cell number compared to the initially seeded 100 000 cells, that indicates better cell attachment to

the surface. However, between day 7 and 14, this increase on PCL/15HA samples was significantly reduced (to 1.5-fold) while cell numbers on PCL/30HA scaffolds showed a four-fold increase, that suggest better spreading and proliferation of the cells in this time period.

Previous research suggested that modulus is a good indicator for the degree of mineralization and toughness is a good predictor for type –I collagen formation [147, 148]. However in the current study, compressive properties of the samples were only slightly influenced by degradation test and cell culturing. The Figure 4.46 and Figure 4.47 show these effects on scaffolds with different composition. A control sample (yellow) is included in the graphs for all three compositions.

Elastic moduli of the samples have not been significantly altered by the degradation test or cell culturing experiments. These results are contradictory to the findings of Erisken et al. when examining the tensile properties of electrospun PCL/TCP meshes seeded with MC3T3-E1 cells after 1 and 4 weeks of cell culturing [103]. The authors observed a slight, but statistically significant increase in modulus after the first week and a two-fold increase after 4 weeks indicating a modest mineralization after 1 week and a significant high degree mineralization after 4 weeks. The 2 week culturing period in the current experiment was selected to check if similar results can be obtained in a shorter term and also to reduce the risk of contamination. Although in the present case compressive properties were examined, a similar tendency was expected. However it has to be pointed out that in the Erisken experiment the samples were thinner (they were only 2D meshes), while in the current case 3D structures with height of 6 mm were seeded from one direction only. Therefore, the less promising results presented here, can be due to a number of reasons:

- lower effective cell seeding surface,
- cells might not penetrated throughout the 6 mm height of the scaffold, and it is possible that while cell activity is prominent in some areas of the sample, degradation takes place in others if the cells have not reached that area.

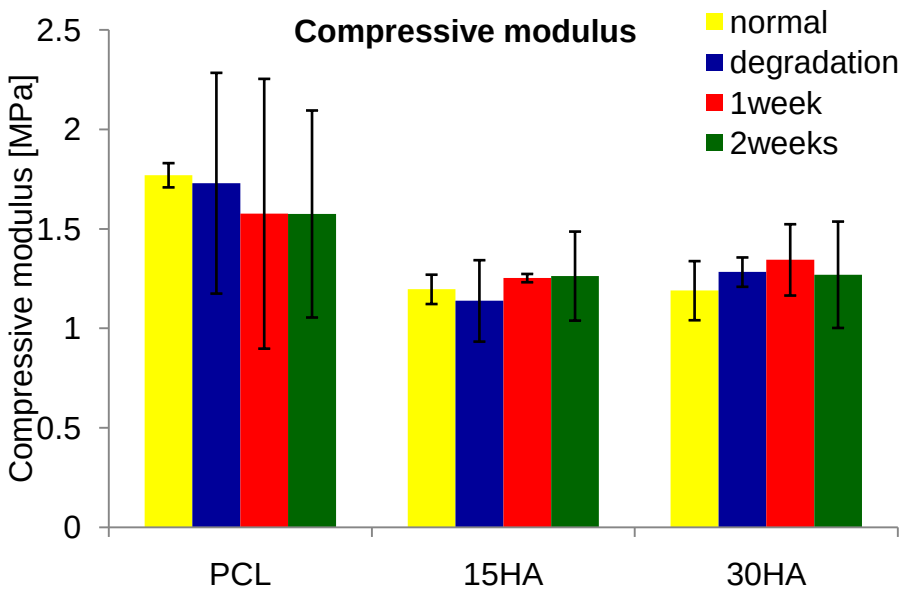

Figure 4.46 Effect of degradation tests and cell culturing on the compressive modulus of scaffolds

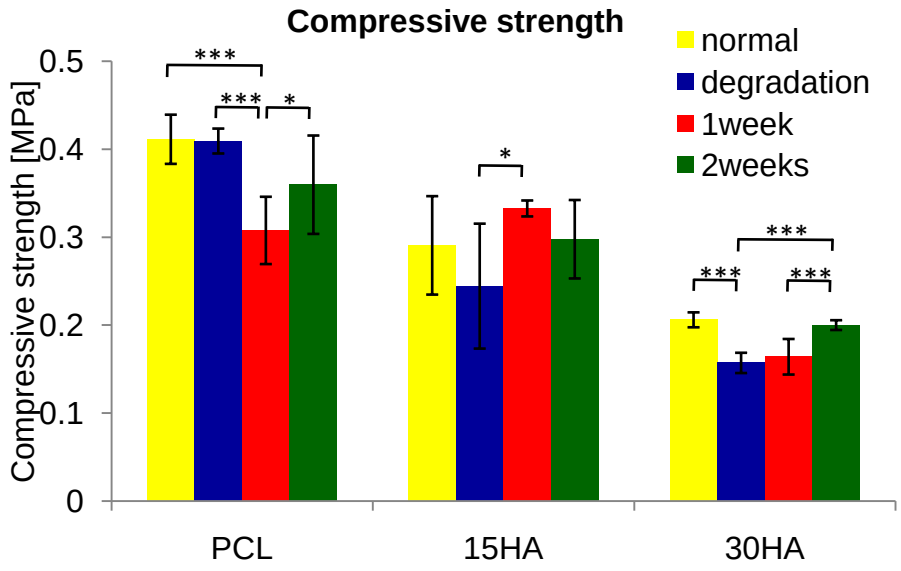

Figure 4.47 Effect of degradation tests and cell culturing on the compressive modulus of scaffolds (*, ** and * indicate significance at p<0.1, p<0.05 and p<0.01, respectively)**

The degradation test resulted in a slight decrease in compressive strength in all cases however the decrease was only significant in case of the scaffolds containing 30wt% HA. During the degradation test HA particles trapped inside or loosely connected to the structure of the struts were detached and washed off. Therefore its effect became more measurable with increasing HA content. In case of PCL samples the cell culturing for 1 week resulted in further loss of compressive strength, however after the second week the strength reached the strength of the control samples. For samples containing 15 wt%

HA an intense improvement was observed just after 1 week, that was maintained for the second week as well. This is in agreement with the results of the Alamar blue assay, which indicated that during the first 7-day period extensive cell colonization of the scaffold occurred, that somewhat slowed down in the second week. In case of scaffolds containing 30wt% HA the enhancement was only significant after the second week that is also in agreement with the obtained Alamar blue results, as it suggested that initial cell attachment to the scaffold surface in the first week was lower, but cell spreading considerably increased during the second week of cell culturing. Overall, the compressive strength was negatively altered with the degradation test, however by week 2 its value reached the strength of the untreated scaffolds in all cases.

Cells in the present experiments were cultured in-vitro in static conditions, without additional stimulants – growth factors – that could further increase cell spreading and proliferation.

4.3.4 Summary and conclusions

Surface roughness of fabricated parts was not altered by material composition. It was determined by the particle size of PCL, which was significantly greater than that of the HA powder. Measured surface roughness (R_a) was in range of 20-40 μm, surface features at this size range have been shown to be favourable for osteoblast cell attachment. The addition of HA reduced hydrophobicity and made PCL scaffolds wettable, that makes the surface more advantageous for protein absorption and cell attachment. Mechanical properties were affected by HA addition, the effect however was strongly dependent on orientation and on the PCL particle size used. Overall, both strength and stiffness was either not altered or was negatively affected when sintering of the polymer matrix of the load bearing struts was poor (that is, limited neck formation and fusion between PCL particles). However, when a proper connectivity of PCL particles was ensured, either by increasing particle size or positioning load bearing struts in a way that the scanning pattern results in a better fusion between particles, the addition of HA increased stiffness of the scaffolds. Dynamic mechanical properties were assessed in tensile mode, and it was found that with sufficient sintering of polymer, the addition of HA improves tensile properties. Alamar blue assay and mechanical testing of the cell seeded scaffolds suggested that the PCL/15HA composition performs better in the first 7-days of cell culturing, however during the second week, performance of scaffolds containing 30HA improved more significantly.

The use of smaller particle size also resulted in considerable improvement of compressive mechanical properties. However, when using the smaller particle size with 15 wt% HA, uneven layer deposition was observed in some layers. In spite of the fact that initial cell activity was better on the PCL/15HA samples, the 30 wt% HA powder composition was selected for further study for the following reasons:

- processability of this powder was better (possibly due to better flowability),

- proper sintering of this composition resulted in improved stiffness compared to the PCL samples, and

- cell attachment and proliferation was confirmed during the first week of cell culturing and during the second week cell activity was improved compared to the lower HA composition.

4.4 Modelling of SLS process parameters

A response surface methodology study was carried out using central composite design (CCD) to describe the influence of orientation and SLS process parameters on mechanical and dimensional properties. These models can assist researchers and manufacturing engineers to achieve desirable part properties. The developed models are useful in predicting the effect of each parameter and help in the selection parameter settings to achieve a given response.

For the reasons detailed at the end of the preceding chapter, the PCL100/30HA blend was selected to fabricate scaffolds with a simple-cubic lattice structure. The identification numbers used for the parameter combinations of each design point are summarized in Table 4.6.

ID no.	FP- Fill power [W]	OP-Outline power [W]	SS-Scan spacing [mm]	Effective Energy Density [J/mm]		Design point
				x-, y-dir	z-dir	
1	8.0	3.0	0.12	0.019	0.024	Factorial
2	11.0	3.0	0.12	0.024	0.029	Factorial
3	8.0	6.0	0.12	0.026	0.036	Factorial
4	11.0	6.0	0.12	0.031	0.041	Factorial
5	8.0	3.0	0.17	0.016	0.021	Factorial
6	11.0	3.0	0.17	0.019	0.024	Factorial
7	8.0	6.0	0.17	0.022	0.032	Factorial
8	11.0	6.0	0.17	0.025	0.035	Factorial
9	7.0	4.5	0.15	0.019	0.026	FP-axial
10	12.0	4.5	0.15	0.025	0.033	FP-axial
11	9.5	2.0	0.15	0.017	0.020	OP-axial
12	9.5	7.0	0.15	0.027	0.039	OP-axial
13	9.5	4.5	0.10	0.028	0.036	SS-axial
14	9.5	4.5	0.19	0.019	0.027	SS-axial
15	9.5	4.5	0.15	0.022	0.029	Centre

Table 4.6 List of parameter combinations used and corresponding identification numbers. The delivered energy density to individual struts in one layer is also shown

Delivered energy density in the various directions was calculated according the following equations:

$$ED = \frac{LP}{SS \times v_{beam,f}} + \frac{OP}{A \times v_{beam,o}} l \qquad \text{Eq. 4.2}$$

where, *ED* is delivered energy density in [J/mm^2], *FP* is laser fill power in [W], *OP* is outline laser power in [W], *SS* is scan spacing in [mm], v_{beam} is the scan speed of the fill (f) and outline (o) scans in [mm/s], *A* is the cross sectional area of the strut in [mm^2] and *l* is the perimeter of the strut cross section in [mm]. The first term of the equation corresponds to the energy delivered from the fill scan pattern (Eq. 2.1) and the second term to the energy delivered from the outline scan patter.

The process parameters examined in this study (laser fill power, outline laser power, and scan spacing) are part-dependent parameters. This means that they can be set independently for each part in the build, as opposed to build-dependent parameters that apply to all parts. Therefore, all specimens – representing the central, axial and factorial points of the design space – were fabricated in one build. This eliminated any possible block-effect from the design space.

All the parameters selected have been shown to have significant effect on the examined responses, however to date direct mathematical relationships have not been established between them. The selection criteria for the parameter ranges investigated have been described in Section 3.5.3.

Multiple scanning of a single layer has been excluded from the designs, as preliminary studies showed that the effect of this parameter is order of magnitudes higher than those listed. Inclusion of multiple scanning in the CCD would have resulted in weaker signal to noise ratios when examining the influence of fill and outline power and scan spacing. Furthermore, only smaller parameter ranges could have been examined. The influence of multiple scanning is introduced and discussed in Section 4.4.5.

4.4.1 Effect of process parameters on mechanical properties

The objective of this study was to develop mathematical models that can describe the dependence of mechanical properties on SLS process parameters. In the following section laser fill power, outline power and scan spacing are directly related to strength and stiffness of PCL/HA scaffolds with respect to testing direction.

4.4.1.1 Compressive modulus

Compressive modulus values obtained in the three building directions are summarized in Figure 4.48 and Table 4.7.

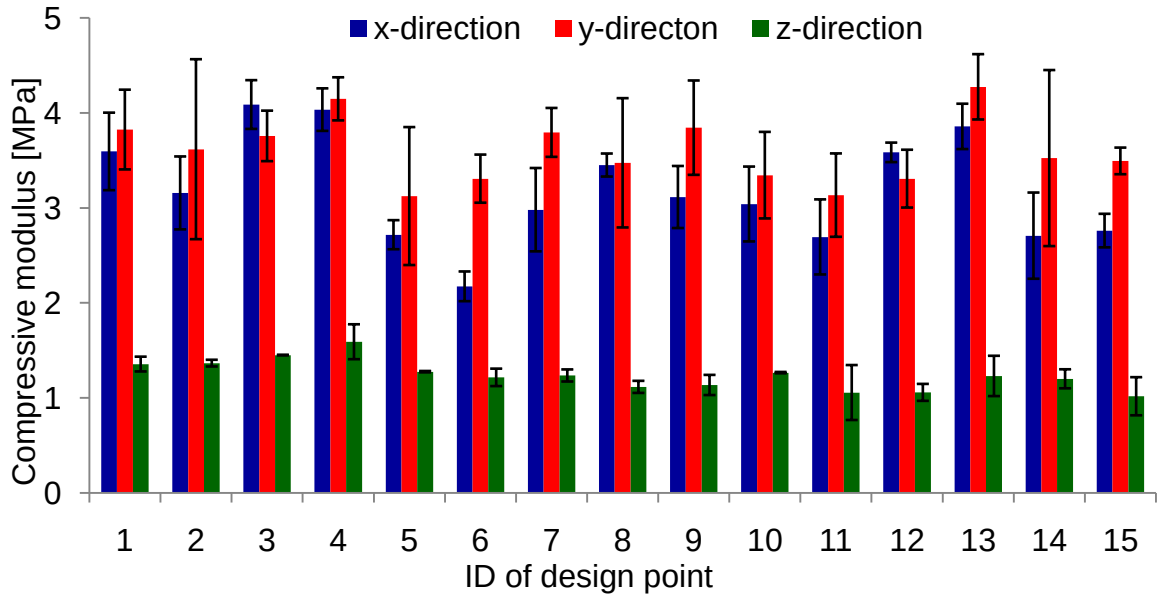

Figure 4.48 Average compressive modulus and standard deviations in the design points of the CCD for the three main manufacturing directions

ID/E	x-direction [MPa]	y-direction [MPa]	z-direction [MPa]
1	3.59±0.41	3.82±0.42	1.36±0.08
2	3.16±0.38	3.62±0.95	1.37±0.04
3	4.09±0.26	3.76±0.27	1.45±0.00
4	4.03±0.22	4.15±0.23	1.59±0.18
5	2.72±0.15	3.12±0.73	1.28±0.01
6	2.17±0.16	3.31±0.25	1.22±0.09
7	2.98±0.44	3.79±0.26	1.24±0.06
8	3.45±0.12	3.47±0.68	1.12±0.06
9	3.11±0.33	3.84±0.50	1.14±0.11
10	3.04±0.39	3.34±0.46	1.27±0.01
11	2.69±0.4	3.13±0.44	1.06±0.29
12	3.58±0.1	3.31±0.30	1.06±0.09
13	3.86±0.24	4.27±0.34	1.23±0.21
14	2.71±0.45	3.52±0.93	1.20±0.10
15	2.76±0.18	3.49±0.14	1.02±0.20

Table 4.7 Average compressive modulus and standard deviations in the design points of the CCD for the three main manufacturing directions

It is clear from the chart that – as already shown in the previous sections – fabricated parts are strongly orientation dependent. As also observed in the previous section parts were significantly weaker in the z-direction, due to insufficient penetration depth of the laser that is further discussed in Section 4.4.2.

Source	Sum of squares	Degrees of freedom	Mean square	F-Value	Prob > F (p-value)
Model	123.37	9	13.71	97.90	< 0.0001
Outline power [OP]	3.09	1	3.09	22.64	< 0.0001
Scan spacing [SS]	6.91	1	6.91	50.72	< 0.0001
Orientation	108.75	2	54.38	399.00	< 0.0001
Orientation × [OP]	1.74	2	0.87	6.39	0.0024
Orientation × [SS]	1.86	2	0.93	6.83	0.0016
$[SS]^2$	1.88	1	1.88	13.77	0.0003
Residual	14.99	110	0.14		
Lack of fit	3.51	33	0.11	0.71	0.8586
Pure Error	11.48	77	0.15		

Table 4.8 ANOVA for parameters and parameter interactions that were found significant after backward elimination

Since orientation is a categorical factor (i.e. it has no numerical value), separate mathematical models are required for each manufacturing direction. Although trends in the three orientations are similar, the influence of factors examined is likely to be different due to the different scanning patterns and layer positions.

The data was fitted with a quadratic model. Model terms (parameters and parameter interactions) that do not have significant contributions to stiffness of the fabricated scaffolds ($p < 0.05$) were eliminated. The results of ANOVA are presented in Table 4.8.

In design of experiments when the goal is to identify the active factors and measure their effect, accuracy of the proposed model is primarily measured with ANOVA and t-test on the model coefficients. For instance, regression coefficients such as R^2 do not have primary importance, as a significant p-value along with a low R^2 can mean a good model, rather than a problem. However, verification of the model was carried out by applying several statistical criteria.

The first step in statistical validation of the proposed model was the lack-of-fit test. The obtained p-value of 0.8586 implies that there is 85.86% chance that variation in the data occurred due to noise. The resulting non-significant lack-of-fit is good, confirming that the proposed model is correct.

Other indicators of accuracy that were used to validate the model were R^2, comparison between adjusted R^2 and predicted R^2, and signal to noise ratio. These values are presented in Table 4.9.

Indicators of accuracy	Value
R^2	0.89
Adjusted R^2	0.88
Predicted R^2	0.87
Signal/Noise ratio	28.8

Table 4.9 Adequacy measures of the proposed model

There is no commonly used "cut-off" point for R^2 in design of experiments. However, when the objective of the experiment goes beyond identifying significant factors, and the aim is to model how the factors and interactions control the response, R^2 should preferably be over 0.7. R^2 for the proposed model was 0.89, which is above the recommended minimum value. R^2 could be artificially increased by adding terms to the model that are not significant, therefore adjusted and predicted R^2 values should also be considered. Adjusted R^2 plateaus when insignificant terms are added to the model, and predicted R^2 will decrease when too many insignificant factors are included. Therefore, it is generally accepted, that if the two values are within 0.2 of each other the model is good. For the current model the difference between the two values is 0.01 and that is highly desirable. The signal to noise ratio is a measure of the range in predicted response relative to its associated error, and its value should be at least 4. Signal to noise ratio of the present model is 27.3 that is considerably above the required value [149].

Various diagnostic plots were also consulted to check validity of the proposed models, the most important ones are presented here. It was reviewed whether the residuals follow a normal distribution, due to the large number of data points and replicates, some moderate scatter is expected and considered normal. Also, actual experimental values were compared to the values predicted by the model. If the model represents a good fit for the experimental data, data points are evenly split by the 45 ˚ line. The normal probability plot and the predicted vs. actual values are presented in Figure 4.49. The plots show that residuals follow a normal distribution and that values predicted by the proposed model are in good agreement with experimental data, and therefore the model can be declared as valid.

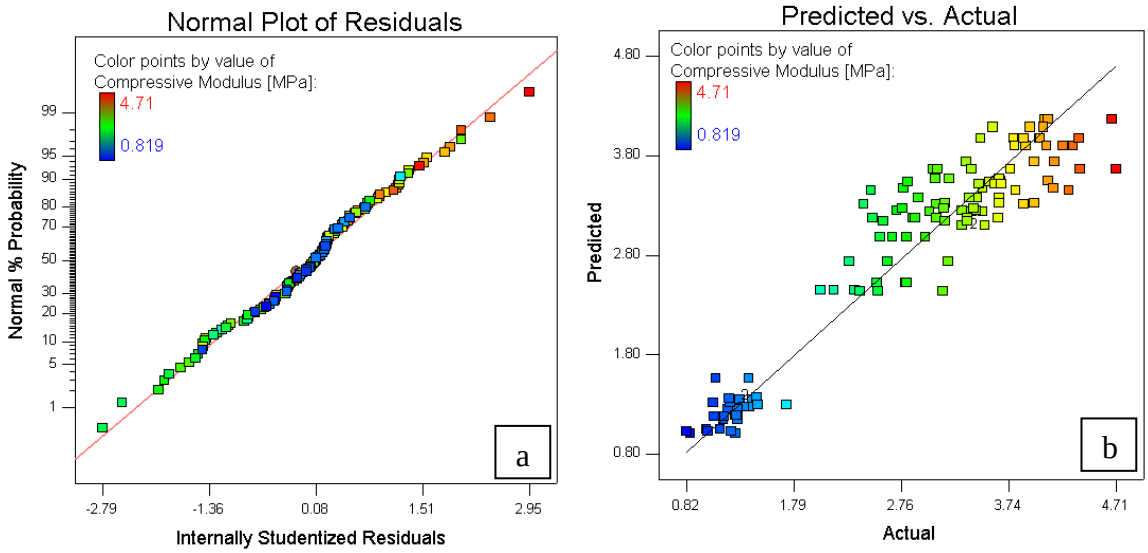

Figure 4.49 Diagnostic plots used to check statistical validity of the proposed model: a) normal plot, b) predicted vs. actual plot

ANOVA identified orientation as the most significant factor. Since it is a categorical factor, in the regression model the experimental dataset is fitted separately for each direction. It may occur that the overall model is identified statistically valid due to the significant contribution of the orientation effect, while the influence of other parameters in certain direction is not sufficient for generating a valid model. To avoid this problem, the statistical adequacy measures described previously (p-value, lack-of-fit, R^2, comparison of adjusted and predicted R^2 signal to noise ratio) were also checked separately for the datasets obtained in each direction. Datasets in the x- and y-direction confirmed adequacy of the model, however in the z-direction model validation resulted in a negative predicted R^2 implying that the overall mean is a better predictor of the response in this direction.

Based on this verification, the proposed model was accepted in the x- and y-direction, while overall mean value was used in the z-direction. The reduced quadratic models used to fit the data had the following form:

$$E = a_0 + a_1 X_2 + a_2 X_3 + a_3 X_3^2 \qquad \text{Eq. 4.3}$$

where, E is the compressive modulus in [MPa], X_2 is the outline laser power in [W], and X_3 is the scan spacing in [mm]. The coefficients of the model terms for the different building directions are presented in Table 4.10.

Model coefficents	x-direction	y-direction
a_0	+8.65	+8.57
a_1	+0.22	+0.08
a_2	-74.21	-66.66
a_3	+200.50	+200.50

Table 4.10 Coefficients of the reduced quadratic model used to relate process parameters to stiffness in the different orientations

The effect of process parameters on stiffness of the scaffolds is discussed separately in each direction as part orientation had by far the greatest influence (Table 4.8). Furthermore, the significance of interactions, which involve orientation, suggests that the influence of process parameters are considerably different in the x- and y-directions.

Perturbation plots can help to compare the effect of all factors at particular points of the design space. Perturbation plots are presented in Figure 4.50 for the two building directions (x and y) at the central point of the design space.

A steep slope or curvature shows that stiffness is sensitive to changes in that factor, while a relatively flat line indicates insensitivity. It is evident from the perturbation plots that scan spacing (C) has the greatest influence on stiffness in both directions.

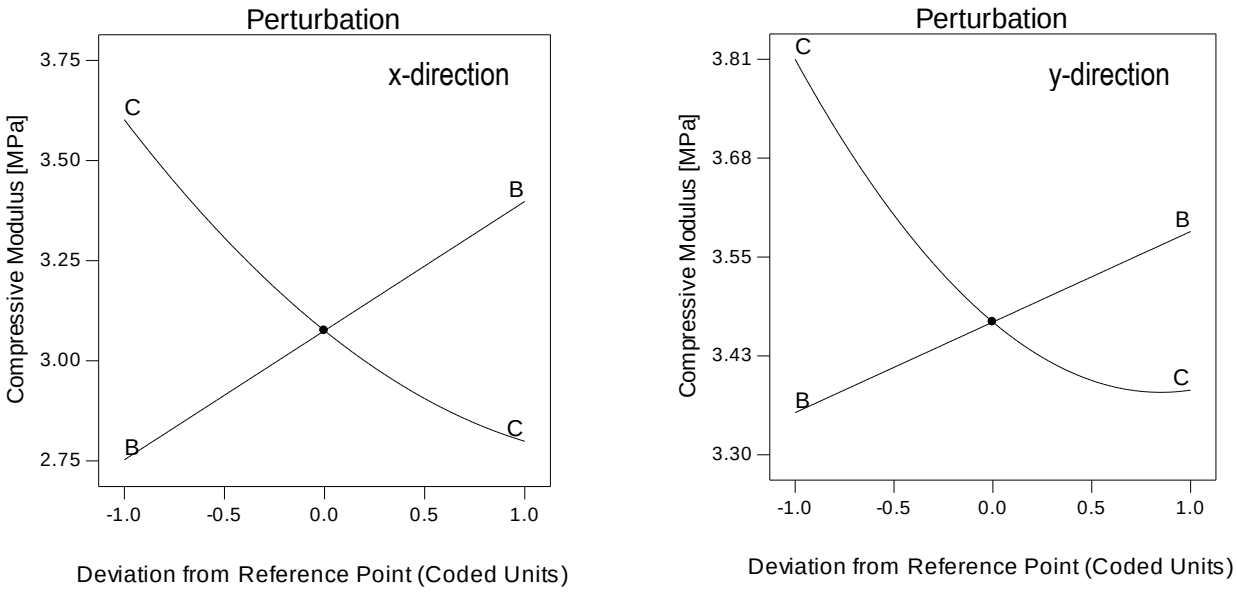

Figure 4.50 Perturbation plots for the x-, and y-directions at the central points of the design space (B-outline laser power, C-scan spacing)

Effect of process parameters on stiffness along the x-direction

As stiffness was most sensitive to changes in scan spacing and outline laser power, these parameters were selected as the two axis of the 3D surface plot that is presented in Figure 4.51. To better illustrate the effect of scan spacing and outline laser power on the compressive modulus values a contour plot is provided in Figure 4.52. The contour plot and the 3D surface response are given for the midpoint of laser fill power (9.5 W), as no significant change in tendencies were observed at the different laser fill power levels. As shown on the contour plot, a two-fold increase can be achieved in stiffness by changing scan spacing and outline laser power only. Compressive modulus is lowest (~2.2 MPa) when scan spacing is at its highest levels (0.17-0.19 mm) during the fill scan - resulting in loosely connected polymer particles - and then outline contour of the struts is scanned at the lowest examined laser power. By using the smallest scan spacing during fill scan - that already results in good sintering and considerably increases thermal conductivity of the powder bed – and then applying the highest examined laser power for the outline scan considerably increased stiffness to 4.5 MPa.

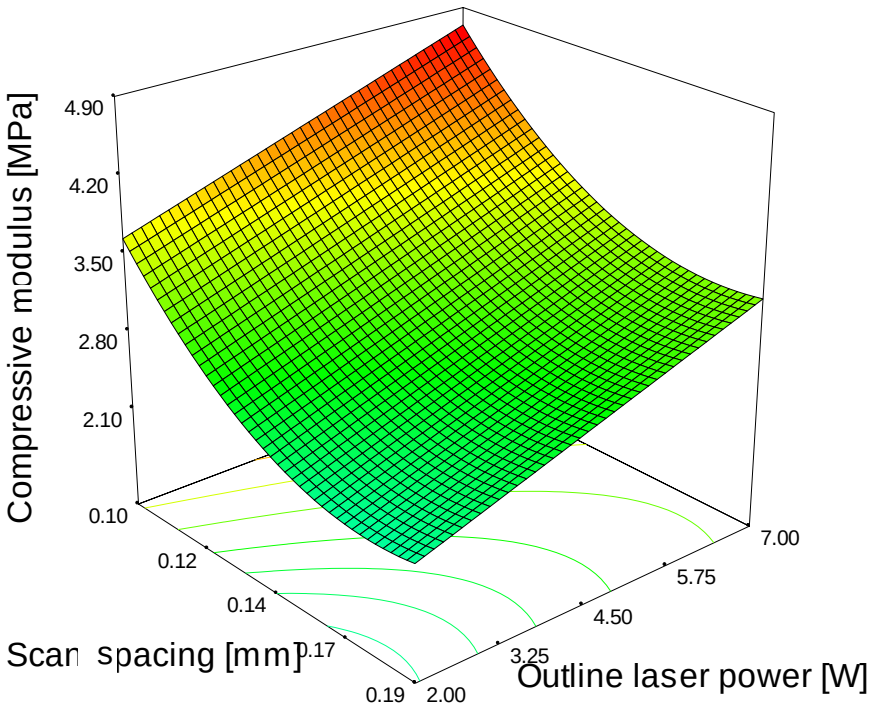

Figure 4.51 3D surface response of scan spacing and outline laser power in the x-direction with respect to stiffness according to the used quadratic model (at midpoint of laser fill power – 9.5 W)

The surface plot clearly indicates the strong quadratic dependence (inverse) on scan spacing and the significant linear dependence on outline laser power. As was expected and is well established in literature, increasing laser power (outline in this case) and decreasing scan spacing results in improved mechanical properties, as more energy is being delivered to each layer [19, 20, 26-33]. Therefore particle coalescence and fusion is better between the polymer particles, leading to a proper integration of the ceramic particles into the matrix. A proportional relationship has been suggested between delivered energy density (and therefore, scan spacing and laser power) and mechanical properties however the nature of this relation has not been examined qualitatively in detail to date. Revealing the higher order relationship of scan spacing to stiffness is a new contribution to the current knowledge on process parameter effects.

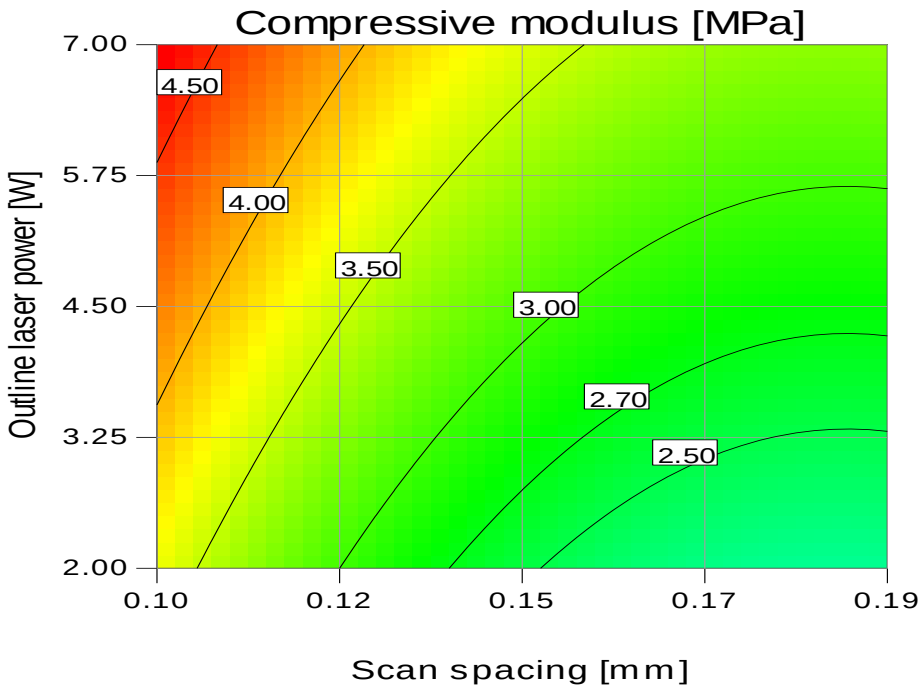

Figure 4.52 Contour plot of changes in compressive modulus with respect to scan spacing and outline laser power (at midpoint of laser fill power – 9.5 W) in the x-direction

Delivered energy density is calculated according to the following equation [19]:

$$Energy\ density = \frac{Laser\ fill\ power}{Scan\ spacing \times Laser\ speed} \qquad \text{Eq. 4.4}$$

That suggests that laser fill power is equally important to scan spacing in determining mechanical properties of the parts. Statistical analysis of the experimental data implies that stiffness is less sensitive to changes in laser fill power in the examined range. This result can be due to two reasons: either the examined range was not wide enough to

produce considerable changes in stiffness or the laser power has indeed less effect on stiffness than scan spacing. The latter argument seems to be more adequate as both parameters were varied over a relatively large range: laser fill power between 7 and 12 W and scan spacing between 0.1 and 0.19 mm. There was a two-fold increase between the two axial values of both parameters. These findings support the results of Song et al. [26] and Dewidar et al. [30]. The authors found that parts fabricated at the same energy density level using smaller scan spacing values are denser and therefore have superior mechanical properties, suggesting a higher order relationship between scan spacing and mechanical properties.

In the x-direction, stiffness was strongly dependent on outline laser power. The effect of this parameter is less investigated and discussed in literature. Traditionally, parts fabricated via SLS are on the centi- or decimeter scale, and therefore the effect of outline scan (with an effective laser diameter, that is <400 µm) along the perimeter of the part is negligible on mechanical properties. However, when sintering lattice structures where feature size (600 µm) is in range of the focused spot size of the laser (400 µm) its effect becomes more prominent. The traditionally used definition of delivered energy density (Eq. 4.3) is not valid for the fabricated micro-lattices, as it only represents the energy delivered to the part while scanning the fill pattern. To get a meaningful delivered energy density value the energy delivered during the outline scan has to be also taken into account. As the outline scan pattern is different in the x- and y-directions than in the z-direction, delivered energy density also varies (Table 4.6). Moreover, the contribution of fill and outline scans to the delivered energy in the main directions is also different. Contribution of outline scans to the overall energy density delivered to the struts built in the x-, and y-direction is half of the energy density delivered to struts built in the z-direction, as in the z-direction the whole perimeter of the cross-sectional area is scanned, while in case of x- and y- struts only half of the perimeter is scanned by the outline pattern.

The application of outline scan after the fill scan can by itself provide an explanation for the observed quadratic scan spacing effect on the stiffness of the fabricated lattices as the application of outline scan introduces a secondary scan spacing effect. Firstly, reduced scan spacing improves sintering of the layers during the fill scan by delivering higher energies to the surface. The second effect is that this better sintering during the fill scan has a direct influence on sintering of the outline scan, because, increase in thermal conductivity of the layer improves efficiency of subsequent sintering.

Effect of process parameters on stiffness along the y-direction

In this direction a boundary condition applies for the accepted model, as the subspace between the higher factorial (0.17 mm) and axial points (0.19 mm) of scan spacing are not predicted well. The model can only be used below scan spacing value of 0.17 mm.

As shown in Figure 4.48, highest compressive modulus values were obtained in this direction. In terms of process parameter influences similar tendencies were observed as in the x-direction. As concluded from the perturbation studies, stiffness was most sensitive to changes in scan spacing and outline laser power, and therefore these parameters have been selected as the axes of the 3D surface response and contour plots presented in Figure 4.53 and Figure 4.54.

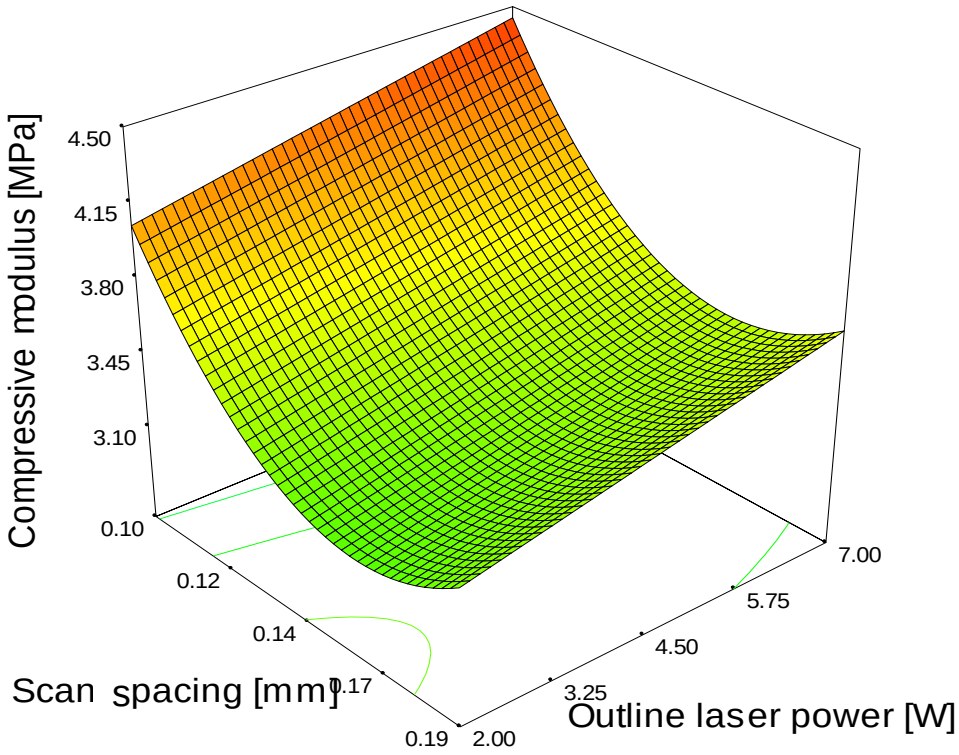

Figure 4.53 3D surface response of scan spacing and outline laser power in the y-direction with respect to stiffness according to the used quadratic model (at the midpoint of examined laser fill power range – 9.5 W)

Similarly to the x-direction, the 3D surface response shows inverse quadratic relation between scan spacing and compressive modulus, and proportional linear relationship between outline laser power and compressive modulus. However, as seen in the contour plot, stiffness in the y-direction was less sensitive to changes in scan spacing – especially at its higher examined ranges between 0.13 - 0.19 mm – than in the x-

direction. Furthermore, overall increase in compressive modulus was also more moderate (from 3.1 to 4.4 MPa) in this direction when increasing the delivered energy density from its lowest to its highest values. A significant difference between the two directions is the length of the scan vector during the fill scan. The strong influence of this geometric parameter has been demonstrated by several researchers [21, 43-45]. Length of the scan vector was 0.6 mm when sintering the y-struts, and 6 mm when sintering the x-struts.

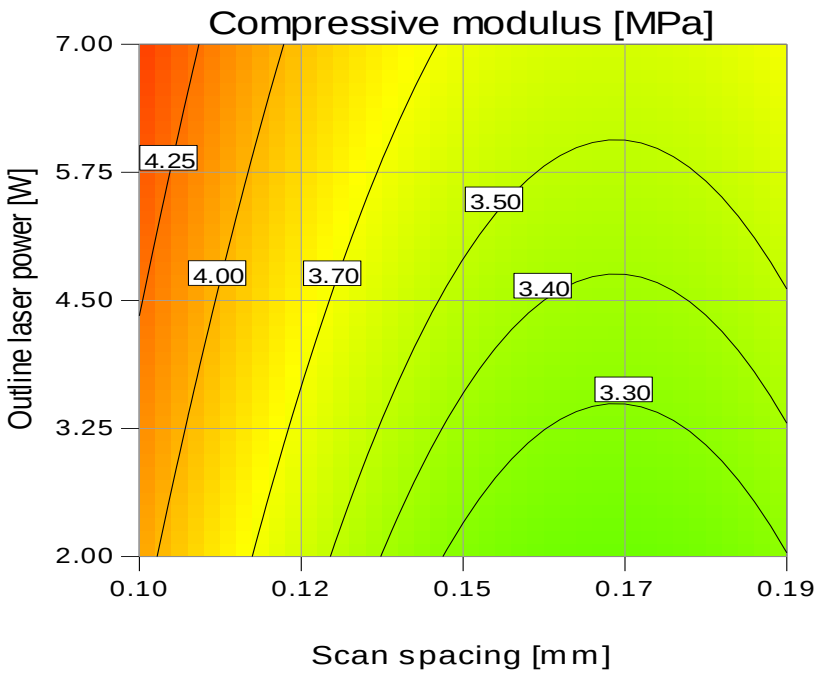

Figure 4.54 Contour plot of changes in compressive modulus with respect to scan spacing and outline laser power (at the midpoint of examined laser fill power range – 9.5 W) in the y-direction

Although, the laser speed of the fill scan is 5080 mm/s (and cannot be altered in the SLS system used), it is significantly slower at the end of its reciprocating motion – at the stroke, right after changing the direction of scanning - as the laser beam is positioned by a mirror system, and it needs time to accelerate to its working speed. Nominally, the laser would scan 0.6 mm in 0.1ms, however due to the directional change, scanning time is likely to be longer, and therefore energy delivered to these struts is higher, that explains improved mechanical properties in this direction.

Effect of process parameters on stiffness along the z-direction

In this direction similar tendencies were observed than for the x- and y-directions, that is reduced scan spacing and increased outline laser power results in improved mechanical properties. During statistical validation of the model in this direction, it was

found that the overall mean (1.23±0.16 MPa) is a better predictor of the response, than the proposed model. Developing a separate, improved model for this direction was attempted by transformations, further model reduction by eliminating less influential parameters, and by applying a lower order fit, however the overall mean was a better predictor of the response in all cases. The problem is associated with insufficient penetration depth of the laser that is further discussed in Section 4.4.4

As shown in the graph of Figure 4.48 lattices had the lowest stiffness in this direction. On average, compressive modulus in this direction was 2-2.5 times below the values measured in the y-direction. Again, this phenomenon is associated with insufficient penetration depth of the laser resulting in poor bonding between subsequently deposited layers, that has a negative effect on mechanical properties.

4.4.1.2 Compressive strength

Compressive strength values obtained in the three building directions are summarized in Figure 4.55 and Table 4.11.

The chart clearly illustrates the strong orientation dependence of the fabricated lattices. The overall trend is similar in all three directions, however preliminary analysis of the experimental data suggested that strength of the samples in the different orientations are not influenced by the same parameters. Therefore, datasets were fitted separately, and models were developed independently for each direction.

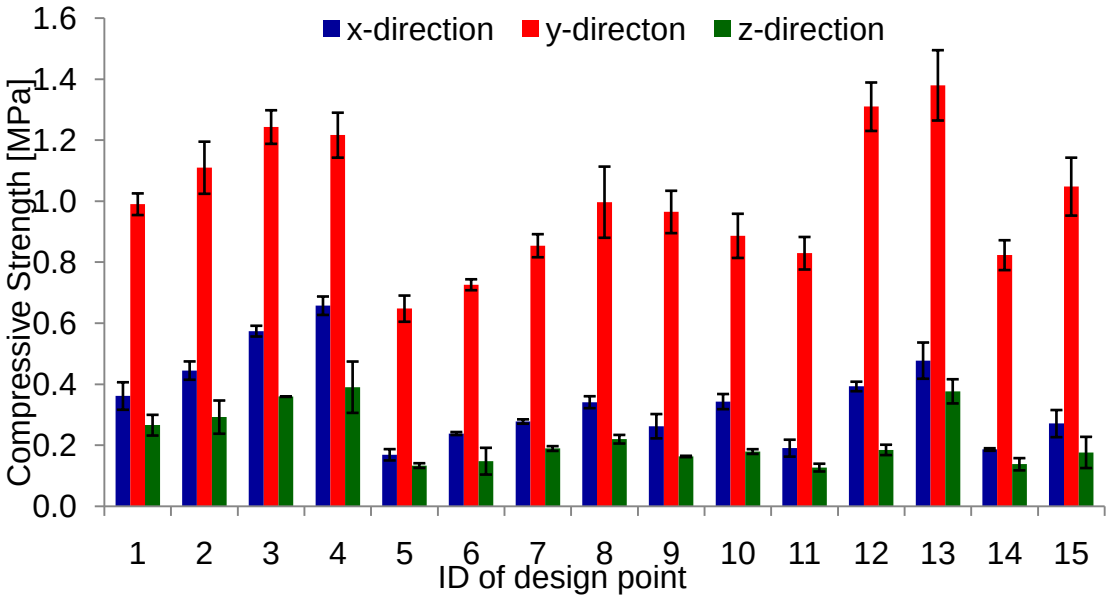

Figure 4.55 Average compressive strength and standard deviations in the design points of the CCD for the three manufacturing directions

ID/E	x-direction [MPa]	y-direction [MPa]	z-direction [MPa]
1	0.36±0.05	0.99±0.04	0.27±0.03
2	0.45±0.03	1.11±0.09	0.29±0.06
3	0.57±0.02	1.24±0.06	0.36±0.00
4	0.66±0.03	1.22±0.07	0.39±0.08
5	0.17±0.02	0.65±0.04	0.13±0.01
6	0.24±0.00	0.73±0.02	0.15±0.04
7	0.28±0.01	0.85±0.04	0.19±0.01
8	0.34±0.02	1.00±0.12	0.22±0.01
9	0.26±0.04	0.97±0.07	0.16±0.00
10	0.34±0.02	0.89±0.07	0.18±0.01
11	0.19±0.03	0.83±0.05	0.13±0.01
12	0.39±0.02	1.31±0.08	0.19±0.02
13	0.48±0.06	1.38±0.12	0.38±0.04
14	0.19±0.00	0.82±0.05	0.14±0.02
15	0.27±0.04	1.05±0.09	0.18±0.05

Table 4.11 Average and standard deviations of compressive strength obtained in the design points of the CCD for the three main manufacturing directions

Model developed for x-direction

The dataset in this direction was fitted with a quadratic model. The results of ANOVA are presented in Table 4.12. Parameters and interactions that have a p-value less than 0.05 were considered statistically significant.

As a standard procedure the first step in validating the proposed model was the lack-of-fit test that is also included in the ANOVA table. The obtained p-value of <0.0001 implies that the lack-of-fit is significant; therefore some concern needs to be given to the model and the experimental data. Statistically a significant lack-of-fit means that the variation of the replicates about their mean is less than the variation of the design points about their predicted values. Therefore, there are two possible reasons for observing a significant lack-of-fit:

- the runs replicate well and their variance is small,

- the model does not predict well the experimental data,
- or some combination of the two.

Source	Sum of squares	Degrees of freedom	Mean square	F-Value	Prob > F (p-value)
Model	0.80	7	0.114	43.21	< 0.0001
Fill power [FP]	0.04	1	0.042	15.74	0.0003
Outline power [OP]	0.21	1	0.210	79.34	< 0.0001
Scan Spacing [SS]	0.50	1	0.495	187.32	< 0.0001
[OP]×[SS]	0.02	1	0.017	6.47	0.0151
$[FP]^2$	0.02	1	0.019	7.06	0.0114
$[OP]^2$	0.01	1	0.014	5.28	0.0272
$[SS]^2$	0.03	1	0.034	12.90	0.0009
Residual	0.10	38	0.003		
Lack of Fit	0.07	7	0.010	10.72	< 0.0001
Pure Error	0.03	31	0.001		

Table 4.12 ANOVA for parameters and parameter interactions that were found significant after backward elimination

Here a point has to be made concerning replication of the current experimental setup: the replicates were not run in independent experiments. They were replicated samples obtained from a single experiment, fabricated in the same build. Therefore, it is likely that the p-value of the lack-of-fit is artificially small meaning that that the error has been underestimated. In this case, lack-of-fit test no longer provides a valid statistical criteria and decisions about the proposed model need to be made based other adequacy criterion.

The second possible reason for observing the significant lack-of-fit is that the model does not predict well the response. To check this, the normal distribution of residuals, and the predicted vs. actual values were consulted and the plots are presented in Figure 4.56. Two outliers can be identified on both diagnostic plots. Except for these two data points, distribution of the residuals is normal, and the predicted values by the model are in good agreement with the experimental data.

Since the plot of predicted vs. actual values is desirable, no further concern was given to the outliers (these two experimental data points were NOT excluded from the model), and it was concluded that the model predicts well and that significant lack-of-fit was detected because the measurements replicate well.

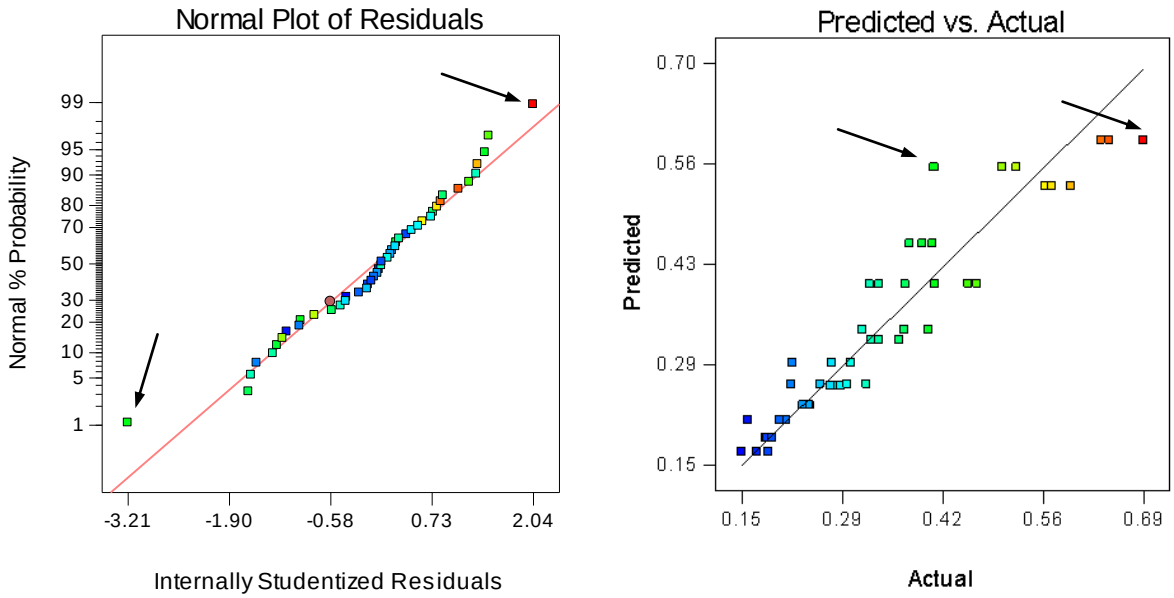

Figure 4.56 Diagnostic plots that were used to check statistical validity of the model (outliers of are marked with arrows)

Decision about using the proposed model was made based on other statistical criteria that are presented in Table 4.13. The square of the correlation coefficient R^2 was significantly over the recommended 0.7 value. The adjusted R^2 was in close proximity of predicted R^2, the difference between the two was 0.03 while cut-off point for the difference is significantly higher at 0.2. Furthermore a high signal to noise ratio of 19.9 was detected for the experimental data that is also considerably above the required value.

Adequacy measure	**Value**
R^2	0.89
Adjusted R^2	0.86
Predicted R^2	0.83
Signal/Noise ratio	19.9

Table 4.13 Adequacy measures of the proposed model

Based on the above measures the proposed model was accepted as valid. The reduced quadratic model that was used to fit the experimental data had the following form:

$$\sigma = \mathbf{2.7} - \mathbf{0.2}\,X_1 + \mathbf{0.05}\,X_2 - \mathbf{19.5}\,X_3 - \mathbf{0.7}\,X_2X_3 + \mathbf{0.01}\,X_1^2 + \mathbf{0.01}\,X_2^2 + \mathbf{63}\,X_3^2$$

Eq. 4.5

where, σ is the compressive strength, X_1 is the laser fill power, X_2 is the outline laser power and X_3 is the scan spacing.

As shown in the ANOVA table (Table 4.12) and reflected in the model, all the examined parameters (fill power, outline power and scan spacing) were found to have a significant effect on compressive strength of the lattices in the x-direction. Furthermore, the interaction between outline laser power and scan spacing was also significant. The perturbation test (Figure 4.57 (a)) was used to compare the effect of the contributing factors.

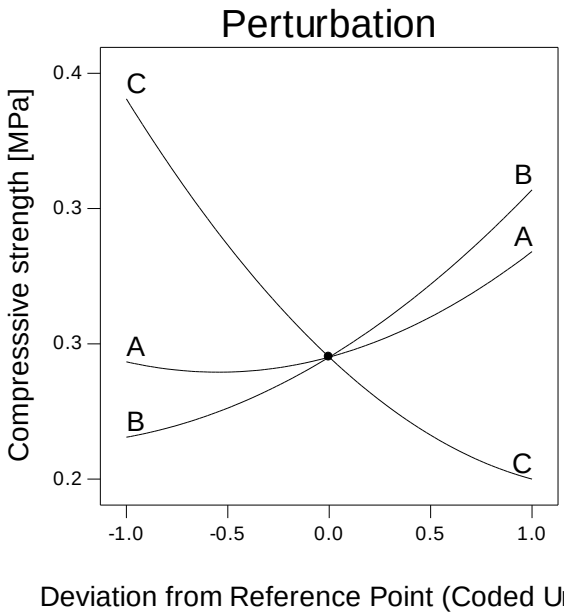

Figure 4.57 Perturbation plot at the central point of design space (A-laser fill power, B-outline power, C-scan spacing)

The perturbation plot implies that scan spacing has the highest contribution in determining strength of the scaffolds. Sensitivity of strength to changes in outline and fill power was similar, but was slightly higher for outline power. Therefore, scan spacing and outline laser power were selected as the two axes of the 3D surface response plot of the design space that is presented in Figure 4.58. By changing these two parameters only (and keeping laser fill power at its midpoint at 9.5 W), a five-fold increase in strength could be achieved. In general, the same observations were made, the same factors were dominant and the contribution of significant factors was similar relative to each other as for the compressive modulus response in this direction. The basic differences between the models of the two responses were:

- in the stiffness model laser fill power was not statistically significant, and

- the quadratic effect of outline laser power and the interaction effect between outline laser power and scan spacing were introduced to the model that describes the strength response, albeit with relatively low contribution.

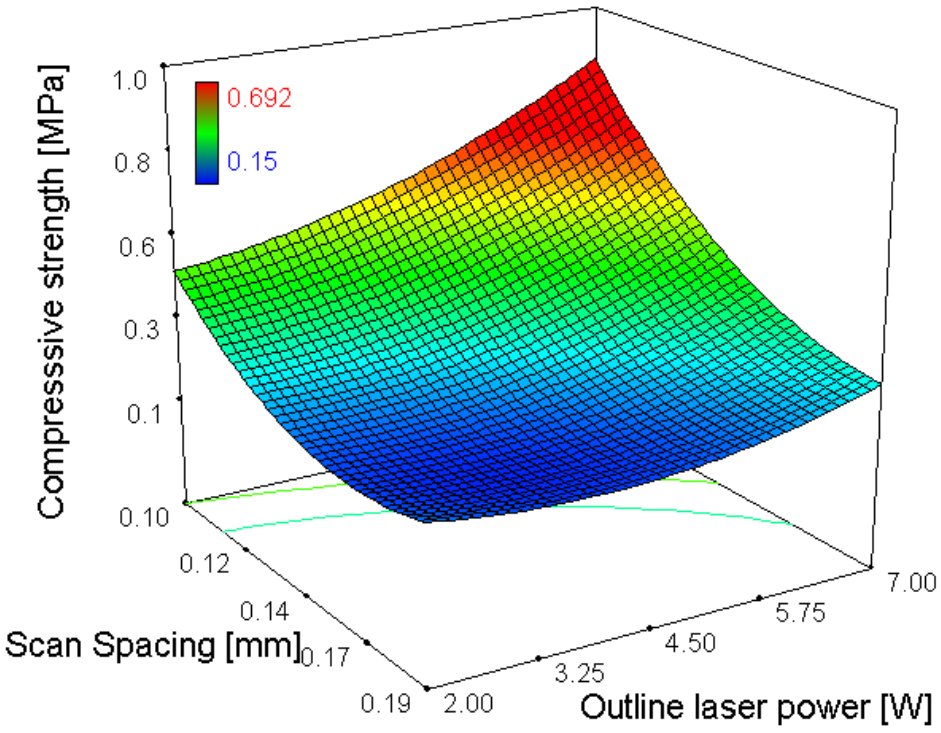

Figure 4.58 3D surface response of compressive strength for changes in scan spacing and outline laser power at laser fill power of 9.5 W (midpoint)

Throughout the design space, the experimental data replicated better for compressive strength than for stiffness. Therefore the statistical analysis of strength was more sensitive to weak effects detected when examining the stiffness response.

As laser fill power (along with scan spacing) determines the amount of energy delivered to the powder bed during the fill scan, it was expected to be significant. This parameter is established in literature as one of the most determining factors for mechanical properties [36, 37, 150]. However, the current study identified scan spacing as a more influential parameter, and showed that when fabricating lattices with features on the micron-scale outline laser power is also more important. The interaction effect between outline laser, power and scan spacing was also expected to be significant, as reduced scan spacing results in improved sintering during the fill scan that means better particle coalescence, better thermal conductivity and denser base material that will improve sintering efficiency of the outline scan.

To better demonstrate the effect of the three parameters contour plots are provided in Figure 4.59 for the two factorial levels of laser fill power (8 and 11W).

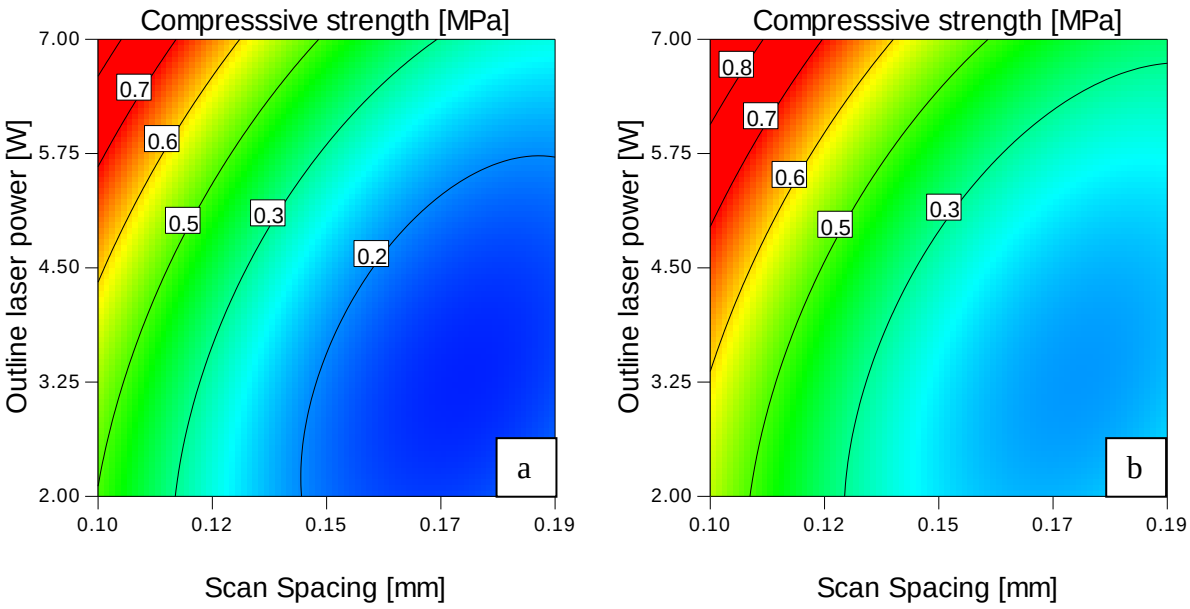

Figure 4.59 Contour plot of the compressive strength response to changes in scan spacing and outline laser power at the two factorial levels of - (a) 8W and (b) 11W - laser fill power.

The plots show that the response is most sensitive to parameter changes in the top left corner of the design space, that is when outline laser power is varied between 3 and 7 W and scan spacing between 0.15 and 0.1 mm. This region corresponds to the highest delivered energy density levels.

Model developed for Y-direction

Compressive strength was highest in this direction. On average, it was 2-3-fold above the values obtained for the other two directions. The dataset was fitted with a quadratic model. The results of the ANOVA are presented in Table 4.14 for the contributing model terms. The proposed model resulted in a significant lack-of-fit and therefore the procedure described for validating the strength response model in the x-direction was followed. The adequacy measures used to verify the models are listed in Table 4.15.

Source	Sum of squares	Degrees of freedom	Mean square	F-Value	Prob > F (p-value)
Model	1.75	2	0.86	91.65	< 0.0001
Outline power [OP]	0.59	1	0.59	63.06	< 0.0001
Scan Spacing [SS]	1.13	1	1.13	120.24	< 0.0001
Residual	0.40	42	0.009		
Lack of Fit	0.24	12	0.020	3.83	0.0014
Pure Error	0.16	30	0.005		

Table 4.14 ANOVA table for parameters that were found significant after backward elimination (compressive strength in x-direction)

Adequacy measure	Value
R^2	0.81
Adjusted R^2	0.81
Predicted R^2	0.79
Signal/Noise ratio	23

Table 4.15 Adequacy measures of the proposed model (compressive strength in x-direction)

All adequacy figures indicated that the model is sound and valid, and therefore the proposed model was accepted. The reduced quadratic model had the following form:

$$\sigma = \mathbf{1.61} + \mathbf{0.08}\, X_2 - \mathbf{6.65}\, X_3 \qquad \text{Eq. 4.6}$$

where, σ is the compressive modulus, X_2 is the outline laser power, and X_3 the is scan spacing.

The perturbation test (presented in Figure 4.60) implied that the response is most sensitive to scan spacing, closly followed by outline laser power. 3D surface and contour plot of the model response at the mid point of laser fill power level is given in Figure 4.61.

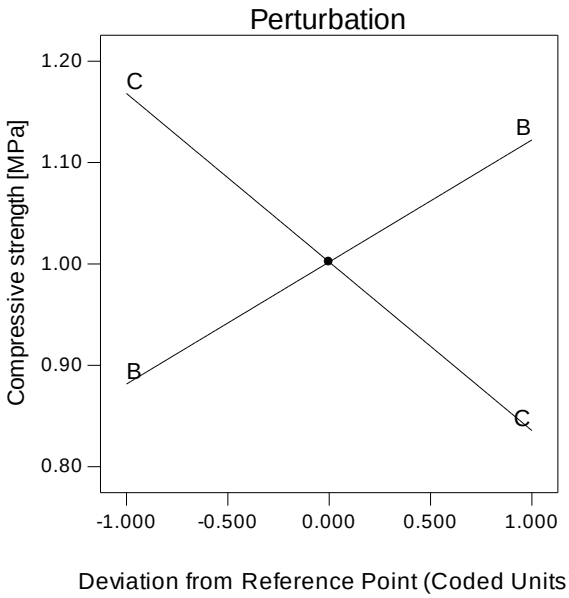

Figure 4.60 Perturbation plot at the central point of design space for the compressive strength response in the y-direction (B-outline laser power, C-scan spacing)

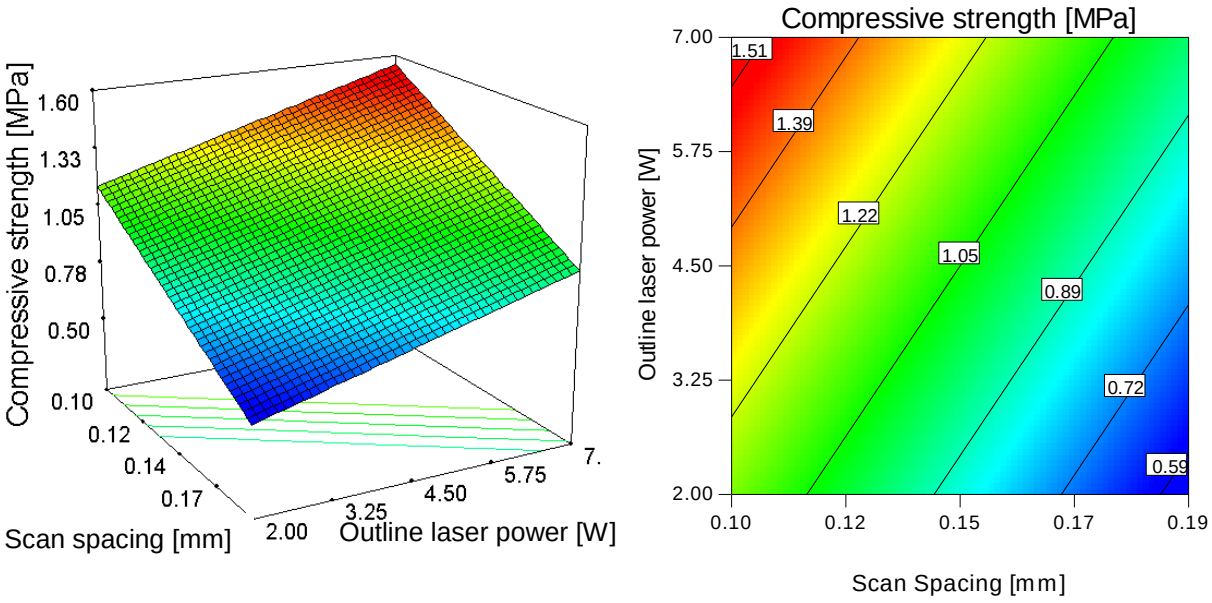

Figure 4.61 3D surface and contour plot of the compressive strength response in the y-direction for changes in outline laser power and scan spacing at the midpoint of laser fill power (9.5 W)

Similar tendencies have been detected as for the stiffness response in this direction. The differences in the two models are due to failiure mechanisms of the lattice at the yield point. While compressive modulus is only dependent on the load bearing struts, strength of the structure is not only determined by the strength of these struts but also by the struts that are perpendicular to loading direction. As has been demonstrated in Section 4.2, failiure in this direction occurs by buckling of y-struts and stretching of struts that

connect y-struts. Therefore, parameters that determine compressive strength of the structure in this direction come from a combination of parameter effects determining the strength of x-, y- and z-struts. As compared to the stiffness response that is primarily determinde by the y-struts.

Model developed for Z-direction

In this direction a boundary condition applies for the accepted model, as the subspace between the higher factorial (0.17 mm) and axial points (0.19 mm) of scan spacing are not predicted well. The model can only be used below scan spacing value of 0.17 mm.

Compressive strength was lowest in this direction, on average 3-4-fold lower values were obtained than in the y-direction. Although slightly lower, measured values were in range of compressive strength obtained in the x-direction. The dataset was fitted with a quadratic model. The results of the ANOVA are presented in Table 4.14 for the contributing model terms.

Source	Sum of squares	Degrees of freedom	Mean square	F-Value	Prob > F (p-value)
Model	0.202	3	0.067	36.72	< 0.0001
Outline power [OP]	0.025	1	0.025	13.86	0.0010
Scan Spacing [SS]	0.124	1	0.124	67.57	< 0.0001
$[SS]^2$	0.030	1	0.030	16.32	0.0004
Residual	0.048	26	0.002		
Lack of Fit	0.027	11	0.002	1.78	0.1492
Pure Error	0.021	15	0.001		

Table 4.16 ANOVA of parameters that were found significant after backward elimination

The lack-of-fit of the proposed model was not significant, residuals had a normal distribution and predicted values were in reasonable agreement with experimental data. The quantitative adequacy measures that represented the statistical criteria for validating the model are listed in Table 4.17.

Adequacy measure	Value
R^2	0.80
Adjusted R^2	0.78
Predicted R^2	0.73
Signal/Noise ratio	18.9

Table 4.17 Adequacy measures of the proposed model

All figures confirmed validity of the proposed model, therefore the reduced mode was accepted:

$$\sigma = \mathbf{0.19} + \mathbf{0.03}\, X_2 - \mathbf{0.07}\, X_3 + \mathbf{0.039}\, X_3^2 \qquad \text{Eq. 4.7}$$

where, σ is the compressive strength, X_2 the is outline laser power and X_3 is the scan spacing. As in all previous cases, the perturbation test implied that scan spacing has the greatest influence on strength. The perturbation plot is shown in Figure 4.62.

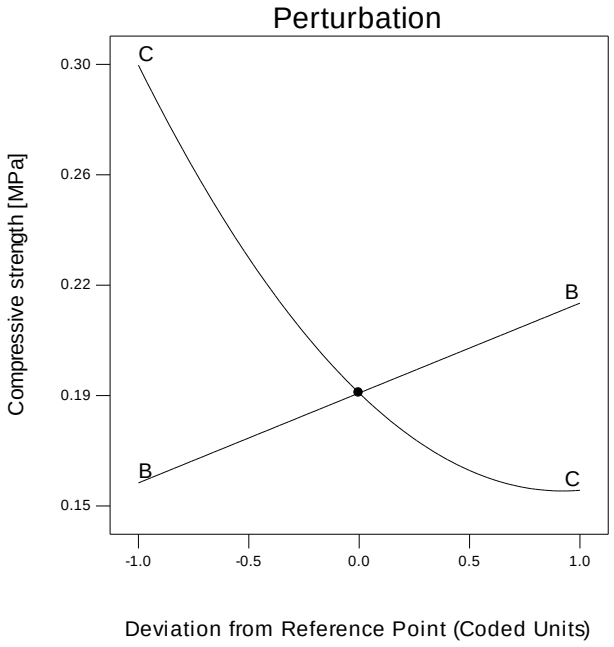

Figure 4.62 Perturbation plot at the central point of design space for the compressive strength response in the z-direction (B-outline laser power, C-scan spacing)

When compressed along the z-direction, the lattice essentially fails by shifting of layers within the z-struts. During the sintering of z-struts the energy delivered to a single layer from the fill and outline scan is distributed differently than for the x- and y-struts. The outline scan scans all four sides of the square-shaped cross-section of the z-struts, while

it only scans two sides in case of x-, and y-struts. Of the total delivered energy density, z-struts receive a considerably greater percentage from the outline scan. That explains insignificance of laser fill power in this direction.

The 3D surface and the contour plot of the model response are given in Figure 4.63.

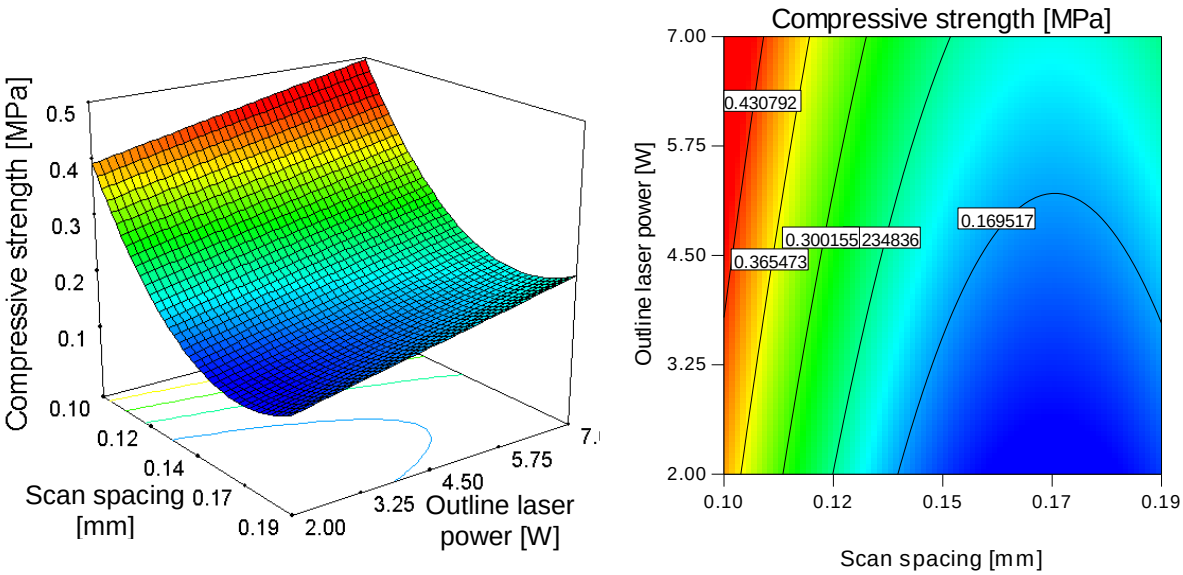

Figure 4.63 3D surface and contour plot of the compressive strength response in the z-direction for changes in outline laser power and scan spacing at the midpoint of laser fill power (9.5 W)

In this direction, no model could be developed for describing dependence of compressive modulus, as statistical analysis suggested that the mean value is a better predictor of the experimental data than any of the proposed models. However, it is suspected that the effects identified for compressive strength are likely to influence compressive modulus, too, and the data could not be fitted due to large variations in measured data. The large variations in modulus is not surprising as the struts of the tested structures are build up of a composite cellular material to which inhomogenicity is inherent. That was especially true for the z-direction as samples were weakest and most fragile in this direction.

An interesting observation is that the total energy density delivered to z-struts is higher in all design points than energy delivered to the x- and y-struts, and still the scaffold is weakest in this direction. It is very likely that this problem occurred because the layer thickness was big compared to the particle size used, and reduction in layer thickness is expected to significantly improve mechanical properties.

In all cases (both for strength and stiffness in all examined directions), the applied statistical analysis identified outline laser power and scan spacing as significant but in general did not pick laser fill power. From these results it is suspected that although delivered energy is an important parameter multiple scanning of a single layer is more significant.

According to this hypothesis mechanical properties are more sensitive to outline laser power because this is the second applied scan to the same layer, and laser fill power only prepares the powder bed before applying the second scan (outline scan). Scan spacing was more efficient than fill power as decrease in scan spacing is associated with increasing the number of laser scans on a given area. As scan spacing values are lowered overlapping of parallel scan vectors increases. The hypothesis that multiple scanning of a layer is more important than process parameters examined in this section is tested in Section 4.4.5.

4.4.2 Influence of delivered energy density

It is generally accepted in published literature that delivered energy density is directly related mechanical properties [19, 20, 26-33]. Therefore the experimental data obtained was also plotted as a function of delivered energy density. Plots are presented for the three main directions in Figure 4.64 - Figure 4.66.

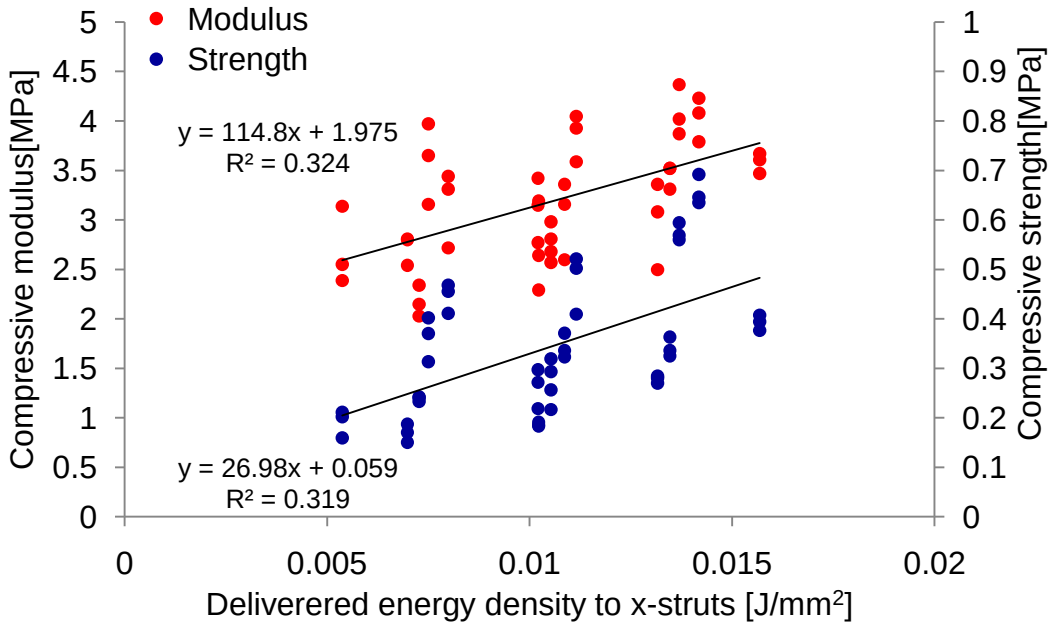

Figure 4.64 Compressive mechanical properties in the x-direction as a function delivered energy density to x-struts

Tripling delivered energy density to x-struts resulted in a two-fold increase in both compressive strength and stiffness along the x-direction.

Tripling delivered energy density to y-struts resulted in over two-fold increase in compressive strength and a moderate increase in compressive modulus along the y-direction.

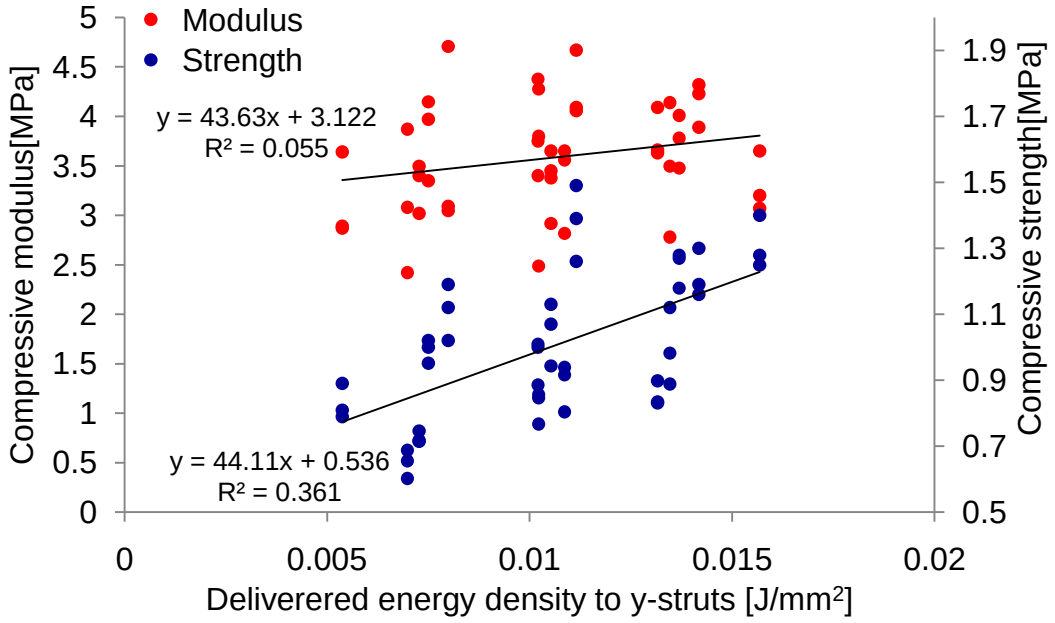

Figure 4.65 Compressive mechanical properties in the y-direction as a function delivered energy density to y-struts

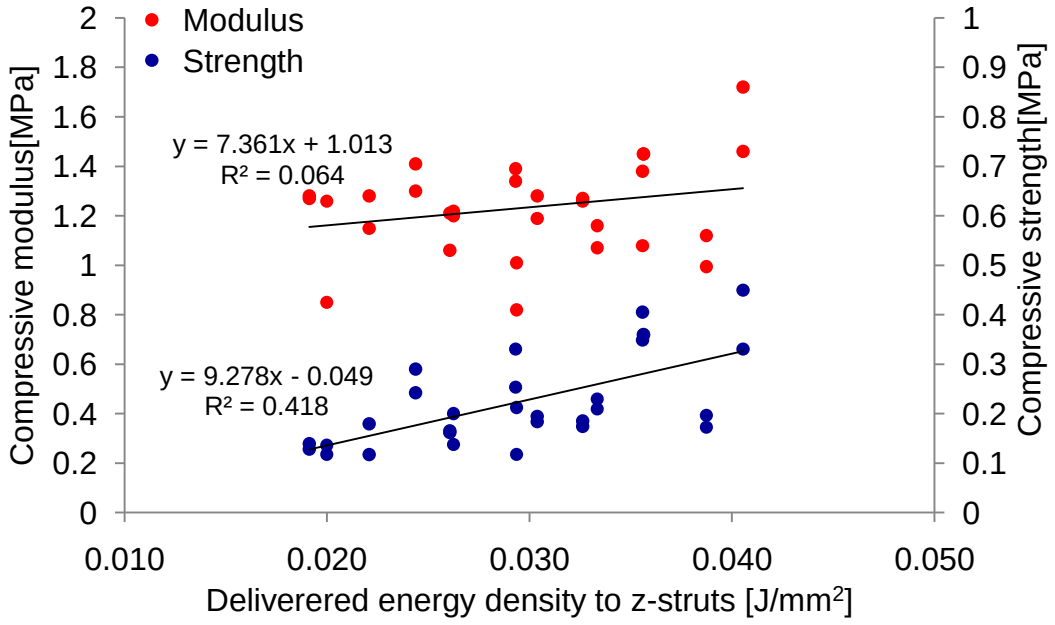

Figure 4.66 Compressive mechanical properties in the z-direction as a function delivered energy density to z-struts

Tripling delivered energy density to z-struts resulted in over three-fold increase in compressive strength and again moderate increase in compressive modulus along the z-direction.

Although the regression fit was very weak in all cases, considerable improvement in compressive properties was seen with increase in delivered energy density that is in agreement with published literature [19, 20, 26-33]. To date most studies only examined part properties in one direction. Two studies examined the effect of delivered energy density and process parameters with respect to part orientation within the powder bed. Caulfield et al. [29] found similar tendencies when testing tensile properties of solid polyamide bars along the x- and z-directions, both in terms of the effect increased energy density and in terms of orientation. In agreement with the present study strength and stiffness along the z-direction was significantly lower than in the x-direction. Contrary to the findings of this work, Jain et al. [42] found that tensile strength and modulus of samples is significantly higher along the x-direction as scan lines are parallel to the direction of loading. The reason for the contradicting results is the difference in tested geometries. In this work lattices with micro features were fabricated as opposed to solid test bars on the centimetre scale, and as discussed before, the shorter length of the scan lines of the y-struts results in superior mechanical properties.

It can be concluded from the results obtained that delivered energy density is not as good a predictor for compressive strength and stiffness as the developed models that account the strongest influences for scan spacing and outline laser power.

4.4.3 Verification of the mechanical models

All models developed experimentally were verified at three randomly picked points in the design space using three replicates. The coding and actual parameter values of the selected points are summarised in Table 4.18.

Code	[FP]	[OP]	[SS]
A	10 W	5.5 W	0.13 mm
B	11 W	6 W	0.11 mm
C	7 W	4 W	0.16 mm

Table 4.18 Coding of points in the design space that were selected for verifying the model

The results of the verification study for the models predicting the compressive modulus is presented in Table 4.19. All individual measurements were within the interval predicted by the proposed models (PI 95%). However, at point B in the x-direction, the average of measurements (3.74±0.15 MPa) was below the predicted average value, and is also out of the set 95% confidence interval.

dir	code	predicted E [MPa]	measured E [MPa]	CI95% for average	M1 [MPa]	M2 [MPa]	M3 [MPa]	PI95% for individual meas.
x	A	**3.58±0.38**	**3.62±0.22**	3.42-3.73	3.61	3.42	3.85	2.82-4.33
x	B	**4.21±0.39**	**3.79±0.15**	3.96-4.45	3.74	3.67	3.95	3.43-4.99
x	C	**2.77±0.38**	**2.68±0.31**	2.63-2.91	2.82	2.89	2.33	2.02-3.53
y	A	**3.72±0.38**	**3.72±0.39**	3.56-3.88	3.93	3.95	327	2.96-4.48
y	B	**4.13±0.39**	**4.22±0.15**	3.89-4.37	4.38	4.09	4.19	3.35-4.91
y	C	**3.35±0.38**	**3.25±0.25**	3.21-3.49	3.05	3.53	3.18	2.59-4.10
z	A	**1.32±0.16**	**1.27±0.13**	-	1.12	1.31	1.38	-
z	B	**1.32±0.16**	**1.27±0.11**	-	1.39	1.25	1.17	-
z	C	**1.32±0.16**	**1.07±0.11**	-	0.97	1.06	1.18	-

Table 4.19 Verification results for the compressive modulus models (CI95%-confidence interval in which the average response is expected, PI95%-prediction interval that contains the true value of individual measurements in 95% of the cases)

The results of the verification study for the models predicting the compressive strength is presented in Table 4.20.

dir	code	predicted E [MPa]	measured E [MPa]	CI95% for average	M1 [MPa]	M2 [MPa]	M3 [MPa]	PI95% for individual
x	A	0.465±0.05	0.464±0.07	0.44-0.50	0.54	0.39	0.46	0.35-0.58
x	B	0.660±0.06	0.600±0.06	0.54-0.78	0.67	0.59	0.54	0.61-0.71
x	C	0.215±0.05	0.223±0.03	0.19-0.25	0.252	0.19	0.23	0.1-0.33
y	A	1.18±0.10	1.19±0.05	0.98-1.38	1.23	1.14	1.21	0.14-1.22
y	B	1.36±0.10	1.39±0.08	1.29-1.42	1.31	1.47	1.4	1.15-1.56
y	C	0.86±0.10	0.84±0.05	0.83-0.90	0.88	0.85	0.79	0.66-1.06
z	A	2.66±0.044	0.253±0.03	0.24-0.29	0.29	0.24	0.23	0.17-0.36
z	B	0.397±0.04	0.390±0.02	0.36-0.44	0.38	0.38	0.41	0.30-0.49
z	C	0.149±0.04	0.143±0.04	0.13-0.17	0.10	0.16	0.17	0.06-0.24

Table 4.20 Verification results for the compressive strength models (CI95%-confidence interval in which the average response is expected, PI95%-prediction interval that contains the true value of individual measurements in 95% of the cases)

The models gave good predictions for the compressive strength, except at point B in the x-direction. The predicted average value was in reasonable agreement with the experimental measurements, and the average was also within the 95% confidence interval. However, two of the individual measurements were out of the predicted range.

This deviation from the model during verification of the model for x-direction in point B, illuminates another important distinction between traditional application of SLS and micro-lattice fabrication. The reason for the problem is that while scan spacing is a parameter that can have continuous values, delivered energy density can only take discrete values (integers), as it is not directly determined by scan spacing but the number of scan lines within the geometry of the sintered features In the present case, the model calculates with 5.45 scan vectors, while in reality the number of scan vectors is only 5, as shown in Figure 4.67.

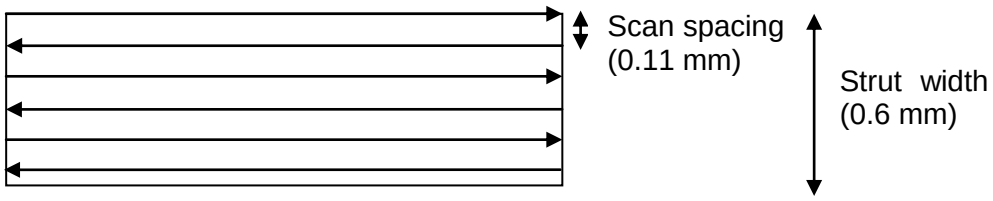

Figure 4.67 Fill scan vectors of struts fabricated in the x-direction

The difference in delivered energy density is negligible when parts and features are on the centimetre scale, however when sintering the designed struts (600 µm) in the x-direction at scan spacing setting of 0.11 there is significant difference in delivered energy density (8%) whether the geometry is sintered with five or six scan vectors.

Therefore, it can be concluded that models developed can predict the compressive strength and modulus values with 90% confidence interval. However, it could be further improved by replacing scan spacing as an input parameter with a discrete parameter that is calculated from scan spacing and the geometry of the sintered feature.

4.4.4 Effect of process parameters on strut dimensions

The image stacks from the micro CT have been analyzed using Matlab Image processing toolbox, according to the procedures described in Section 3.4.3.

Firstly, as shown in Figure 4.68 (a) the outer perimeter of the strut cross-section was determined by morphologically closing the particles that were identified as solid (either ceramic or polymer). From this the apparent cross-sectional area (CSA) has been obtained. Then a second routine was run on the images, that instead of morphologically closing the area opened it using a 1 pixel structuring element, this revealed the actual or effective cross-sectional area of the strut. Porosity can be obtained by subtracting the effective area from the apparent area.

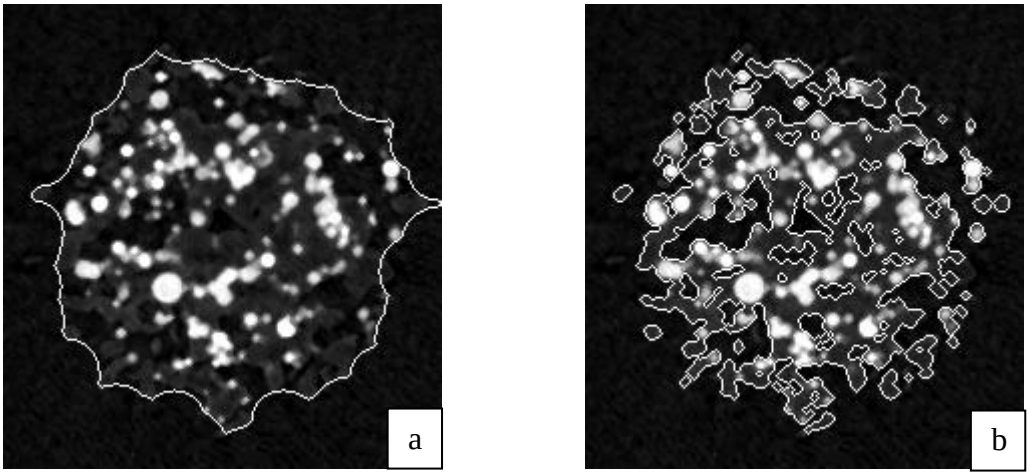

Figure 4.68 Morphological closing (a) and opening (b) of the strut cross section to obtain apparent and effective cross sectional area and to calculate porosity of the strut (data from design point no. 3 in z direction)

As already mentioned in the previous sections, dimensions and cross sectional shape of the struts is strongly directional dependent and it fundamentally contributes to the anisotropic mechanical behaviour demonstrated. For a strut that was fabricated in the centre point of the design space (0.15 mm scan spacing, 9.5 W laser fill power, 4.5 W outline laser power) average of measured data is presented in Table 4.24. Designed cross sectional area of the struts is 0.36 mm^2.

	Apparent CSA [mm^2]	Effective CSA [mm^2]	Porosity [%]
x-struts	0.375±0.039	0.297±0.033	20.8
y-struts	0.566±0.066	0.458±0.034	19.1
z-struts	0.400±0.022	0.318±0.022	20.5

Table 4.21 Average apparent and effective cross sectional areas, and porosity of the struts built in the different directions

The differences between orientations are not only in the values but also in the shape of the cross sectional area, as shown in Figure 4.69. The figure illustrates the deformations induced by two scanning patterns and shrinkage.

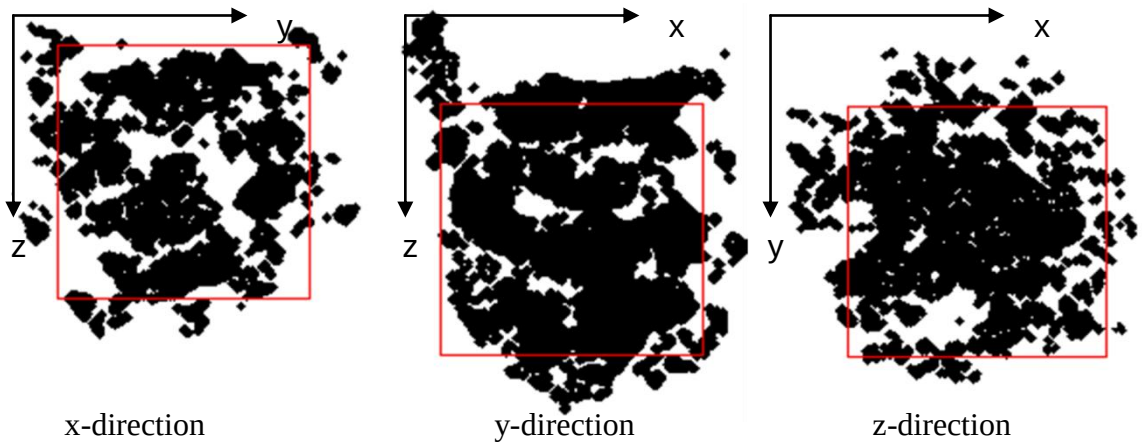

Figure 4.69 Formation of cross sectional shape in the three main building directions

The designed square cross section has been replicated as a semi-oval shape in the x- and y-struts, and as a circular cross section in the z-struts. Heat conduction in the powder bed and laser intensity change along its radius can account for the formation of the semi-oval cross section of the x- and y-struts. Once a layer is sintered, its top surface is plane but the bottom surface curves due to the excess powder sintering around the intentionally sintered areas, thus distorting the designed geometry. Additionally, at the size-scale examined the effect is more pronounced. The laser has a Gaussian intensity distribution along its diameter that also results in a strongly curved bottom surface since the scan length is less than two-times the laser diameter. Furthermore, the top surface of the struts cross section becomes concave due to shrinkage, although this distortion is less observable than the one in the bottom. The cross sectional distortion from the designed square shape in the z-struts can be explained by the outline scan that due to diameter of the laser cannot follow sharp edges.

As in the case of compressive strength, preliminary statistical analysis confirmed that in the different directions, apparent and effective cross sectional area is affected by different parameters; therefore the obtained dataset was analyzed and fitted separately in three main directions. As the procedure of statistical validation has been detailed in the preceding chapter, and dimensional responses are sensitive to the same process parameters as the mechanical properties, data analysis, and model development are not introduced in detail. Only simplified ANOVA tables, and the adequacy measures used to justify the model are displayed throughout this section. The models developed are introduced for each direction and are discussed in relation to mechanical properties.

Models for X-struts

The average of apparent and effective CSAs obtained in the 15 design points of the CCD are shown in Figure 4.70. For comparison the average compressive moduli attained for the same design points are also provided. It can be seen from the graph that both apparent and effective CSA follow similar tendencies as the compressive modulus, suggesting that the dimensional responses investigated have similar dependencies on process parameters. A simplified ANOVA table for the parameters found to be significant in determining the apparent and effective CSA is presented in Table 4.22. Adequacy indicators of the proposed models are listed in Table 4.23.

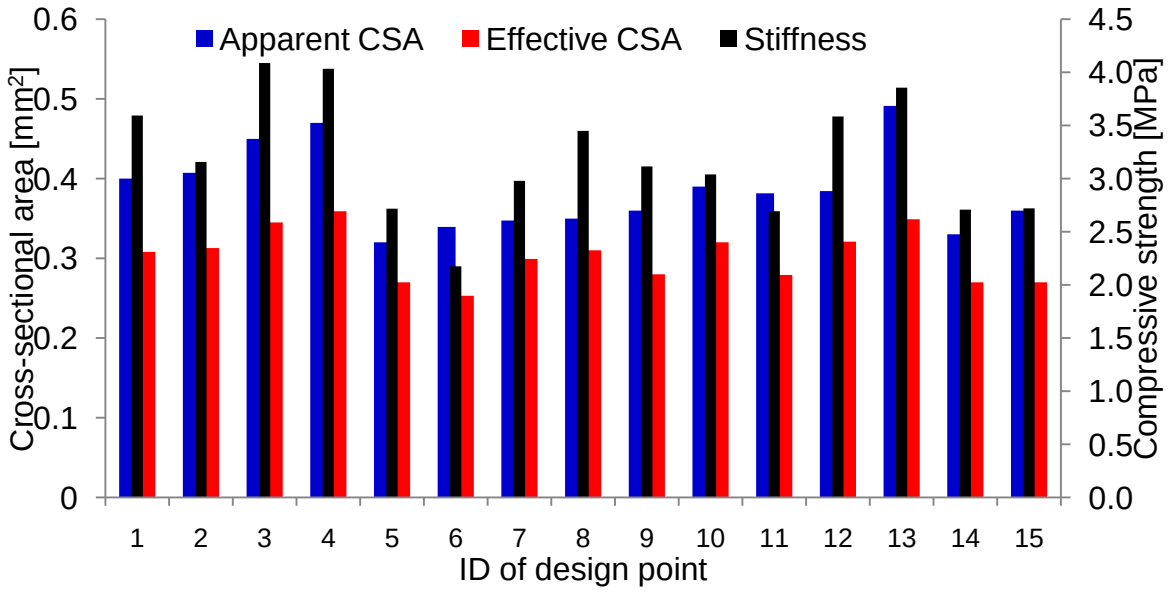

Figure 4.70 Averages of obtained apparent and effective cross sectional areas of x-struts, and their comparison to stiffness of the lattices at different points of the design space

	df	Apparent CSA		Effective CSA	
		F-value	p-value	F-value	p-value
Model	3	33.51	< 0.0001	23.5	< 0.0001
Outline power [OP]	1	5.09	0.0406	35.5	< 0.0001
Scan Spacing [SS]	1	86.13	< 0.0001	65.6	< 0.0001
$[SS]^2$	1	9.3	0.0087	22.9	0.0006
Residual	14				
Lack of fit	11	0.83	0.6460	0.85	0.6219
Pure Error	3				

Table 4.22 Results of ANOVA for the parameters that were found significant in affecting apparent and effective cross sectional area (CSA) of the x-struts

Adequacy measure	Apparent CSA	Effective CSA
R^2	0.88	0.75
Adjusted R^2	0.85	0.70
Predicted R^2	0.81	0.61
Signal/Noise ratio	19	12

Table 4.23 Adequacy measures of the proposed model for apparent and effective cross sectional area (CSA) of the x-struts

Based on the above adequacy measures the models were accepted. The reduced quadratic models had the following forms:

$$CSA_{apparent} = \mathbf{1.13} - \mathbf{0.07}X_2 - \mathbf{9.04}X_3 + \mathbf{24.70}X_3^2 \quad \text{Eq. 4.8}$$

$$CSA_{effective} = \mathbf{0.74} - \mathbf{0.012}X_2 - \mathbf{5.94}X_3 + \mathbf{27.18}X_3^2 \quad \text{Eq. 4.9}$$

where, X_2 is the outline laser power, and X_3 is the scan spacing.

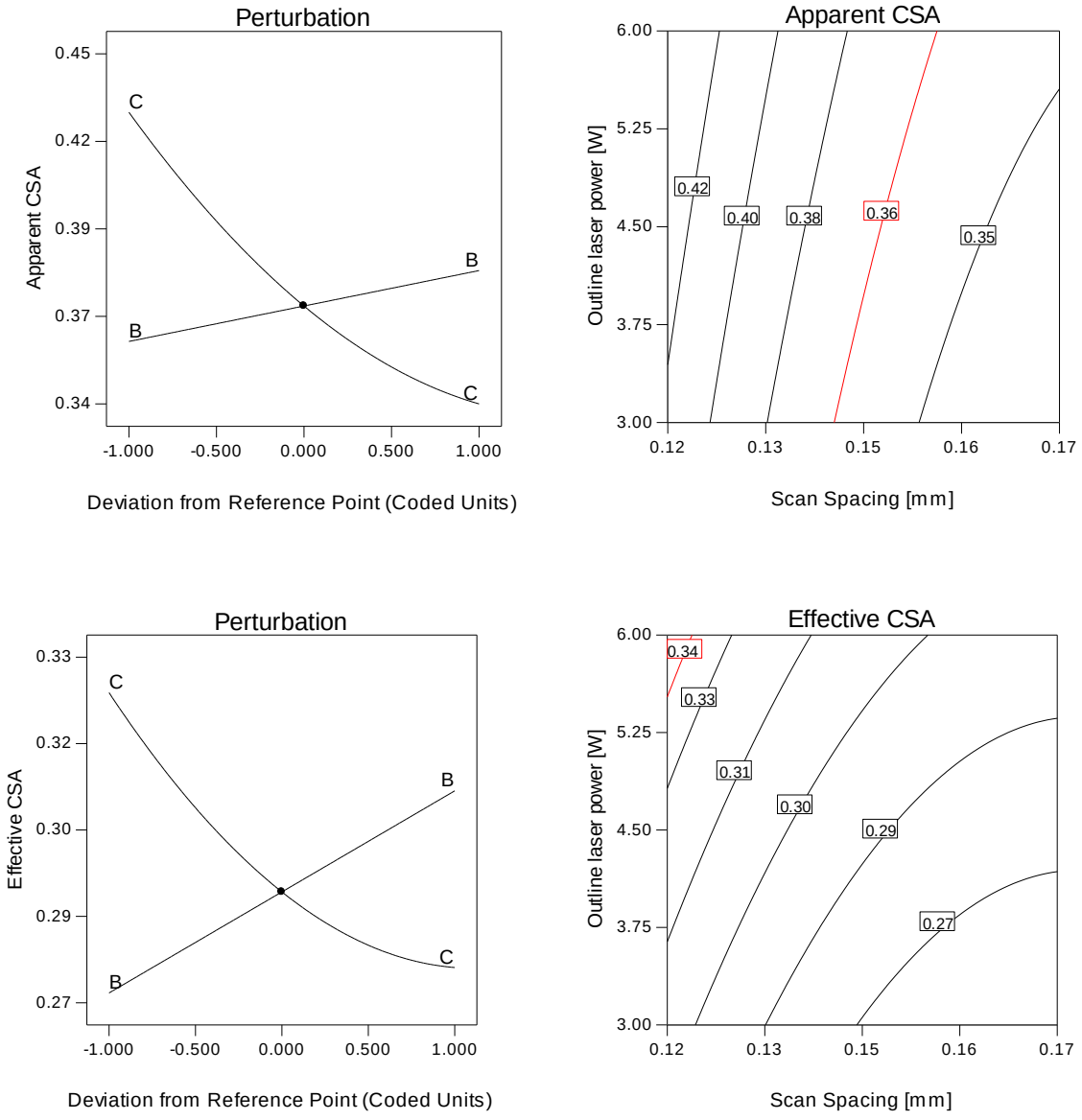

Figure 4.71 Results of perturbation test and contour plot for the changes in apparent and effective CSA with respect to the most influential parameters in the x-direction (B-outline laser power, C-scan spacing)

Perturbation and contour plots for both the apparent and effective CSA is presented in Figure 4.71. The parameter effects show very similar tendencies to the ones detected for compressive modulus in this direction.

That is not surprising as stiffness is directly related to relative density that is determined by the effective cross sectional area of load bearing struts. In Figure 4.72 effective CSA is plotted against the average compressive modulus of the relevant design points. The data points can be reasonably well fitted (R^2=0.86) a power low expression where the power constant is 1.6.

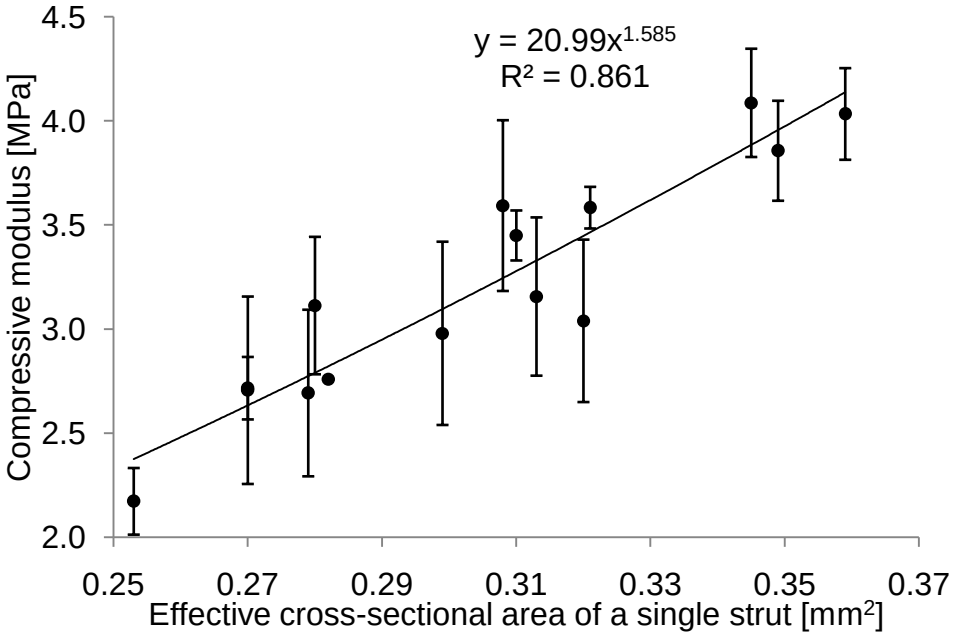

Figure 4.72 Relationship between effective cross sectional area of x-struts and compressive modulus along the x-direction

The power constant for cellular solids normally changes between 1 and 2, 1 representing a stretch- while 2 representing a bending-dominated response to compression loading. The obtained value of 1.6 indicates that compression of x-struts results in a behaviour that is the combination of the two with bending being slightly more dominant.

Models for Y-struts

The averages of obtained apparent and effective CSAs in the 15 design points of the CCD are shown in Figure 4.73. For comparison the compressive moduli for the same design points are also provided. It can be seen from the graph that both the apparent and effective CSA follow similar tendencies of compressive modulus, suggesting that the dimensional responses have similar dependencies on process parameters.

A simplified ANOVA table for the parameters found to be significant in determining the apparent and effective CSA is presented in Table 4.24. Adequacy indicators of the proposed models are listed Table 4.25.

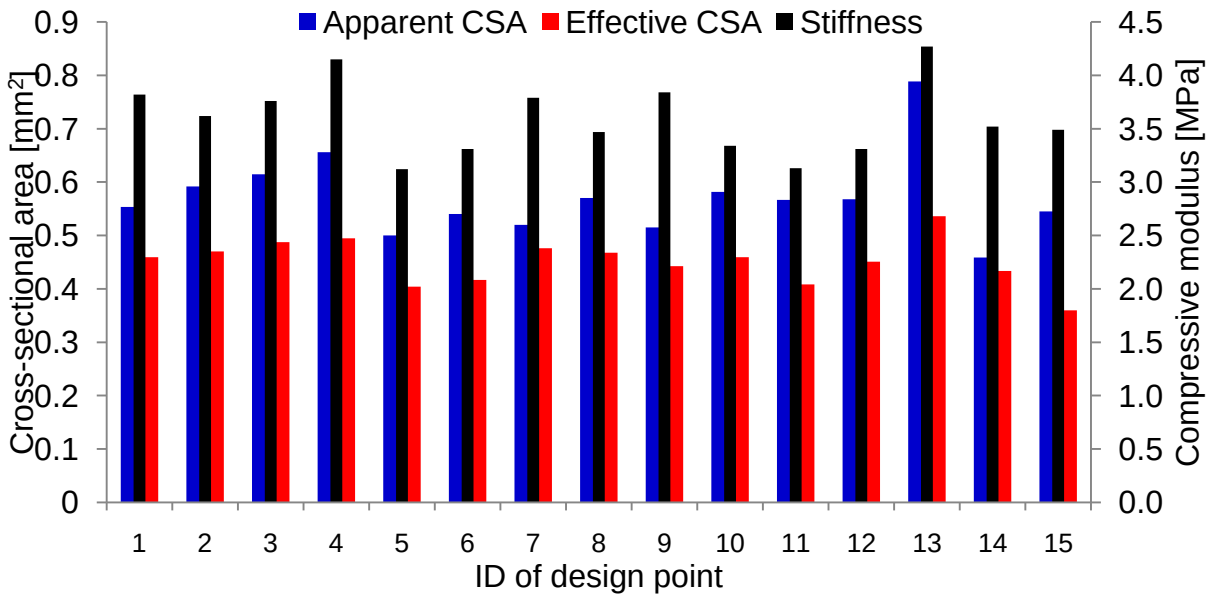

Figure 4.73 Average of obtained apparent and effective cross sectional areas of y-struts, and their comparison to stiffness of the lattices at different points of the design space

Source	df	Apparent CSA		Effective CSA	
		F-value	p-value	F-value	p-value
Model	3	28.69	< 0.0001	27.52	< 0.0001
Fill power [FP]	1/0	15.49	0.0015	-	-
Outline power [OP]	1	6.18	0.0202	22.77	0.0003
Scan Spacing [SS]	1	64.4	< 0.0001	37.76	< 0.0001
$[SS]^2$	0/1	-	-	22.03	0.0003
Residual	14				
Lack of fit	11	1.47	0.4169	2.03	0.3060
Pure error	3				

Table 4.24 Results of ANOVA for the parameters that were found significant in effecting apparent and effective cross sectional area (CSA) of the struts in the x-direction

Adequacy measure	Apparent CSA	Effective CSA
R^2	0.86	0.93
Adjusted R^2	0.83	0.89
Predicted R^2	0.76	0.78
Signal/Noise ratio	16.6	18.3

Table 4.25 Adequacy measures of the proposed model for apparent and effective cross sectional area (CSA) of the x-struts

Based on the above adequacy measures the models were accepted. The reduced quadratic models had the following forms:

$$CSA_{apparent} = \mathbf{0.64} + \mathbf{0.014}X_1 + \mathbf{8.69}X_3 - \mathbf{1.68}X_3 \quad \text{Eq. 4.10}$$

$$CSA_{effective} = \mathbf{1.12} + \mathbf{0.012}X_2 - \mathbf{9.21}X_3 + \mathbf{28.54}X_3^2 \quad \text{Eq. 4.11}$$

where, X_1 is the laser fill power, X_2 is the outline laser power, and X_3 is the scan spacing.

Perturbation and contour plots for both apparent and effective CSA are presented in Figure 4.71. The parameter effects show very similar tendencies to the ones detected for compressive modulus in this direction, especially the effective CSA. The best fit for the apparent CSA response was a linear model, and this model also identified laser fill power as a significant factor. However, for effective CSA - that determines relative density and therefore directly related to compressive modulus - the same parameter contributions were detected as for the compressive modulus response. The similarity between the two is also a confirmation that that the parameters identified and the model are correct. The contour plots show that within the factorial values of significant process parameters the apparent CSA is considerably above the designed 0.36 mm^2. Effective CSA is smaller, due to porosity present within the struts, however it is still greater that the designed value.

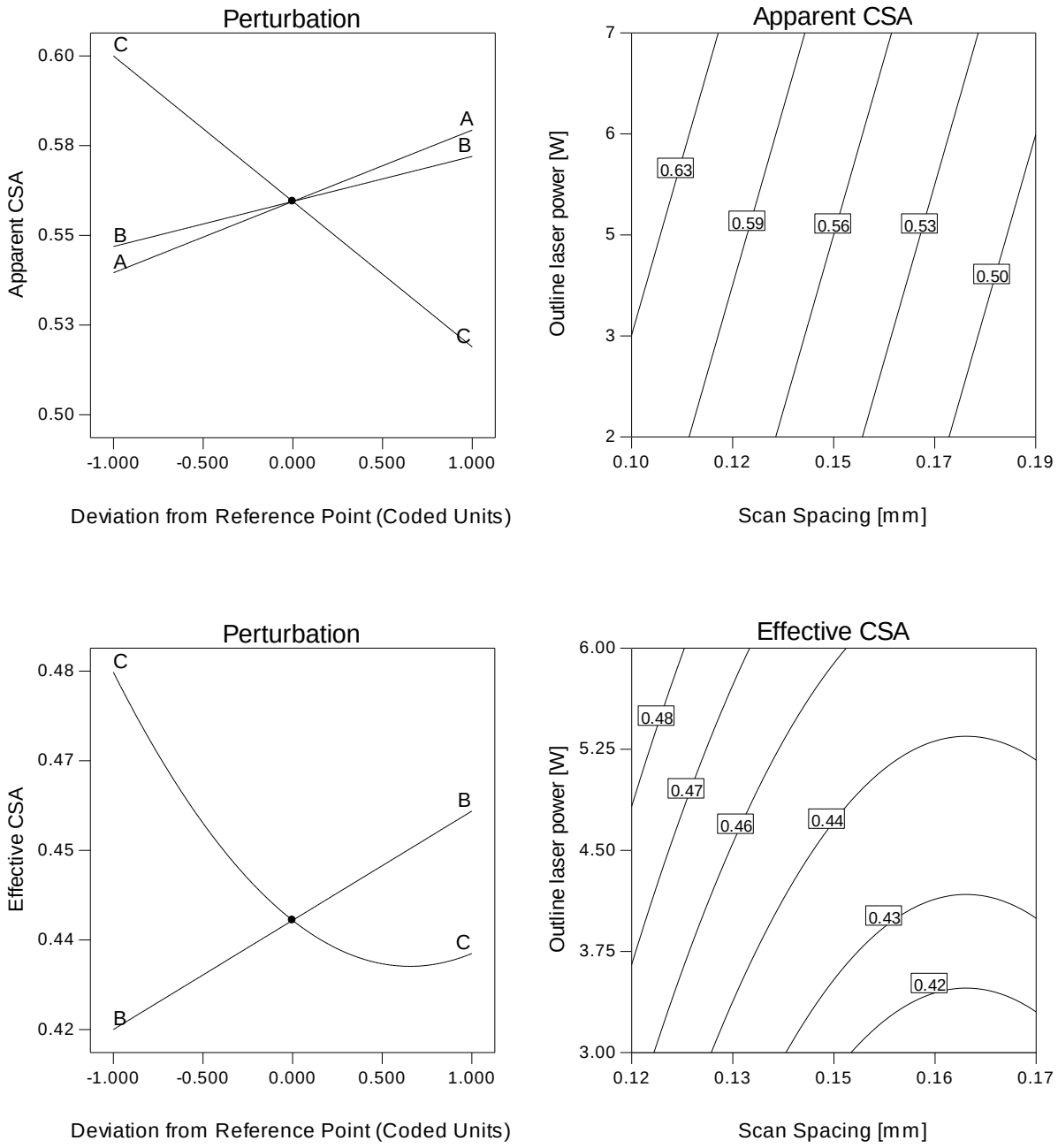

Figure 4.74 Results of perturbation test and contour plot for the changes in apparent and effective CSA with respect to the most influential parameters in y-direction (B-outline laser power, C-scan spacing)

In Figure 4.75 effective CSA is plotted against the average compressive modulus of the relevant design points. The data points can be reasonably well fitted (R^2=0.72) with a power low expression where the power constant is 1.1. It has been seen in the previous section that the lattices had a significantly higher modulus along the y-direction, than along the x-direction. The significantly lower power constant for the effective CSA – compressive modulus relationship indicates y-struts exhibit a stretch dominated behaviour during compression testing at small strains.

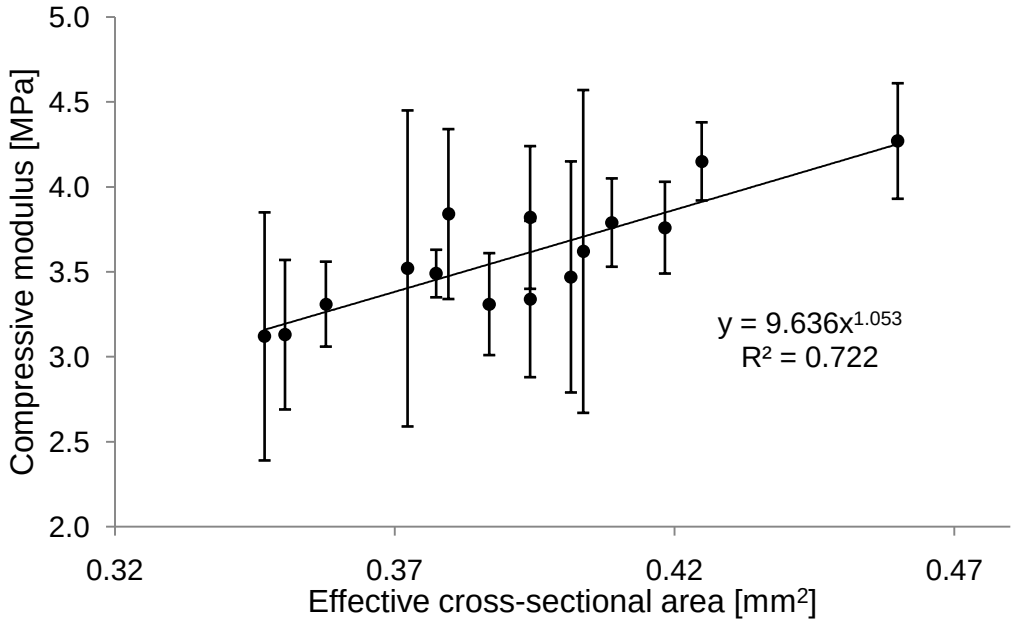

Figure 4.75 Relationship between effective cross sectional area of y-struts and compressive modulus along the y-direction

As seen in Table 4.21 there is only 1.7% difference between average porosity of x- and y- struts that would not explain the significant increase in mechanical properties by itself. As it was shown in Figure 4.69 the cross sectional shape of x- and y-struts is slightly different. In the x-struts porosity is present throughout the cross sectional area, while in case of y-struts, porosity is significantly higher in the outer areas, as individual particles stuck to the sintered strut due to heat conduction of the powder bed.

Models for Z-struts

The averages of apparent and effective CSAs in the 15 design points of the CCD are shown in Figure 4.76. The effective CSA changed similarly to compressive modulus throughout the design space, however deviations from these tendencies were seen for the apparent CSA. The compressive modulus response of the lattices along the z-direction could not be fitted with an adequate model (at $p<0.05$), nor could the observed effective or apparent density response. ANOVA indicated that for both apparent and effective CSA the average is a better predictor than any of the models investigated.

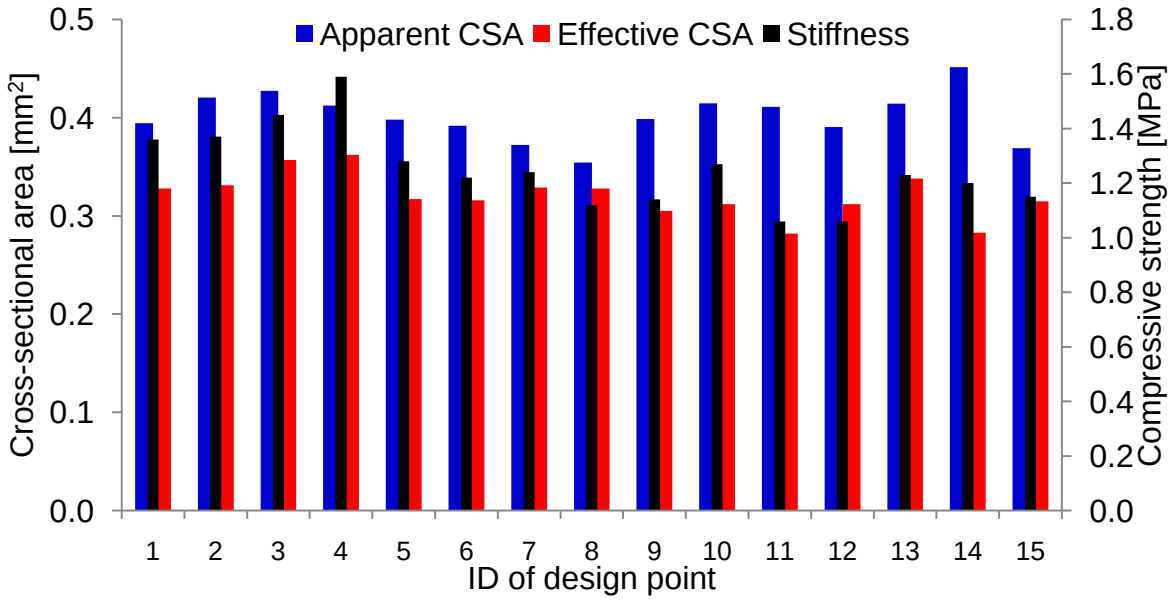

Figure 4.76 Average of apparent and effective cross sectional areas obtained for z-struts, and their comparison to stiffness of the lattices at different points of the design space

When relating compressive modulus to effective cross sectional area, the fit was significantly weaker (R^2=0.56) than for the x- or y-struts. The power constant was 1.21 that indicates stretch domination during compression that is surprising as lattices in this direction were significantly weaker than in the x-direction where the failure mechanism is more shifted to bending.

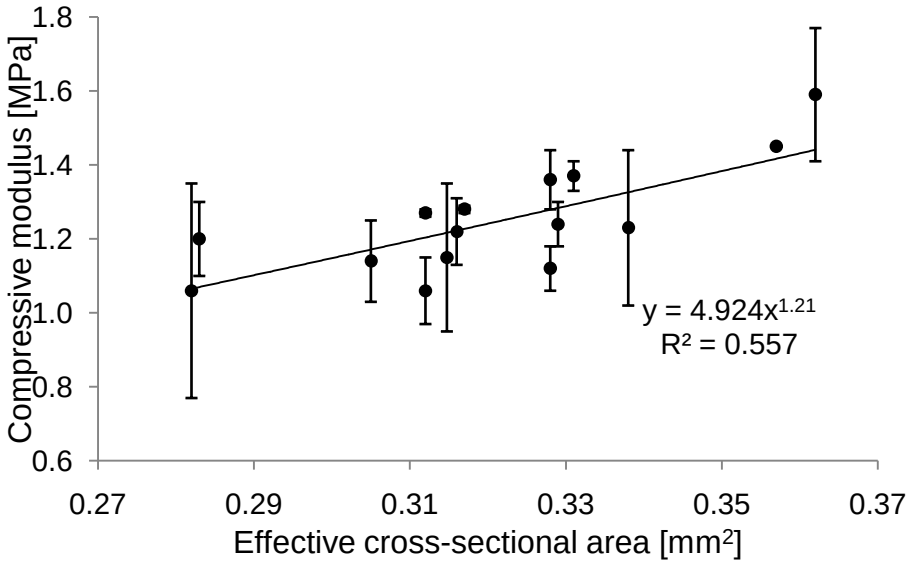

Figure 4.77 Relationship between effective cross sectional area of z-struts and compressive modulus along the z-direction

The problem with struts in this direction is illustrated in Figure 4.78.

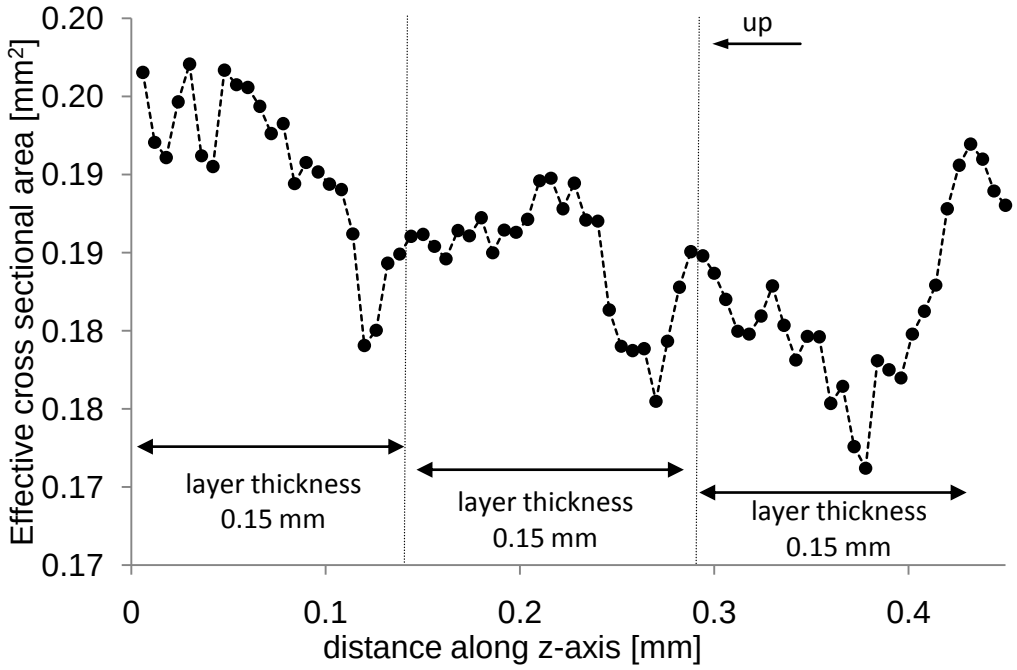

Figure 4.78 Change of effective cross sectional area of z-struts along the z-axis at design point no. 14

The graph shows that there is a significant decrease in effective cross sectional area of the struts towards the bottom of each layer indicating that the penetration depth of laser is smaller than the set layer thickness. Although, delamination of fabricated samples was not observed, the graph suggests that a smaller layer thickness would be more adequate for the material used. Furthermore, as the part is built (upwards) there is an overall increase in dimensions that is due to heat building up in the powder bed as the build progresses. All these effects caused significant variations in the data and therefore tendencies of SLS parameter dependence were hard to identify at the set significance level.

The compressive strength of lattices was not related to the obtained dimensional responses as strength of the lattice along a selected direction depends on the strength of all three struts. For instance, when the lattice is loaded along the y-direction, y-struts buckle, while the other two struts are loaded in tension, and the yield point marks failure of connecting struts.

In Section 4.3.2.2, when the effect of HA addition was investigated on mechanical properties it was seen that incorporation of HA increases compressive modulus in the x- and y-direction, but not in the z-direction. The reason for this is likely to be the inadequate layer thickness and the significant differences in CSA close to the bottom and close to the top of the sintered layer, as illustrated in Figure 4.79.

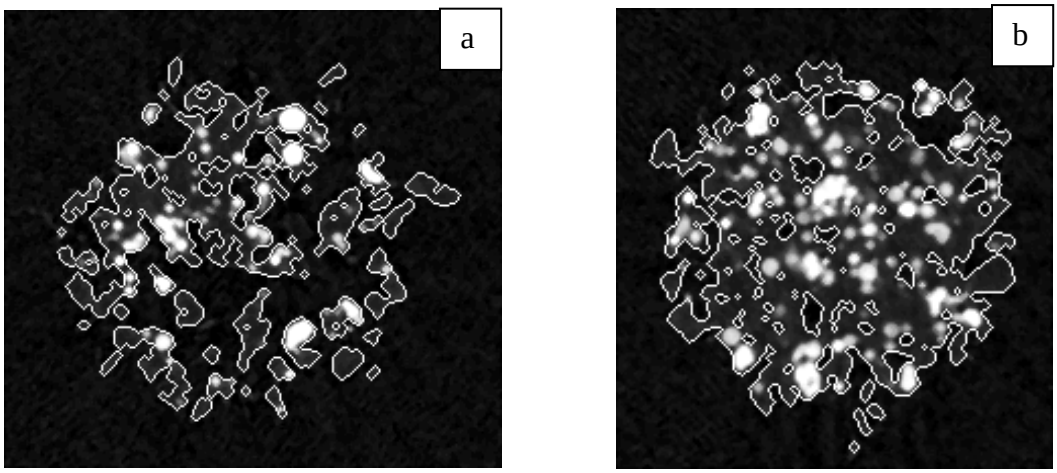

Figure 4.79 Effective cross sectional area of z-struts (a) close to the bottom and (b) close to the top of a sintered layer (at design point no. 14)

The figure shows that close to the top of the sintered layer incorporation of HA into the polymer matrix is good, while close to the bottom where there is limited necking between PCL particles, HA particles are mostly just stuck to the PCL and therefore has no reinforcing effect.

4.4.5 Multiple scanning of a layer

The influence of multiple scanning on mechanical properties and part dimensions is not explored in literature. In this experiment the effect of applying multiple scans to a single layer was examined at five levels while keeping total delivered energy constant. To achieve this, parallel to increasing scan count the laser power used was reduced. In all cases a total of 6 W power was delivered to each layer (1 × 6 W ... 5 × 1.2 W). Both compression and tensile testing specimens were fabricated to evaluate the effect of using multiple scan counts in the weakest direction.

In previous cases laser fill power up to 12 W was used, however in this experiment its value was kept low to enable examination of several scan counts. The lattices were subjected to compression along the z-direction as for the powder used (at layer thickness of 0.15 mm) this direction was the weakest.

The results of compression testing are presented in Figure 4.80.

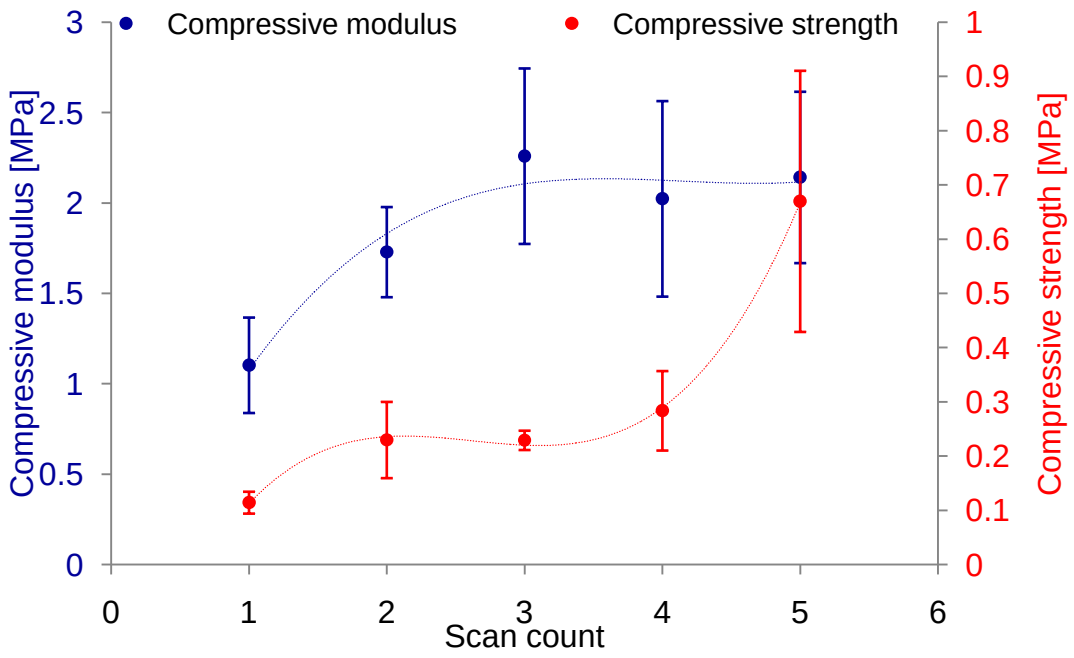

Figure 4.80 Compressive modulus and strength as a function of scan count at constant delivered energy density

Increasing scan count from 1 to 3 resulted in a two fold increase in compressive modulus. However, further increasing scan count had no statistically significant effect on stiffness of the samples. Compressive strength on the other hand, showed a slighter improvement (still two-fold) when increasing scan count from 1 to 3, and the increase became even more noticeable (six-fold) when the energy was delivered in 5 scans. Compressive modulus increased from 1.10±0.26 MPa to 2.14±0.47 MPa, and compressive strength increased from 0.11±0.02 MPa to 0.67±0.24 MPa by delivering the same energy density in 5 scans instead of 1.

2D lattices were fabricated for tensile testing. As the reduced part chamber did not enable fabrication of such long specimen along the z-direction, lattices were fabricated along the x-axis that was the second weakest. Results of the tensile testing are presented in Figure 4.81.

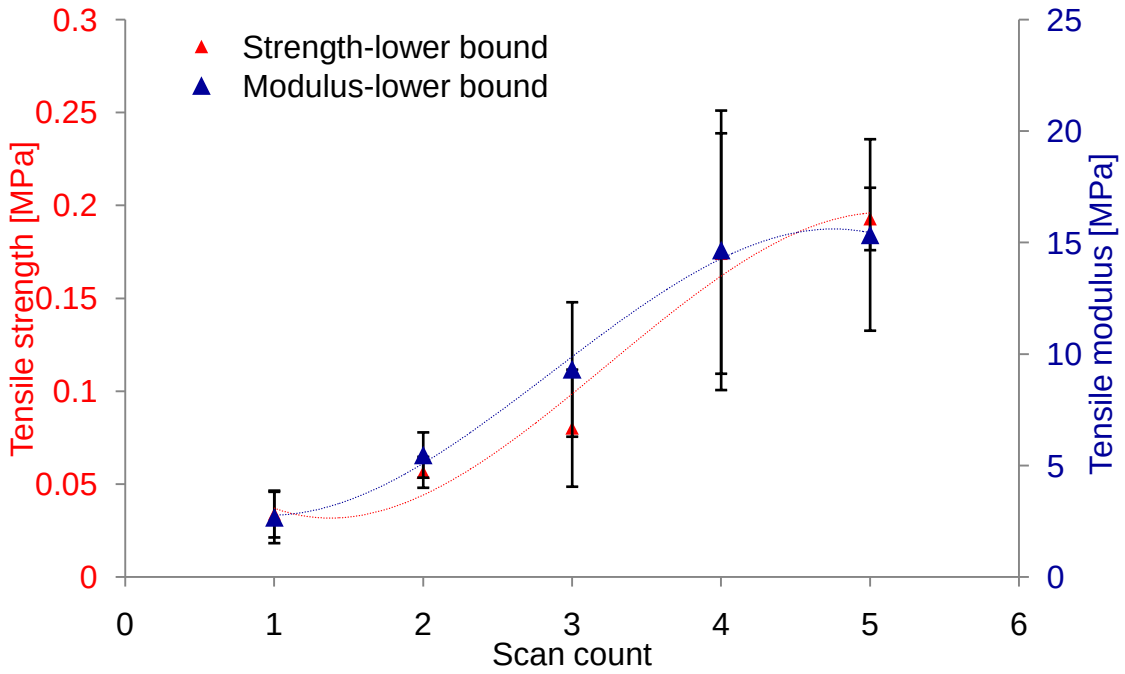

Figure 4.81 Tensile modulus and strength as a function of scan count at constant delivered energy density

The increase in scan count from 1 to 5, resulted in a four-fold increase in both tensile strength and stiffness. Overall, tensile modulus increased from 2.68±1.15 MPa to 15.35±4.29 MPa, and compressive strength from 0.03±0.01 MPa to 0.19±0.02 MPa. There were great deviations in obtained data, especially at high scan count numbers. The reason for this is heat building up within the powder bed as the build progresses. The replicate of the same treatment group (for tensile testing) were placed on top of each other, and this positioning introduced a block effect into the experiment. Within the same treatment group, the lowest value was obtained for the first sintered sample and the highest for the last.

Delivering a given amount of energy density to the parts in several scans did not only improved mechanical properties but also significantly increased dimensions of the features. The effect of multiple scanning on feature dimensions is illustrated in Figure 4.82 and in Figure 4.83.

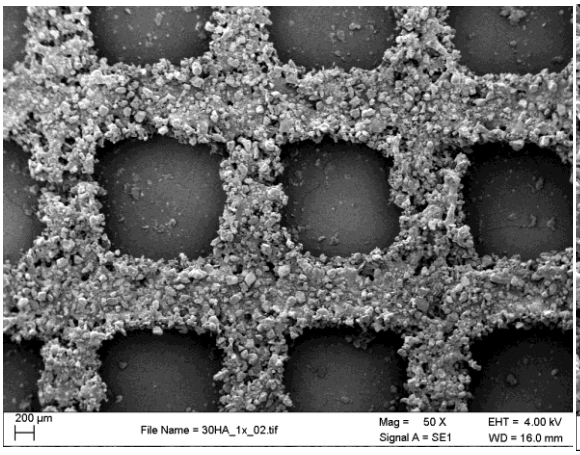

1×6W

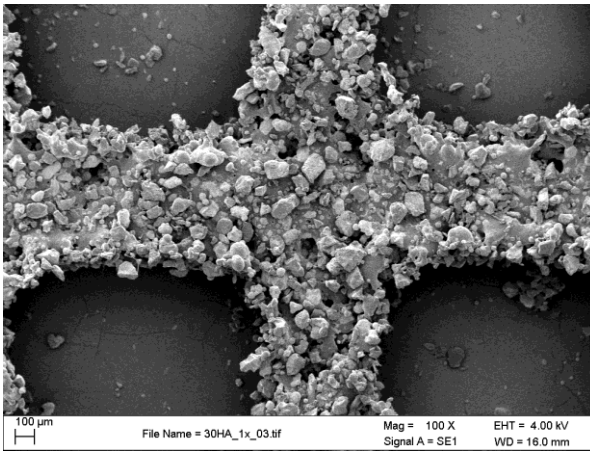

1×6W

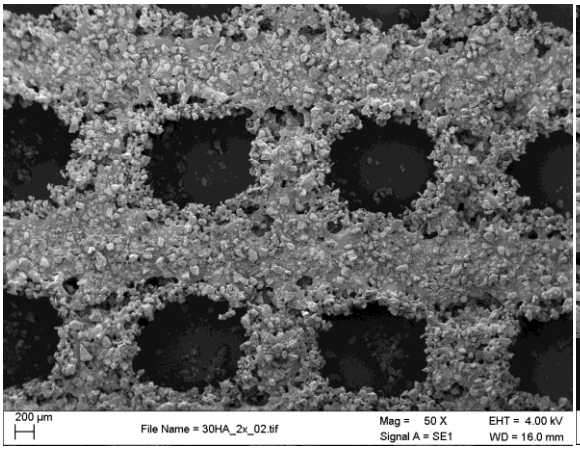

2×3W

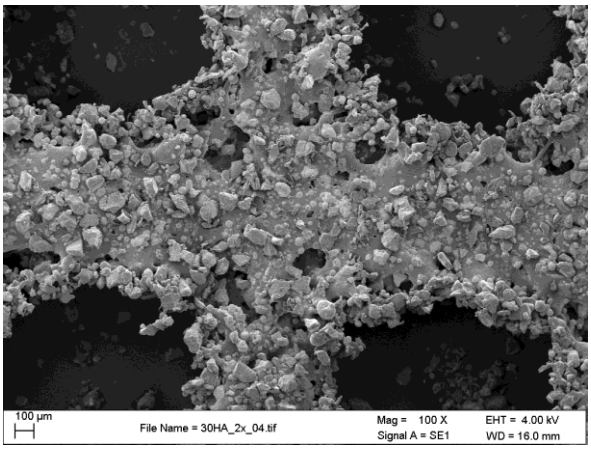

2×3W

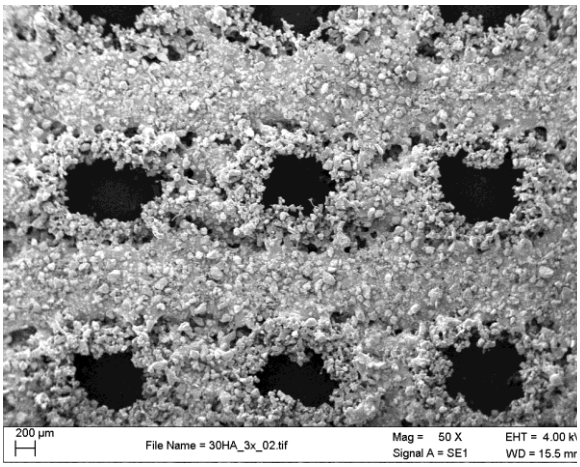

3×2W

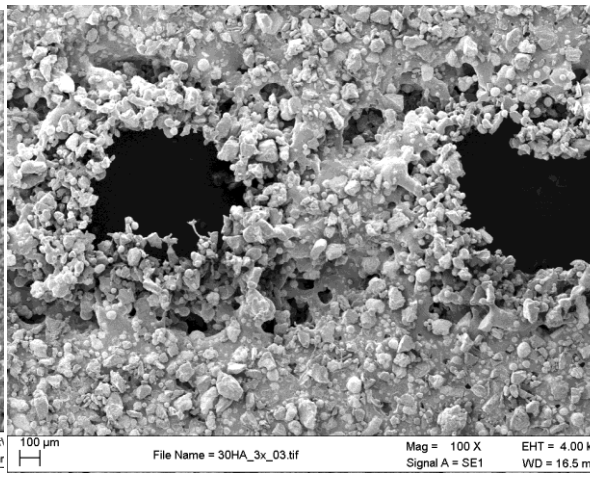

3×2W

Figure 4.82 Effect of multiple scanning on dimensions of the struts (Part 1)

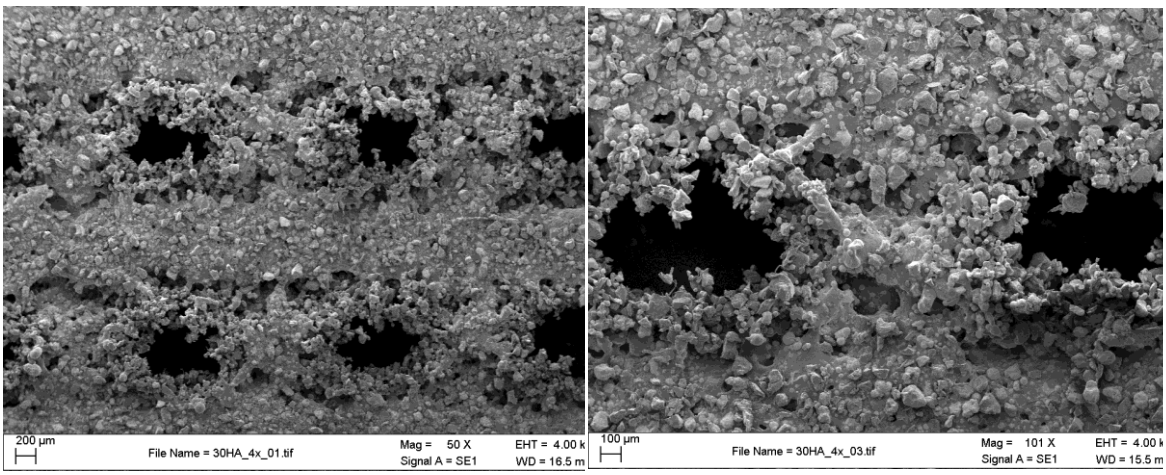

4×1.5W 4×1.5W

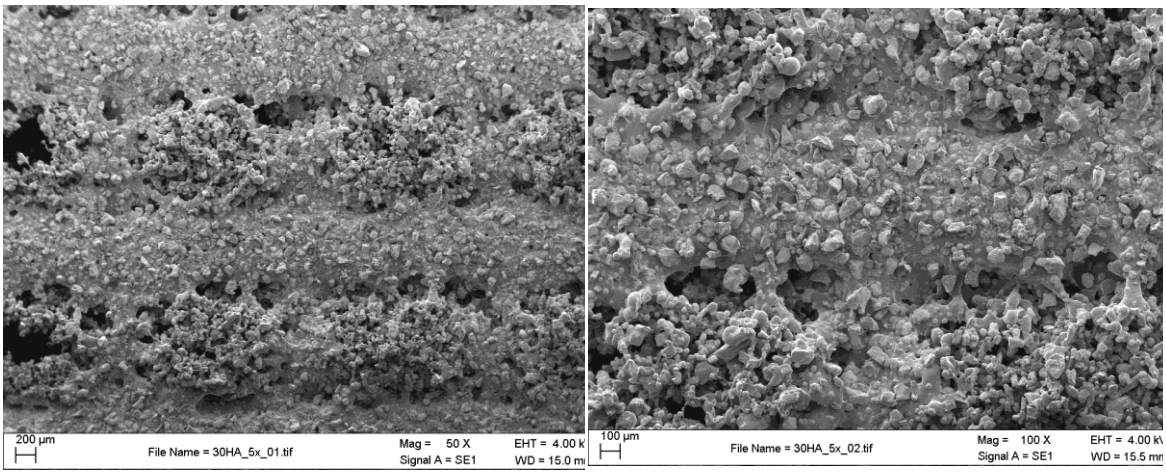

5×1.2W 5×1.2W

Figure 4.83 Effect of multiple scanning on dimensions of the struts (Part2)

Feature shapes and sizes are relatively well reproduced when applying up to two scans to a single layer, above this scan count number too much excess powder sticks to the sintered features. When scan count was 5, the amount of excess powder stuck to the struts was so high that the designed pores were reproduced as a weakly interconnected network of particles. In the resulting structure the designed solid regions are reproduced as solid with minimal porosity (1-3%), and the designed pores are reproduced as a cellular solid with high porosity. The sintered excess powder is weak and can fall apart easily; however the compressed air (6 Bars) used to depowder the samples was not enough to demolish the structure. The pore sizes in the filled in pores ranged from 20 – 200 µm. Despite its low dimensional accuracy the structures produced at high scan count numbers could be used for tissue engineering, as the reproduced solid regions ensure good initial mechanical properties of the solid structures, while the reproduced highly porous region can serve as a substrate to which cells can be seeded.

To test the upper bound of mechanical properties for the PCL/30HA composition that is achievable with the SLS system used, a new set of 2D lattices were fabricated for tensile testing. This time, the effect of heat building up along the z-direction was also investigated. Specimens were fabricated along the y-direction (which is the strongest), and to allow the heat to build up within the part-bed 2D lattices were placed closer to each other. In the previous case there were three layers between subsequent specimens while in the current case it was reduced to one. The results of the experiments with respect to scan count are shown in Figure 4.84.

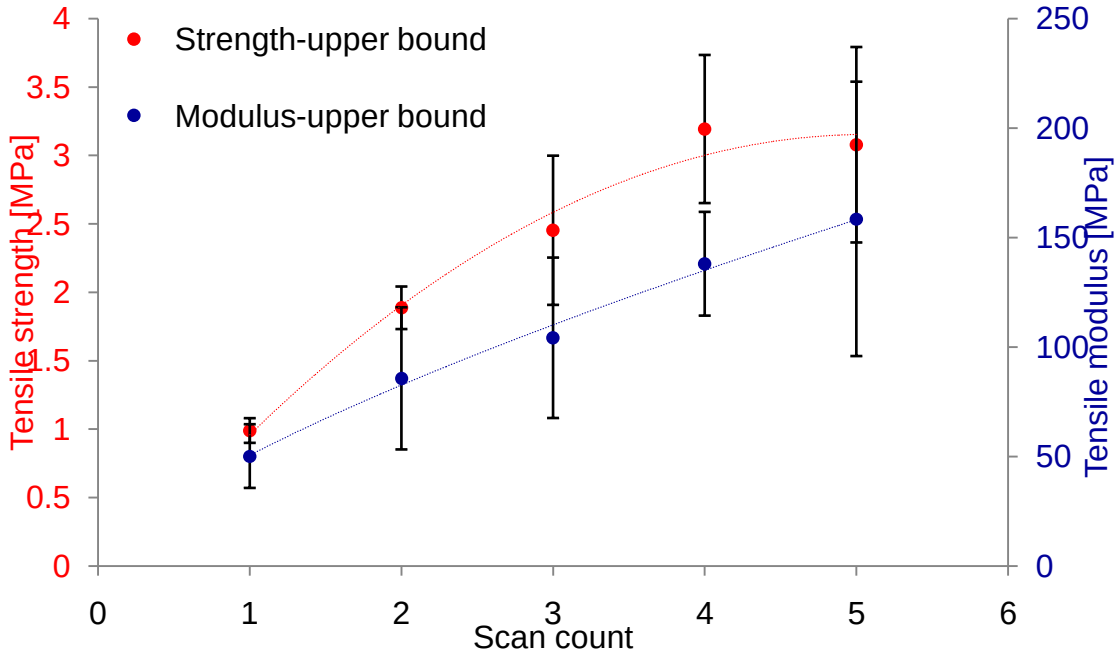

Figure 4.84 Tensile modulus and strength as a function of scan count at constant delivered energy density

Both tensile properties examined demonstrated significant improvements with the increase of scan count from 1 to 5, tensile modulus increased from 50±14 MPa to 159±63MPa, and tensile strength from 1.0±0.1 MPa to 3.1±0.7 MPa. The significant standard deviations in the data are due to positioning of the samples, as the higher the position of the sample within the powder bed, the more heat builds up and the better the mechanical properties. The highest mechanical properties (E=160 MPa, σ=3MPa) achieved by varying these two parameters, are within the range reported for human cancellous bone [12, 144].

To evaluate the effects of scan count and bed position simultaneously, ANOVA was carried out on the data set, results for tensile modulus are presented in Table 4.26, and for tensile strength in Table 4.27.

Source	Sum of squares	Degrees of freedom	Mean square	F-Value	Prob > F (p-value)
Model	17.34	8	2.17	24.30	< 0.0001
Scan count	14.20	4	3.55	39.80	< 0.0001
Position	2.27	4	0.57	6.36	0.0046
Residual	1.16	13	0.09		

Table 4.26 ANOVA table for tensile strength

Source	Sum of squares	Degrees of freedom	Mean square	F-Value	Prob > F (p-value)
Model	49795	8	6224	14.89	< 0.0001
Scan count	33328	4	8332	19.93	< 0.0001
Position	17118	4	4279	10.24	0.0006
Residual	5435	13	418		

Table 4.27 ANOVA table for tensile modulus

The analysis showed that both changes in scan count and in positioning have a statistically significant effect on tensile properties, however the effect of positioning, especially with respect to compressive strength is less important than the effect of scan count.

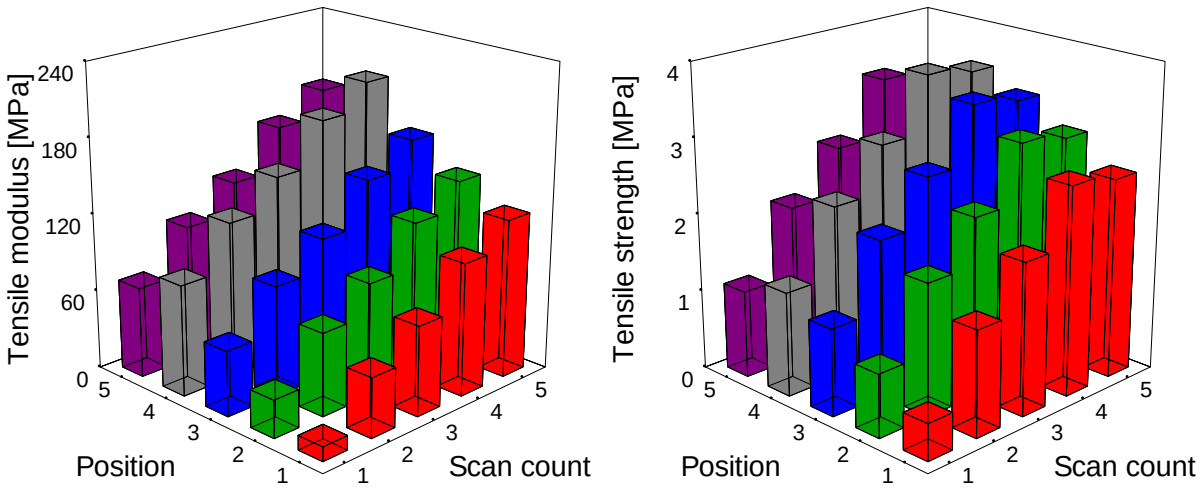

Figure 4.85 3D plot for changes in (a) tensile modulus and (b) tensile strength with respect to scan count and position (1 representing the 1st sintered specimen, 2 the subsequently sintered 2nd specimen on above the 1st, and so on) within the powder bed

The influence of the scan count and position within the powder bed along the z-direction are also illustrated on a 3D plot for both responses in Figure 4.85.The effects

of these two parameters are not documented in literature, therefore these findings represent a new contribution to the current knowledge on SLS process parameters.

4.4.6 Summary and conclusions

Mechanical properties

Of the build dependent SLS parameters examined, scan spacing was found to be the most dominant in all cases. The CCD that has been carried out revealed the quadratic nature of its influence on compressive properties of the fabricated lattices. The second most important parameter in all cases was outline laser power. In the examined range laser fill power was not found significant.

Mathematical models that describe the relationship between part-dependent SLS parameters and compressive properties have been developed. The models can predict compressive modulus and strength (taking anisotropy of fabricated samples into account) with 90% confidence interval. Although, constants of the models are valid for the examined powder blends (PCL/30HA with average polymer particle size of 56 μm), the trends described by the equations can be applied for micro-lattices (with similar feature sizes) fabricated from other materials.

Feature dimensions

Models that describe the dependence of apparent and effective CSA struts built in x- and y-directions to SLS process parameters have been developed. The statistical analysis confirmed the significance of the same parameters that were identified for the compressive modulus response.

Relating the obtained dimensional profile of the struts to the corresponding compressive modulus revealed that load response of x-struts is more bending dominated while that of y-struts is more stretch dominated.

The μ-CT data also showed that the selected layer thickness was not appropriate for the material, as the laser could only partially penetrate through the layer resulting in great variation in the data and deterioration of mechanical properties, particularly in z-direction

Multiple scanning and upper bound of achievable mechanical properties

The influence of multiple scanning on mechanical properties has not been examined to date. This study demonstrated that mechanical properties can be significantly improved at constant energy density levels by applying multiple scanning. The experiments showed that multiple scanning is more important than the previously studied SLS parameters, proving the hypothesis that strong significance of scan spacing and outline laser power can be contributed to multiple scanning of the layers.

When fabricating tensile specimens on top of each other a strong block effect was observed induced by heat building up within the powder bed. This effect can be used to further increase mechanical properties. The highest tensile properties achieved by applying multiple scanning and positioning samples at the top of the build was E=160 MPa, and σ=3 MPa.

5 CONCLUSIONS

The objective of this final chapter is to clarify the findings reported in the previous chapters and to explicitly relate them to the research questions that motivated this study.

1.) **What are the capabilities and limitations of current SLS technology when shifting its function from rapid prototyping to direct manufacturing of 3D biodegradable scaffolds with micron-scale features?**

SLS is a technology designed to create prototypes, therefore its capabilities and limitations needed to be explored in detail as the objective of this research was to create functional parts for a specific application where high requirements apply.

This research showed that features as small as 600 µm that is 1.5 times the nominal focused beam diameter can be successfully created. 600 µm is within the range required for tissue engineering applications, however reduction in focused laser beam diameter could improve accuracy significantly and reduce the smallest attainable feature size.

The main issues experienced during fabrication were dimensional and mechanical anisotropy of the reproduced geometries, and porosity within the designed solid regions. Both are known to be inherent to the technology. However, in the context of creating 3D micro-lattices, these phenomenons were significantly more pronounced than has been demonstrated in literature. The shape and size of the strut cross sections designed were reproduced poorly and differently in every direction. By using smaller particle sizes deviations from the nominal dimensions were considerably reduced, however the shape remained distorted. Serious anisotropy was observed in the mechanical behaviour of the fabricated lattices. Parts were always strongest along the y-direction, and depending on processing parameters, particle size and layer thickness were weakest along the x- or z- direction. The orientation did not only induce variations in compressive modulus and strength values but the actual failure mechanism of the lattices was substantially altered.

Porosity was present in the designed solid regions. That combined with the designed macrostructure resulted in lower strength and stiffness values than one might expect. However, this micro-porosity within the struts proved desirable for cell adhesion, furthermore reduction of porosity would only be possible at the expense of dimensional accuracy.

SLS technology has the capability to fabricate structures required for tissue engineering, and many of limitations can be overcome by the insight gained from this study.

2.) Although most SLS systems are only capable of sintering polymers, is it possible to improve characteristics of the scaffolds with the introduction of a ceramic phase similar to the inorganic part of natural bone in terms of surface characteristics and mechanical properties?

Two compositions were tested and compared in terms of thermal properties, surface characteristics, mechanical properties, biological response and manufacturing processability. The examined blends contained 15 and 30 wt % HA.

The introduction of HA slightly increased melting temperature of the polymer and facilitated its crystallization, however it did not induce any changes in its crystallinity.

Surface roughness of the scaffolds was 30-40 μm that is favourable for cell adhesion and it was not significantly altered by addition of the ceramic phase. PCL is a strongly hydrophobic material. Hydrophobicity of fabricated scaffold surfaces was significantly reduced with the addition of HA, furthermore samples that contained 30 wt% of HA became completely wettable. These modifications to the scaffold surface are also desirable for successful seeding of osteoblast.

The effect of HA addition on mechanical properties was dependent on how strong the sintering was among the polymer particles. When sintering of the polymer resulted in good integrity, HA particles could limit molecular motion in PCL, resulting in increased compressive modulus. However, when sintering of the polymer was weak HA particles could not properly integrate into the polymer particles, and remained party exposed to the surface, therefore, the same amount of HA addition induced inferior mechanical properties. HA addition can improve mechanical properties, but good sintering is needed.

During biocompatibility testing of scaffolds fabricated from the two PCL/HA compositions, cell adhesion and proliferation was observed for both. Both alamar blue proliferation assay and mechanical testing of cultured samples confirmed that cell proliferation was better on PCL/15HA scaffolds after 1 week of cell culturing, however

the improvement of cell activity during the second week was more significant for PCL/30HA scaffolds.

In terms of processability the addition of HA improved flowability of powder. During layer deposition some problems were encountered with the PCL/15HA blend, while, the PCL/30HA powder resulted in smoother deposition than the pure PCL powder.

Overall of the tested compositions the PCL/30HA blend was found to be the most advantageous for processing and for the application, it did not change roughness but reduced hydrophobicity and showed positive influence on mechanical properties.

3.) How do SLS process parameters influence mechanical properties and dimensions of 3D structures with micron-scale features?

SLS is still a relatively new manufacturing technology and therefore continued development of the technology based on understanding of the effect of process parameters is needed to take the technology forward to new applications.

Central composite design (CCD) was used to develop models that directly relate mechanical properties of the fabricated scaffolds and dimensions of reproduced features to build-dependent SLS process parameters, namely laser fill power, outline laser power and scan spacing. Of these, the effect of laser fill power and scan spacing is well established, however no direct relationship has been proposed for their influence on the examined responses. Outline laser power has not been examined to date in published literature.

Regardless of the response (mechanical or dimensional) scan spacing was always the most important factor followed by outline laser power, however actual contribution of the parameters was strongly dependent on orientation. As a new contribution to current knowledge on the effect of scan spacing, its quadratic nature had been established.

Mathematical models that are able to predict the mechanical properties of lattices and dimensions of struts fabricated along the x-, and y-directions have been developed, which enable SLS users to tailor characteristics of functional parts by adjusting process parameters prior manufacturing. The used CCD however was not appropriate to develop statistically significant models for most responses in the z-direction. This resulted from

improper selection of the layer thickness used, as μ-CT data revealed, also explaining why this direction was the weakest in terms of mechanical properties.

The analysis of results suggests that although delivered energy density is important, in determining the examined responses multiple (double) scanning of the deposited layers is more important. Enormous improvements of mechanical properties were demonstrated, proving the hypothesis that mechanical properties are more sensitive to multiple scanning than to changes in delivered energy density. The study also revealed that increasing part bed temperature indirectly, by allowing heat to build up, also results in improved mechanical properties.

4.) Is SLS a viable technology to fabricate polycaprolactone composite scaffolds for tissue engineering?

This study demonstrated that SLS is a viable technology for the production of biodegradable scaffolds with predesigned external and internal geometry. Fabricated scaffolds have surface characteristics that are highly desirable for cell adhesion and proliferation. While low mechanical properties of PCL/HA scaffolds fabricated are not adequate for load bearing applications, mechanical properties within the lower range reported for human cancellous bone were achieved. Mechanical properties can be further improved by optimizing SLS process parameters and exploiting insight into the deformation and failure mechanism gained in this study. The PCL/HA scaffolds fabricated within the framework of this research are applicable matrices that can serve as a substrate for cell attachment growth and proliferation and these structures represent good alternatives for existing scaffolds.

6 REFERENCES

1 Guyton, A. Textbook of medical physiology. *The American Journal of the Medical Sciences*, 1967, **253**(1), 126.

2 Weiner, S., Traub, W. and Wagner, H. Lamellar bone: structure–function relations. *Journal of structural biology*, 1999, **126**(3), 241-255.

3 Weiner, S. and Wagner, H. The material bone: structure-mechanical function relations. *Annual Review of Materials Science*, 1998, **28**(1), 271-298.

4 Wagner, H. and Weiner, S. On the relationship between the microstructure of bone and its mechanical stiffness. *Journal of Biomechanics*, 1992, **25**(11), 1311-1320.

5 Seal, B.L., Otero, T.C. and Panitch, A. Polymeric biomaterials for tissue and organ regeneration. *Materials Science and Engineering: R: Reports*, 2001, **34**(4-5), 147-230.

6 Webster, T.J., Siegel, R.W. and Bizios, R. Osteoblast adhesion on nanophase ceramics. *Biomaterials*, 1999, **20**(13), 1221-1227.

7 Hollister, S.J., Maddox, R.D. and Taboas, J.M. Optimal design and fabrication of scaffolds to mimic tissue properties and satisfy biological constraints. *Biomaterials*, 2002, **23**(20), 4095-4103.

8 Laurencin, C.T., Khan, Y., Ma, P.X. and Elisseeff, J. Polymer/Calcium Phosphate Scaffolds for Bone Tissue Engineering. In Ma, P.X. and Elisseeff, J., eds. *Scaffolding in Tissue Engineering*, pp. 253-265 (CRC Press, Taylor & Francis Group, Boca Raton, 2006).

9 Lenza, R.F.S., Vasconcelos, W.L., Jones, J.R. and Hench, L.L. Surface-modified 3D scaffolds for tissue engineering. *Journal of Materials Science: Materials in Medicine*, 2002, **13**(9), 837-842.

10 Boyan, B.D., Hummert, T.W., Dean, D.D. and Schwartz, Z. Role of material surfaces in regulating bone and cartilage cell response. *Biomaterials*, 1996, **17**(2), 137-146.

11 Reilly, D.T. and Burstein, A.H. The mechanical properties of cortical bone. *The Journal of Bone and Joint Surgery*, 1974(56), 1001-1022.

12 Goldstein, S.A. The mechanical properties of trabecular bone: dependence on anatomic location and function. *Journal of Biomechanics*, 1987, **20**(11-12), 1055-1061.

13 Eosoly, S. Mechanical testing and finite element modeling of bioresorbable, cellular polymers. *MSc Thesis* (Budapest University of Technology and Economics, Budapest, 2006).

14 Yeong, W.-Y., Chua, C.-K., Leong, K.-F. and Chandrasekaran, M. Rapid prototyping in tissue engineering: challenges and potential. *Trends in Biotechnology*, 2004, **22**(12), 643-652.

15 Hutmacher, D. Scaffolds in tissue engineering bone and cartilage. *Biomaterials*, 2000, **21**(24), 2529-2543.

16 Sachlos, E. and Czernuszka, J. Making tissue engineering scaffolds work. Review: the application of solid freeform fabrication technology to the production of tissue engineering scaffolds. *European cells & materials*, 2003, **5**, 29-39.

17 Rosen, D.W. Design for Additive Manufacturing: A Method to Explore unexplored regions of the design space. *Eighteenth Annual Solid Freeform Fabrication Symposium*, pp. 402-415 (The University of Texas at Austin, Austin, Texas, 2007).

18 Rosen, D.W. Computer-aided design for additive manufacturing of cellular structures. *Computer-Aided Design and Applications*, 2007, **4**(1-6), 585-594.

19 Nelson, J.C. Selective Laser Sintering: A definition of the process and an empirical sintering model. *PhD Thesis*, p. 232 (The University of Texas at Austin, Austin, 1993).

20 Evans, R.S. Indirect Rapid Manufacturing of Carbide Composites. *PhD thesis* (University of Texas at Austin, Austin, 2005).
21 Gibson, I. and Shi, D. Material properties and fabrication parameters in selective laser sintering. *Rapid Prototyping Journal*, 1997, **3**(4), 129-136.
22 Wiria, F.E., Leong, K.F., Chua, C.K. and Liu, Y. Poly-[epsilon]-caprolactone/hydroxyapatite for tissue engineering scaffold fabrication via selective laser sintering. *Acta Biomaterialia*, 2007, **3**(1), 1-12.
23 German, R.M. *Sintering Theory and Practice*. (John Wiley & Sons Inc. , 1996).
24 Leong, K.F., Cheah, C.M. and Chua, C.K. Solid freeform fabrication of three-dimensional scaffolds for engineering replacement tissues and organs. *Biomaterials*, 2003, **24**(13), 2363-2378.
25 Shi, Y., Li, Z., Huang, S. and Zeng, F. Effect of the properties of the polymer materials on the quality of selective laser sintering parts. *Proceedings of the Institution of Mechanical Engineers -- Part L -- Journal of Materials: Design & Applications*, 2004, **218**(3), 247-252.
26 Song, Y. and König, W. Experimental study of the basic process mechanism for direct selective laser sintering of low-melting metallic powder. *CIRP Annals*, 1997, **46**(1), 127–130.
27 Williams, J.D. and Deckard, C.R. Advances in modeling the effects of selected parameters on the SLS process. *Rapid Prototyping Journal*, 1998, **4**(2), 90-100.
28 Ho, H.C.H., Gibson, I. and Cheung, W.L. Effects of energy density on morphology and properties of selective laser sintered polycarbonate. *Journal of Materials Processing Technology*, 1999, **89-90**, 204-210.
29 Caulfield, B., McHugh, P.E. and Lohfeld, S. Dependence of mechanical properties of polyamide components on build parameters in the SLS process. *Journal of Materials Processing Technology*, 2007, **182**(1-3), 477-488.
30 Dewidar, M.M., Dalgarno, K.W. and Wright, C.S. Processing conditions and mechanical properties of high-speed steel parts fabricated using direct selective laser sintering. *Proceedings of the Institution of Mechanical Engineers -- Part B -- Engineering Manufacture*, pp. 1651-1663 (Professional Engineering Publishing, 2003).
31 Tontowi, A. and Childs, T. Density prediction of crystalline polymer sintered parts at various powder bed temperatures. *Rapid Prototyping Journal*, 2001, **7**(3), 180-184.
32 Savalani, M.M., Hao, L., Zhang, Y., Tanner, K.E. and Harris, R.A. Fabrication of porous bioactive structures using the selective laser sintering technique. *Proceedings of the Institution of Mechanical Engineers -- Part H -- Journal of Engineering in Medicine*, pp. 873-886 (Professional Engineering Publishing, 2007).
33 Subramanian, K., Vail, N., Barlow, J. and Marcus, H. Selective laser sintering of alumina with polymer binders. *Rapid Prototyping Journal*, 1995, **1**(2), 24-35.
34 Chua, C.K., Leong, K.F., Tan, K.H., Wiria, F.E. and Cheah, C.M. Development of tissue scaffolds using selective laser sintering of polyvinyl alcohol/hydroxyapatite biocomposite for craniofacial and joint defects. *Journal of Materials Science: Materials in Medicine*, 2004, **15**(10), 1113-1121.
35 Hao, L., Savalani, M.M., Zhang, Y., Tanner, K.E. and Harris, R.A. Effects of material morphology and processing conditions on the characteristics of hydroxyapatite and high-density polyethylene biocomposites by selective laser sintering. *Proceedings of the Institution of Mechanical Engineers -- Part L -- Journal of Materials: Design & Applications*, 2006, **220**(3), 125-137.
36 Miller, D., Deckard, C. and Williams, J. Variable beam size SLS workstation and enhanced SLS model. *Rapid Prototyping Journal*, 1997, **3**(1), 4-11.

37 Simchi, A. and Pohl, H. Effects of laser sintering processing parameters on the microstructure and densification of iron powder. *Materials Science and Engineering A*, 2003, **359**(1-2), 119-128.
38 Hardro, P., Wang, J. and Stucker, B. A design of experiment approach to determine the optimal process parameters for rapid prototyping machines. *Proceedings of the Joint Conference of the Fifth International Conference on Automation Technology and the 1998 International Conference of Production Research*, Taipei, 1998).
39 Chatterjee, A.N., Kumar, S., Saha, P., Mishra, P.K. and Choudhury, R. An experimental design approach to selective laser sintering of low carbon steel. *Journal of Materials Processing Technology*, 2003, **136**, 151-157.
40 Kruth, J. and Kumar, S. Statistical Analysis of Experimental Parameters in Selective Laser Sintering *Advanced Engineering Materials*, 2005, **7**(8).
41 Simchi, A. and Pohl, H. Effects of laser sintering processing parameters on the microstructure and densification of iron powder. *Materials Science & Engineering A*, 2003, **359**(1-2), 119-128.
42 Jain, P., Pandey, P. and Rao, P. Experimental investigations for improving part strength in selective laser sintering. *Virtual and Physical Prototyping*, 2008, **3**(3), 177-188.
43 Low, K.H., Leong, K.F., Chua, C.K., Du, Z.H. and Cheah, C.M. Characterization of SLS parts for drug delivery devices. *Rapid Prototyping Journal*, 2001, **7**(5), 262-267.
44 Cheah, C.M., Leong, K.F., Chua, C.K., Low, K.H. and Quek, H.S. Characterization of microfeatures in selective laser sintered drug delivery devices. *Proceedings of the Institution of Mechanical Engineers -- Part H -- Journal of Engineering in Medicine*, 2002, **216**(6), 369-383.
45 Leong, K., Chua, C., Gui, W., Verani and Verani. Building Porous Biopolymeric Microstructures for Controlled Drug Delivery Devices Using Selective Laser Sintering. *The International Journal of Advanced Manufacturing Technology*, 2006, **31**(5), 483-489.
46 Thompson, D. and Crawford, R. Computational quality measures for evaluation of part orientation in freeform fabrication. *Journal of Manufacturing Systems*, 1997, **16**(4), 273-289.
47 Ning, Y., Wong, Y. and Fuh, J. Effect and control of hatch length on material properties in the direct metal laser sintering process. *Proceedings of the Institution of Mechanical Engineers, Part B: Journal of Engineering Manufacture*, 2005, **219**(1), 15-25.
48 Williams, J.M., Adewunmi, A., Schek, R.M., Flanagan, C.L., Krebsbach, P.H., Feinberg, S.E., Hollister, S.J. and Das, S. Bone tissue engineering using polycaprolactone scaffolds fabricated via selective laser sintering. *Biomaterials*, 2005, **26**(23), 4817-4827.
49 Chen, Y. Non-uniform Offsetting and its Applications in Laser Path Planning of Stereolithography Machine. *Eighteenth Annual Solid Freeform Fabrication Symposium*, pp. 174-186Austin, Texas, 2007).
50 Chua, C.-K., Leong, K.-F. and Lim, C.S. *Rapid Prototyping: Principles and Applications in Manufacturing*. (World Scientific, 2003).
51 Wang, X. Calibration of shrinkage and beam offset in SLS process. *Rapid Prototyping Journal*, 1999, **5**(3), 129-133.
52 Dai, K. and Shaw, L. Distortion minimization of laser-processed components through control of laser scanning patterns. *Rapid Prototyping Journal*, 2002, **8**(5), 270-276.

53 Raghunath, N. and Pandey, P. Improving accuracy through shrinkage modelling by using Taguchi method in selective laser sintering. *International Journal of Machine Tools and Manufacture*, 2007, **47**(6), 985-995.
54 Tumor, I., Thompson, D., Wood, K. and Crawford, R. Characterization of surface fault patterns with application to a layered manufacturing process. *Journal of Manufacturing Systems*, 1998, **17**(1), 23-36.
55 Bacchewar, P., Singhal, S. and Pandey, P. Statistical modelling and optimization of surface roughness in the selective laser sintering process. *Proceedings of the Institution of Mechanical Engineers, Part B: Journal of Engineering Manufacture*, 2007, **221**(1), 35-52.
56 Ning, Y., Fuh, J., Wong, Y. and Loh, H. An intelligent parameter selection system for the direct metal laser sintering process. *International Journal of Production Research*, 2004, **42**(1), 183-199.
57 Partee, B., Hollister, S.J. and Das, S. Selective Laser Sintering Process Optimization for Layered Manufacturing of CAPA® 6501 Polycaprolactone Bone Tissue Engineering Scaffolds. *Journal of Manufacturing Science & Engineering*, 2006, **128**(2), 531-540.
58 Tan, K.H., Chua, C.K., Leong, K.F., Cheah, C.M., Cheang, P., Abu Bakar, M.S. and Cha, S.W. Scaffold development using selective laser sintering of polyetheretherketone-hydroxyapatite biocomposite blends. *Biomaterials*, 2003, **24**(18), 3115-3123.
59 Wiria, F., Chua, C., Leong, K., Quah, Z., Chandrasekaran, M. and Lee, M. Improved biocomposite development of poly(vinyl alcohol) and hydroxyapatite for tissue engineering scaffold fabrication using selective laser sintering. *Journal of Materials Science: Materials in Medicine*, 2008, **19**(3), 989-996.
60 Tan, K.H., Chua, C.K., Leong, K.F., Cheah, C.M., Gui, W.S., Tan, W.S. and Wiria, F.E. Selective laser sintering of biocompatible polymers for applications in tissue engineering. *Bio-Medical Materials & Engineering*, 2005, **15**(1/2), 113-124.
61 Simpson, R.L., Wiria, F.E., Amis, A.A., Chua, C.K., Leong, K.F., Hansen, U.N., Chandrasekaran, M. and Lee, M.W. Development of a 95/5 poly(L-lactide-co-glycolide)/hydroxylapatite and beta-tricalcium phosphate scaffold as bone replacement material via selective laser sintering. *Journal of Biomedical Materials Research Part B: Applied Biomaterials*, 2008, **84B**(1), 17-25.
62 Hao, L., Savalani, M.M., Zhang, Y., Tanner, K.E. and Harris, R.A. Selective Laser Sintering of Hydroxyapatite Reinforced Polyethylene Composites for Bioactive Implants and Tissue Scaffold Development. *Proceedings of the Institution of Mechanical Engineers -- Part H -- Journal of Engineering in Medicine*, 2006, **220**(4), 521-531.
63 Zhou, Y., Hirao, K., Yamauchi, Y. and Kanzaki, S. Effects of heating rate and particle size on pulse electric current sintering of alumina. *Scripta Materialia*, 2003, **48**(12), 1631-1636.
64 Zhang, Y., Hao, L., Savalani, M., Harris, R. and Tanner, K. Characterization and dynamic mechanical analysis of selective laser sintered hydroxyapatite-filled polymeric composites. *Journal of Biomedical Materials Research Part A*, 2008(3).
65 Tan, K.H., Chua, C.K., Leong, K.F., Naing, M.W. and Cheah, C.M. Fabrication and characterization of three-dimensional poly(ether-ether-ketone)/hydroxyapatite biocomposite scaffolds using laser sintering. *Proceedings of the Institution of Mechanical Engineers -- Part H -- Journal of Engineering in Medicine*, 2005, **219**(3), 183-194.
66 Naing, M., Chua, C., Leong, K. and Wang, Y. Fabrication of customised scaffolds using computer-aided design and rapid prototyping techniques. *Rapid Prototyping Journal*, 2005, **11**(4), 249-259.

67 Cheah, C., Chua, C., Leong, K. and Chua, S. Development of a tissue engineering scaffold structure library for rapid prototyping. Part 1: investigation and classification. *The International Journal of Advanced Manufacturing Technology*, 2003, **21**(4), 291-301.
68 Cheah, C., Chua, C., Leong, K. and Chua, S. Development of a tissue engineering scaffold structure library for rapid prototyping. Part 2: parametric library and assembly program. *The International Journal of Advanced Manufacturing Technology*, 2003, **21**(4), 302-312.
69 Das, S., Hollister, S.J., Flanagan, C., Adewunmi, A., Bark, K., Chen, C., Ramaswamy, K., Rose, D. and Widjaja, E. Freeform fabrication of Nylon-6 tissue engineering scaffolds. *Rapid Prototyping Journal*, 2003, **9**(1), 43-49.
70 Zhou, W., Lee, S., Wang, M., Cheung, W. and Ip, W. Selective laser sintering of porous tissue engineering scaffolds from poly(l -lactide)/carbonated hydroxyapatite nanocomposite microspheres. *Journal of Materials Science: Materials in Medicine*, 2008, **19**(7), 2535-2540.
71 Gibson, L.J. and Ashby, M.F. *Cellular Solids: Structure and Properties*. (Cambridge University Press, Cambridge, 1997).
72 Brezny, R. and Green, D.J. The effect of cell size on the mechanical behavior of cellular materials. 1990, **38**(Acta Metallurgica et Materialia), 2517-2526.
73 Papka, S. and Kyriakides, S. In-plane crushing of a polycarbonate honeycomb. *International Journal of Solids and Structures(UK)*, 1998, **35**(3), 239-267.
74 Papka, S.D. and Kyriakides, S. Experiments and full-scale numerical simulations of in-plane crushing of a honeycomb. *Acta Materialia*, 1998, **46**(8), 2765-2776.
75 Ashby, M. The properties of foams and lattices. *Philosophical Transactions of the Royal Society A: Mathematical, Physical and Engineering Sciences*, 2006, **364**(1838), 15.
76 Deshpande, V.S. and Fleck, N.A. Collapse of truss core sandwich beams in 3-point bending. *International Journal of Solids and Structures*, 2001, **38**(36-37), 6275-6305.
77 Deshpande, V., Ashby, M. and Fleck, N. Foam topology: bending versus stretching dominated architectures. *Acta Materialia*, 2001, **49**(6), 1035-1040.
78 Zhu, H.X., Knott, J.F. and Mills, N.J. Analysis of the elastic properties of open-cell foams with tetrakaidecahedral cells. *Journal of the Mechanics and Physics of Solids*, 1997, **45**(3), 319-325.
79 Li, K., Gao, X.L. and Roy, A.K. Micromechanics model for three-dimensional open-cell foams using a tetrakaidecahedral unit cell and Castigliano's second theorem. *Composites Science and Technology*, 2003, **63**(12), 1769-1781.
80 Li, K., Gao, X.L. and Subhash, G. Effects of cell shape and cell wall thickness variations on the elastic properties of two-dimensional cellular solids. *International Journal of Solids and Structures*, 2005, **42**(5-6), 1777-1795.
81 Roberts, A. and Garboczi, E. Elastic moduli of model random three-dimensional closed-cell cellular solids. *Acta Materialia*, 2001, **49**(2), 189-197.
82 Roberts, A. and Garboczi, E. Elastic properties of model random three-dimensional open-cell solids. *Journal of the Mechanics and Physics of Solids*, 2002, **50**(1), 33-55.
83 Zhou, J., Mercer, C. and Soboyejo, W. An investigation of the microstructure and strength of open-cell 6101 aluminum foams. *Metallurgical and Materials Transactions A*, 2002, **33**(5), 1413-1427.
84 Grenestedt, J. and Tanaka, K. Influence of cell shape variations on elastic stiffness of closed cell cellular solids. *Scripta Materialia*, 1999, **40**(1), 71-78.

85 Grenestedt, J. and Bassinet, F. Influence of cell wall thickness variations on elastic stiffness of closed-cell cellular solids. *International Journal of Mechanical Sciences*, 2000, **42**(7), 1327-1338.
86 Simone, A. and Gibson, L. Effects of solid distribution on the stiffness and strength of metallic foams. *Acta Materialia*, 1998, **46**(6), 2139-2150.
87 Woß, A., Stampfl, J. and Fratzl, P. Cellular solids beyond the apparent density-an experimental assessment of mechanical properties. *3D-techniques in Materials Science*, 2004, **6**, 113.
88 Singamaneni, S., Chang, S., Jang, J., Davis, W., Thomas, E. and Tsukruk, V. Mechanical properties of composite polymer microstructures fabricated by interference lithography. *Physical Chemistry Chemical Physics*, 2008, **10**(28), 4093-4105.
89 Rezwan, K., Chen, Q., Blaker, J. and Boccaccini, A. Biodegradable and bioactive porous polymer/inorganic composite scaffolds for bone tissue engineering. *Biomaterials*, 2006, **27**(18), 3413-3431.
90 Gunatillake, P. and Adhikari, R. Biodegradable synthetic polymers for tissue engineering. *Eur Cell Mater*, 2003, **5**(1).
91 Rodrigues, C., Serricella, P., Linhares, A., Guerdes, R., Borojevic, R., Rossi, M., Duarte, M. and Farina, M. Characterization of a bovine collagen–hydroxyapatite composite scaffold for bone tissue engineering. *Biomaterials*, 2003, **24**(27), 4987-4997.
92 Rocha, L., Goissis, G. and Rossi, M. Biocompatibility of anionic collagen matrix as scaffold for bone healing. *Biomaterials*, 2002, **23**(2), 449-456.
93 Li, X., Feng, Q., Jiao, Y. and Cui, F. Collagen-based scaffolds reinforced by chitosan fibres for bone tissue engineering. *Polymer International*, 2005, **54**(7), 1034-1040.
94 Yang, X., Bhatnagar, R., Li, S. and Oreffo, R. Biomimetic collagen scaffolds for human bone cell growth and differentiation. *Tissue Engineering*, 2004, **10**(7-8), 1148-1159.
95 Niemeyer, P., Krause, U., Fellenberg, J., Kasten, P., Seckinger, A., Ho, A. and Simank, H. Evaluation of mineralized collagen and -tricalcium phosphate as scaffolds for tissue engineering of bone using human mesenchymal stem cells. *Cells Tissues Organs*, 2004, **177**(2), 68-78.
96 Liao, S., Cui, F., Zhang, W. and Feng, Q. Hierarchically biomimetic bone scaffold materials: nano-HA/collagen/PLA composite. *Journal of Biomedical Materials Research*, 2004, **69**(2), 158-165.
97 Jung, Y., Kim, S.-S., Kim, Y.H., Kim, S.-H., Kim, B.-S., Kim, S., Choi, C.Y. and Kim, S.H. A poly(lactic acid)/calcium metaphosphate composite for bone tissue engineering. *Biomaterials*, pp. 6314-63222005).
98 Freed, L., Vunjak-Novakovic, G., Biron, R., Eagles, D., Lesnoy, D., Barlow, S. and Langer, R. Biodegradable polymer scaffolds for tissue engineering. *Nature Biotechnology*, 1994, **12**(7), 689-693.
99 Jiang, T., Abdel-Fattah, W.I. and Laurencin, C.T. In vitro evaluation of chitosan/poly(lactic acid-glycolic acid) sintered microsphere scaffolds for bone tissue engineering. *Biomaterials*, 2006, **27**(28), 4894-4903.
100 Habraken, W.J.E.M., Wolke, J.G.C. and Jansen, J.A. Ceramic composites as matrices and scaffolds for drug delivery in tissue engineering. *Advanced Drug Delivery Reviews*, 2007, **59**(4-5), 234-248.
101 Chim, H., Hutmacher, D.W., Chou, A.M., Oliveira, A.L., Reis, R.L., Lim, T.C. and Schantz, J.T. A comparative analysis of scaffold material modifications for load-bearing applications in bone tissue engineering. *International Journal of Oral and Maxillofacial Surgery*, 2006, **35**(10), 928-934.
102 Dietmar W. Hutmacher, T.S., Iwan Zein, Kee Woei Ng, Swee Hin Teoh, Kim Cheng Tan,. Mechanical properties and cell cultural response of polycaprolactone

scaffolds designed and fabricated via fused deposition modeling. *Journal of Biomedical Materials Research*, 2001, **55**(2), 203-216.
103 Erisken, C., Kalyon, D.M. and Wang, H. Functionally graded electrospun polycaprolactone and [beta]-tricalcium phosphate nanocomposites for tissue engineering applications. *Biomaterials*, 2008, **29**(30), 4065-4073.
104 F. Causa, P.A.N., L. Ambrosio, G. Ciapetti, N. Baldini, S. Pagani, D. Martini, A. Giunti,. Poly-ε-caprolactone/hydroxyapatite composites for bone regeneration: In vitro characterization and human osteoblast response. *Journal of Biomedical Materials Research Part A*, 2006, **76A**(1), 151-162.
105 Kacey G. Marra, J.W.S., Prashant N. Kumta, Paul A. DiMilla, Lee E. Weiss,. In vitro analysis of biodegradable polymer blend/hydroxyapatite composites for bone tissue engineering. *Journal of Biomedical Materials Research*, 1999, **47**(3), 324-335.
106 Kweon, H., Yoo, M.K., Park, I.K., Kim, T.H., Lee, H.C., Lee, H.-S., Oh, J.-S., Akaike, T. and Cho, C.-S. A novel degradable polycaprolactone networks for tissue engineering. *Biomaterials*, 2003, **24**(5), 801-808.
107 Savarino, L., Baldini, N., Greco, M., Capitani, O., Pinna, S., Valentini, S., Lombardo, B., Esposito, M., Pastore, L. and Ambrosio, L. The performance of poly-e-caprolactone scaffolds in a rabbit femur model with and without autologous stromal cells and BMP4. *Biomaterials*, 2007, **28**(20), 3101-3109.
108 Shor, L., Güçeri, S., Wen, X., Gandhi, M. and Sun, W. Fabrication of three-dimensional polycaprolactone/hydroxyapatite tissue scaffolds and osteoblast-scaffold interactions in vitro. *Biomaterials*, 2007, **28**(35), 5291-5297.
109 Vincenzo Guarino, F.C., Paolo A. Netti, Gabriela Ciapetti, Stefania Pagani, Desiree Martini, Nicola Baldini, Luigi Ambrosio,. The role of hydroxyapatite as solid signal on performance of PCL porous scaffolds for bone tissue regeneration. *Journal of Biomedical Materials Research Part B: Applied Biomaterials*, 2008, **86B**(2), 548-557.
110 Olah, L., Filipczak, K., Jaegermann, Z., Czigany, T., Borbas, L., Sosnowski, S., Ulanski, P. and Rosiak, J. Synthesis, structural and mechanical properties of porous polymeric scaffolds for bone tissue regeneration based on neat poly (epsilon-caprolactone) and its composites with calcium carbonate. *Polymers for Advanced Technologies*, 2006, **17**(11-12), 889-897.
111 Mark, J. *Polymer data handbook.* (Oxford University Press New York, 1999).
112 Ali, S., Zhong, S., Doherty, P. and Williams, D. Mechanisms of polymer degradation in implantable devices. I. Poly (caprolactone). *Biomaterials*, 1993, **14**(9), 648.
113 Sinha, V.R., Bansal, K., Kaushik, R., Kumria, R. and Trehan, A. Poly-[epsilon]-caprolactone microspheres and nanospheres: an overview. *International Journal of Pharmaceutics*, 2004, **278**(1), 1-23.
114 Pitt, C.G., Chasalow, F.I., Hibionada, Y.M., Klimas, D.M. and Schindler, A. Aliphatic polyesters. I. The degradation of poly(&epsis;-caprolactone) <I>in vivo</I>. *Journal of Applied Polymer Science*, 1981, **26**(11), 3779-3787.
115 Dairui Chen, Hongli Chen, Jianzhong Bei and Shenguo Wang. Morphology and biodegradation of microspheres of polyester-polyether block copolymer based on polycaprolactone/polylactide/poly(ethylene oxide). *Polymer International*, 2000, **49**(3), 269-276.
116 Rohner, D., Hutmacher, D.W., Cheng, T.K., Oberholzer, M. and Hammer, B. In vivo efficacy of bone-marrow-coated polycaprolactone scaffolds for the reconstruction of orbital defects in the pig. *Journal of Biomedical Materials Research Part B: Applied Biomaterials*, 2003, **66B**(2), 574-580.
117 Agrawal, C. and Athanasiou, K. Technique to control pH in vicinity of biodegrading PLA-PGA implants. *Journal of Biomedical Materials Research*, 1997, **38**(2).

118 Hutmacher, D., Kirsch, A., Ackermann, K. and Hürzeler, M. A tissue engineered cell-occlusive device for hard tissue regeneration--a preliminary report. *The International journal of periodontics & restorative dentistry*, 2001, **21**(1), 49.
119 Shikinami, Y. and Okuno, M. Bioresorbable devices made of forged composites of hydroxyapatite (HA) particles and poly-L-lactide (PLLA): Part I. Basic characteristics. *Biomaterials*, 1999, **20**(9), 859-877.
120 Lee, G. Selective Laser Sintering of calcium phosphate materials for orthopedic implants. *PhD Thesis* (University of Texas at Austin, Austin, 1997).
121 Webster, T.J., Ergun, C., Doremus, R.H., Siegel, R.W. and Bizios, R. Enhanced functions of osteoblasts on nanophase ceramics. *Biomaterials*, 2000, **21**(17), 1803-1810.
122 Dorozhkin, S. Calcium orthophosphates. *Journal of Materials Science*, 2007, **42**(4), 1061-1095.
123 Bohner, M. Calcium orthophosphates in medicine: from ceramics to calcium phosphate cements. *Injury*, 2000, **31**, 37-47.
124 Livingstone, T.J. *Ceramics for Medical Applications*. (Dublin City Univercity, 2008).
125 Dorozhkin, S. Calcium Orthophosphates in Nature, Biology and Medicine. *Materials*, 2009, **2**(2), 399-498.
126 Anselme, K. Osteoblast adhesion on biomaterials. *Biomaterials*, 2000, **21**(7), 667-681.
127 Corden, T.J., Jones, I.A., Rudd, C.D., Christian, P., Downes, S. and McDougall, K.E. Physical and biocompatibility properties of poly-[var epsilon]-caprolactone produced using in situ polymerisation: a novel manufacturing technique for long-fibre composite materials. *Biomaterials*, 2000, **21**(7), 713-724.
128 Endres, M., Hutmacher, D., Salgado, A., Kaps, C., Ringe, J., Reis, R., Sittinger, M., Brandwood, A. and Schantz, J. Osteogenic induction of human bone marrow-derived mesenchymal progenitor cells in novel synthetic polymer-hydrogel matrices. *Tissue Engineering*, 2003, **9**(4), 689-702.
129 Ciapetti, G., Ambrosio, L., Savarino, L., Granchi, D., Cenni, E., Baldini, N., Pagani, S., Guizzardi, S., Causa, F. and Giunti, A. Osteoblast growth and function in porous poly [epsilon]-caprolactone matrices for bone repair: a preliminary study. *Biomaterials*, 2003, **24**(21), 3815-3824.
130 Azevedo, M., Reis, R., Claase, M., Grijpma, D. and Feijen, J. Development and properties of polycaprolactone/hydroxyapatite composite biomaterials. *Journal of Materials Science: Materials in Medicine*, 2003, **14**(2), 103-107.
131 Chen, B. and Sun, K. Poly (-caprolactone)/hydroxyapatite composites: effects of particle size, molecular weight distribution and irradiation on interfacial interaction and properties. *Polymer Testing*, 2005, **24**(1), 64-70.
132 Evans, M. *Optimisation of manufacturing processes - A response surface approach*. (Maney Publishing, London, 2003).
133 Montgomery, D.C., Runger, G.C. and Hubele, N.F. *Engineering statistics*. (John Wiley and Sons Inc, Hoboken, NJ, 2001).
134 Anle Yang, R.W., Pinfang Zhu,. Thermal analysis and miscibility of chitin/polycaprolactone blends. *Journal of Applied Polymer Science*, 2001, **81**(13), 3117-3123.
135 Wunderlich, B. *Macromolecular Physics, Volume 3: Crystal Melting*. (Academic Press, London, 1980).
136 Jianyuan Hao, M.Y., Xianmo Deng,. Biodegradable and biocompatible nanocomposites of poly(ε-caprolactone) with hydroxyapatite nanocrystals: Thermal and mechanical properties. *Journal of Applied Polymer Science*, 2002, **86**(3), 676-683.

137 Wang, Y., Rodriguez-Perez, M.A., Reis, R.L. and Mano, J.F. Thermal and thermomechanical behaviour of polycaprolactone and starch/polycaprolactone blends for biomedical applications. *Macromolecular Materials and Engineering*, 2005, **290**, 792-801.
138 Chen, B. and Sun, K. Mechanical and dynamic viscoelastic properties of hydroxyapatite reinforced poly([epsilon]-caprolactone). *Polymer Testing*, 2005, **24**(8), 978-982.
139 Sachlos, E. and Czernuszka, J. Making tissue engineering scaffolds work. Review: the application of solid freeform fabrication technology to the production of tissue engineering scaffolds. *Eur Cell Mater*, 2003, **5**, 29-39.
140 Lehnert, D., Wehrle-Haller, B., David, C., Weiland, U., Ballestrem, C., Imhof, B. and Bastmeyer, M. Cell behaviour on micropatterned substrata: limits of extracellular matrix geometry for spreading and adhesion. *Journal of cell science*, 2004, **117**(1), 41-52.
141 Chen, C., Mrksich, M., Huang, S., Whitesides, G. and Ingber, D. Micropatterned surfaces for control of cell shape, position, and function. *Biotechnology Progress*, 1998, **14**(3), 356-363.
142 Matsuzaka, K., Frank Walboomers, X., Yoshinari, M., Inoue, T. and Jansen, J.A. The attachment and growth behavior of osteoblast-like cells on microtextured surfaces. *Biomaterials*, 2003, **24**(16), 2711-2719.
143 Ken Webb, V.H.P.A.T. Relative importance of surface wettability and charged functional groups on NIH 3T3 fibroblast attachment, spreading, and cytoskeletal organization. *Journal of Biomedical Materials Research Part B: Applied Biomaterials*, 1998, **41**(3), 422-430.
144 Goulet, R., Goldstein, S., Ciarelli, M., Kuhn, J., Brown, M. and Feldkamp, L. The relationship between the structural and orthogonal compressive properties of trabecular bone. *Journal of Biomechanics*, 1994, **27**(4), 375-377.
145 Guedes, R.M., Simões, J.A. and Morais, J.L. Viscoelastic behaviour and failure of bovine cancellous bone under constant strain rate. *Journal of Biomechanics*, 2006, **39**(1), 49-60.
146 Linhart, W., Peters, F., Lehmann, W., Schwarz, K., Schilling, A.F., Amling, M., Rueger, J.M. and Epple, M. Biologically and chemically optimized composites of carbonated apatite and polyglycolide as bone substitution materials. *Journal of Biomedical Materials Research*, 2001, **54**(2), 162-171.
147 Burr, D.B. The contribution of the organic matrix to bone's material properties. *Bone*, 2002, **31**(1), 8-11.
148 Garnero, P., Borel, O., Gineyts, E., Duboeuf, F., Solberg, H., Bouxsein, M.L., Christiansen, C. and Delmas, P.D. Extracellular post-translational modifications of collagen are major determinants of biomechanical properties of fetal bovine cortical bone. *Bone*, 2006, **38**(3), 300-309.
149 Myers, R., Montgomery, D. and Anderson-Cook, C. *Response surface methodology: process and product optimization using designed experiments*. (Wiley, 2009).
150 Hardro, P., Wang, J. and Stucker, B. A design of experiment approach to determine the optimal process parameters for rapid prototyping machines. *Proceedings of the Joint Conference of the Fifth International Conference on Automation Technology and the 1998 International Conference of Production Research*Taipei, 1998).
151 Lakes, R. Size effects and micromechanics of a porous solid. *Journal of Materials Science*, 1983, **18**(9), 2572-2580.

A. Appendix I. - SLS Screening Experiments Using Duraform

Materials and Methods

Selective laser sintering of Duraform has been carried out at the Institute of Technology Tallaght. Sinterstation 2500^{plus} with a low power, λ=10.6 μm continuous wave, CO_2 laser focused to a 400 μm spot was used to fabricate the scaffolds. Prior to the design of experiments, calibration of the SLS system was performed using a millimeter – scaled calibration part and default parameter settings (

Table 6.1a) to identify the necessary shrinkage compensations. The calibration indicated that a shrinkage compensation of 2.9 % is necessary in the X and Y direction, and 2.8 % in the Z direction. After SLS processing was completed, the scaffolds were allowed to cool overnight in the build chamber and were removed from the part bed. Excess powder was brushed off from the exterior and the internal architecture was cleaned using compressed air with a pressure of 2-6 Bars.

Parameter	Level
Laser fill power	5W
Scan count (fill)	1
Outline laser power	11W
Scan count (outline)	1
Scan spacing	0.15mm
Layer thickness	0.1 mm
Preheat temperature	143 C

a.)

Parameter	Lower level	Higher Level
Laser Fill Power	6 W	16 W
Outline laser power	0 W	10 W
Scan spacing	0.1 mm	0.2 mm
Strut size	0.6 mm	0.8mm

b.)

Table 6.1 (a) Default parameter settings for calibration parts, (b) Factors and factor levels used in the Taguchi array

The present study carries out 3 sets of experiments. It investigates the effects of relative density (1) and process parameters (2) on the mechanical properties of the scaffolds, and the effect of process parameters on the accuracy (3) of the manufactured parts.

Dependence of mechanical properties on relative density

Applications of scaffolds as temporary bone substitutes in the field of tissue engineering cause them to be loaded in compression, therefore only compressive mechanical properties are studied and evaluated. Disk-shaped scaffold structures (Fig. 6.1a) with orthogonal channels, designed in Pro/ENGINEER 2005 and imported to STL file format were used to investigate the compressive mechanical properties of cellular solids with different relative densities. The strut and pore sizes were alternated between 0.45 – 1 and 1.4 – 1.95 mm respectively to achieve different relative density levels, the range of 40 – 10 v% was examined in 5 v% increments. In order to treat the scaffold structure as a continuum, it had to be ensured that the ratio of specimen diameter to unit cell size was less than 20 [72, 151]. At each relative density level five replicates were manufactured at default parameter settings.

Specimens were compressed to failure using an Instron 4202 universal electromechanical testing machine at a rate of 1 mm/s using 50 kN load cell. Compressive Young's modulus and yield strength were determined in accordance with ISO 604:2002 standard. Since in the present experiment series, polyamide was used, which is not a potential material for tissue engineering applications due to lack of bioresorbability, normalized values are being displayed and analyzed. Solid control specimens were manufactured in order to be able to normalize the calculated compressive properties.

Dependence of mechanical properties on process parameters

It is assumed that at a given relative density level the mechanical properties of the specimens can be improved by changing the parameter settings. The examined process parameters were scan spacing, that is the distance between two parallel laser scan lines, laser fill power, that is the power in watts at which the scan lines are sintered, and outline laser power, that is the power in watts at which the contour of the object is sintered, additionally the strut size of the scaffold was also included in the design.

In order to reduce the number of treatment combinations Taguchi's L8 array was used as a one-half replication of 2^4 full factorial design of experiments to identify the process parameters and interactions that have a significant effect on the mechanical properties.

This array enables the examination of 4 factors at two levels including the effects of three interactions.

Table 6.1b summarizes the factors and factor levels that were examined.

Analysis of variance (ANOVA) was accomplished using Design-Expert 7.1 demo version to find the factors significantly affecting the compressive properties of the scaffolds. Disk – shaped lattice geometries (Fig. 6.1a) with 0.25 relative density were employed to conduct the experiment. Three replicates were fabricated from each treatment combinations, and specimens were compression tested as described above.

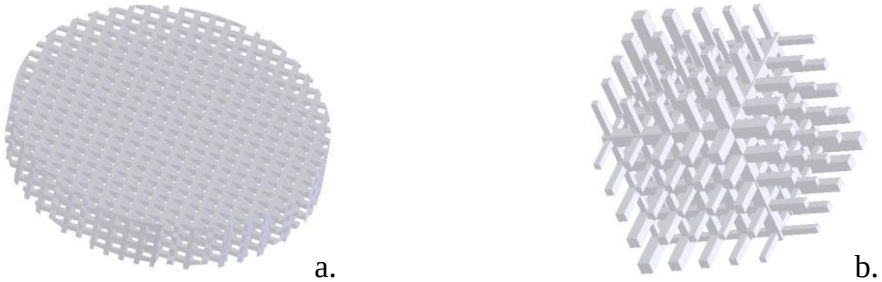

a. b.

Figure 6.1 Geometries designed for mechanical testing (a) and accuracy analysis (b)

Dependence of accuracy on process parameters

Accuracy of the manufacturing process was investigated using lattice like scaffolds (Fig. 6.1b). Geometries (Fig. 6.1b) were designed with strut sizes of 400µm, 500µm, 600µm, 700µm and 800µm in each of the tree axis planes (XY, XZ, YZ). This resulted in fewer test specimens. The parts were designed in Pro/ENGINEER 2005 and exported to the SLS system via the STL format.

The widths of struts were measured from two directions. For example, the widths of the struts built in the Z direction were measured in both the XZ and YZ plane. A micrograph of the strut was taken in both planes using Reichert MeF2 inverted light optical microscope that was then analyzed using Buehler Omnimet Enterprise image analysis software. Grayscale thresholding was executed on the micrographs to separate the struts from the background by representing the two different ranges of grayscale values with different color bitplanes. Binary operations were applied to improve image quality and remove artifacts. Once the borders of the struts were accurately mapped the mean width of the strut was calculated.

Since the goal of the experiment is to identify the process parameters having significant effect on the accuracy of the struts built in X, Y and Z direction, factorial design of experiments was used to examine the effect of 3 process parameters, namely laser fill power, outline laser power and scan spacing.

Factors	Level 1	Level 2	Level 3	Level 4	Level 5
Strut Size	0.4	0.5	0.6	0.7	0.8
Manufacturing direction	X	Y	Z	-	-
Measuring direction	Side1	Side2	-	-	-
Fill Laser Power	6	16	-	-	-
Outline Laser Power	0	10	-	-	-
Scan spacing	0.1	0.2	-	-	-

Table 6.2 Values of process parameters used in the factorial design of experiment

Table 6.2 indicates the factors and factor levels of the general factorial design of experiments setup. The design has 240 ($5\times3\times2^4$) different treatment combinations and 3 replicates were manufactured from each treatment combination. The process parameters that are not included in the design were used at their default value. Analysis of variance (ANOVA) was carried out to identify the significant effects of the parameters on the accuracy and compressive properties of the manufactured struts.

Results and Discussions

Dependence of mechanical properties on relative density

Gibson and Ashby discussed [71] that three distinct regions of behavior can be identified as a cellular material is compressed and it was found that the designed scaffolds behave in the exact the same way.

The stress-strain response of the fabricated scaffolds (Fig. 6.2a) is shown at different relative density levels, ranging from 0.1-0.4. First a linear elastic slope that is characterized by elastic compression of the struts can be observed at all levels, that is followed by the elastic/plastic collapse region, when the struts buckle and plastic hinges are formed in the structure, further stress compresses the solid material itself, resulting in steep densification. An increase in relative density of the structure improved the Young's modulus (Fig. 6.2b), the increase can be described by Eqs. 6.1.

$$\frac{E}{E_s} = C_1\left(\frac{\rho}{\rho_s}\right)^{k_1} \qquad \text{Eq. 6.1}$$

According to Gibson and Ashby's model compressive mechanical properties would improve quadratically (k_1=2) with decreasing porosity.

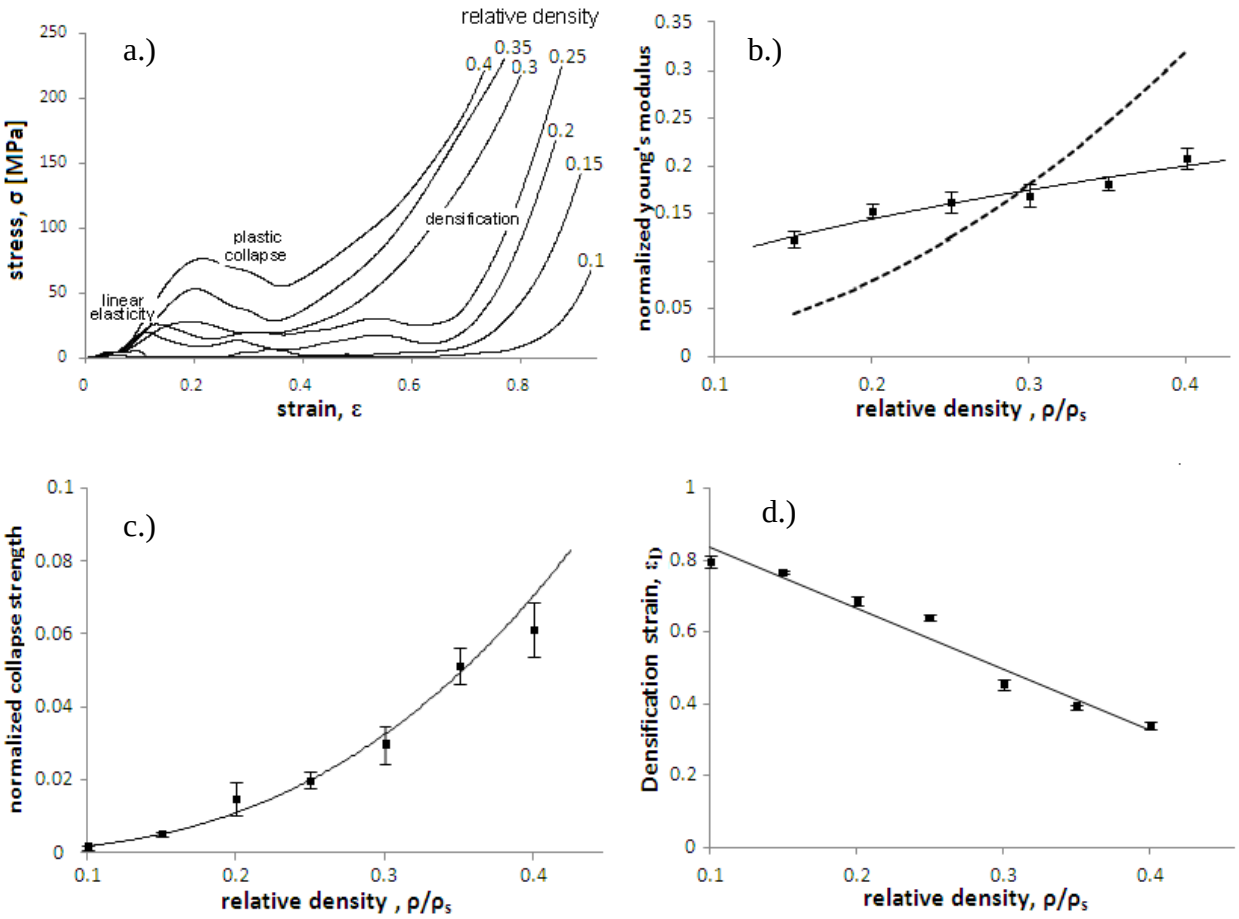

Figure 6.2 (a) Stress strain map for scaffolds manufactured by SLS, (b) relationship between the relative density and the normalized modulus (continous line – measured data, dotted line – Gibson-Ashby model), (c) relationship between the relative collapse strength and the relative density, (d) relationship between the densifications strain and the relative density of the scaffolds

However, measured data deviated from this model. For lower relative densities, when the strut sizes were smaller measured values were significantly higher than predicted by the model, and for high relative densities, when strut sizes were greater measured values were observably lower than predicted resulting in a slower increase (k_1=0.5). This deviation from the model can be attributed to the strut size effect, this will be described in more detail in a later section. As smaller struts appear more dense they therefore have

significantly better mechanical properties. C_1 is a constant relating to the geometry and in case of the investigated specimens it was found to be 0.3. This value accounts for both the pre-designed structure and the unintentional manufacturing induced porosity that is present in the designed solid regions.

The increase in relative density elevated the collapse stress as shown in the collapse region of the stress-strain map (Fig. 6.2a) and in Fig. 6.2c. The relationship between the collapse stress and the relative density of the structure is given by Eqs. 2.

$$\frac{\sigma_{collapse}}{\sigma_{ys}} = C_2\left(\frac{\rho}{\rho_s}\right)^{k_2} \qquad \text{Eq. 6.2}$$

The constants fitting the examined data are k_2=2.5 and C_2=0.8, again the latter constant summarizes the effects of both the designed and manufacturing induced geometry. The relative density increase also resulted in reduced densification strain, as shown in Fig. 6.2d.

As the relative density increases the densification begins at a lower strain level. The decrease of densification strain as a function of relative density can be described by Eqs. 3 applying the constant C_3=1.7.

$$\varepsilon_D = 1 - C_3\left(\frac{\rho}{\rho_s}\right) \qquad \text{Eq. 6.1}$$

As the application of scaffolds is in physiological environment, it must be pointed out that physiological strains are below 1-2%. Therefore from a tissue engineering point of view only the linear elastic region and the collapse stress are relevant, since in case of the examined scaffold structures collapse stress was reached around 2-3% of strain. The above equations govern the behavior of the SLS fabricated scaffold with respect to relative density; however it is hypotized that by altering process parameters at a given relative density level the mechanical properties can be significantly changed.

Dependence of mechanical properties on process parameters

To identify the process parameters that have a significant effect on the compressive properties of the scaffolds laser fill power, outline laser power and scan spacing were simultaneously and systematically varied according to Taguchi's L8 array. Table 6.3 summarizes the results of the statistical analysis after pooling the most insignificant factors as errors. The F value compares the variance of the model/parameter with the

variance of the residuals (difference between experimental data and predicted values). The p value indicates the probability of the model/factor erroneously being identified as significant. The critical value of p was set to 0.05, no parameter above this value was considered significant.

ANOVA table for Young's modulus

Source	SS	df	MS	F	p
Model	354.5	4	88.6	16.8	0.021
Outline	100.1	1	100	19.0	0.022
FillxOutl	18.4	1	18.4	3.5	0.158
Scan s.	7.2	1	7.2	1.3	0.323
Strut s.	228.7	1	228	43.4	0.007
Residual	15.7	3	5.2		
Total	370.37	7			

ANOVA table for yield strength

Source	SS	df	MS	F	p
Model	40.6	3	13.5	21.9	0.006
Outline	25.2	1	25.2	41.0	0.003
Scan s.	7.4	1	7.4	12.1	0.02
Stut s.	7.8	1	7.8	12.7	0.02
Residual	2.4	4	0.6		
Total	43.1	7			

Table 6.3 ANOVA tables for the compressive properties (SS - sum of squares, df – degrees of freedom, MS – mean of squares, F – MSmodel/MSresidual, F value, p – probability of seeing the observed F value if there is no factor effect)

ANOVA confirmed outline laser power and strut size as influential factors for the Young's modulus, and outline laser power, scan spacing and strut size for compressive yield strength. None of the interactions that had been included in the Taguchi array were detected to have any impact on the compressive mechanical properties. The correlation coefficient, which measures the strength of a linear relationship between the experimental data and the predicted values of the regression model for the Young's modulus and the compressive strength, was 0.84 and 0.90 respectively.

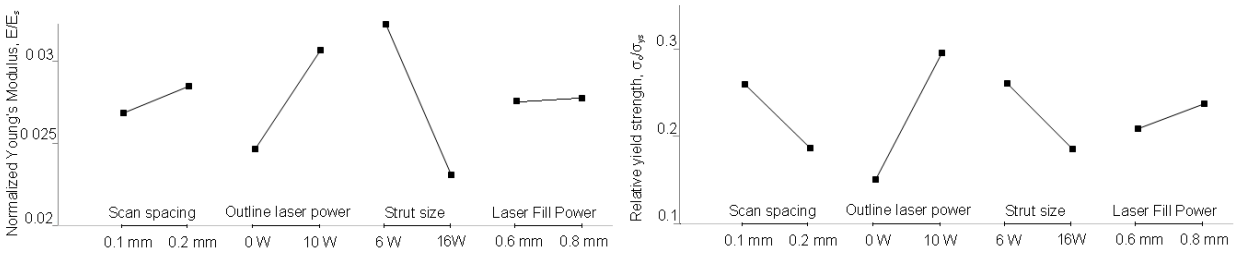

Figure 6.3 Influence of the design parameters on the mechanical performance (a) Young's modulus and (b) yield strength

Contrary to expectations, at this size level where scan line length is within the range of the laser beam diameter, no effect that can be attributed to the laser fill power was identified. The load bearing struts of the designed disk-shaped scaffolds were fabricated in the Z direction, where the scan line length was 0.6 – 0.8 mm compared to the laser beam diameter of 0.4 mm. It is assumed that the above scan line lengths (0.4 mm) did not trigger the laser.

However outline laser power was detected as a strongly determinative factor, its increased value considerably improved mechanical properties of the tested scaffolds. Increased outline laser power shifts the border of linear elasticity and plastic collapse to the right on the stress-strain map (Fig. 6.2a) as the linear elastic region becomes steeper and the collapse stress increases resulting in improved modulus and strength values.

Also, measurably improved properties were observed in smaller strut sizes and it is presumed that outline laser power is responsible for the strong strut size effect as scanning electron micrographs revealed that in the struts built in the Z direction only the outline contour was successfully fabricated (Fig. 6.4). When the same outline laser power was applied on the two different strut sizes (0.6 and 0.8 mm) the effective laser diameter was the same (average 180 μm at 10 W), but the actual scanned area relative to the whole cross-section of the strut was approximately 20 % higher in the smaller struts (Fig. 6.4 a, b), this could explain the significant increase in compressive properties for the smaller struts. In struts where the fill laser scan vector length is close to the diameter of the laser beam it would seem that the laser is not triggered. However the outline scan vector is triggered and because the size of the strut is close to the diameter of the laser beam this seems to result in a densely sintered strut, for small strut sizes where the laser beam would overlap as it scans around the outside of the strut. In the case of larger struts, where the fill laser vector has not been triggered, the outline scan vector results in

a hollow strut. Furthermore, as previously shown by Cheah et al. [44] when a single line is sintered the start and end portion of the line will be more dense that is caused by the extra deposited surface energy due to the acceleration and deceleration of the laser beam (dwell time). This can also be a possible explanation for the improved mechanical properties of the scaffolds with smaller struts and therefore with shorter scan line lengths.

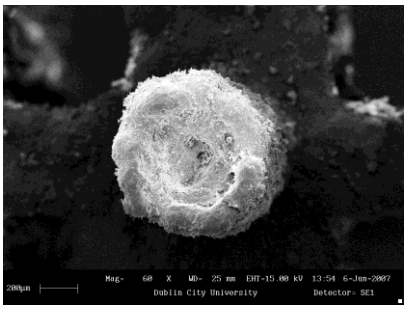

a.)

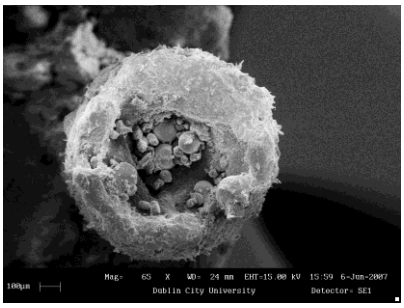

b.)

Figure 6.4 Cross-section of struts fabricated in the Z building direction (a) 0.6 mm, (b) 0.8 mm strut at P_{OI}=10 W

Scan spacing was identified as a process parameter that significantly contributes to the yield strength of the scaffolds indicating the importance of the strength of the structure at the intersection of X, Y and Z struts, where plastic hinges are formed. If scan spacing is reduced the scanned areas will receive significantly higher levels of energy density, which results in the fabrication of denser struts in the X and Y direction, and therefore the collapse stress of the scaffold is elevated. It means that decreasing scan spacing has the same effect on the stress-strain map (Fig. 6.2a) as increasing the relative density of the scaffold.

There were a number of unexpected results. It was observed that the outline contour in the cross section of the struts built in the Z direction was always present, even in build parameter combinations where the outline laser power was disabled and set to 0 W. However, we were not able to verify that the outline contour is scanned when outline laser power is turned off since if both outline and laser fill power were set to zero, no parts were fabricated.

In the present study only one fabrication direction was examined and only the struts built in the Z direction were loaded. In further studies the effect of different fabrication directions should also be investigated.

Dependence of accuracy on process parameters

Accurate reproduction of the designed scaffolds is essential in order to ensure that the predesigned geometrical features favorable to bone cells during cell culturing and the predicted mechanical properties can be precisely reproduced. Commercial SLS machines are not designed to fabricate geometries with micron-scale features. The smallest attainable feature size is limited by the diameter of the laser that is 0.4 mm but in many cases the scan lines of the 0.4 mm struts did not trigger the laser and these struts were not formed.

In general the geometry of the designed scaffolds was not properly reproduced. All the struts incorporated to the geometry were designed to be prisms with square cross-sections, but none of the fabricated struts reproduced this cross section. Figure 6.5 shows the typical cross-section of the struts that was attained in the 3 building directions. The designed square cross section has been replicated as a semi-circular (half-moon) cross-section in the X and Y direction and as a circular cross-section in the Z building direction. No significant difference has been detected between the dimensions of the Z struts in the ZY and ZX plane, but the dimensions of the X and Y struts in the XY plane were considerably greater than in the ZX and ZY plane, for the that reason measurements from two sides have been included in the design of experiments.

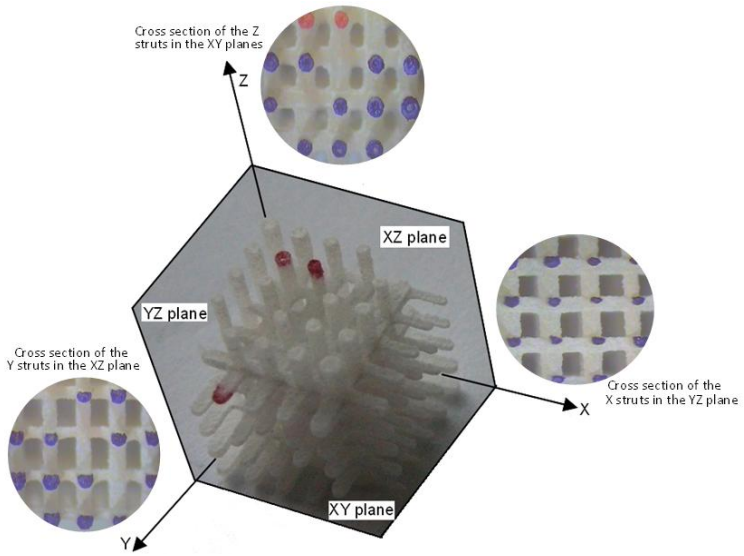

Figure 6.5 Manufacturing induced deformations in the cross section of the struts in the different building directions

Heat conduction of the powder bed and the laser intensity change along its radius can account for the formation of the semi-circular cross sections in the X and Y direction. Once a layer is sintered, its top surface is plane but the bottom surface curves due to the excess powder sintering around the intentionally sintered layer that distorts the designed geometry in the XZ and YZ plane. Additionally, at the examined size-scale the effect is more pronounced since the laser has a Gaussian intensity distribution along its diameter that results in a strongly curved bottom surface since the scan length is less than two-times the laser diameter. Shrinkage is also present in these struts, less observable than the curvature in the bottom surface but their top surface also becomes concave. The cross sectional difference in the struts manufactured in the Z direction can be explained by the outline scan. In the SEM images (Fig. 6.4) only the outline scan can be observed, it indicates that the laser might not be triggered when the scan length is between 0.4 and 0.8 mm.

The deviation from the target dimension was between -25% and +35% in the X struts and -5 and +90% in the Y struts, lower values in this range represent the measurement from the XZ and YZ plane respectively, while greater values are from the measurements taken in the XY plane. Deviation of the Z strut dimensions from the designed value was between -10 and 36% in both measuring directions.

Struts of 0.4 mm in size were not fabricated in most cases when the outline laser power was turned off, if fabricated there was observable damage; therefore this strut size was not included in further statistical analysis. By removing the 0.4 mm strut sizes from the model, residuals were significantly reduced and the remaining data better fit the regression curve.

Table 6.4 presents the ANOVA summary for the accuracy analysis after backward elimination regression with α set to 0.1. Build and measure directions are not real design factors; they were added to the model to be able to include and emphasize the uneven accuracy of the fabricated scaffolds in the different building and measuring directions and to avoid associating the parts with an average value that is less descriptive. Strut size is not a real design factor either, but different levels of this factor were included to verify the significant parameters on the different strut size geometries. ANOVA detected outline laser power and scan spacing as significant process parameters, one-way interaction between scan spacing and laser fill power were found to be significant, therefore only these parameters and interactions were further analyzed.

Influence of scan spacing is more pronounced when the laser fill power is used at its higher level, that is 16W, it explains the significant influence of the one-way interaction between the scan spacing and the laser fill power (DF). Scan spacing has a constant size decreasing effect on all struts; meaning that as the scan spacing is increased from 0.1 to 0.2 mm, the dimensions of the struts decrease. When accuracy is expressed as percentage deviation from the designed dimension, than scan spacing had a positive effect on the struts manufactured in the Y and Z direction; however it had adverse effect on the X struts, negative in the XZ and positive in the XY plane. The higher energy density supplied to the area in case of lower scan spacing could be an explanation for these accuracy results.

Source	**SS**	**Df**	**MS**	**F**	**P**
Model	3613459	26	138979	43	< 0.0001
A-Strut size	**1520237**	**3**	**506745**	**159**	**< 0.0001**
B-Build direction	647034.9	2	323517	101	< 0.0001
C-Measuring direction	301071	1	301071	94	< 0.0001
D-Laser fill power	6965	1	6965	2	0.1410
E-Outline laser power	**435057**	**1**	**435057**	**136**	**< 0.0001**
F-Scan spacing	**279874**	**1**	**279874**	**87**	**< 0.0001**
AB	93098	6	15516	4	0.0001
AC	29152	3	9717	3	0.0301
BC	58047	2	29023	9	0.0002
BE	57897	2	28948	9	0.0002
BF	23596	2	11798	3	0.0266
CE	34964	1	34964	10	0.0011
DF	**126461**	**1**	**126461**	**39**	**< 0.0001**
Error/Residual	525312	165	3183		
Total	4138772	191			

Table 6.4 ANOVA tables for accuracy (SS - sum of squares, df – degrees of freedom, MS – mean of squares, F – MSmodel/MSresidual, F value, p – probability of seeing the observed F value if there is no factor effect)

However this explanation suggests that laser fill power should also have the same effect on accuracy, but this factor was found to be insignificant at p=0.14 (Table 6.4).

The importance of outline laser power with respect to the accuracy of the specimens was expected in all directions since the outline contour has an important role in determining the dimensions of the struts. Outline laser power had a constant size increasing effect that in terms of dimensional deviation was negative on the struts manufactured in the X and Z directions and again adverse on the X struts in the different measuring directions. The width of these struts significantly exceeds the designed width in the XY plane and is measurably below this value in the XZ plane, which is the consequence of the manufacturing induced deformation in the cross - section (square reproduced as half moon) of these strut.

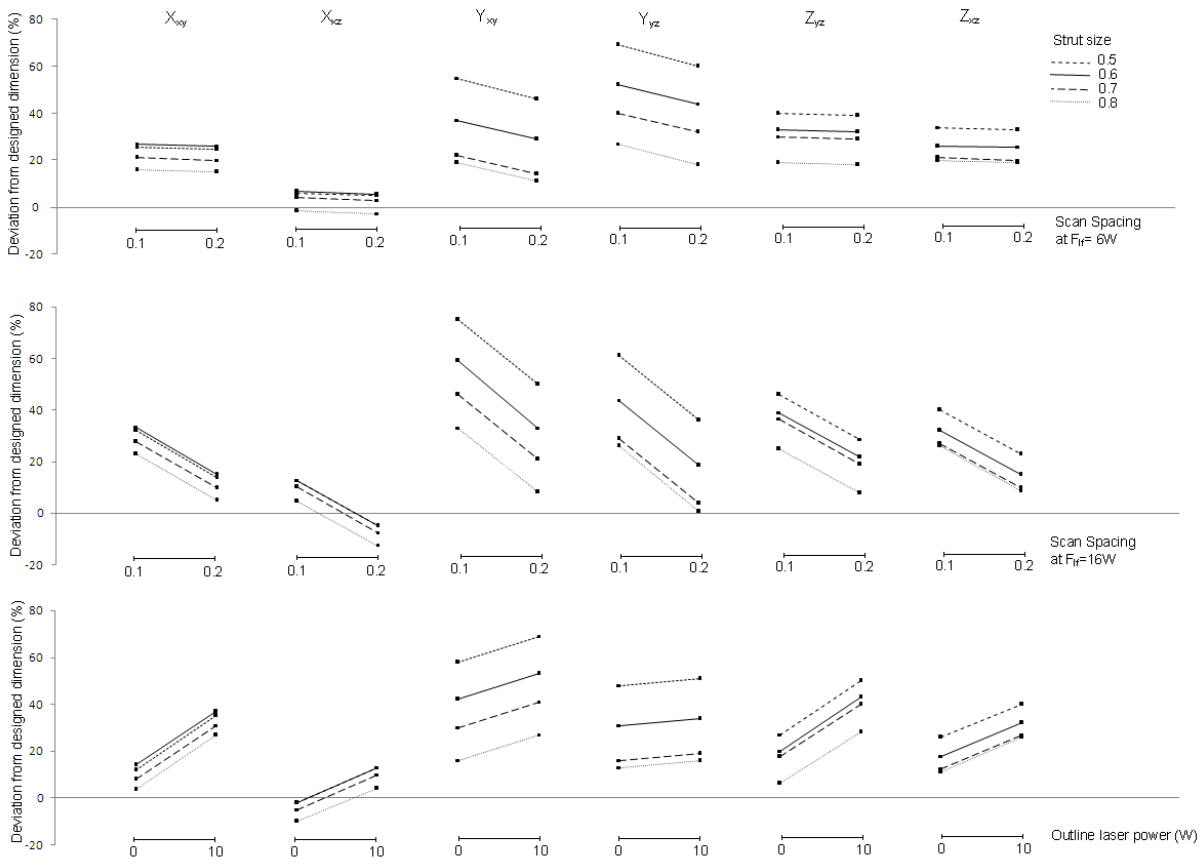

Figure 6.6 Process parameter effects on different strut sizes in different building and measuring directions, strut size range displayed is from 0.5 – 0.8 mm, target is being 0% of deviation

B. Appendix II.-Degradation and cell culturing procedures

This section details the procedures used for degradation and cell culturing experiments.

To assess degradation of fabricated scaffolds, fabricated samples were transferred to 24 well plates with sterile forceps. Samples were sterilized with 70% ethyl alcohol for 2 hours and then alcohol was washed away by several copious washes with sterile PBS (phosphate buffered saline). Samples were suspended in 2 ml sterile PBS (10 mM, pH 7.4) and then incubated under standard tissue culture conditions (37 °C and %5 CO_2). The degradation medium was changed aseptically weekly. After 1 weeks of incubation, samples were removed, washed with copious amount of distilled water and after blotted dry, were compression tested (n=3).

For determination of cell attachment; MC3T3 Mouse calvarial osteoblast cells were cultured under standard tissue culture conditions (37 ºC, 5% CO_2) in alpha-MEM medium (Gibco, USA) supplemented with 10 % Foetal Bovine serum and 1 % Penicillin/Streptomycin. All experiments were conducted with cell between passage 4-8. Samples were sterilized by immersion into 70% Ethyl alcohol for 2 hours and following washing steps with sterile PBS. Samples were stored in culture medium in a CO_2 incubator overnight to promote protein adsorption. The cells were trypsinized and the cell number was quantified by tryphan blue and then seeded onto samples, at a concentration 1x105 cells/cm^2 in 20 µL of medium. After an initial attachment period, the medium was completed to 500 µL.

To assess cell attachment, proliferation and morphology; samples were stained with DNA binding fluorescent reagent DAPI (to stain nuclei) and FITC-labelled Phalloidin (A fungal toxin with specific affinity to f-actin fibrils; to visualize cell cytoskeleton). Samples were fixed with 3.7% formaldehyde for 5 minutes and then rinsed with PBS. Afterwards cells were permeabilized by treatment with 0.1% Triton X solution. After removal of Triton-X; samples were incubated in 1% PBS-BSA solution at 37 °C for 30 minutes to decrease non-specific absorption of the dyes. Afterwards 1:1000 dilution of DAPI and 1:200 dilution of FITC-Phalloidin was applied to the samples and the samples were incubated in the dark for 15 minutes. After washing with copious amount of PBS, the samples were observed under an epifluourescence microscope under single or multiple fluorescence modes (Olympus, Japan).

Cell attachment and proliferation was quantified by Alamar Blue Cell proliferation assay (AbBiotech, USA) at 1 day and 7 days and 14 days post seeding. Alamar Blue solution (10% in serum free alpha MEM medium) was applied onto the samples and absorbance of the dye at 562 and 595 nm, was determined after one hour of incubation in culture. Absorbance readings were converted to dye reduction % as per instructions of the provider. Dye reduction (%) is indicative of cellular metabolic activity, i.e. higher reduction signifies higher cell number.

After toluidine blue staining, cells were fixed in osmium tetroxide for 30 min. Thereafter specimens were dehydrated through a series of ascending alcohols (50–100%) dried in Hexamethyldisilazane (HMDS) and left to air dry before sputter coating with gold. Samples were then viewed in a Zeiss EVO LS15 scanning electron microscope.

C. Appendix III. - Anisotropy of lattices with different macrostructures

In this set of experiments the PCL75 powder batch was exclusively used. In addition to the simple cubic lattice fabricated in the previous set, two other geometries were also manufactured. CAD models and their relative densities are presented in Figure 6.7. Dimensions of the simple cubic geometry were presented in Figure 3.1, for the Gibson-Ashby geometry the outer dimensions were preserved (6×9.6×9.6 mm) as well as the size of the struts (0.6 mm) and that of pores (1.2 mm). The outer dimension of the reinforced cubic structure was (5.1×9.6×9.6 mm), width of horizontal and vertical struts were 0.6 mm, diameter of diagonal struts was 1 mm. Relative density of the structures was not designed to be equal as comparison of different topologies at a given density level was not the subject of this work and achieving similar outer dimensions and complying with dimensional constraints imposed by the capability of the machine was considered more important than producing the exact same relative density for all structures. Designed relative density of all the structures was 0.3±0.04. This 6% variation in relative density accounts for less than 6 % variation in mechanical properties (Section 2.4).

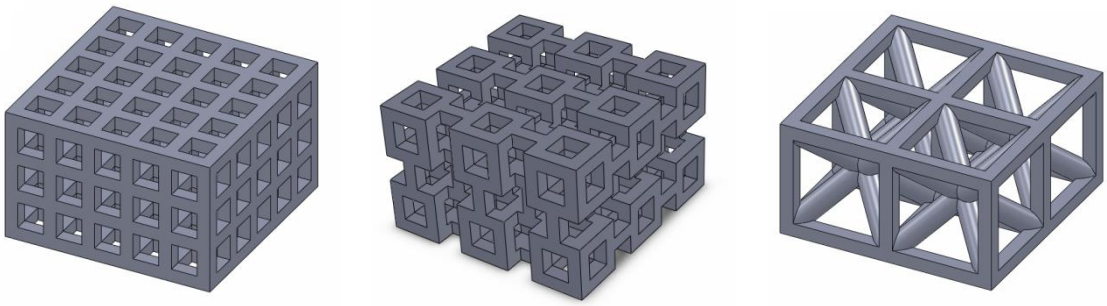

Simple lattice structure (relative density: 0.32) | Gibson-Ashby geometry (relative density: 0.3) | Reinforced cubic structure (relative density: 0.26)

Figure 6.7 Different designs of lattice structures and their relative densities

The objective was to examine mechanical behaviour and failure mechanism in SLS fabricated lattices. The most widely used periodic lattice structures (simple cubic, Gibson Ashby and reinforced cubic) were selected so that experimental results of this work can be related and compared to data available in literature and to analytical models that can easily be derived for these simple structures.

Results and Discussions

A detailed description of the observed mechanical behaviour has already been given in Section 4.2.1 for the simple-cubic lattices produced from PCL75. Therefore, only the Gibson-Ashby (GA) and the reinforced-cubic structures are presented below.

Produced GA structures showed very similar mechanical behaviour when built in the x- and y-directions, although parts were slightly weaker in the x-direction. Elastic modulus of samples in the x-direction was 1.23±0.13 and in the y-direction was 1.43±0.17 MPa. Modulus in the z-direction (0.66±0.06 MPa) was considerably below these values. While in terms of compressive strength the opposite tendency was seen. Highest value was measured in the z-direction (0.13±0.03MPa), followed by the y-direction (0.07±0.01 MPa) and lowest in the x-direction (0.07±0.01 MPa). Stress-strain response of the structures is shown in Figure 6.8.

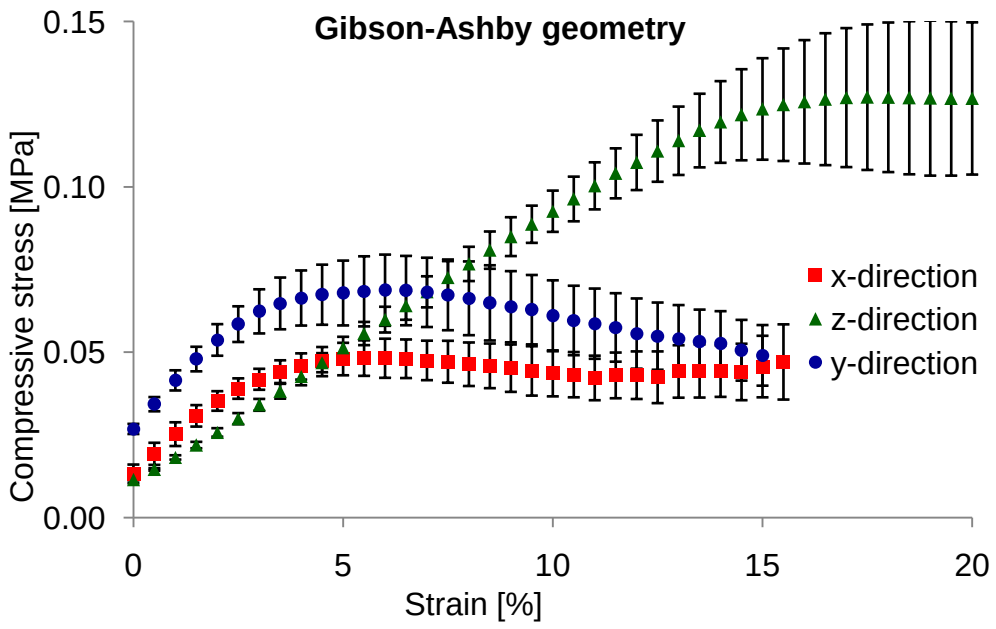

Figure 6.8 Compressive stress-strain response of Gibson-Ashby geometries in the three main building direction

The curves of the x- and y-directions almost run parallel to each other, however post-yield behaviour is slightly different as strain-softening is apparent in the y-direction while in the x-direction a constant stress level is maintained by further compression of the samples. Samples in the z-direction had a distinct response: yielding of the material occurred at significantly higher stress and strain values. Examination of the samples revealed the same differences. Figure 6.9 shows the micrographs of the compressed GA lattices in the different building directions. The same failure mechanism is seen in the x-

and y-direction, where loading was parallel with the built layers. The layers delaminate most severely along the conjunction of the z- and y-struts. Since, with this batch of powder, uneven layer deposition was observed during fabrication, bonding between subsequent layers is likely to be corrupted.

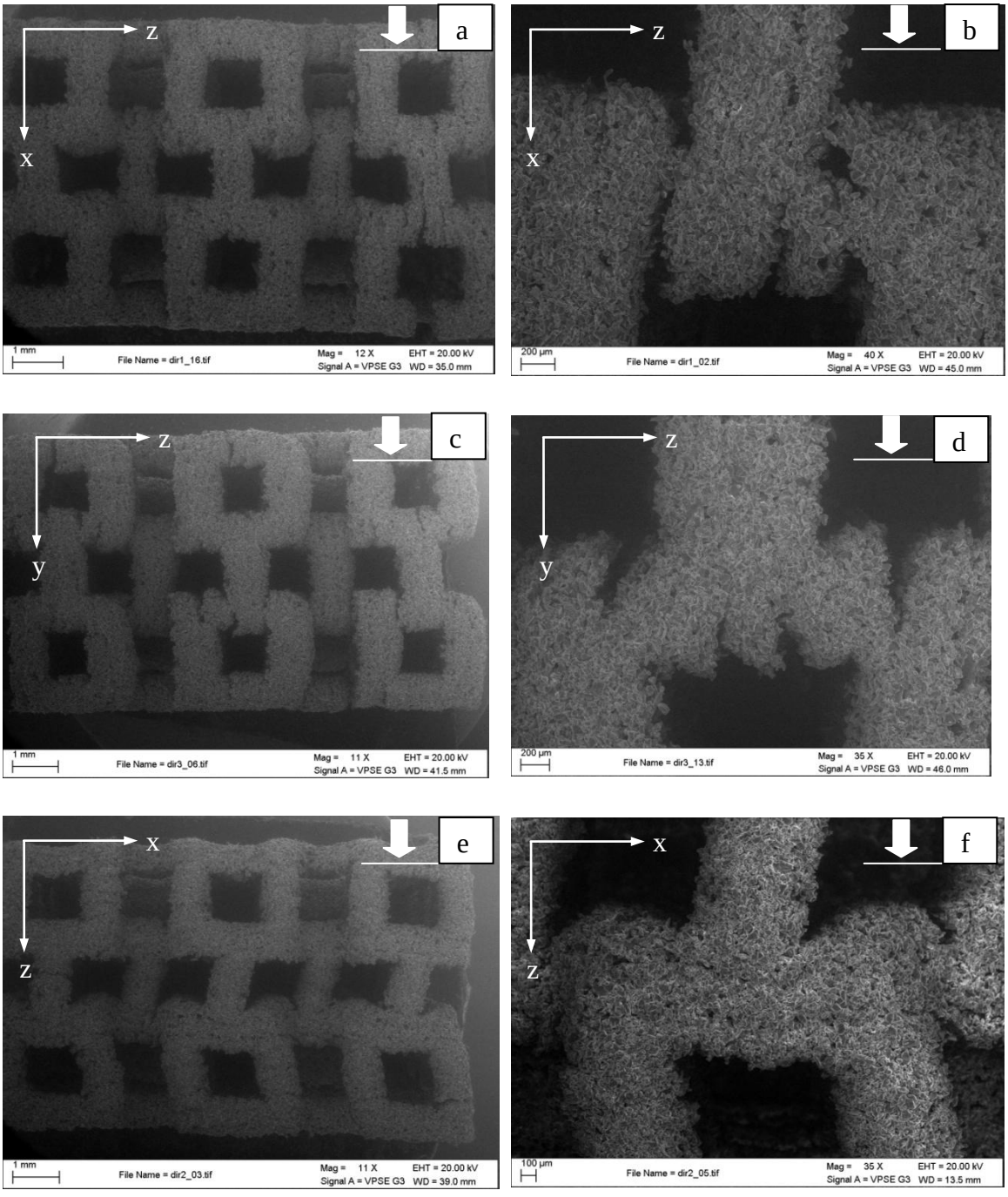

Figure 6.9 SEM images of compressed Gibson-Ashby lattices after subjecting them to strains below 20%: (a,b) x-direction, (c,d) y-direction, (e,f) z-direction

Failure mechanism in the z-direction was very different. Plastic hinges were formed at the conjunction of z- and x-struts and the z-struts tilted. At the beginning, individual struts tilt in random positions within the structure then the failure is localized within one

single layer that in the current case was the designed middle layer. First, instabilities (tilting of z-struts) were localized to this layer and with increased strain it propagated to the bottom layer. The close-up image (conjunction of x- and y-struts) shows that the x-struts are slightly bent. It is established in literature that the GA geometry is a bending dominated structure, which explains why it has considerably lower strength and stiffness than the examined simple-cubic structure. For instance, a bending dominated foam or GA structure, with a relative density of 0.1 is ten-times less stiff then an absolutely-stretch dominated structure (triangulated lattice) of the same relative density [75]. Therefore the GA geometry represents the lower bound of mechanical properties.

Reinforced-cubic lattices had the highest modulus in the y-direction (1.22±0.15 MPa) followed by the x (0.97±0.11 MPa) and z (0.66±0.094 MPa). Compressive strength was highest in the y-direction (0.15±0.02 MPa), followed by the z (0.09±0.01 MPa) and y (0.05±0.01 MPa). The compressive stress-strain response of the structures in the various building directions is shown in Figure 6.10.

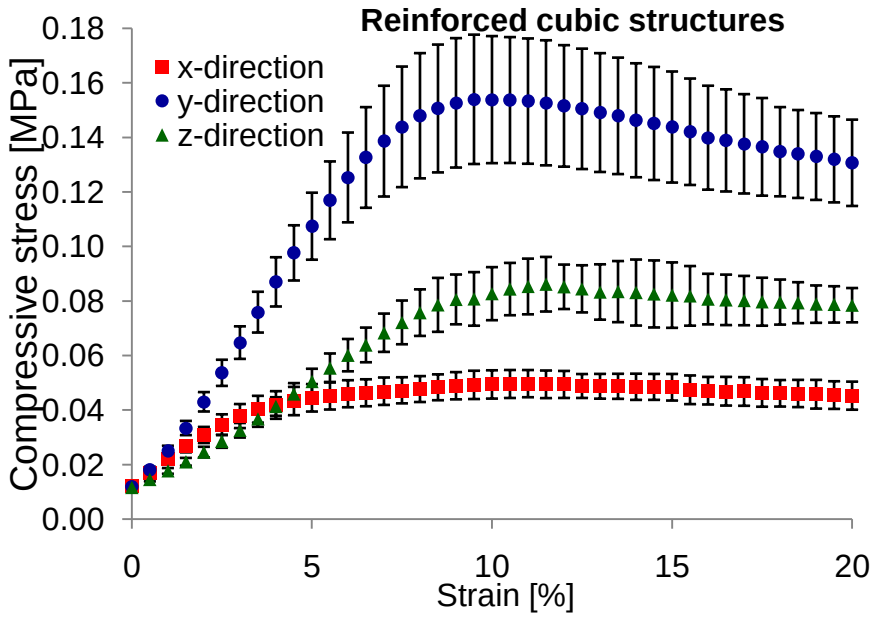

Figure 6.10 Compressive stress-strain response of reinforced cubic structures in the three main building directions

The curves confirm that structures were substantially stronger in the y-direction, however post yield strain softening was observed during compression of these lattices. In the x- and z-directions although measured stress and strain values were different the character of the response curves was similar. Beyond the yield point a plateau was maintained at a constant stress level, that makes these samples more favourable for

energy absorbing applications. Compressed reinforced-cubic structures were examined under SEM and micrographs are shown in Figure 6.11.

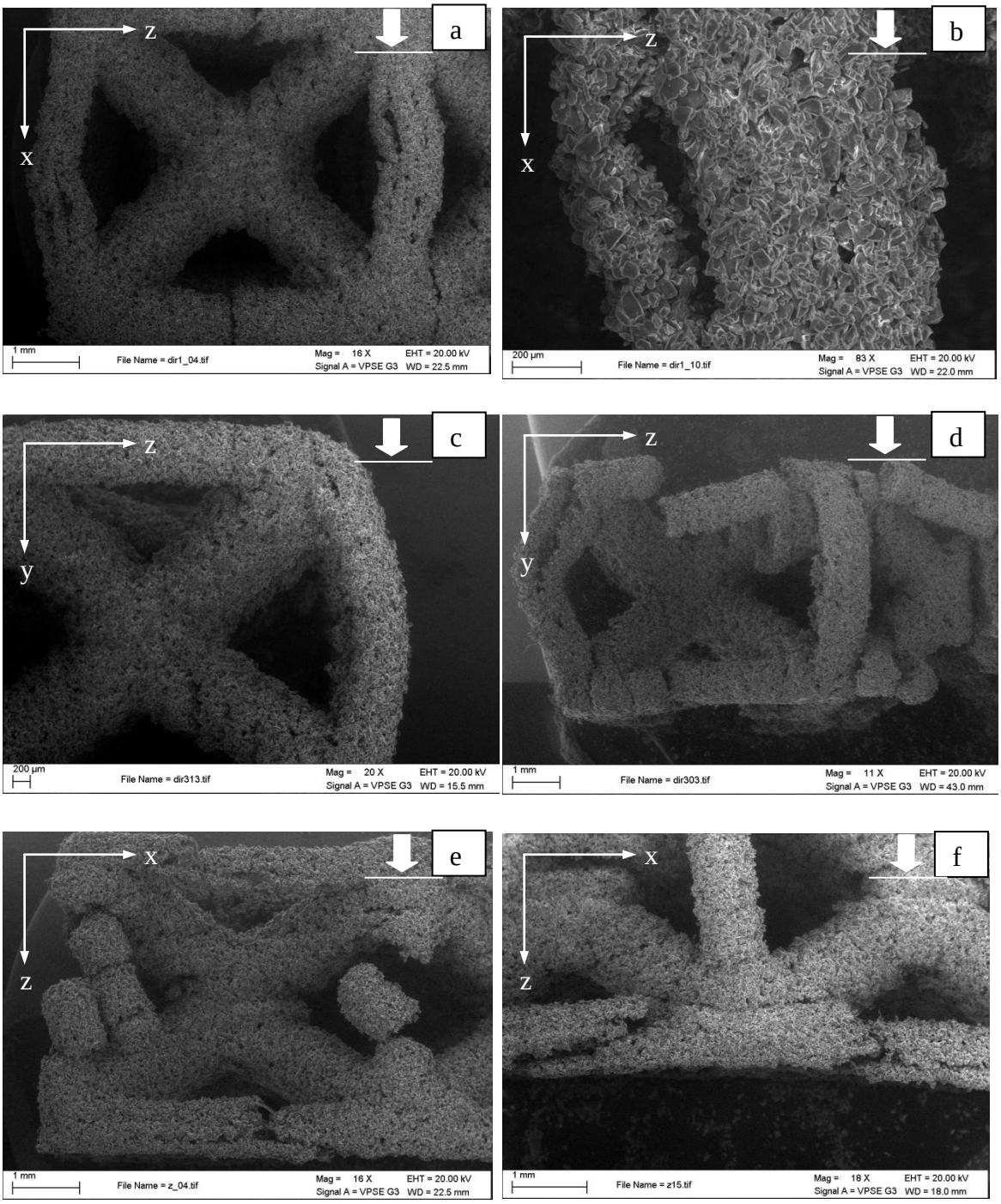

Figure 6.11 SEM micrographs of reinforced cubic structures: fabricated and tested at strain levels below 20% in the (a, b) x-direction, (c, d) y-direction and (e, f) z-direction

In the x-direction, first struts parallel to loading direction (x) buckled. The buckling was plastic as permanent deformation occurred via layer delamination. As strain was

increased (above 40%), struts perpendicular to the loading direction failed by stretching. Diagonal struts were relatively well preserved, however at high strains layer delamination was also present within these struts. It has to be pointed out that diagonal struts had bigger designed cross sectional area (0.554 mm^2 as compared 0.36 mm^2 of the x-struts). Similar failure mechanisms were seen in the y-direction, however it occurred at significantly higher strains. In the z-direction, failure started with deformation of the x-struts, plastic failure occurred via delamination and shifting of the layers within the strut. Then the load was borne by the diagonal struts, their deformation at higher strains initiated stretching of the x-struts. Again, as layer delamination played an important role in the plastic deformation of the samples in all directions, mechanical properties are expected to increase with elimination of the problem associated with uneven powder deposition.

When comparing the different designed geometries, simple-cubic lattices had the highest strength and stiffness values in each direction. Overall reinforced cubic structures were the weakest, except in the y-direction where the GA geometries had a considerably lower modulus and similar strength. These results are similar to the findings of Woß et al. [87] when testing similar lattices with constant relative density fabricated via SLS. This study, however did not examine the effect of orientation, and all samples were fabricated in the z-direction. The authors found that (among the structures tested in the current study) the simple-cubic structure was the strongest in terms of strength and stiffness and that this geometry exhibited the most severe strain-softening, which is very much in agreement with the current study.

A summary of the obtained mechanical properties for the various designed structures is presented in Figure 6.12 and Figure 6.13. The study demonstrated that tendencies in directional dependence are not limited to the firstly examined simple cubic structure but are valid for other micro-lattices that have different designed macro-topologies.

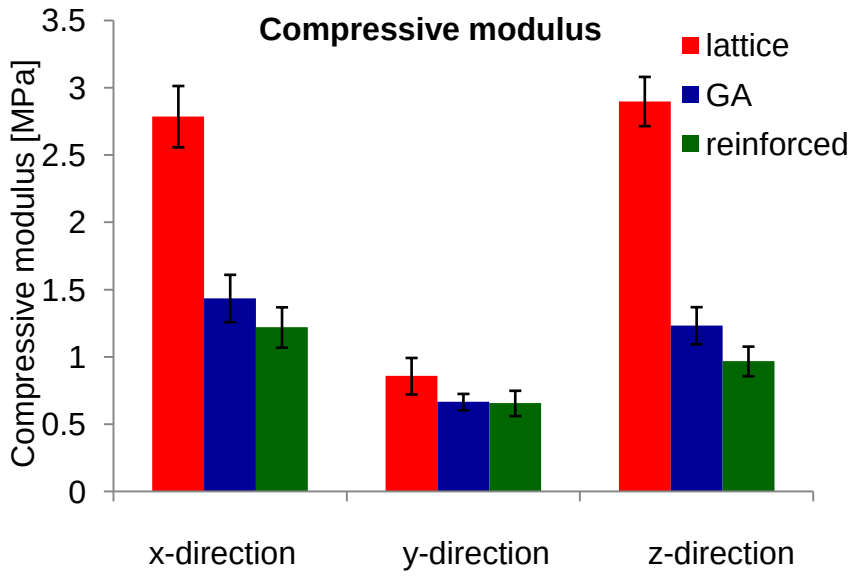

Figure 6.12 Compressive modulus of different designed structures fabricated using PCL75

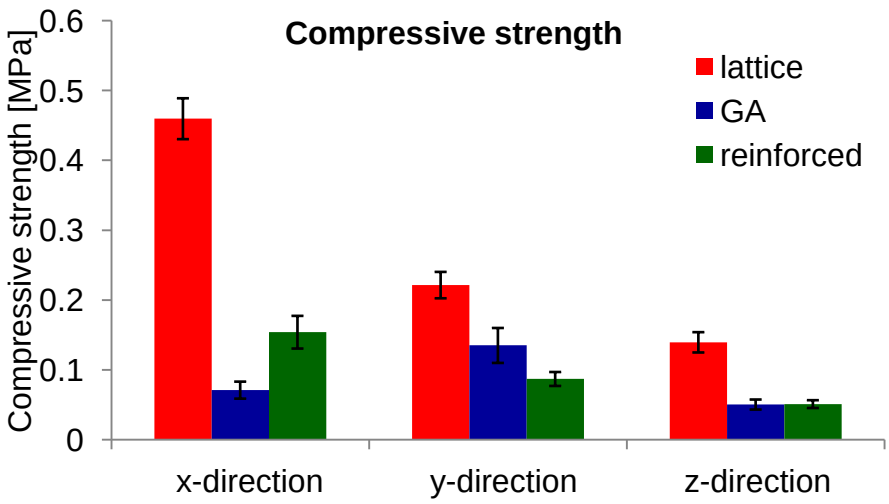

Figure 6.13 Compressive strength of different designed lattices fabricated using PCL75